The University Of Sheffield.

Amorphous Carbon Coating Systems for Pressurised Water Reactor Tribological Applications

Student: Jack L. Cooper

Academic Supervisors: Adrian Leyland & Allan Matthews

Industrial Supervisor: David Stewart

Nuclear Engineering Doctorate

Department of Materials Science and Engineering, University of Sheffield

Submission Date: August 2018

Abstract

Pressurised water reactors provide a very challenging environment for material selection, especially when components also have tribological applications. The high temperature and pressure of the water can cause premature failures due to corrosion and degradation of material properties, with costly consequences.

This Engineering Doctorate investigated the suitability of hard, wear resistant amorphous carbon coatings as one possible solution for Rolls-Royce to help meet the current demands of the nuclear industry to increase the lifetime, safety and reliability of components in PWR power systems, as long as the coatings can survive exposure to the extreme environment involved.

The first aim of the project was to examine the effect of high-temperature high-pressure water on the hydrothermal stability of commercial and lab-deposited amorphous carbon coatings. Four types of amorphous carbon coatings of particular interest were selected and exposed to high temperature water in pressure vessels then characterised to help understand their thermal and chemical stability and degradation behaviour.

The second aim of the EngD was to understand the effect of coating composition and architecture on the performance in high-temperature high-pressure water. Coatings were analysed in detail after hydrothermal exposure to determine possible failure modes and select promising coating features for future investigations.

At relatively low temperatures below 240°C it was found that all the studied coatings survived with little change in their coating properties. When the autoclave temperature was increased to 280°C however, hydrogen-containing diamond-like amorphous carbon coatings in particular suffered severe spallation, whereas hydrogen-free, graphite-like

amorphous carbon coatings remained intact, with most showing little change in their film properties. Following the characterisation, several material degradation mechanisms were discussed as the possible cause the observed film spallation, based on the observed changes.

Acknowledgments

I would like to begin by expressing my thanks to my academic supervisors Dr. Adrian Leyland and Professor Allan Matthews at the University of Sheffield and also my industrial supervisor Dr. David Stewart at Rolls-Royce for their guidance and support over the course of my Engineering Doctorate. I also want to show my appreciation for my sponsors Rolls-Royce and the Engineering and Physical Sciences Research Council for providing funding for this Engineering Doctorate.

I would like to extend my gratitude to the staff at the University of Sheffield, especially Dr. Ian Ross for his help with the transmission electron microscopy; Dr. Peter Korgul, Dr. Cheryl Shaw and Dr. Peng Zeng for their tutorship and patience with the electron microscopes; Dr Nik Reeves-McLaren for training me in Raman spectroscopy; Miss Dawn Bussey for teaching me to use the nanoindenter; and Mr. Andrew Fairburn for his help conducting the spectrometry testing. A special thank you also goes to Richard Kangley, without whom I would have surely gone insane polishing samples.

I would also like to thank all the members of the Research Centre in Surface Engineering for their comradery, especially our postdoctoral researchers Dr Alison Beck and Dr John Kavanagh whose initial experimental work helped to inform and guide my research. I also wish to thank all the staff and students at the University of Manchester involved with the Nuclear Engineering Doctorate, especially Dr. Jonathan Duff for his work conducting the autoclave experiments. I am additionally very grateful to Professor Gary Doll and his research group at the University of Akron for depositing some of the coatings studied in this thesis.

Finally, I want to express how extremely thankful I am to my parents Fiona and Peter, my brother and sister Gwilym and Ella, and also all of my friends and colleagues that have helped me during this journey. I also wish to thank Caroline and Oscar for their unconditional love and encouragement that brightens my life. You have all shown immeasurable support throughout my time working towards my doctorate and I love you all dearly.

Table of contents

List of abbreviations

a-C Hydrogen free amorphous carbon

a-C:H Hydrogen containing amorphous carbon

a-C:H:Me Metal doped hydrogen containing amorphous carbon

a-C:Me Metal doped hydrogen free amorphous carbon

ADF Annular dark field transmit ion electron microscope detector

AFM Atomic force microscopy

AISI 304SS American Iron and Steel Institute austenitic grade 304 stainless steel

AISI 431SS American Iron and Steel Institute martensitic grade 304 stainless steel

BF Bright field transmit ion electron microscope detector

BS Back scattered detector scanning electron microscope detector

BWR Boiling water reactor

C Carbon

CAPCIS Company formed from the Corrosion & Protection Centre and University of Manchester Institute of Science & Technology

CCD Charge-coupled device

CFUMSIP Closed Field Unbalanced Magnetron Sputter Ion Plating

Cr Chromium

CrN Chromium nitride

CVD Chemical vapour deposition

DC Direct current

DLC Diamond-like carbon

EDX Energy-dispersive X-ray spectroscopy

EELS Electron energy loss spectroscopy

EngD Engineering Doctorate

FIB Focused ion beam

GLC Graphite-like carbon

HAS 40100 Proprietary Rolls-Royce stainless steel alloy, similar composition to AISI 431

H/E The ratio of hardness to elastic modulus, related to the wear rate of materials

IBAD Ion beam-assisted deposition

ICPMS Inductively coupled plasma mass spectrometry

IPA Isopropyl Alcohol

MSIB Mass selected ion beam deposition

O Oxygen

PBS Phosphate-buffered saline

PECVD Plasma-enhanced chemical vapour deposition

PIII Plasma-immersion ion implantation

ppb Parts per billion

PTFE Polytetrafluoroethylene

PVD Physical vapour deposition

PWR Pressurised water reactor

Ra Profile roughness parameter

RF Radio frequency

R-R PLC Rolls-Royce public limited company

SE Secondary electron

SEM Scanning electron microscope

SCC Stress corrosion cracking

STEM Scanning transmission electron microscope

ta-C Tetrahedrally bonded amorphous carbon

TEM Transmission electron microscope

Ti Titanium

UK United Kingdom

W-C Tungsten carbide

List of figures

List of tables

Chapter 1: Introduction and background

1.1 Introduction

This Engineering Doctorate was a collaborative project between Rolls-Royce and the University of Sheffield. The project aimed to help gain fundamental understanding and resolve several issues relating to the use of amorphous carbon coatings in pressurised water reactor systems.

Amorphous carbon coatings have the potential to help solve some of the tribological issues Rolls-Royce would like to address in their pressurised water reactors. By varying chemical composition and deposition techniques it is possible to attain various desirable tribological properties. This Engineering Doctorate project aims to build upon existing knowledge of amorphous carbon coatings and also to gain a fundamental understanding of specific coatings in demanding PWR environments.

As one of the eventual applications is in the propulsion of nuclear submarines it was important for Rolls-Royce to source commercial coatings from companies with robust supply chains available in the United Kingdom. If a coating was found during this analysis that satisfied the desired performance in autoclave conditions it could provide useful knowledge when developing an optimised coating system for PWR applications.

The following chapter examines the industrial background and drivers for the Engineering Doctorate project. It will first give a brief overview of the nuclear fission reactor system and the typical conditions found in pressurised water reactors. It will then look at some of the materials used and tribological challenges posed by designing and operating a nuclear reactor. Finally the market position of Rolls-Royce will be

briefly analysed to help understand why the work in this nuclear Engineering Doctorate should be undertaken.

1.2 Project aims and objectives

Project Aims

The aims of this project were as follows:

(i) To investigate the hydrothermal stability limits of two commercially available and two lab-deposited amorphous carbon coatings when exposed to high-temperature high-pressure water in order to assess their suitability for use in pressurised water reactors.

The commercial coatings previously identified for investigation by Rolls-Royce were a diamond-like hydrogenated amorphous carbon coating and a graphite-like non-hydrogenated amorphous carbon coating.

Based on the knowledge of the graphite-like coating the two lab-deposited films were of a similar architecture but with differing metal dopants and interlayers to investigate their effect on the hydrothermal performance.

Chapter 3 of the thesis is focused on this investigation into the hydrothermal stability of amorphous carbon coatings in high-temperature high-pressure water.

(ii) To gain an understanding of the composition, structure, and features of the commercial and lab-deposited amorphous carbon coatings before and after exposure to high-temperature high-pressure water to determine their effect on coating performance and possible degradation mechanisms.

Chapter 4 records this study into the effect of different amorphous carbon coating properties on performance and failure in high-temperature high-pressure water.

Project Objectives

In order to investigate the thermal stability of amorphous carbon films in high-temperature high-pressure water, the commercial diamond-like and graphite-like amorphous carbon coatings were first exposed to deionised water in a Parr bomb pressure vessel at 240°C for periods of 24 hours and 7 days. The objective of these initial experiments was to quickly determine the whether the coatings showed signs of film delamination when observed by optical microscopy before and after exposure to determine their performance in lower bound pressurised water reactor temperatures. The methods used are outlined in Section 2.4.1 and the results are shown in Section 3.2 of the thesis.

The amorphous carbon coatings identified in the aims of this EngD were chosen to help answer the unresolved questions Rolls-Royce had about the effect of changing composition, structure, and deposition parameters on the relative hydrothermal performance of the coatings.

Coating Type A had been previously investigated for possible use in pressurised water reactors by Roll-Royce but had performed poorly at higher autoclave temperatures. There was a desire for further understanding of the material degradation mechanism in the diamond-like hydrogenated commercial amorphous carbon coating to determine what was causing the observed material failures. Further information on the different coatings is detailed in Section 2.2 of the thesis.

Coating Type B was a graphite-like non-hydrogenated amorphous carbon coating also chosen for further experimentation as it performed well in the previous studies conducted by Rolls-Royce but knowledge of its structure and composition were limited.

During this EngD study, the knowledge gained about the promising Coating Type B was then used to deposit Coating Type C with a similar composition and structure to perform experiments comparing the effect of changing interlayers and dopant materials. Coating Type D had the same deposition method as Coating Type C but the interlayer and doping material was changed from chromium to titanium to investigate the effect on coating performance during autoclave exposure.

To further investigate the limits of the commercial coatings and compare them with the lab-deposited amorphous carbon films all of the coating types were exposed to high-temperature high-pressure deionised water at 280°C for 7 days in an autoclave pressure vessel, as detailed in Section 2.4.2. Once again the coatings were examined using optical microscopy in Section 3.3 before and after the exposure to compare and identify any signs of degradation for later in-depth analysis.

All four of the exposed coating types were then characterised using scratch adhesion testing method outlined in Section 2.4.3 to determine whether the adhesion of the as-received coatings was sufficient enough to show that it was a mechanism associated with the exposure to high-temperature high-pressure water was causing film spallation, not just fundamentally poor coating adhesion. The results of this investigation are recorded in Section 3.4.

To assess the hydrothermal stability of all the coating types nanoindentation was used to measure hardness changes in the amorphous carbon films as shown in experimental methods Section 2.4.4. Reductions in hardness shown in results Section 3.5 have previously been linked to the graphitisation of amorphous carbon film with increasing temperature, with large decreases in hardness often linked to eventual coating failure in the previous Rolls-Royce studies [1].

Raman spectroscopy was then used as outlined in Section 2.4.5 to detect any changes in the amorphous carbon film structure by deconvolution of the peak data and then comparing differences in characteristic peak positions before and after pressure vessel exposure as the carbon bonding graphitises with temperature. Changes in peak position recorded in Section 3.6 could then be compared with the nanoindentation and optical microscopy to determine the effect of carbon bonding stability on coating failure after exposure to high-temperature high-pressure water.

In order to gain a fundamental understanding of the spallation mechanism in the commercial diamond-like carbon coating a sample was compared before and after exposure to high temperature and pressure water in an autoclave for 7 days. This sample was then compared with a sample from a previous Rolls-Royce investigation where the coating type had been exposed to high temperature water between 240˚C and over 300˚C in an autoclave environment for 2 years.

The characterisation of the coating degradation was conducted by scanning electron microscopy in Section 4.2 and transmission electron microscopy of a cross-section of the spalled area in Section 4.3 combined with energy-dispersive x-ray spectroscopy and electron energy loss spectroscopy of the changes observed in the distinct layers of the coating caused by degradation. The objective of characterising the autoclave exposed coatings was to obtain evidence to determine which of several possible degradation mechanisms was most likely to be causing the observed coating failure.

The structure and composition of the previously down-selected graphite-like non-hydrogenated commercial coating in Section 4.3.4 was also compared with the similar laboratory deposited chromium doped graphite-like amorphous carbon coating in Section 4.3.5 by using the transmission electron microscope to identify favourable

structures and compositions for possible further investigation or development. Reasons for their promising performance in autoclave conditions were then discussed by comparing coating features seen during microscopy and the Raman and nanoindentation data from as-received and from autoclaved samples.

1.3 Background to industrial problem

1.3.1 Nuclear fission reactors

Nuclear reactors are power systems used to create energy through the control of a sustained nuclear reaction. The process of nuclear fission involves the use of radioactive material to bombard and split atomic nuclei to create lighter atoms in a self-sustaining exothermic chain reaction [2]. This process produces large amounts of kinetic energy and electromagnetic radiation which are used to heat a working fluid, often water, helium or molten salts [3]. This then drives a heat engine which can be used to produce power for electricity or propulsion [4].

Nuclear power can be a very divisive technology. Proponents emphasize the safety and reliability, high energy density, and low CO_2 emissions associated with modern reactor designs [5] [6] [7] . Opponents often cite high capital costs, nuclear weapon proliferation concerns, past containment incidents, and safe disposal of irradiated waste as the main issues facing nuclear power [8] [9] [10] [11].

There have been significant changes in the nuclear power industry in the course of this EngD. As a result of the incident at the Fukushima Daiichi BWR plant in 2011 the safety of nuclear reactors following natural disasters was brought into question, with Japan subsequently shutting down most of its reactors [12]. As a consequence of the incident, Germany has also planned to speed up shut down all of its existing reactors by 2022 [13]. There have also been concerns with the commissioning of new builds as Westinghouse and Areva have experienced major financial and logistical issues with their new plants and reactors [14] [15].

There are therefore several internal and external risks involved with developing and operating nuclear technology as various risk factors have the potential to affect the demand for nuclear products and services internationally [16].

A major motivation in the nuclear industry is to provide life-time extensions to existing reactors [17]. This is due to the capital investment and risk associated with building a new reactor outweighing the continued operating costs of an existing reactor. As un-mitigated wear and corrosion eventually lead to component failure the degradation of material properties in reactors limits the length of time they can run safely and productively without costly repairs and maintenance [18]. One way of effectively increasing the life-time of nuclear plant could be with the use of coatings to improve the tribological performance of key components within the reactor. Protective coatings applied to surfaces in new or existing reactor systems could help to reduce the degradation of the underlying material and extend the safe operational life-time of the nuclear plant. The potential for amorphous carbon coatings to extend reactor life-time is explored and discussed in this thesis.

1.3.2 Pressurised water reactor power systems

PWRs are light water reactors consisting of two loops of pressurised, high temperature water as shown in the schematic diagram in Figure 1.1 [19]. The primary loop on the left in the figure contains the reactor pressure vessel and fuel core where the temperature of the water is increased by the radiation emanating from the radioactive elements in the fuel rods. There is then a transfer of energy from the primary loop through a heat exchanger to the separate secondary loop, which is then used to power turbines. Typical pressures and temperatures across the reactor range from around 290°C to 330°C and pressures typically between 6 and 16MPa at different points around

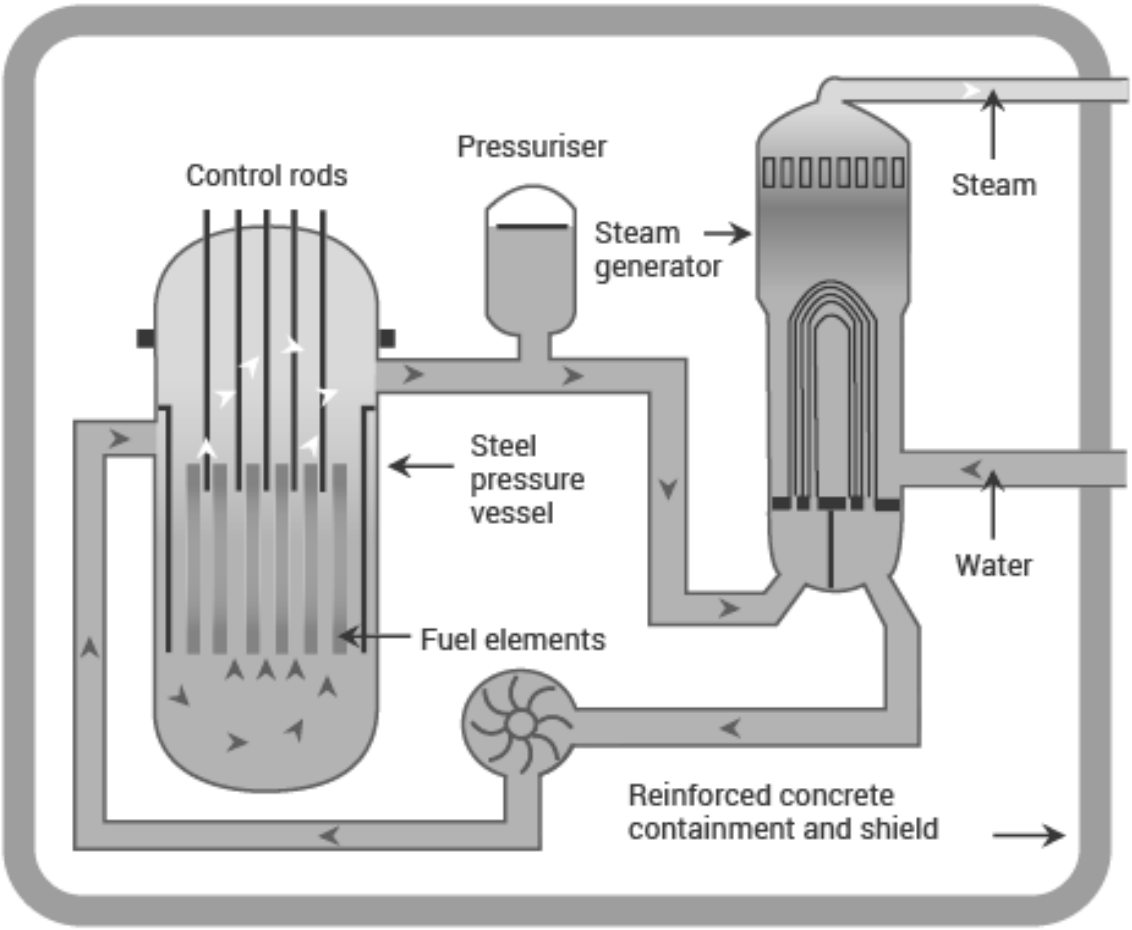

Figure 1.1 A schematic diagram of a pressurised water reactor [19].

the system [20]. Unlike boiling water reactors the PWR uses a pressuriser to maintain pressure in the primary water circuit to prevent it from boiling [21].

A major advantage of nuclear power comes from the energy density of the fuel [22]. This is of particular significance to the propulsion of naval vessels as refuelling costs time and money and most fossil fuels take up more weight and space than their nuclear equivalents [23]. In the current political environment nuclear non-proliferation has limited the usage of nuclear reactors to naval defence vessels like submarines and aircraft carriers and also land-based commercial reactors.

1.3.3 Pressurised water reactor chemistry

Chemistry of the reactor water is very important to the operation of the PWR because it allows the operators to control the radioactivity levels and conditions suitable for reduced corrosion of reactor materials. The water conditions in the PWR primary loop are typically fully deaerated with boric acid and lithium hydroxide in solution [24]. The additives act to maintain and control the subcritical operation of the nuclear reaction (boric acid) and to control the pH (lithia). Throughout the reactor the minimisation of any contaminants is highly desirable as they can cause component failure or become irradiated. The water in the secondary loop also uses chemical additives to help reduce corrosion and prevent loss of material performance through degradation mechanisms [25].

As amorphous carbon coatings have good chemical inertness in many applications they could be useful in the protection of component materials as they reduce the impurities and corrosion issues associated with some plating techniques.

1.3.4 Nuclear materials and tribology

Pressurised water reactors use a varied toolbox of materials to perform different functions in the plant. Stainless steel alloys make up the bulk of the materials used in the design of a typical PWR, however a variety of other materials are also used throughout the reactor to improve the performance of different components.

Stainless steel alloys contain a minimum of 10.5wt% chromium and can provide components with many useful properties including corrosion resistance, toughness, ductility, strength, and work hardenability. Stainless steels are used frequently in PWR environments as their mechanical properties reduce the need to maintain or replace components as often during the lifetime of the plant [26].

The use of alloys containing high levels of cobalt are a problem in nuclear reactor engineering as synthesis of the radionuclide cobalt-60 leads to particularly active and harmful waste [27]. Materials that have the potential to release anions like chlorides, fluorides and sulphides should also be avoided as they are associated with the stress corrosion and environmentally assisted cracking of stainless steels and other plant materials [28]. This means alternative surface engineering materials like polytetrafluoroethylene (PTFE) and molybdenum disulphide are not suitable for application in PWR environments despite possessing potentially useful tribological properties. There are also concerns over the environmental impact of chromium plating as hexavalent chromium (Cr(VI)) is highly genotoxic if released into the environment at any stage of the engineering process [29].

Zirconium and its alloys are also materials frequently used in the reactor, often to clad the fuel rods. They are useful for application in a pressurised water reactor as they have

good corrosion and thermal properties, as well as a low neutron cross section [30]. However they can sometimes be susceptible to hydrogen embrittlement and corrosion mechanisms related to the water chemistry of the reactor. In order to help reduce the effect of these degradation mechanisms some nuclear plant operators have used dense amorphous carbon films deposited on the surface of the cladding to provide a protective corrosion resistant layer that also has favourable tribological properties [31].

A major problem with PWR tribology is that oil based lubricants cannot be employed due to difficulties in their maintenance and usage in a pressurised, high temperature water flow [32]. Some amorphous coatings could therefore be a suitable option for coating components within the reactor as their self-lubricating properties allow wear resistance and low friction with very little contamination when compared to some other plating and thermal sprayed coatings.

Stopping a commercial reactor for maintenance is usually very costly as no power is produced during this time and extra levels of hazard protection must be employed when working with radioactively contaminated materials. Maintenance of submarine reactors involves additional problems as they must be brought into a dry dock and carefully dismantled, reducing the defensive capabilities available to the naval force. Increasing the lifetime of components through careful material selection could also lead to lower levels of irradiated waste due to fewer replacements during service. This also means less cost involved with decommissioning the nuclear reactors at the end of their lifecycle.

High purity nuclear graphite has also been used extensively in the history of nuclear reactors as both a moderator and reflector. Research into the effect of radiation on nuclear grade graphite may give some insight into the long-term behaviour of in-situ amorphous carbon coatings with graphite-like properties [33].

1.3.5 Rolls-Royce PLC

The company associated with this nuclear Engineering Doctorate project is Rolls-Royce. The business has divisions in civil and defence aerospace, energy, marine and nuclear providing integrated power systems and services. Capabilities include providing products and services to the naval nuclear reactor and civil sectors, as well as providing support services to land-based civil nuclear power generation both in the UK and around the world. The company provides components and engineering systems and support services for both existing and planned reactor builds, as well as providing small nuclear submarine reactors to the UK Royal Navy.

The United Kingdom's fleet of Astute-class nuclear submarines are powered by the Rolls-Royce PWR2 design. With the renewal of the Trident program the PWR3 plant, an improvement on the PWR2 design will be used to power the fleet of Successor-class submarines [34]. Being able to source components and services from within the UK is very important to national security as the supply chain for building nuclear power systems needs to be available independently. Small modular reactors are also of commercial interest to Rolls-Royce as the experience gained from working with naval reactors has potential for industrial power generation in other sectors [35] [36]. With increasing concerns about the environmental impact of greenhouse gas emissions and energy security associated with fossil fuels, nuclear power has the potential to reduce the impact of an energy gap when adapting to a more sustainable mixture of power generation in the UK [37].

Previous work by Rolls-Royce and The University of Sheffield has included the study of commercial amorphous carbon coatings when exposed to high temperature water in autoclaves. This work was conducted to assist the pressurised water reactor designers

and servicers at Rolls-Royce with suitable amorphous carbon coating options to be applied in situations where low friction and wear were desirable in the high-temperature high-pressure water. Rolls-Royce approached the University of Sheffield with the aim of gaining a further fundamental understanding of these coatings and also to work towards an optimised coating system for PWR applications. The coating should have stability over a long lifetime, possibly several decades, without servicing. The target is to exploit the desirable tribological conditions attainable with the studied amorphous carbon coatings in order to reduce friction and wear to improve the efficiency and lifetime of components within the reactor.

From this project Rolls-Royce aimed to gain a valuable understanding of the performance of commercial amorphous carbon coatings in service and also develop an optimised coating system for tribological use around the pressurised water reactor. By using the attractive tribological properties of high hardness, low friction coefficients, low wear rates, and chemical inertness achievable with different amorphous carbon coatings Rolls-Royce aimed to add value by improving the performance and extending the service lifetime of their PWR components.

1.4 Current state-of-art in amorphous carbon coatings

As this Engineering Doctorate focused on the use of amorphous carbon coatings for tribological applications, this section covers the fundamental chemistry of amorphous carbon films, including their bonding and structures. It then looks at the methods available for depositing amorphous carbon films and the effect of composition and dopants on the tribological properties of the coating. Finally it explores the current industrial applications of the coatings and how they perform in different conditions.

1.4.1 Carbon bonding and allotropic structures

Carbon is a non-metallic element whose properties can vary significantly with their allotropic state. The allotropic structures that carbon can exhibit are due to three atomic hybridisations; sp^1, sp^2 and sp^3. The sp^3 configuration consists of a carbon atom with four tetrahedrally oriented valence electrons as shown in Figure 1.2 [38]. The electrons found in the sp^3 orbitals form exceptionally strong σ bonds with adjacent atoms, leading to the outstanding physical properties frequently found in the sp^3 bonded allotropes. In the sp^2 hybridisation the four valence electrons are split, with three forming trigonally

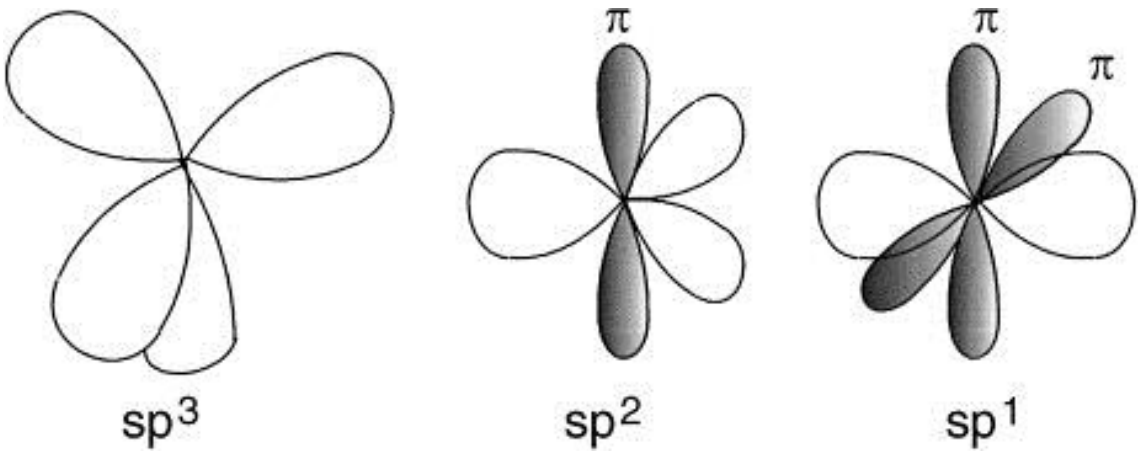

Figure 1.2 The configuration of carbon bonding hybridisations sp^1, sp^2 and sp^3. [38]

oriented orbitals with σ bonding and one creating a pπ orbital normal to the sigma plane forming weaker π bonds with other nearby π orbitals. The sp^1 hybridisation exhibits a split in the bonding types whereby two of the valence electrons enter π orbitals, with the other two electrons forming σ bonds in the σ orbitals.

Carbon allotropes include graphite, diamond, graphene, and various fullerenes, with the bonding structures shown in Figure 1.3. Diamond has a structure of covalently bonded sp^3 carbon in a cubic crystal lattice. The tetrahedrally oriented valence electron orbitals in the sp^3 allotrope form a crystal structure of strong directional σ bonds of equal strength with neighbouring carbon atoms. This leads to the exceptional physical properties of hardness and wear resistance commonly associated with diamond. Conversely, graphite has sp^2 bonded carbon in a two dimensional hexagonal lattice planes. This structure arises from the sp^2 hybridisation forming strong bonds with the adjacent σ bonds to create hexagonal planes, which are then weakly connected by van der Waals bonds between these layers. The weak van der Waals forces allow shear forces between the planes, with humidity reducing friction further as the interlayer

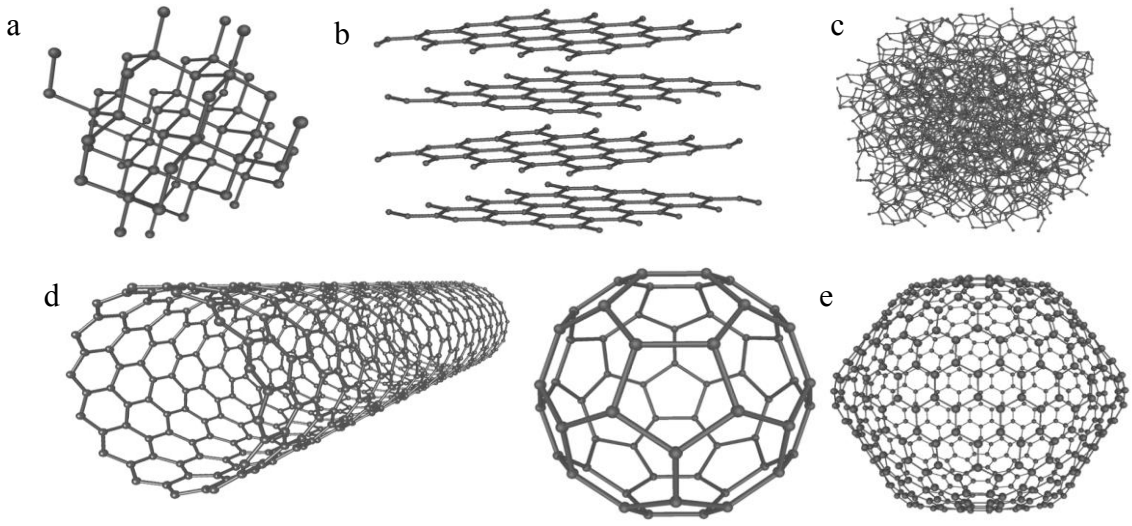

Figure 1.3 Bonding structures of carbon, a) Diamond, b) Graphite, c) Amorphous, d) Carbon Nanotube, e) Fullerenes.

bonding forces are lowered.

Other allotropes include Graphene, single sheets of the sigma bonded sp^2 planes found in graphite. Graphene has several interesting properties including excellent electrical and thermal conductivity [39], as well as many applications in the field of optics and chemical doping currently under investigation by researchers [40]. By applying atomic force microscopy-based nanoindentation techniques to a single sheet of suspended graphene it has also been found to be one of the hardest materials known to science, with a Young's modulus of 1.0 TPa [41].

Graphene is also the building block for the group of allotropes called fullerenes. The term fullerene refers to the group of spherical or tube-like carbon structures which include Buckminsterfullerene and carbon nanotubes. Research into the application of fullerenes for tribological purposes has also shown that fullerene-included nano-oil has been produced to reduce friction in engineering applications [42].

The allotrope that was researched in this Engineering Doctorate was amorphous carbon. This carbonaceous material contains an amorphous network of sp^2 and sp^3 bonded carbon atoms. Amorphous carbon can possess a wide variety of properties dependant on various physical and chemical variables and deposition techniques, as described later in this chapter. The term diamond-like carbon (DLC) is often used when referring to amorphous metastable carbon materials which contain a significant proportion of the sp^3 bonding found in the microstructure of diamonds. They typically have characteristic properties similar to those of diamond including high hardness, low wear, chemical inertness and low friction coefficient [43]. Another variation of amorphous carbon is graphite-like carbon (GLC). Graphite-like carbon also contains an amorphous combination of sp^2 and sp^3 carbon but has a higher ratio of sp^2 bonding compared to

DLC coatings. GLC coatings have some properties similar to those of graphite, like low friction coefficient, but have higher wear rates and lower hardness values compared to DLC coatings [44].

1.4.2 Amorphous carbon coating deposition techniques

Depositing amorphous carbon coatings involves the bombardment of the target substrate material by positively charged carbon ions whilst maintaining enough energy from impacting force to drive the compression of sp^2 bonds to sp^3 type bonding. This enforced carbon densification results in a compressive stress in the growing film [45]. It has also been found that amorphous coatings frequently follow the initial substrate morphology closely leading to increased local film stresses as the deposition thickness increases [46].

The first major developments in amorphous carbon coatings were explored in the 1970s by Aisenberg and Chabot. Their work synthesised diamond-like carbon by ion beam deposition on room temperature substrates, producing thin, hard, insulating, chemically inert films. They also conducted experiments with the films using a 1 Mrad cobalt-60 source, the results of which suggested encouraging radiation resistance [47]. Further studies into amorphous carbon films were also conducted by Spencer *et al.* [48] by an ion beam deposition process similar to that of Aisenberg and Chabot. Later work from Bubenzer *et al.* in 1980s focused on the optical properties of RF-plasma deposited DLC films [49]. Research was also conducted on the electronic properties of DLC, however it was later suggested that the application of DLC coatings in this field would be either unsuccessful or uncompetitive when compared to other materials developed. It quickly became apparent in these early studies that the properties of amorphous carbon films would make them difficult to characterise. The main problem was that their insulating nature caused the samples to attain charge, making the usage of Auger spectroscopy and electron microscopy difficult.

Interest was also greatly increased in the 80's due to new deposition techniques that allowed carbon coatings to be created by cathodic arc physical vapour deposition. These coatings allowed the growth of the 'hydrogen free' tetrahedral amorphous carbon (ta-C) with very low hydrogen percentages.

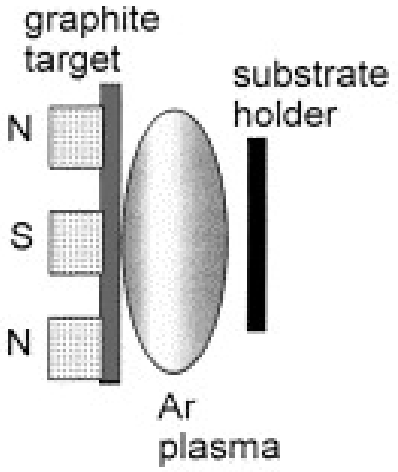

Figure 1.4 Schematic diagram of sputtering deposition technique [38].

The current methods used to produce amorphous carbon coatings are variations of physical vapour deposition (PVD) and chemical vapour deposition (CVD) processes [43].

Physical Vapour deposition of amorphous carbon involves various techniques to produce a vapour of the target material by physical processes which are then deposited as coatings on the target material.

Sputtering is the PVD technique commonly used for commercial DLC coating applications and involves RF or DC sputtering a carbon target by argon plasma [38]. To improve the coating deposition rate a magnet is placed behind the graphite target as shown on the left of Figure 1.4, causing an increase in plasma ionisation as the electrons spiral towards the target. A variation of this method involves using ion beam assisted deposition [IBAD] to sputter both the graphite target and the deposited film with Ar

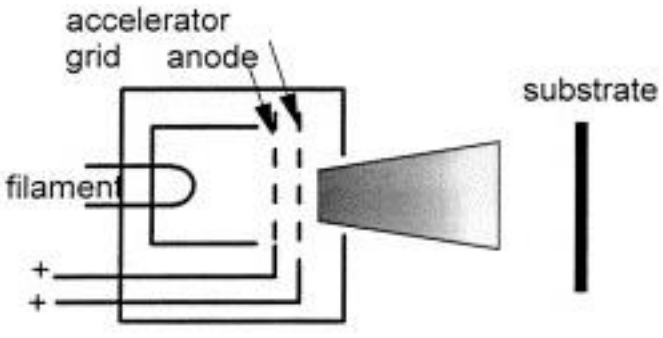

Figure 1.5 Schematic diagram of ion beam deposition technique [38].

ions as shown in Figure 1.5, increasing sp^3 bonding and densification as the coating material is further energised by the ion beam [50]. Sputtering is often the method most used for coating industrial components as the deposition process is relatively easy to predict and control and the technique can be scaled up to coat larger components [51].

Ion beam deposition of amorphous carbon films involves the ionisation of a carbon source by plasma, and then accelerating the ions using a voltage bias electrode through a grid to form a beam onto the substrate surface. The ions are usually obtained from either the sputtering of a graphite cathode or, as in the technique developed by Kaufman, from the ionisation of a hydrocarbon precursor gas. This method involves the inclusion of neutral and hydrocarbon species incident in the flux at the substrate, thus reducing the relative ion flux [52]. Mass selected ion beam deposition [MSIB] involves the separation of specified ions of certain species and energies. The division is performed by ion divergence when passed through a mass selecting magnetic filter. This method allows coatings of tetrahedral amorphous carbon to be produced. However the growth rate is slow, with adhesion and thickness limited by the compressive stresses in the deposited films. Another disadvantage is the increased cost and size of the coating equipment, limiting the popularity of industrial application [53].

Deposition by cathodic arc is a technique sometimes used to produce amorphous carbon films by initiating an arc on the surface of a carbon cathode using a striker as shown in Figure 1.6 to produce pure carbon plasma. The carbon ions can

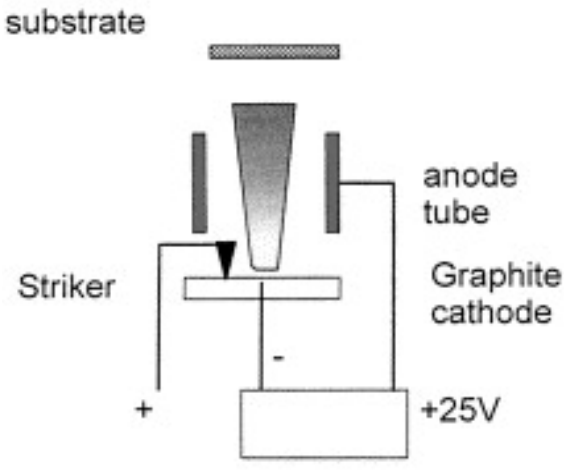

Figure 1.6 Schematic diagram of cathodic arc deposition technique [38].

then be filtered by magnets to create a singly charged beam. A similar resulting ta-C coating can be achieved by laser ablation of a carbon target to produce a carbon plasma plume [54].

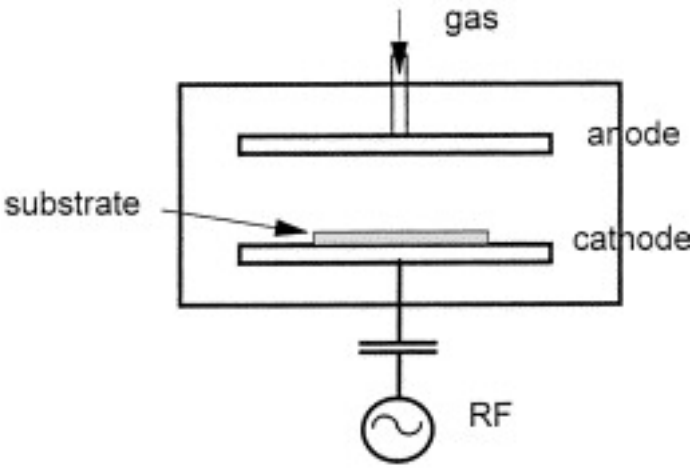

Figure 1.7 Schematic diagram of plasma deposition technique [38].

Amorphous carbon coatings deposited by chemical vapour deposition are made by using carbon-containing precursor gases that build a film on the surface of the substrate on contact.

Plasma enhanced chemical vapour deposition [PECVD] is a very popular technique for depositing amorphous carbon in the laboratory and commonly involves the use of a biased substrate which is bombarded by an ionised hydrocarbon RF plasma created between two electrodes, as shown schematically in Figure 1.7. This environment causes ions to energetically bombard the surface of the substrate causing the film to increase in density and improving mechanical properties [55].

Plasma Immersion Ion Implantation [PIII] involves positioning the substrates directly in the plasma source and applying a very high voltage (>20kV) pulse-bias, allowing complex-shaped components to be coated as the technique is non-line-of-sight [56]. Several experiments into amorphous carbon films deposited by PIII show that by changing the coating parameters and elemental content it is possible to attain improvements in performance that could aid in the development of an amorphous carbon coating system for PWR applications.

Xuejing *et al.* found that by varying the acetylene to argon ratio in the precursor gas mixture it was possible to affect the sp^2 and sp^3 content of the deposited films [57]. Their results showed that argon fractions below 50% produced a more diamond-like coating due to the bombardment of the argon ions. When the argon content was above 50% the produced films were more graphite-like in nature and had better adhesion to the substrate.

Mitsuo *et al*. found that the hardness of the PIII deposited amorphous carbon films could be decreased by increasing the acetylene pressure, the process time and the bias voltage [58]. They reasoned that the hardness reduction was linked with decreasing stress in the films due to the heating effect these parameters create, though they found the effect was saturated after process times of 120 minutes.

Experimental work performed by Ming Xu *et al.* demonstrated that PIII equipment can be used to provide alternate means of doping amorphous carbon coatings. They used the ion implantation of tungsten on a-C:H films to form W-C nanocrystallites near the surface of the coating. The effect of the ion implantation was an increase in the hardness due to the compressive stress, however it also caused the surface of the amorphous carbon to graphitise which acted to decrease the friction coefficient of the film when compared with typical W-C films [59].

The scaling–up of plasma immersion ion implantation technology is of particular interest to industry as it allows large component areas to be coated with hard, strongly adherent coatings. Collaborative work performed by the Los Alamos National Laboratory and General Motors aimed to demonstrate the applicability of large-scale PIII deposition to manufacturing and produced amorphous carbon films that were highly adherent with a high deposition rate [60]. Work by Bugaev *et al.* built on this

experimentation to deposit diamond-like films on substrates which had increasing adhesion as the intrinsic stresses were reduced by increasing ion bombardment [61].

1.4.3 Composition, structure, and dopants

By changing the elemental composition of amorphous carbon coatings it is possible to dramatically alter the properties exhibited. The two most important factors affecting the mechanical properties of amorphous carbon films are the hydrogen content and the ratio of sp^2 to sp^3 bonding [52]. A helpful way of categorising amorphous carbon films is with the use of the ternary phase diagram from Robertson [38] as shown in Figure 1.8, first proposed by W. Jacob and W. Möller [62]. In coating applications amorphous carbon is often classified by its prevalent bonding types, hydrogen content and contained dopants. These coating groups are referred to as tetrahedral amorphous carbon [ta-C], hydrogenated amorphous carbon [a-C:H], and metal doped hydrogenated amorphous carbon [a-C:H:Me] [63]. The percentage of hydrogen included in the coating creates a large variation in the mechanical and chemical properties of the films. The term tetrahedral amorphous carbon (ta-C), first coined by McKenzie [64] to distinguish from sp^2 a-C, is used to describe amorphous carbon films with the largest sp^3 content and lowest hydrogen content. They have mechanical, optical and electronic properties close to that of diamond [43]. The inclusion of hydrogen in the hydrogenated a-C:H films tends to decrease the Young's modulus and hardness of the film [43]. The density is also decreased with increased hydrogen percentage, along with the thermal stability

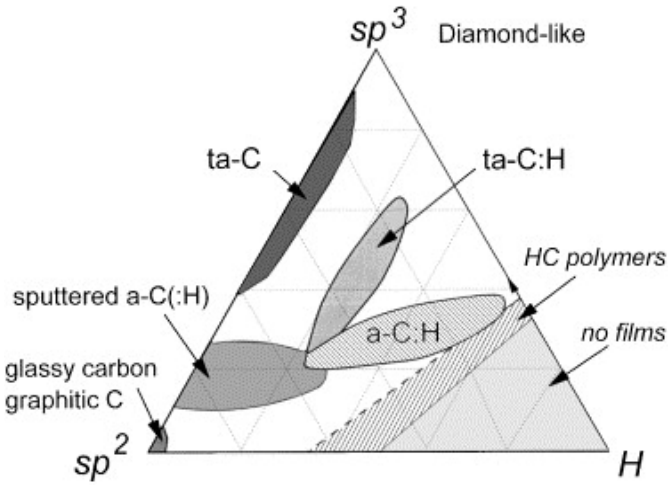

Figure 1.8 The ternary phase diagram for carbon films with sp^3, sp^2 and hydrogen. [38]

and internal stress during deposition [38]. At high hydrogen concentrations the dangling sp^3 C bonds are terminated by hydrogen and impart relatively low density and hardness to the film [43].

Amorphous carbon films are also frequently doped with other elements to optimise coatings for specific applications and environments [43]. Adhesion of the coating to metallic substrate materials can be improved by layering/doping with elements like silicon, nitrogen, and various metals to reduce stress and delamination effects [65]. Commercial coatings often use a metallic interlayer or series of metal-metal nitride /carbide interlayers between the substrate and coating in order to reduce stress arising from mismatch between the dissimilar materials. Chromium based materials are often used in this layer in many commercial coatings as they act to improve adhesion to the substrate and reduce corrosion pathways. Deposition temperature and in-service temperature and conditions have an effect on coating performance that should be taken into account when designing coatings.

Reducing the thermal expansion coefficient mismatch during thermal cycling can also decrease the internal stresses between the amorphous carbon film and the substrate [66]. For example, with the inclusion of silicon it is possible to reduce the internal stress during deposition, increase the thermal stability at high temperatures and maintain a low friction coefficient at higher humidity [67].

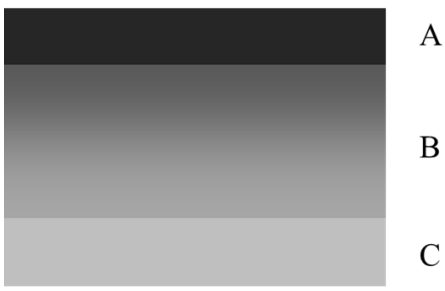

Figure 1.9 Typical commercial amorphous carbon coating structure, A) functional amorphous carbon coating, B) a graded adhesive interlayer or multilayer, C) component substrate material.

An important aspect of the research into an optimised amorphous carbon

coating system concerns the use of functional interlayers between the film and substrate as in Figure 1.9. Carbide forming transition metals are frequently used as functional interlayers [43], however the range of elements used in commercial coatings for nuclear applications is limited due to radioactivity and corrosion concerns in the reactor environment [68]. Adding functional interlayers to the coating can also assist in reducing corrosion related to capillary intrusion through pore defects in the film [69]. From the autoclave work conducted previously by Rolls-Royce it was found that the amorphous carbon coatings deposited without an interlayer all completely delaminated, highlighting their importance of the interlayer to overall coating performance [1].

1.4.4 Coating tribology and stability

The tribology of amorphous carbon films can be very complex, displaying great variations with coating composition and environmental exposure. Wear mechanisms and mechanical properties can vary dramatically dependent on the environment; temperature, pressure, and chemical interactions [70]. In ambient environmental conditions the typical tribology for amorphous carbon involves the formation of a tribolayer of lubricious graphitised material on the surface of the counterface [43]. This layer acts to reduce the friction and wear between the two surfaces [71].

This section will review studies into the effect of aqueous environments on DLC, mainly conducted in the biomedical and automotive fields. These included static tests on the thermal stability of DLC in high temperature, high pressure water and also the effect various levels of humidity and water immersion had on DLC coatings during wear testing.

Experiments into the thermal stability of ta-C DLC films in water at elevated temperatures and pressures were conducted by Calderón-Moreno [72]. Figure 1.10 shows that between the temperatures of 200 and 400°C in water at a pressure of 6MPa

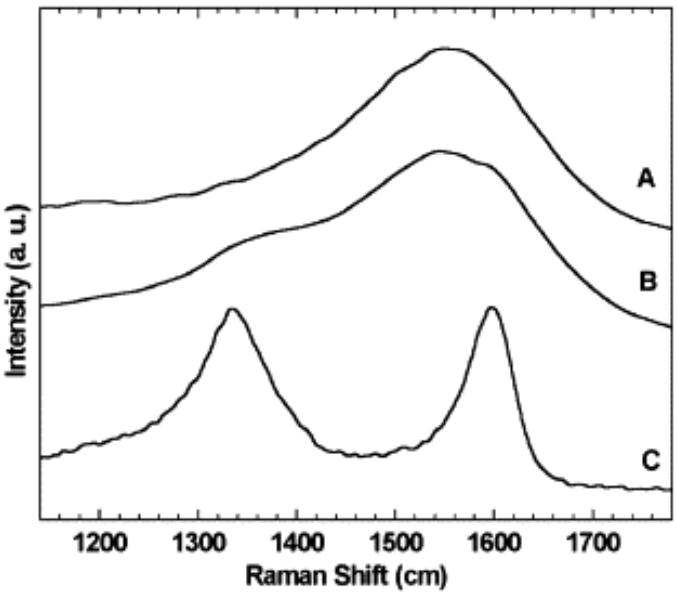

Figure 1.10 Raman peak shifts with increasing water temperature during experiment A conducted at 200°C, experiment B at 400°C, and experiment C at 600°C. [72]

(conditions typically found in the secondary loop of PWRs), there was a shift in the Raman spectroscopy peaks with an increase in intensity around 1350cm^{-1} and a movement of the peak at around 1550cm^{-1} to around 1600cm^{-1}. These changes in the Raman spectrum suggest a partial graphitisation of the ta-C film as sp^3 bonds are converted to sp^2 bonds [38]. The application of Raman spectroscopy to characterise changes in amorphous carbon films after degradation in service is discussed further in section 2.5.4 of the thesis. At higher temperatures this trend continued until a complete conversion to a nanographitic sp^2 amorphous carbon was observed over 600°C. Initial work at the University of Sheffield with static autoclave tests support these findings, with many commercial DLC coatings unable to withstand the pressurised water at elevated temperatures, even without any applied mechanical loading [1].

An investigation conducted by Tallant *et al.* into the effect of different environments on a diamond-like carbon CVD coating containing hydrogen concluded that the studied films were structurally stable up to around 260°C [73]. They found that boiling de-ionised water at around 95°C caused no changes in the Raman spectra of the film before and after exposure, but they did report that the coating had a tendency to partially flake off the tungsten substrate. The study also looked at the effect of a humid environment at 225°C on the DLC coating but also observed no changes in the Raman spectra of the films, as well as recording the conversion of the coating to nano-crystalline graphite above 300°C in ambient air.

Research by Andersson *et al.* found that introducing water vapour into a pin-on-disc wear testing chamber where both the substrate and counterface were coated caused a significant decrease in friction coefficient from 0.6 to 0.07 for an cathodic arc deposited hydrogen free amorphous carbon films, whereas the highly hydrogenated PECVD DLC

films saw a slight increase [74]. Drees *et al.* also found the hydrogenated a-C:H coatings failed suddenly and catastrophically in pin-on-disc tests against a steel counterbody when exposed to aqueous environments, an effect they attributed to the adhesive delamination of the coating at the coating-substrate interface [75].

Work conducted by Chandra *et al.* into the effect of aqueous environments on the mechanical stability of DLC coatings for biological applications showed that exposure to water at 37°C for 4 weeks produced no change in the DLC coatings, however exposure to a phosphate buffered saline solution caused extensive damage and delamination as it infiltrated and attacked the interface through pores and cracks in the coating. It was also found that increasing the temperature caused an increase in coating damage as this capillary action was exaggerated [76].

In other tribological studies Masuko *et al.* have found that increasing the substrate roughness of stainless steels can help to reduce delamination of hydrogenated CVD amorphous carbon coatings during sliding wear tests in water [77]. They also found that slightly polishing the diamond-like carbon surface reduced the wear on the counterface caused by increasing the substrate roughness.

The performance of two commercial amorphous carbon coatings immersed in distilled water high load sliding wear tests were studied by Stallard *et al* [78]. They found that the hydrogen free amorphous carbon-chromium multilayer coating (Graphit-iC) deposited by closed field unbalanced magnetron sputtering survived the tests in water, maintaining a low friction coefficient throughout. The wear rates of the Graphit-iC coating was found to be equal to or less than those found when exposed to air. A secondary coating (Dymon-iC), a PECVD deposited a-C:H, failed the test even at relatively low loads.

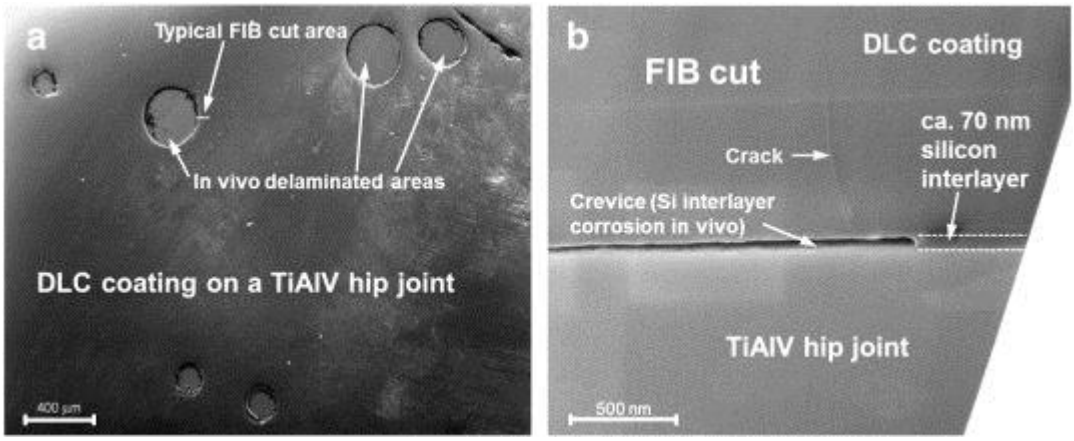

Figure 1.11 A top-down SEM image of a delaminated DLC coating after in vivo testing b) A FIB cross-section showing the crevice corrosion of the adhesive interlayer. [79]

Coating spallation was observed by Hauert *et al.* in their study of the long-term adhesion of diamond-like carbon coatings for in vivo biomedical applications [79]. Figure 1.11 shows a top-down SEM image of the spalled coating on the left and on the right the corresponding FIB cross-section of the coating showing crevice corrosion of the interface material leading to delamination. The environmental conditions of their experiment differ significantly from the autoclave conditions in this project using deionised water however it is possible that localised corrosion systems could develop in the sample.

They also examined the effect of stress corrosion cracking on reactively formed interfaces in the coating. Figure 1.12 shows the open crack in the reactively formed interface material

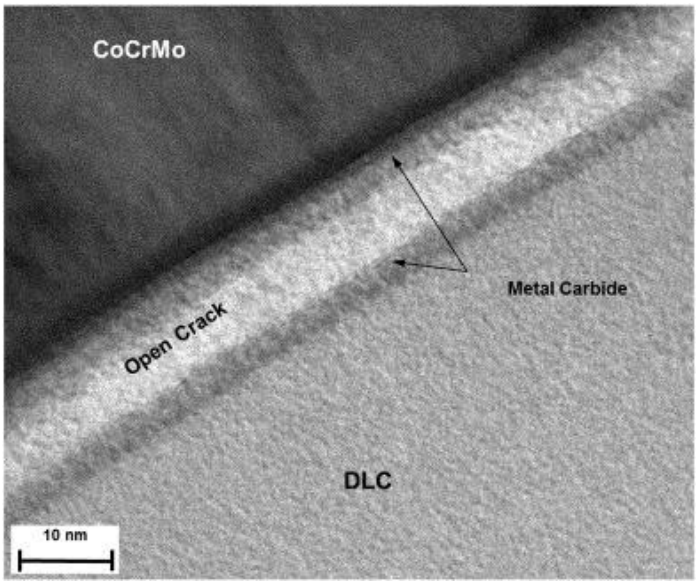

Figure 1.12 TEM micrograph of interface between CoCrMo substrate and amorphous carbon coating. SCC is present in the carbide interface during immersion in PBS [79].

between the substrate and coating caused by SCC during immersion in PBS.

Rolls-Royce sponsored research by Sutton *et al.* also looked at the tribology of three commercial diamond-like carbon coatings in distilled water [80]. Coating A in this report is similar to the Graphit-iC coating used by Stallard and also shows similar behaviour; the coating initially has a high coefficient of friction before dropping back down to a stable level as the transfer layer forms on the counterface material. Although these tests might be a useful indicator of amorphous carbon coating characteristics in tribological tests in water it is also important to consider the effect of increasing temperature and pressure on both the integrity of the coating and the nature of the tribology.

A variety of different coating types were selected so that their experimental performance could be connected to certain material properties. This knowledge could then later be used to help develop an optimised coating system. During the initial stages of this Engineering Doctorate Rolls-Royce worked with the Research Centre in Surface Engineering at the University of Sheffield to down-select from a large variety of potential commercial coatings using autoclave testing, as shown in Table 1 [1].

Table 1 Performance of amorphous carbon coatings in the previous autoclave tests [1].

Know details of amorphous carbon coating classification and interlayer structure	Autoclave exposure and coating performance
Diamond-like a-C:H on CrN, Cr	2 year autoclave test 250-300°C: partial coating spallation, >300°C significant coating spallation 7 day autoclave test 280°C: partial coating spallation 6 day autoclave test 280°C: significant coating spallation 3.7 day (power failure) autoclave test at 300˚C: partial coating spallation
Graphite-like a-C on Cr/C multilayer, Cr/C ramp layer, CrN, Cr	2 year autoclave test: 250-300°C no coating spallation, >300°C no coating spallation 3.7 day (power failure) autoclave test at 300˚C: no coating spallation
Diamond-like a-C:H on CrC, CrN, Cr	2 year autoclave test 250-300°C: no coating spallation, >300°C complete coating spallation 3.7 day (power failure) autoclave test at 300˚C: complete coating spallation
Diamond-like a-C:H:Si	7 day autoclave test 280°C: complete coating spallation
Diamond-like a-C:H:Si on CrN	7 day autoclave test 280°C: some coating pitting
Graphitic a-C:H	7 day autoclave test 280°C: complete coating spallation
Graphitic a-C:H on CrN	7 day autoclave test 280°C: significant coating spallation

Polymeric a-C:H	7 day autoclave test 280°C: complete coating spallation
Polymeric a-C:H on CrN	7 day autoclave test 280°C: some coating pitting
a-C:H on graded CrC, CrCN, CrN	7 day autoclave test 280°C: partial coating spallation around edges 3.7 day (power failure) autoclave test at 300˚C: partial coating spallation
Columnar a-C:H on graded CrC, CrCN, CrN	7 day autoclave test 280°C: coating discolouration 3.7 day (power failure) autoclave test at 300˚C: complete coating spallation
Diamond-like a-C:H on CrN, Cr	3.7 day (power failure) autoclave test at 300˚C: partial coating spallation
Diamond-like a-C:H on a-C:Cr, CrN	3.7 day (power failure) autoclave test at 300˚C: partial coating spallation

1.4.5 Amorphous carbon coating applications

The attractive properties attainable with amorphous carbon mean that a large volume of research and development has been directed into creating coatings for engineering components and electronics. The main focus of current research is into the favourable mechanical and chemical properties of amorphous carbon coatings for engineering components.

Due to the properties of high hardness, good chemical inertness and low friction the amorphous carbon films are excellent for protective coating applications wherein the tribology is important in providing increases in efficiency and extensions in lifetime to components like valves, seals, cutting tools bearings and pumps [81] [82].

The formation of the self-lubricious graphitic transfer layers means that it is often desirable to use amorphous carbon coatings in situations where the usage of oil-based lubricants is limited. This is the case in vacuum environments for components to be used in space, but also for systems where elemental contamination is a factor like food processing and possibly nuclear reactor systems. A significant volume of research has been conducted in the application of amorphous carbon films for biological applications as the coating offers a near chemically inert surface with low friction and wear, ideal for usage in the lubrication and protection of artificial joints [83] or heart valves [84].

The usage of diamond-like carbon coatings is often limited by their high internal compressive stress and low mechanical toughness [38]. Due to the typically low mechanical toughness of amorphous carbon films functional interlayers are often applied to the substrate to act as load support when coating a load-bearing engineering component [43]. The usage of metallic dopants can also act to improve coating

performance as they give the dispersion of both hard metallic carbide and pure metal nanocrystallites in the carbon matrix [85]. This gives the coatings a desirable combination of properties; the high hardness associated with ceramics alongside the low elastic modulus typical of polymeric compounds [65]. This amalgam gives metal doped amorphous carbon coatings the high H/E ratios typically associated with excellence in wear resistance [86].

A lot of the commercially available amorphous carbon coatings are designed for use in automotive applications or material tooling and are often applied where desirable material properties like low friction coefficients and high hardness are useful in adding performance increases to components [43] . However they are usually designed to work with lubricating oils, not the high temperature water found in pressurised water reactors. Due to the relative sizes of the markets and demand for coatings, coatings designed specifically for nuclear applications are limited so existing coatings are often adapted for purposes they are not optimised for. In this project is was therefore likely that the commercial coatings studied would not be designed with pressurised water reactor applications in mind but any useful features found during this investigation could be used to help specify future coating depositions for the specific environmental conditions involved in such applications.

1.5 Summary

Based on the project specification from Rolls-Royce and a review of the available literature the project aims were to investigate the hydrothermal stability of the amorphous carbon coatings when exposed to high-temperature high-pressure water and then to identify and understand the features and compositions of the coatings before and after exposure to determine their effect on coating performance and possible degradation mechanisms.

These considerations were used to develop an experimental programme that involved using the available coatings in a series of experimental objectives to explore coating performance in the context of the project aims. The materials and experimental methods used are covered in further detail in the following chapter.

Chapter 2: Materials and experimental methods

2.1 Introduction

This chapter will detail the materials and experimental methods used to complete the objectives of the project. It will first examine the rationale behind the material selection of the coatings and substrates used in this project, including how each was chosen to answer the specific questions of the Engineering Doctorate. Next it will cover the experimental techniques used to test the performance of the materials in certain simplified pressurised water reactor conditions and what issues they were addressing. Finally it will look at the characterisation techniques used to analyse the performance of the different coatings to gain a fundamental understanding of the material mechanisms affecting each of the coatings.

2.2 Coatings

The first two coatings studied in this project were the diamond-like hydrogenated amorphous carbon commercial Coating Type A, and the graphite-like non-hydrogenated commercial Coating Type B. The detailed architecture of the coatings was studied by TEM and EELS in results Section 4.3.

Later in the project the graphite-like amorphous carbon Coating Type C was a lab-deposited with a coating architecture based on the knowledge of Coating Type B, with chromium doping and interlayers. Coating Type D was also lab-deposited with the same method as Coating Type C but the chromium was replaced with titanium.

For the purpose of this project it was not necessary to focus on the commercial origins of the coatings, therefore they will not be listed here. The commercial coatings studied were not originally designed with pressurised water reactor conditions in mind therefore they will only be referred to in reference to their properties and performance during characterisation when exposed to the autoclave conditions.

2.2.1 Coating Type A

The first coating focused on in this project was an amorphous carbon film deposited by combined physical vapour deposition and plasma assisted chemical vapour deposition. The carbon coating was described by the manufacturer as a diamond-like carbon with high sp^3 content, containing hydrogen and no metal dopants (a-C:H). The coating is deposited at temperatures under 250°C and has a chromium nitride interlayer for improved loadbearing. The manufacturer states that the coating should survive up to 300°C depending on the environmental conditions present.

Figure 2.1shows the as-received surface of Coating Type A. The ridges seen on the surface of the diamond-like carbon coating follow the polishing marks from the underlying morphology of the stainless steel substrate. Figure 2.2 is an optical

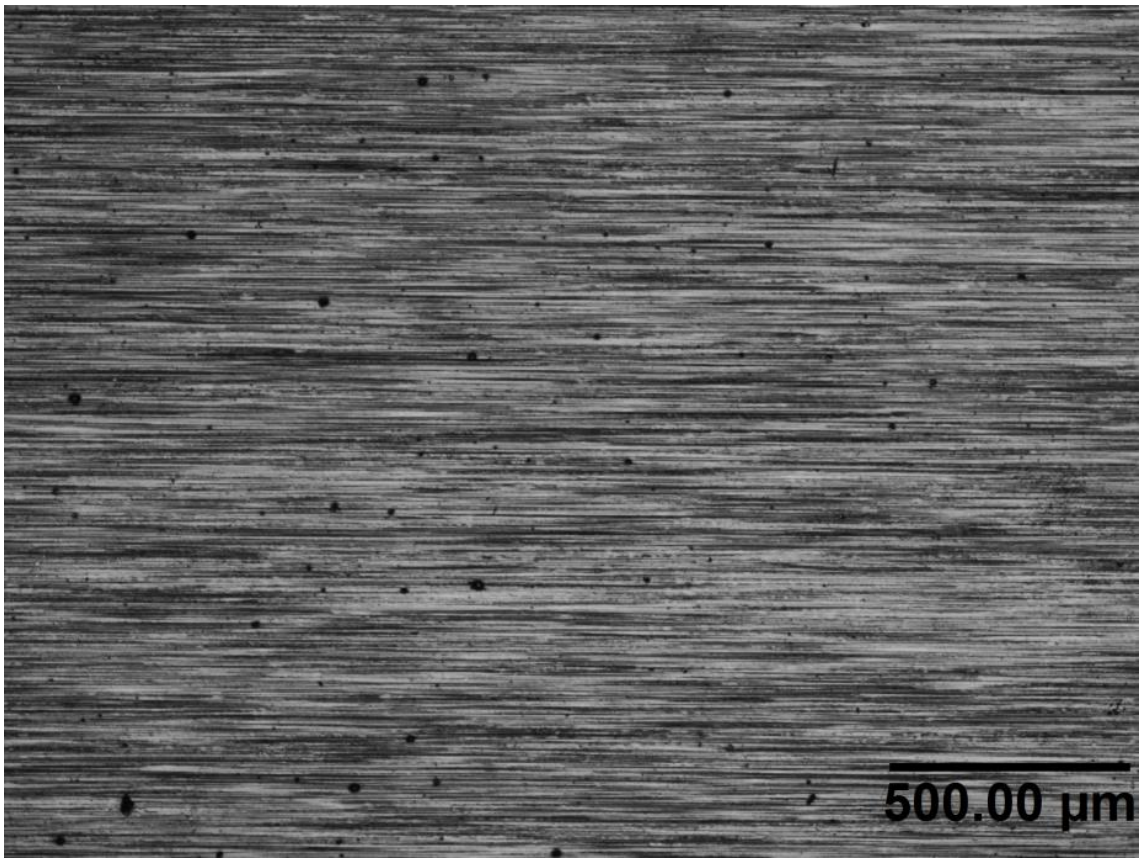

Figure 2.1 An optical micrograph of the as-received surface of Coating Type A.

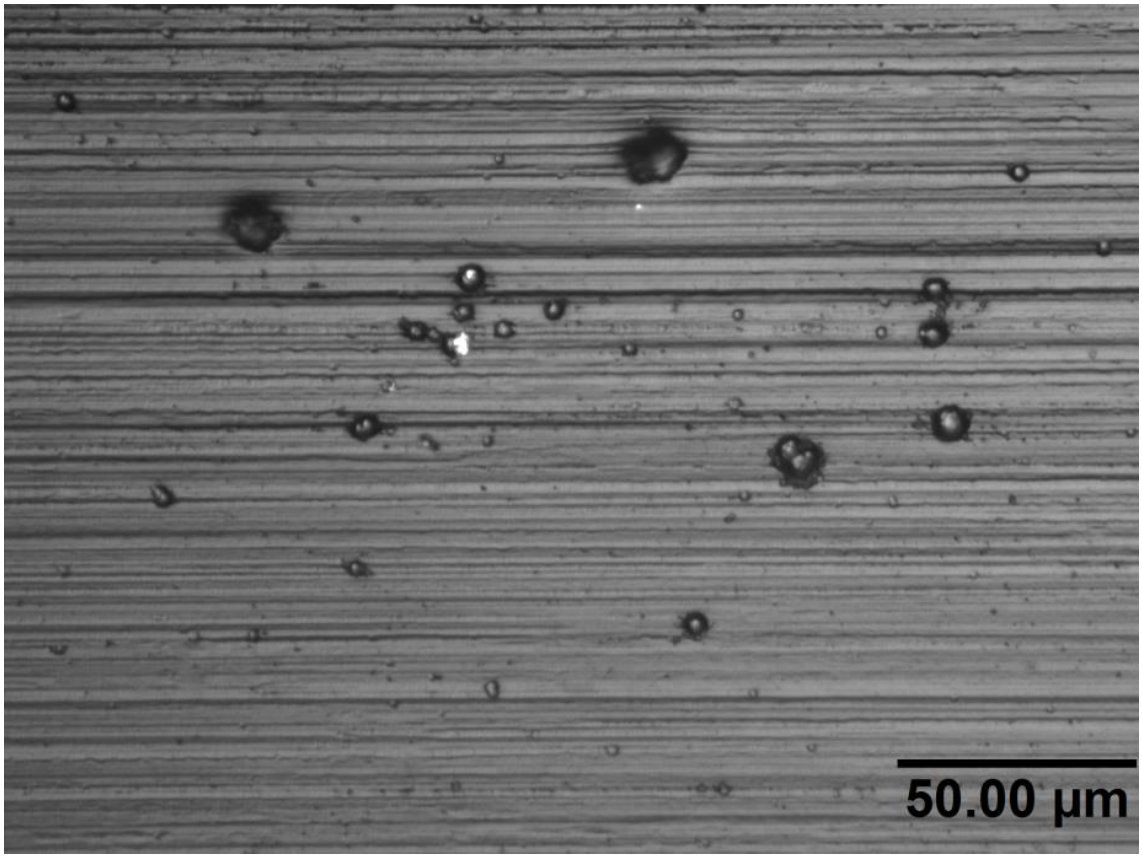

Figure 2.2 An optical micrograph of the as-received surface of Coating Type A with defects.

micrograph of small defects present on the sample surface, in some cases raised asperities and in places (such as the larger defect in Figure 2.3) revealing lighter areas of the underlying interlayer materials.

The number of Coating Type A samples available for this project was somewhat limited as the commercial coatings were originally acquired several years ago during a separate Rolls-Royce project. The coatings are quite rough relative to the recently prepared samples as the amorphous carbon followed the underlying substrate morphology as shown previously in the optical micrograph in Figure 2.1 and the optical profilometry image in Figure 2.4 [1].

The proprietary recipes of the coatings tend to change with time so in order to assess the behaviour of coatings that were chosen for the application back then it was necessary to

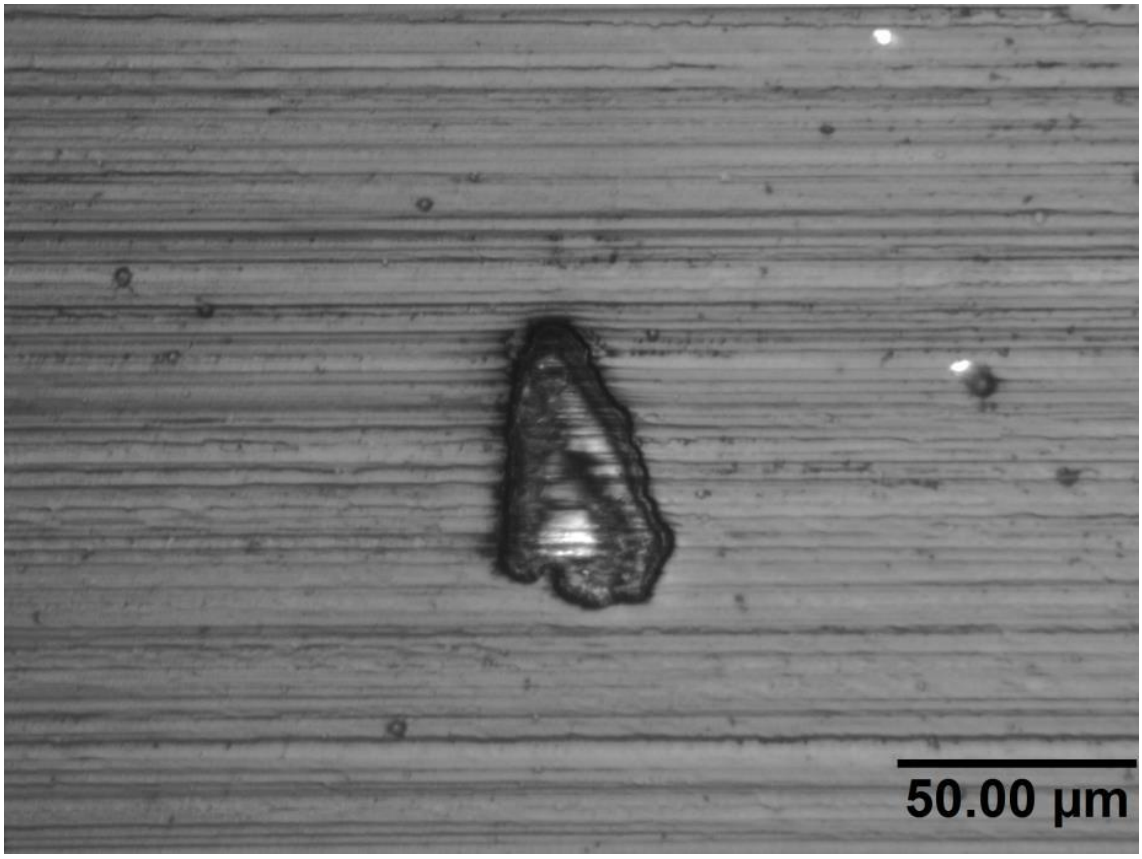

Figure 2.3 An optical micrograph of the as-received surface of Coating Type A with large defect.

work with the remaining older coatings. This meant that there was some variation in the substrate materials of the still existing samples. The previous Rolls-Royce high temperature autoclave tests used Haynes 25 as the substrate material and the experiments performed in this project were deposited on HAS 40100. Fortunately, the previous R-R testing had shown that the two different substrate materials have little influence on the hydrothermal performance of the coatings themselves [1].

The coating was originally selected by Rolls-Royce partly due to robustness of the multinational supply chain. Rolls-Royce are interested in learning more about this coating because long term autoclave experiments revealed significant spallation of the coating at medium and high temperatures. Further autoclave experiments performed with R-R showed that there was even significant spallation over shorter time periods [1].

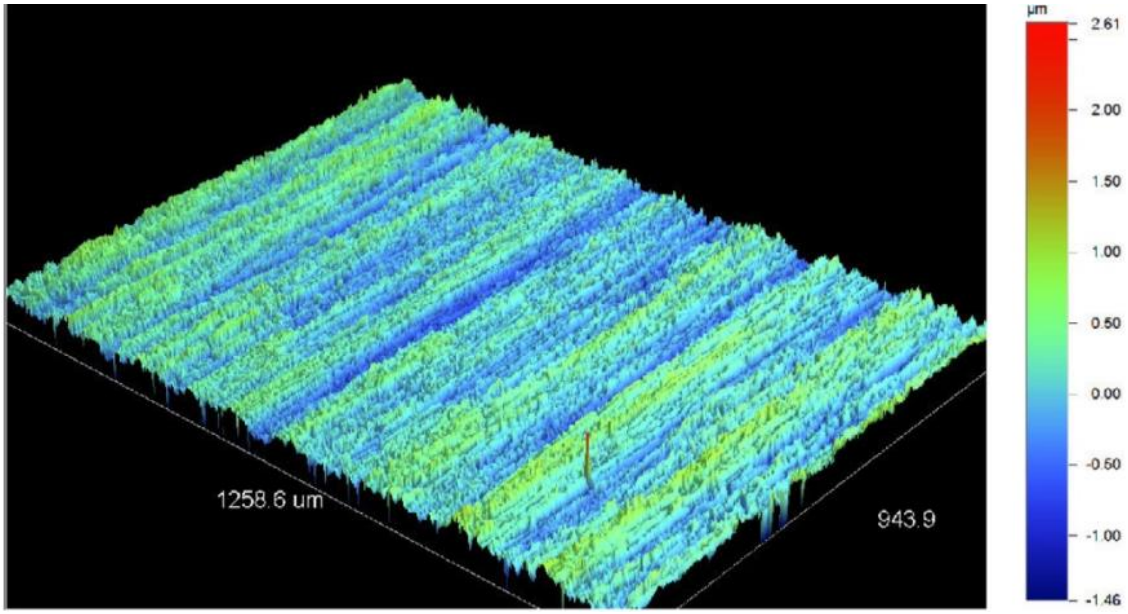

Figure 2.4 Optical profilometry of Coating Type A [1].

2.2.2 Coating Type B

The next coating to be studied was a graphitic-like carbon film (a-C) deposited by closed field unbalanced magnetron sputter ion plating shown schematically in Figure 2.5. The interlayer system for the coating was a CrN base layer on the surface of the substrate, followed by a Cr adhesion layer, on top of which was a graded Cr/C

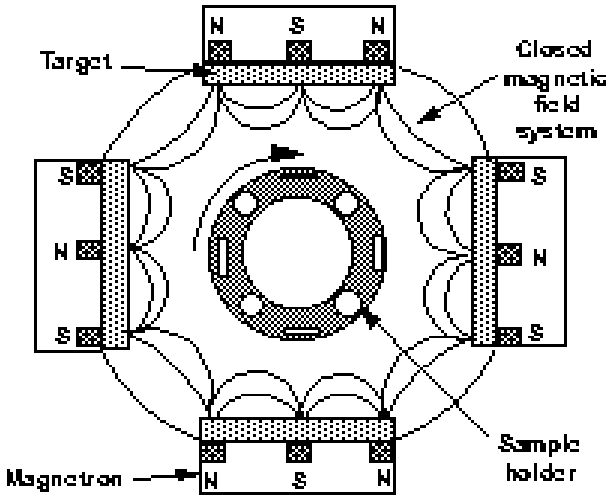

Figure 2.5 Schematic diagram of the closed field unbalanced magnetron sputter ion plating system.

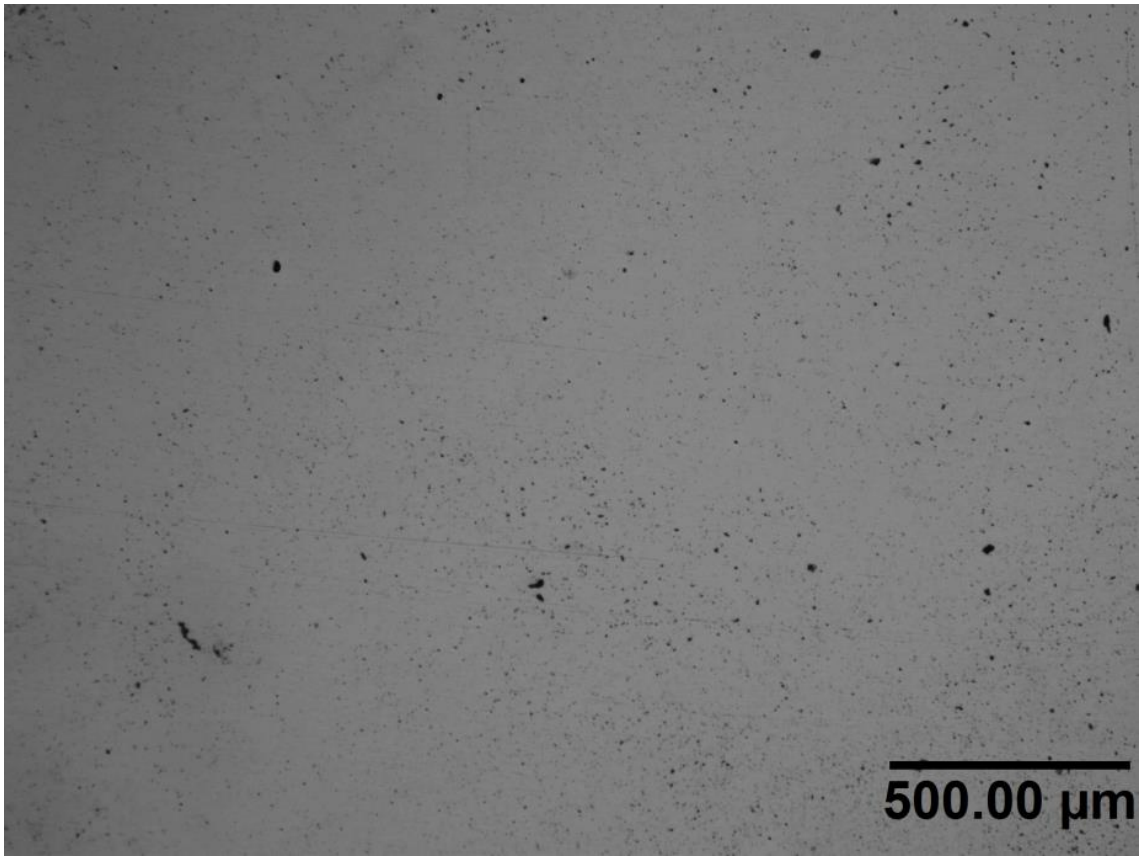

Figure 2.6 An optical micrograph of the as-received surface of Coating Type B.

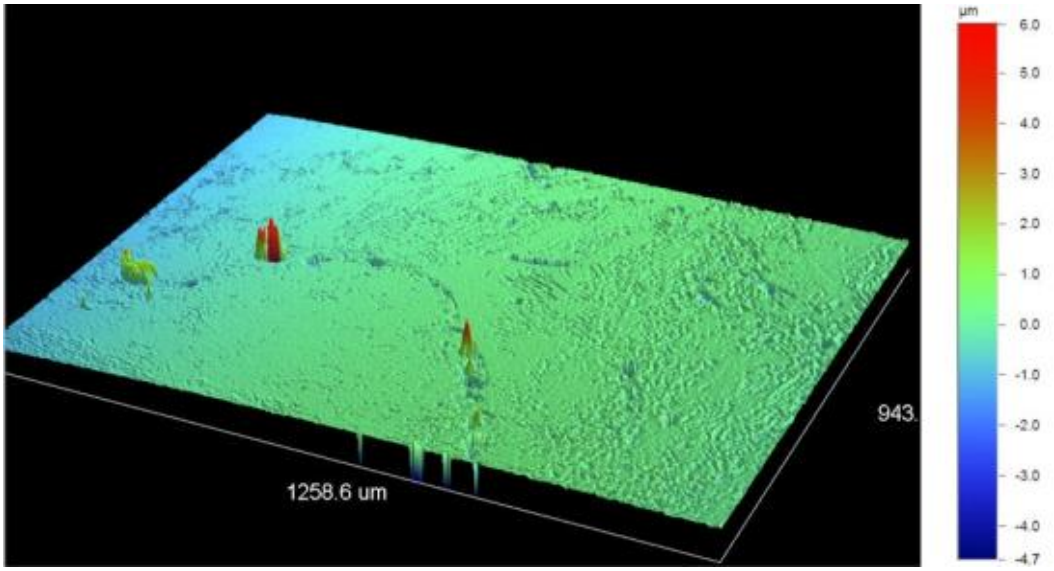

Figure 2.7 Optical profilometry of Coating Type B [1].

multilayer. The multilayer Cr/C interlayer system was created by rotating the substrate holder in the centre of the CFUMSIP chamber and varying the power applied to the alternating chromium and carbon targets. Finally the amorphous carbon coating was deposited on the top as shown in the optical micrograph of the coating surface in Figure 2.6 and the optical profilometry in Figure 2.7.

Unlike Coating Type A this coating contained no hydrogen as it was co-sputtered from carbon and chromium targets rather than deposited from a hydrocarbon precursor gas.

This coating was selected for further study in this project as it performed well in previous Roll-Royce experimental investigations into the effect of high temperature and high pressure water conditions, maintaining coating integrity for 2 years [1]. The coating was deposited by a smaller company in comparison with Coating Type A so there may be concerns over the supply chain for coating components depending on the volume of coatings required.

2.2.3 Coating Type C

The interlayer structure of Coating Type C is similar to that of Coating Type B, an amorphous carbon film on top of a Cr layer with a Cr/C interlayer, however in this case the carbon coating was Cr doped (a-C:Cr) and there was no CrN baselayer. The method of deposition was also co-sputtering of C/Cr and the coating is graphite-like, containing no hydrogen addition during the deposition process.

An optical micrograph of the surface of Coating Type C is shown in Figure 2.8. The deposition of Coating Type C was requested in order to have a sample comparable with Coating Type B but also to explore the effect of changing interlayers and dopants when compared with Coating Types B and D. This coating was also deposited using closed-

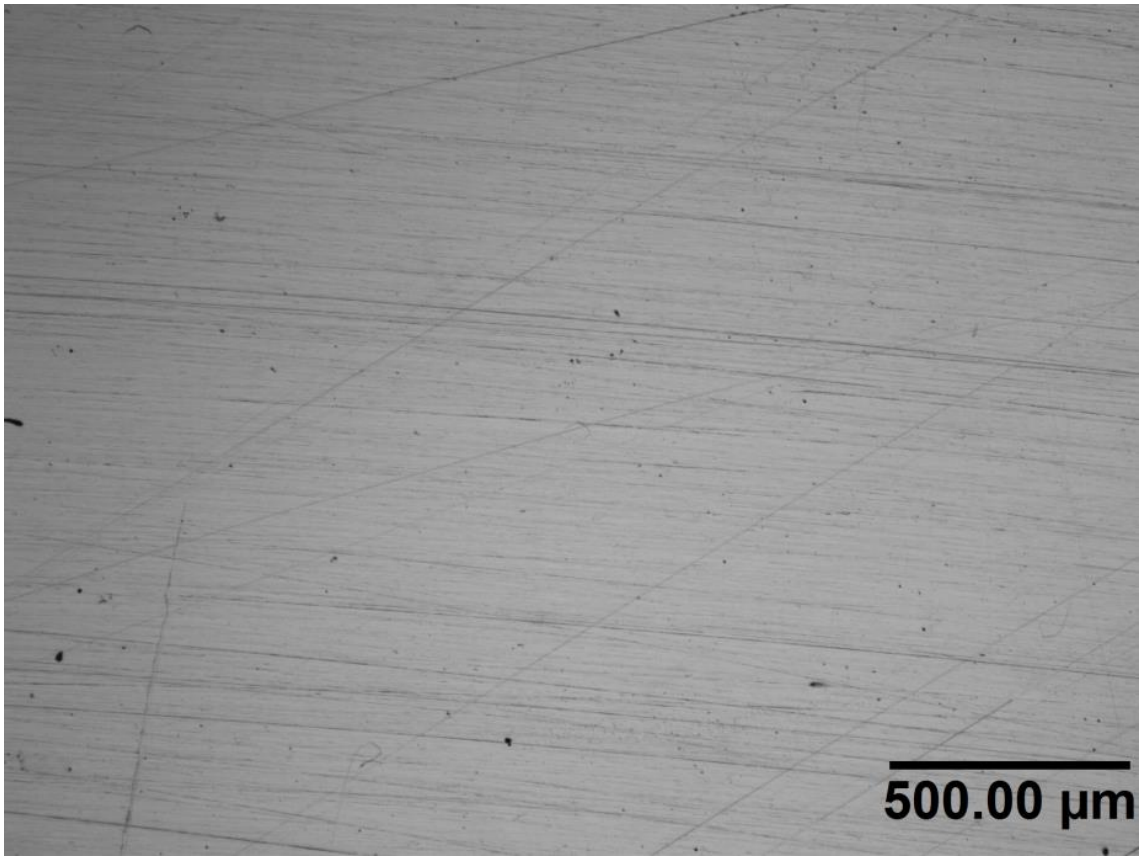

Figure 2.8 An optical micrograph of the as-received surface of Coating Type C.

field unbalanced magnetron sputtering system at the University of Akron, shown schematically in Figure 2.3.

2.2.4 Coating Type D

The structure and deposition process of Coating Type D is the same as that of Coating Type C but the chromium in the interlayer and coating has been replaced with titanium (a-C:Ti). The surface of the Ti doped amorphous carbon coating is shown in Figure 2.9.

One of the more important aspects of selecting or developing a suitable amorphous carbon coating is the composition and characteristics of the interlayer between the substrate and coating. Coating Type D should offer a structure similar to that of Coating Types B and C, where Coating Type B is known to work well in the testing conditions. However by replacing the Cr in the other coatings it allowed a comparison between the interlayer and doping materials to be made.

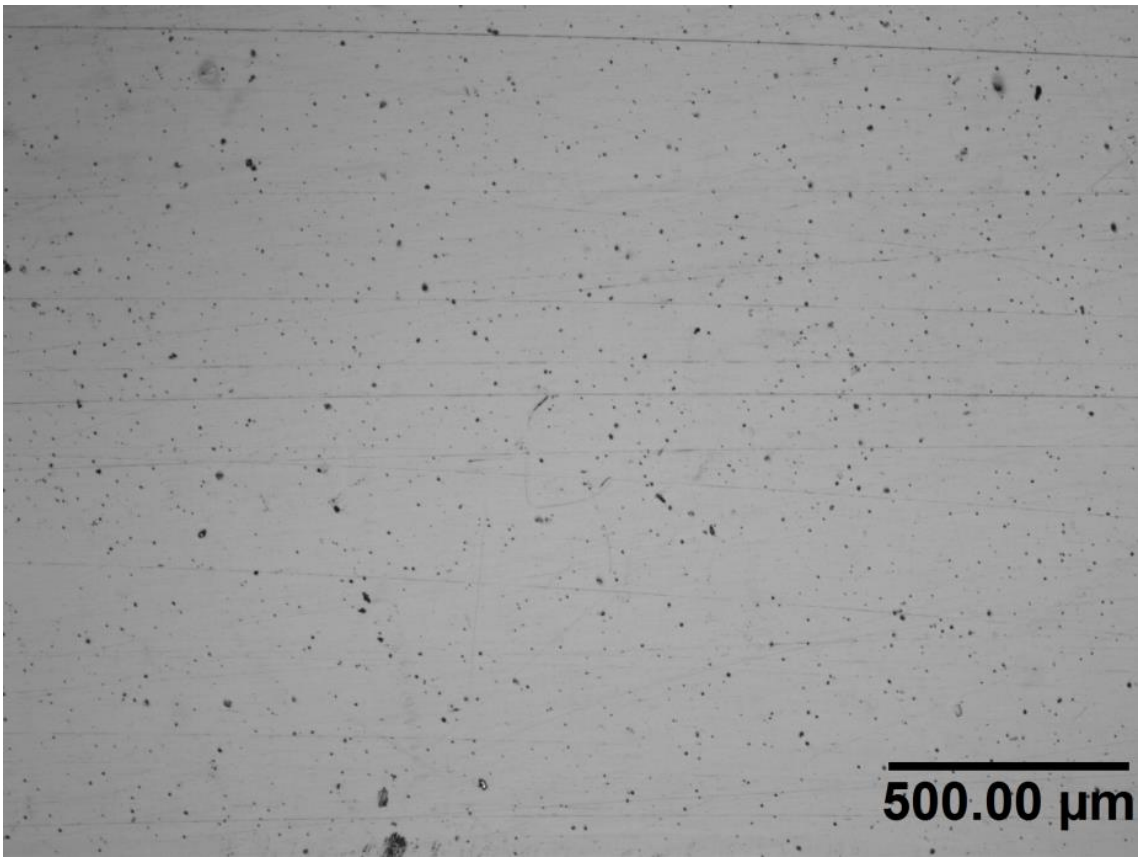

Figure 2.9 An optical micrograph of the as-received surface of Coating Type D.

This amorphous carbon coating was also deposited using closed-field unbalanced magnetron sputtering at the University of Akron.

2.3 Substrates

The substrate materials used in these experiments were mostly stainless steel alloys. Stainless steels are steel alloys that contain at least 10.5% chromium by mass. Stainless steel is commonly used in the manufacture of PWR components as it has some of the useful properties of carbon steels with a greater corrosion resistance in many environments.

Although commonly used in PWR components due to their corrosion resistance there are some mechanisms that can lead to material degradation in the plant. Stress corrosion cracking is a particular concern [87].

The project also looked at the degradation of the coatings deposited on Haynes 25 substrates from some two year high temperature autoclave experiments performed with CAPCIS. From previous Roll-Royce work it was found that the differences in substrate materials had no significant effect on the performance of the coatings as there were no observable changes in delamination or material degradation during autoclave exposure. It was found that the coatings tended to fail at the metallic interlayer/amorphous carbon interface rather than occurring at the substrate surface.

The substrates used in this project were AISI 304 and 431 stainless steels, along with the Rolls-Royce HAS40100 alloy and Haynes 25 used for the previous Rolls-Royce experiments with Coating Type A. The compositions of commercially available materials used are recorded in Table 2.

The substrates used in the experiments in this EngD project were prepared for coating by grinding using 120, 240, 400, 600, and 800 grit silicon carbide grinding papers and

then the final polishing was completed using 3µm and 1µm diamond suspension spray to give a Ra 1µm finish.

Table 2 Weight percentage compositions of the commercially available substrate materials. HAS40100 has a composition similar to AISI431 but is not included in the table as it is a proprietary Rolls-Royce alloy.

Weight %	C	Co	Cr	Fe	Mn	Ni	P	S	Si	W
AISI 304 Stainless Steel [87]	0-0.08	-	18.0-20.0	66.5-74.0	0-2.0	8.0-10.5	0-0.045	0-0.030	0-0.75	-
AISI 431 Stainless Steel [88]	0-0.20	-	15.0-17.0	78.2-83.8	0-1.0	1.3-2.5	0-0.040	0-0.030	0-1.0	-
Haynes 25 [89]	0.05-0.15	Bal	19.0-21.0	0-3.0	1.00-2.00	9.0-11.0	0-0.03	0-0.03	0-1.0	14.0-16.0

2.3.1 Stainless steel AISI 304

AISI 304 stainless steel is an austenitic steel alloy with good strength, fracture toughness, corrosion resistance, and ductility [88]. It has commonly been used in the manufacture of structural components in the pressurised water reactor as these material properties made it suitable for the challenging pressures, temperatures, and environmental conditions [89].

The more recent commercial coatings in this project including Coating Types B, C, and D were all deposited on AISI 304 SS alloy as the material was easier and faster to prepare consistent substrates for coating and better corrosion resistance in comparison to the AISI 431 SS alloy, with no significant observable difference in the effect on coating degradation between the various substrate alloys used during testing [1].

2.3.2 Stainless steel AISI 431

AISI 431 stainless steel is a martensitic steel alloy with good corrosion resistance [90][84]. The alloy is magnetic and also has good strength and toughness, as well as high hardness and wear resistance. The stainless steel alloy is often used in pressurised water reactor applications like pumps and valves where austenitic stainless steels are not suitable due to their poor resistance to sliding wear and cavitation erosion [91]. The initial Rolls-Royce investigation into commercial coatings performance used this alloy alongside the AISI 304 SS substrate in order to observe any differences in coating degradation between the different substrate materials. In this study the samples of Coating Type B used in the Parr bomb tests were deposited on AISI 431 SS as the alloy

was close to the composition of the proprietary HAS40100 used in the substrate of some available samples of Coating Type A.

2.3.3 Stainless steel HAS40100

The HAS40100 alloy is a proprietary Rolls-Royce alloy with properties and composition very similar to that of AISI 431SS. This alloy was used as the substrate for some of the earlier Rolls-Royce coating samples that were used in the previous autoclave experiments. The samples of Coating Type A used for the recent autoclave experiments in this project were deposited on HAS40100.

2.3.4 Haynes 25

Haynes 25 is a cobalt based alloy with excellent performance in high temperature applications [92]. It has good corrosion resistance combined with good formability, as well as excellent high temperature strength due to solid solution strengthening. In this study the coating samples used to assess the performance of Coating Type A from a previous 2 year autoclave exposure investigation by Rolls-Royce were deposited on Haynes 25.

2.4 Experimental Methods

This section of the report will cover the techniques selected in order to complete the various different objectives of the Engineering Doctorate project.

The first experimental procedures involved using a Parr bomb autoclave to analyse the effect of high temperature water on the coatings. The coatings were then analysed using nanoindentation, Raman spectroscopy and microscopy techniques to assess their thermal stability performance.

Further tests were then conducted using an autoclave at higher temperatures to study any material degradation mechanisms and loss of performance with increasing temperatures. The coatings were also then analysed by a range of microscopy and spectroscopy techniques.

In order to examine the effect of changing the coating interlayers the same experiments were conducted on both the commercial and lab deposited samples to identify advantageous features that could be used in future optimised coatings.

Due to the variation in substrate materials due to limited sample availability, for clarity the materials used in each of the experimental methods are shown in Table 3.

Table 3 Materials used in each of the experimental procedures.

Experimental Method	Materials Used
Parr Bomb	Coating Type A on HAS40100 As received. Coating Type B on AISI 431 SS As received.
Autoclave	Coating Type A on HAS40100 As received. Coating Type B on AISI 304 SS As received. Coating Type C on AISI 304 SS As received. Coating Type D on AISI 304 SS As received.
Nanoindentation	Coating Type A on HAS40100 As received, after 24hr/7day Parr bomb, and after 7 day autoclave. Coating Type B on AISI 431 SS As received, after 24hr/7day Parr bomb, and on AISI 304 after 7 day autoclave. Coating Type C on AISI 304 As received and after 7 day autoclave. Coating Type D on AISI 304 As received and after 7 day autoclave.
Raman Spectroscopy	Coating Type A on HAS40100 As received, after 24hr/7day Parr bomb, and after 7 day autoclave. Coating Type B on AISI 304 SS As received, after 24hr/7day Parr bomb, and on AISI 304 after7 day autoclave.
Focused Ion Beam Milling	Coating Type A on HAS40100 As received, after 7 day autoclave, and on Haynes 25 after 2 year autoclave. Coating Type B on AISI 431 SS As received. Coating Type C on AISI 431 SS As received.

Scanning Electron Microscopy	Coating Type A on Haynes 25 after 2 year autoclave.
Transmission Electron Microscopy	Coating Type A on HAS40100 As received, after 7 day autoclave, and on Haynes 25 after 2 year autoclave. Coating Type B on AISI 431 SS As received. Coating Type C on AISI 431 SS As received.
Energy-dispersive X-ray Spectroscopy	Coating Type A on HAS40100 As received and on Haynes 25 after 2 year autoclave.
Electron Energy Loss Spectroscopy	Coating Type A on HAS40100 As received, after 7 day autoclave, and on Haynes 25 after 2 year autoclave. Coating Type B on AISI 431 SS As received. Coating Type C on AISI 431 SS As received.

2.4.1 Parr bomb

The first experiment involved using a Parr bomb to expose the coating samples to high temperature water for periods of 24 hours and 7 days. This equipment allowed the performance of the amorphous carbon coatings in very simplified pressurised water reactor operating conditions to be examined. If the coatings had delaminated at the relatively low temperature used in the exposure it would immediately rule out the need for further experiments at higher temperatures and durations.

The vessel used in these experiments was the 4744 45ml general purpose acid digestion Parr bomb from the Parr Instrument Company [93]. The equipment consists of a thick-walled PTFE cup with a volume of 45mL as shown in the right side of Figure 2.10. This PTFE vessel then sits inside a broad flange sealed stainless steel vessel on the left in Figure 2.10. The Parr bomb was designed to operate at temperatures of up to 250°C. The vessel has a built in mechanical fuse in the form of a rupture disc between the

Figure 2.10 4744 45ml general purpose acid digestion Parr bomb.

PTFE lid and the spring-loaded steel cap. In order to reduce the risk of rupturing the seal during heating and needing to replace it the experiment was limited by the oven controller to 240°C, with an overheat cut-off at 245°C. Although this temperature was lower than the previous autoclave tests it was still useful to find out whether the coatings could be suitable for lower temperature applications inside the secondary loop of the pressurised water reactor system, or whether they failed at the lower temperatures as well.

The first step was to conduct a 24 hour exposure at 240°C. If the coatings completely failed in this timespan then it would not be worth doing an extended experiment as there would be no additional knowledge to gain, saving further testing time. It was also useful to expose the coatings for a shorter amount of time as the autoclave experiments conducted previously did not reveal whether the coatings failed immediately or after a longer period of material degradation.

If not already sectioned into suitable sizes from characterisation experiments conducted previously the coated samples were sectioned to dimensions of 25mm x 15mm x 5mm using a Buehler IsoMet 5000 precision cutter. Previous R-R autoclave experiments showed that cutting or polishing the ends of the samples had no effect on the level of spallation found on the surface of the studied coatings.

The coating samples were then cleaned with a detergent solution and rinsed in water to remove most of the cutting fluid and swarf material from the surface. They were then further cleaned in an ultrasonic bath by immersion in a beaker of isopropyl alcohol for 5 minutes, with the solution replaced with clean IPA and then repeated for a further 5 minutes.

The samples were then placed into the bottom of the PTFE cylinder inside the Parr bomb vessel and 20ml of deionised water was poured in so that they were fully immersed. The vessel was then placed on the metal shelf and the oven was heated to 240°C and maintained at that temperature for the duration of the testing period.

At the end of each experimental period the vessel was removed from the oven and allowed to cool for a period of 24 hours. After the vessel had cooled the samples were then removed for characterisation. The PTFE vessel was then washed thoroughly with deionised water for the next experiment.

As there was not an accessible way to analyse the water quality quickly with the available equipment the analysis was conducted after the experiment. Water samples were taken from the 7 day Parr bomb exposures and inductively coupled plasma mass spectrometry (ICPMS) was used to analyse the chemical compositions of the liquid and the separated particulate matter after the experiment. The samples were analysed by ionising the collected water sample by inductive heating of the solution and particulates into plasma. The plasma was then analysed by mass spectrometry to determine the elements present in parts per billion.

2.4.2 Autoclave

The next experiment was a further investigation of the coating performance under more aggressive higher temperature water conditions. Previous Rolls-Royce experiments have shown that Coating Type A will consistently show significant spallation when exposed to water temperatures in excess of 280°C. This experiment aimed to expose Coating Type A to conditions known to cause significant material failure in order to compare the performance relative to Coating Type B.

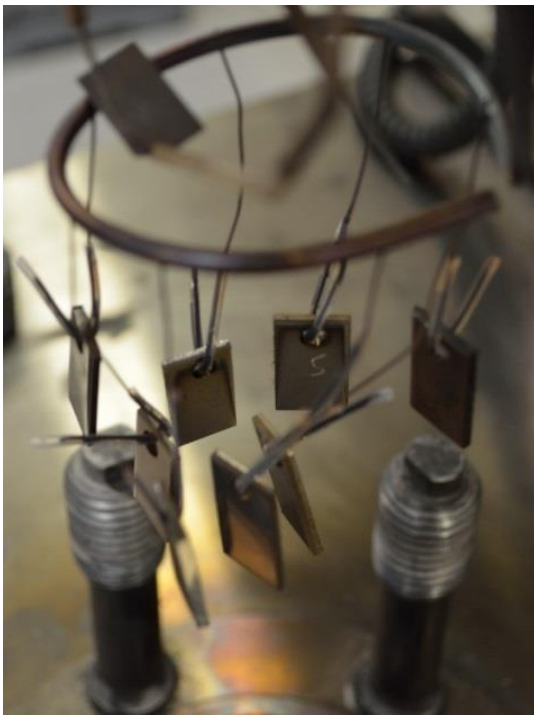

Figure 2.11 The sample hanger setup used for autoclave testing.

The Coating Types C and D were also immersed during the experiment to investigate the effect interlayers of chromium and titanium have on the coating performance. A static 900ml autoclave at the University of Manchester was used to conduct this experiment to expose the amorphous carbon samples to higher water temperatures. It offered much greater control of the environmental conditions in comparison to the Parr bomb experiments [94].

The vessel was first pre-cleaned using deionised water at a temperature of 300˚C for at least 24 hours until a conductivity of <2.5 μS cm^{-1} was achieved. The coated samples were then mounted on an insulated hanger as in Figure 2.11 so that they could be fully immersed in the water without touching the sides when lowered into the autoclave vessel.

The autoclave vessel was then filled with deionised water and sealed with the samples inside. The process of deaerating the deionised water in the autoclave was then started by sparging with nitrogen until the oxygen level was less than 100 ppb. More nitrogen was then pumped into the vessel to achieve an overpressure of around 5 to 10 bar above the water vapour pressure to prevent the deionised water from leaving the liquid phase inside the autoclave during the experiment. The reliability of this preparation process to achieve the required operating conditions had been ascertained during the previous Roll-Royce autoclave tests at the University of Manchester so the procedure remained the same [1].

The autoclave was then slowly heated to a temperature of 280°C and held and monitored over a period of 7 days until the end of the experiment. At the end of the 7 days the autoclave was then slowly cooled to a temperature of 60°C and the vessel opened. The samples were allowed to fully air dry before sealing in Al foil for transport and storage.

Figure 2.12 Partially spalled surface of Coating Type A after 2 year CAPCIS autoclave test for Rolls-Royce.

The previous Rolls-Royce autoclave experiments conducted with CAPCIS were 2 years in duration at two temperatures between 240 and over 300˚C. This temperature range was selected in order to provide a range of similar conditions to those found in a pressurised water reactor. The period of 2 years also allowed the performance of the coatings to be examined for an extended period of time.

Figure 2.12 shows a sample of Coating Type A after the 2 year autoclave exposure at CAPCIS. The sample shown was studied during this EngD to determine the degradation processes that led to the spallation of the amorphous carbon coating across large sections of the surface.

Coating Type A and Coating Type B were also previously tested for a period of 6 days at 280˚C in an autoclave by the company Element Sheffield. This experiment resulting in the delamination of the amorphous carbon film in Coating Type A while Coating Type B remained intact; however there were some concerns over sulphurous contamination of the vessel from previous experiments.

A study by Rolls-Royce on the testing indicated that the autoclave procedure at CAPCIS had issues with contamination of the water with iron and chromium oxides, possibly due to previous experiments or corrosion of the substrates, coatings, or autoclave vessel. The autoclave testing at the University of Manchester was intended to help remove some of the uncertainty surrounding the presence of contamination as the environmental conditions and vessel cleaning was carefully controlled.

2.4.3 Scratch adhesion testing

Scratch adhesion testing was conducted to assess the mechanical adhesion of the coatings to the sample substrates. This helped to determine the strength of the amorphous carbon film bonding to the underlying material layers in the coatings before autoclave exposure [95]. It was useful to perform the experiment on the samples as it provided a simple method to determine whether the coatings were failing due to poor adhesion in their as-received condition or whether the autoclave environment was causing degradation. The experiment was conducted using a VTT scratch adhesion tester at the University of Sheffield.

The coating samples were each scratched four times with a diamond tip for a length of 10mm at 0.2 mm/s with the normal load linearly increasing from 10 to 100N across the length of the scratch.

Data for the normal and frictional forces was recorded along the length of the scratch during the experiment. When combined with optical micrographs it was possible to determine the critical load at which coating adhesive failure occurred and therefore whether the amorphous carbon film had sufficient adhesion in an as-received state to say that the autoclave exposure was causing coating delamination, rather than poor bonding during deposition [96].

2.4.4 Nanoindentation

From the previous Rolls-Royce work it was found that the changes in coating hardness measured by nanoindentation before and after exposure to high temperature water were a good indicator of the hydrothermal stability performance of the coating in the testing environment [1]. Nanoindentation involves driving a diamond tip of known geometry into the surface of the sample and measuring the displacement against the applied load. From the resulting load/displacement curves the hardness of the coatings can be calculated and compared to show changes in the coating properties [86].

The technique used to analyse the nanoindentation data in this project was the Oliver and Pharr method [97]. Figure 2.13 shows a typical load/displacement curve for the nanoindent with the maximum load P_{max}, maximum displacement h_{max}, final depth h_f, and the gradient of the upper portion of the unloading curve related to the elastic unloading stiffness S. In Figure 2.14 the contact geometry of the unloading of the nanoindent is shown with the load P, contact area radius a , the indent depth h, the material sink-in h_s, the final indent depth h_f, the depth in which contact is maintained h_c, and half-

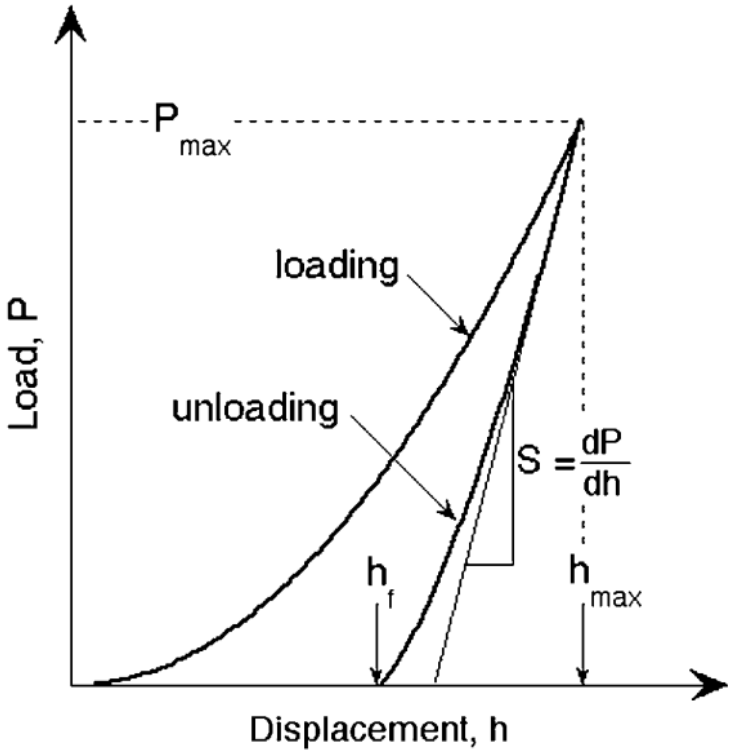

Figure 2.13 Load/ displacement curve for nanoindentation. [98]

included angle ϕ. From these values the hardness for each of the indents can be derived and defined as $H = P_{max} / A$, where A is the area of the ident [98].

The hardness of the samples before and after autoclave exposure was measured using the Triboscope NanoIndenter. A Berkovich three-sided pyramid indenter tip was used during the experiment. The tip is useful for measuring the hardness of thin films as the low loads involved ensure that the effect of the substrate is less than for typical hardness tests like the Vickers or Rockwell test [99].

The coatings were sectioned using the Buehler IsoMet 5000 precision saw to produce samples of sizes suitable for attaching to the metallic disc mounts. They were then cleaned using a beaker of isopropyl alcohol in an ultrasonic bath for 5 minutes twice to remove surface contaminants. It was important to remove any contamination as it reduced the areas in which nanoindent arrays could be positioned as they can give false hardness readings and make the indenter tip dirty.

The samples were then mounted on circular metal discs to assist the magnetic holder on the nanoindenter in securing and keeping the sample still during the characterisation

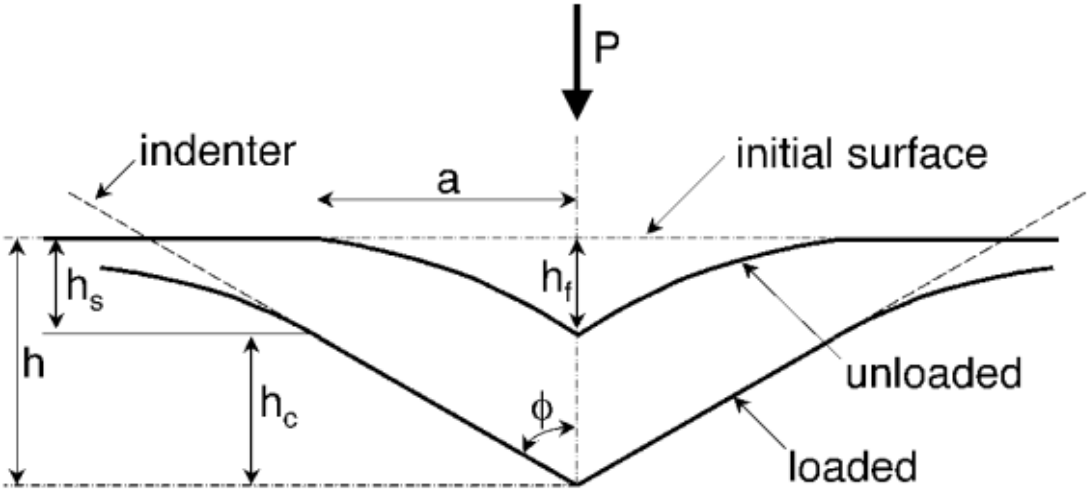

Figure 2.14 Schematic diagram of the nanoindentation unloading contact geometry [98].

process. It was important to position the indents above the metallic discs during indentation as it provided a flat surface that would not move around under the loading of the sample.

Indentation depth was kept to around ten percent of the coating thickness so that the hardness of the coating was measured and not the substrate [100], the maximum force applied to the coatings was 3000μN. This gave indentation depths of around 70 to 100nm depending on the hardness of each of the coatings. These depths were within the recommended displacements for the tip geometry to give reliable readings. Analysis of the loading curves sometimes involves discounting some of the indentation curves due to major dissimilarities with the ideal curve shapes. These irregularities can often be caused by roughness in the sample surface.

The nanoindentation data was then used to analyse any changes in hardness caused by the high temperature water tests in order to characterise the material stability of the various amorphous carbon coatings.

2.4.5 Raman spectroscopy

Raman spectroscopy was used to analyse the changes in composition of the amorphous carbon coatings before and after the experiments involving exposure to high temperature water. The equipment used in this investigation was a Renishaw inVia Raman microscope using a green (514nm) argon ion laser.

This non-destructive characterisation technique uses the scattering of a monochromatic light, typically a laser beam, to determine molecular composition and bonding of the material [101]. When the laser light source interacts with the molecules in the sample some of the electromagnetic energy is shifted. These interactions with the molecules cause changes in the wavelength of the light when compared with the photon source, which can then be detected and subsequently displayed as a characteristic spectrum [102].

Raman spectroscopy was a useful technique for judging changes in the composition and bonding present in the amorphous carbon coatings as the progression of the graphitisation process after exposure to high temperature water could be measured relative

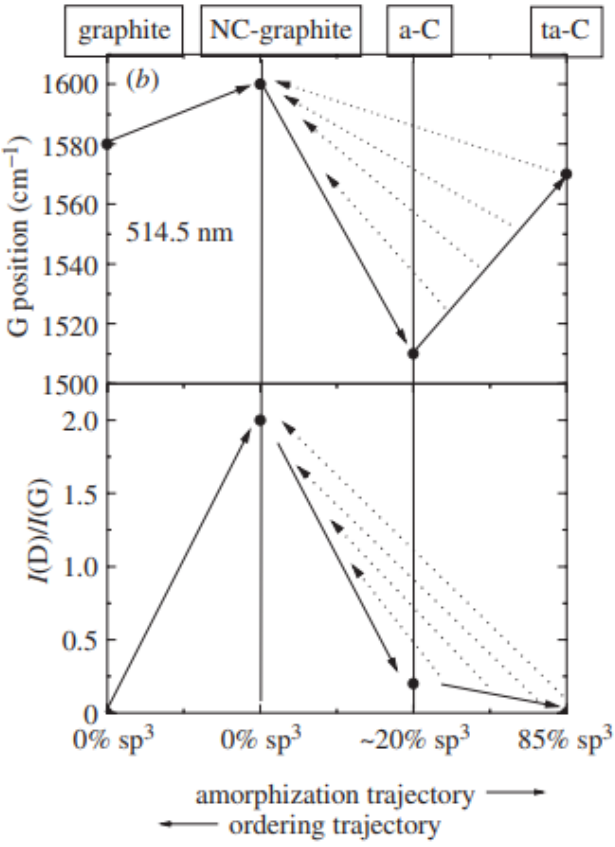

Figure 2.15 Schematic variation of G peak position and I(D)/I(G) ratio with carbon amorphisation and ordering trajectories [104].

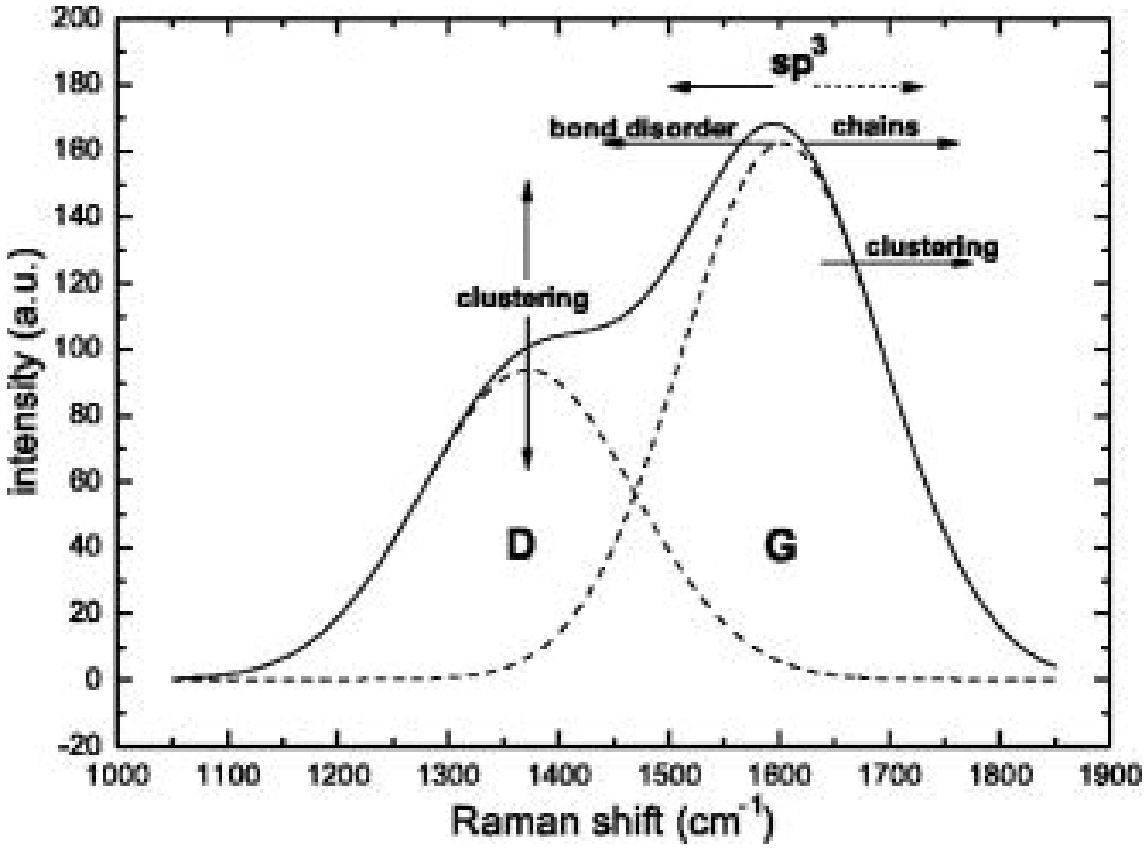

Figure 2.16 A schematic diagram of the D and G Raman peaks in a typical amorphous carbon film [105].

to the as-received coatings [72]. When characterising amorphous carbon the G peak and the D peak for carbon were very important in determining the nature of the material microstructure as the G peak in carbon allotropes arises due to the bond stretching of sp^2 atoms and the D peak is related to the breathing modes of the sp^2 atoms bonded in rings [103].

Figure 2.15 shows the amorphisation and ordering trajectories of the G peak position and I(D)/I(G) ratio for carbon Raman peaks [104]. As the material in the coating graphitises the relative sp^3 content is reduced and there are changes in the relative peak intensities related to the shifts in allotropic structure of the carbon as shown in Figure 2.16 [105].

After collecting the experimental data the Raman spectra were deconvoluted into the D and G carbon peaks using a combination of Renishaw WiRE and OriginPro. Gaussian peak fitting was used to deconvolute the D and G peaks as amorphous films are disordered [101]. This provided semi-quantifiable data to compare the carbon peak positions before and after exposure to high-temperature high-pressure water.

The Raman data collected in this EngD project was used in conjunction with nanoindentation data as they are both relatively quick and simple methods to characterise coating graphitisation and hydrothermal stability performance in amorphous carbon coatings.

2.4.6 Focused ion beam milling

Focused ion beam milling was used to prepare the samples for scanning electron microscopy, energy-dispersive x-ray spectroscopy, transmission electron microscopy, and electron energy loss spectroscopy. The FIB equipment was the FEI Quanta 200 3D at the University of Sheffield.

Focused ion beam milling was chosen over other methods like sectioning, grinding and polishing or fracturing of the samples because the fragile structure of the spalled area would have been compromised by other available techniques [106]. It also allowed specific sections of the sample to be chosen easily which would be difficult with preparation by dimpling.

FIB does however sometimes have issues with the preferential milling of certain materials within the samples. Much like the different rates of deposition in the coating rigs this is due to the different sputter rates of each material [106]. For this reason it was important to also prepare as-received coating samples to compare any changes in features. This

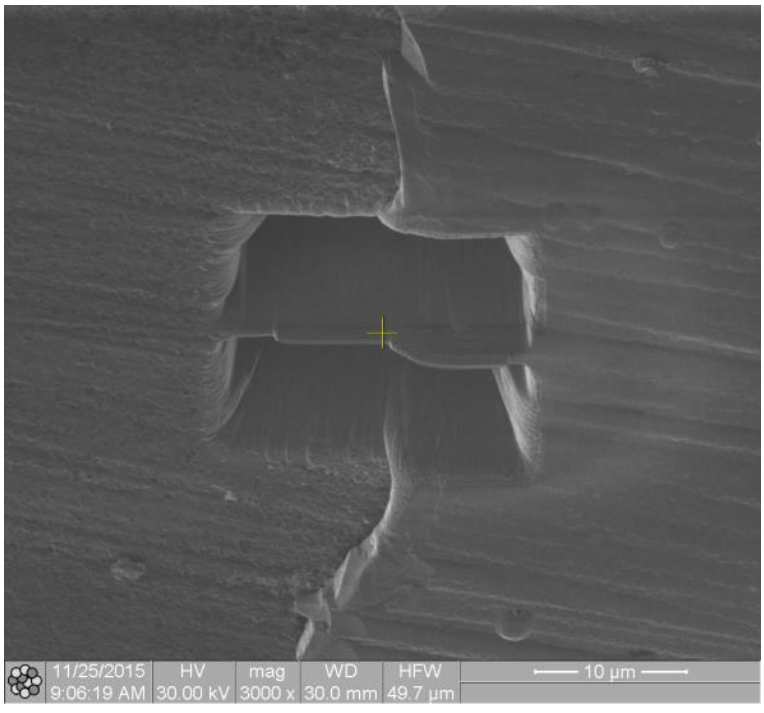

Figure 2.17 Focused ion beam trenches situated on edge of spalled Coating Type A.

helped to determine whether characteristics originated from material degradation due to autoclave exposure or the focused ion beam milling itself.

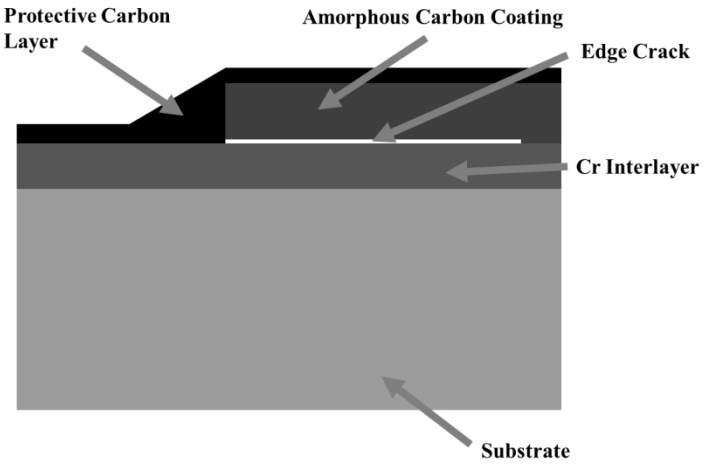

Figure 2.18 Schematic diagram of the TEM foil prepared from Coating Type A after the 2 year autoclave test.

There can also be issues with gallium ion implantation from the milling beam and also resputter of the milled material onto features in the sample. It is therefore useful to determine the composition of the substrate during elemental analysis to understand the origin of unexpected compositional elements.

The technique was used to prepare TEM foils of Coating Type A in several different conditions; as-received; after the 2 year autoclave test at CAPCIS; and after the 7 day autoclave test at the University of Manchester, as well as producing a cross-section of the coating for study in the SEM. It was also used to prepare TEM foils of Coating Types B and C to determine the structure, composition and bonding in their interlayers to analyse useful

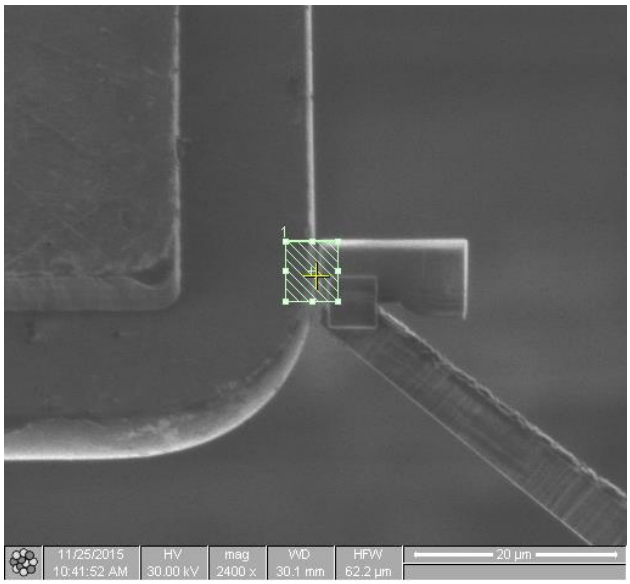

Figure 2.19 Position of Omniprobe on sample substrate during attachment to copper TEM grid.

features for coating stability in high temperature water conditions.

For the spalled coating sample the milled area was positioned on the edge of the step where the amorphous carbon film had delaminated as shown in Figure 2.17. This position was chosen so that the different layers in the cracked area and near the crack tip could be examined while leaving a section of the exposed substrate. It was necessary to attach the omniprobe to the exposed substrate during lift-out and manipulation of the sample as in Figure 2.18 and Figure 2.19. If the omniprobe was attached to the fragile partially delaminated amorphous carbon film there would be a chance of it separating during the lift-out process. This was due to cracking from the autoclave testing observed during the milling at the edge of the delaminated step during the preparation of the coating TEM foil.

As the amorphous carbon coatings had similar properties to the protective layer it was necessary to apply a relatively thick 5μm protective carbon deposition in the FIB instrument in order to protect the area of interest during milling. Some experimenting was necessary in order to mill the coating and substrate trenches while leaving the structure of the delaminated coating in the central foil intact.

The focused ion beam was also used for some imaging of the sample during milling to determine possible features of interest as it gave a more detailed image of the samples than the SEM also installed with the equipment.

2.4.7 Scanning electron microscopy

The FEI Inspect F scanning electron microscope (SEM) was used to examine the structure of the coating in a FIB cross-section. An SEM uses an electron beam to scan the surface of the sample in a raster pattern causing disruptions in an interaction volume within the material as shown in Figure 2.20 [107]. The changes in the secondary electrons emitted, or reflected backscattered electrons, are then picked up by detectors and used to produce detailed micrographs of the target material. Secondary electrons are useful for studying the topography of the substrate due to image contrast caused by the 'edge effect', whereby more secondary electrons are emitted near the edge or points of features as the interaction volume is closer to the surface of the material [108]. The SEM can also give some information about the relative atomic number of the elements in the interaction volume. Heavy elements are better at backscattering electrons in the samples and so appeared brighter in the contrast of the image produced [109]. These backscattered electrons can also cause further emission of secondary electrons which increase brightness in SE micrographs. This project used a combination of SE and

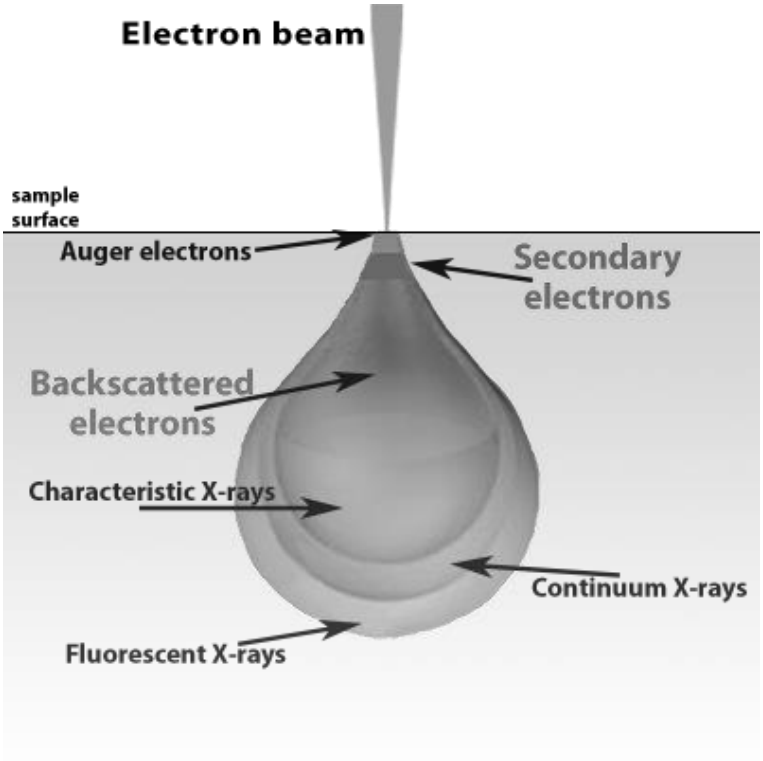

Figure 2.20 Schematic diagram of electron beam interaction [107].

BS detectors during the scanning electron microscopy characterisation to gain insights into the coating topologies and compositions.

In this project the scanning electron microscope was mainly used to analyse the topography of the open pathway running through the upper layers of Coating Type A after exposure in the 2 year autoclave experiment. This technique was chosen as it allowed a better initial understanding of the coating degradation mechanism as different mechanical or chemical processes would have dissimilar appearances. The FEI Quanta 200 3D also had the capability to capture micrographs with SEM but the imaging resolution of the Inspect F was more suitable for examining the fine feature topography found in the samples of this project. The cross-section site was chosen to be the stepped edge of the spalled amorphous carbon coating in Coating Type A after exposure to the autoclave testing. Scanning electron microscopy was used to analyse the overall structure of the coating and determine the layer through which the degradation mechanism was progressing.

Some elemental mapping of Coating Type A was also conducted by energy-dispersive x-ray spectroscopy in conjunction with scanning electron microscopy to determine the composition of the coating near the tip of the crack seen in the FIB milling. This was an attempt to analyse the chemical effects occurring at the crack tip to see if they were causing further propagation.

2.4.8 Transmission electron microscopy

In order to better understand the mechanisms of material degradation the samples were examined using the JEOL JEM-2010F and JEOL R005 transmission electron microscopes at the University of Sheffield. The TEM produced images of the ultra-thin samples by passing a focused beam of electrons through the material. The electrons that pass through the sample then form a transmission illumination on the detectors which could then be recorded with the CCD camera. This project also used scanning transmission electron microscopy (STEM) to scan the surface of the sample to produce micrographs for mapping and linescans in energy dispersive X-ray spectroscopy and electron energy loss spectroscopy. The TEM was used to increase the resolution of the sample imaging from the SEM study in order to analyse the development of detailed features in the coating structures before and after exposure to the autoclave testing. The TEM was conducted in parallel with EDX and EELS to determine the composition of each of the thin layers in the coatings.

The sample imaging was conducted in both annular dark field (ADF) and

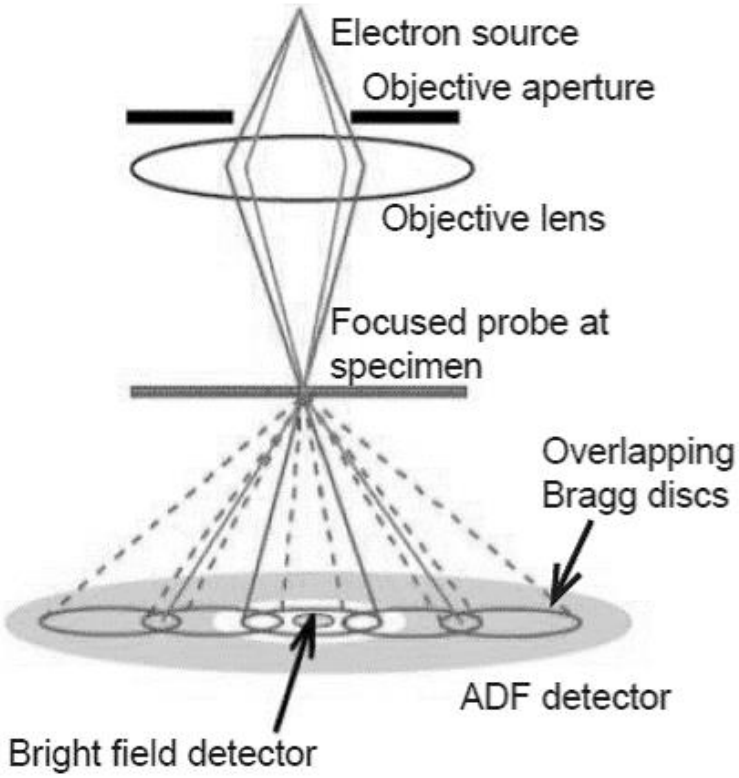

Figure 2.21 Schematic diagram of STEM image formation [110].

bright field (BF) detection modes. The schematic diagram in Figure 2.21 shows the positioning of the two detectors [110]. The annular dark field detector collects electrons incoherently scattered through higher angles to produce images with atomic number contrast, with heavier atoms appearing brighter. The collection efficiency is higher than BF imaging as the annular detector is larger than the BF on-axis detector. The bright field detector produces image contrast through measuring Bragg interference in the cone of illumination on-axis with the electron beam. The image contrast can be harder to interpret when compared to ADF micrographs as bright field images are affected by sample thickness and phase contrast. The detectors are often used together to with EELS and EDX to gain a better interpretation and understanding of the sample.

The work with the JEOL JEM-2010F field emission gun TEM microscope on Coating Types A and B was conducted at 200kV. An as-received sample of Coating Type A was prepared in addition to the autoclave exposed samples to compare the features caused by the autoclave experiments and those caused by the focused ion beam milling during the sample preparation. A sample of Coating Type A from the 7 day autoclave test at the University of Manchester was analysed with the TEM to determine the method of material degradation seen in the spallation of the coating during the experiment. A sample of Coating Type A that went into the 2 year CAPCIS autoclave study was also examined to analyse the features, composition, and bonding of the layers found in the coating observed with the scanning electron microscope.

Finally, transmission electron microscopy was used to compare the structure, composition, and bonding in the commercial coatings and the depositions from the University of Akron to look for features that affect the performance of the coatings during the autoclave testing. The work on Coating Type C was performed on the JEOL

R005 aberration corrected microscope at 300kV. The equipment uses two asymmetrical lenses to correct the aberrations in the electron lenses and provide electron beam focus to <1Å diameter [111].

2.4.9 Energy-dispersive x-ray spectroscopy

The technique of energy-dispersive x-ray spectroscopy (EDX) was used to analyse the composition of the coatings in the scanning electron microscope and transmission electron microscope. EDX works by detecting the X-rays generated from the interaction volume when the sample is bombarded with a high energy electron beam. Quantitative analysis of the X-ray spectrum emitted is then used to determine the local chemical composition of the material by matching energy levels with corresponding atomic shells for each of the elements present. Like scanning electron microscopy the beam can also be used to raster scan the surface to produce elemental maps or line-scans.

When used in a scanning electron microscope the spatial resolution is determined by the interaction volume of the electron beam with the sample material as in Figure 2.18 [107]. The volume also depends on the density of the material and the accelerating voltage, increasing with lower z numbers and increasing voltage. When used in the TEM the X-rays emitted are from a far smaller interaction volume depth as the prepared samples are extremely thin. This gives a better spatial resolution as the X-rays detected are from a focused area under the electron beam. An advantage of EDX is that it is good at picking up heavier elements as the L and M peaks from electron shells are usually higher than the background signal compared with the K peaks.

2.4.10 Electron energy loss spectroscopy

Electron energy loss spectroscopy (EELS) was used to analyse the composition and bonding in each of the coating layers before and after exposure in order to determine the mechanisms involved in deposition and degradation of the coatings.

EELS can be used to analyse the samples by passing a beam of electrons with a low range of known energies through the material and measuring the change in energy loss as they undergo inelastic scattering as shown schematically in Figure 2.22 [112]. The energy loss spectrum detected will have peaks corresponding to these atomic interactions that match with certain elemental features of the material. The samples needed to be very thin for EELs to work effectively as the scattered electrons rely on passing through the entire sample to produce the spectra.

Electron energy loss spectroscopy is a complementary technique to energy-dispersive x-ray spectroscopy as they both have different advantages in analysing the presence of different elements in the sample. Electron energy loss spectroscopy is better at measuring lighter elements as the energy loss spectra signals are stronger when less energy is lost during scattering.

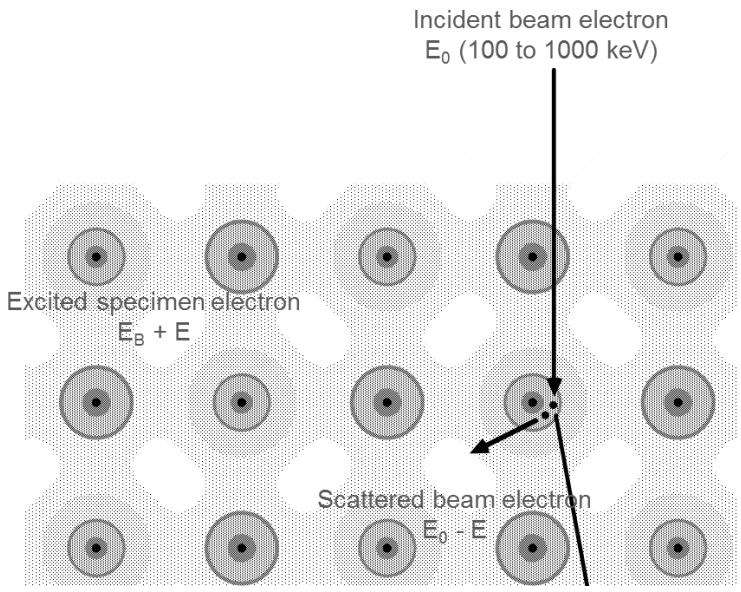

Figure 2.22 Electron energy loss from atoms in the material [112].

2.5 Summary

This chapter outlined the materials and the experimental methods used to investigate the project objectives. The chapter detailed the coating types and substrates used, as well as the experimental methods and their desired contribution to knowledge.

The following two chapters cover the results of the experimental investigations and are followed by a discussion of their meaning.

Chapter 3 details the investigation into the hydrothermal stability of amorphous carbon coatings in high-temperature high-pressure water.

Chapter 4 details the effects of different amorphous carbon coating properties on hydrothermal stability performance and failure in high-temperature high-pressure water.

Chapter 5 is a discussion of these results and what they mean in the context of the aims of the thesis.

Chapter 3: Hydrothermal stability of amorphous carbon coating properties in high-temperature high-pressure water

3.1 Introduction

This chapter details the results of the first aim to investigation into the hydrothermal stability of the four amorphous carbon coating types of interest to Rolls-Royce.

Rolls-Royce had previously conducted work in order to identify coatings that perform well when exposed to hydrothermal conditions found in pressurised water reactors, examining a significant variety of commercial coatings as shown in Table 1 (p.34). From these tests Rolls-Royce identified two commercial amorphous carbon coatings for further investigation in order to find their hydrothermal stability limits, Coating Type A and Coating Type B.

The first step to understanding the hydrothermal performance of the coatings was to determine the level of degradation when exposed to high temperature water environments in a Parr bomb pressure vessel. If the coating did not adhere to the component substrate during even the relatively low operational conditions then any advantageous tribological properties it had were irrelevant to the eventual PWR application.

The experimental testing initially focused on these two coatings in order to gain an understanding of their stability performance in hydrothermal conditions before then

conducting further autoclave experiments at a higher temperature, also including laboratory prototype Coatings C and D for comparison.

The hydrothermal stability of the coatings was then assessed by comparing optical microscopy, nanoindentation, and Raman spectroscopy before and after exposure to high-temperature high-pressure water.

3.2 Parr bomb results

3.2.1 Coating Type A

The coating sample used had a slight pre-existing scratch on the surface as shown on the right section in Figure 3.1 but this did not lead to any significant localised spallation of the coating after the experiment as shown in Figure 3.2.

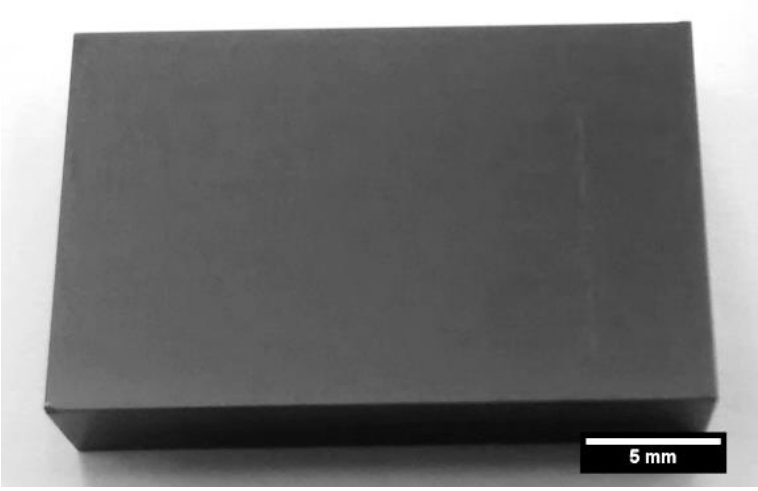

Figure 3.1 Coating Type A before the 24 hour Parr bomb experiment.

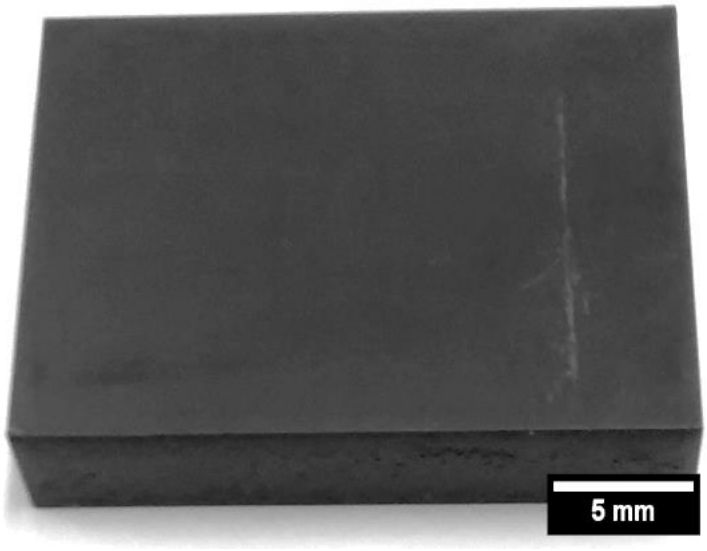

Figure 3.2 Coating Type A after the 24 hour Parr bomb experiment.

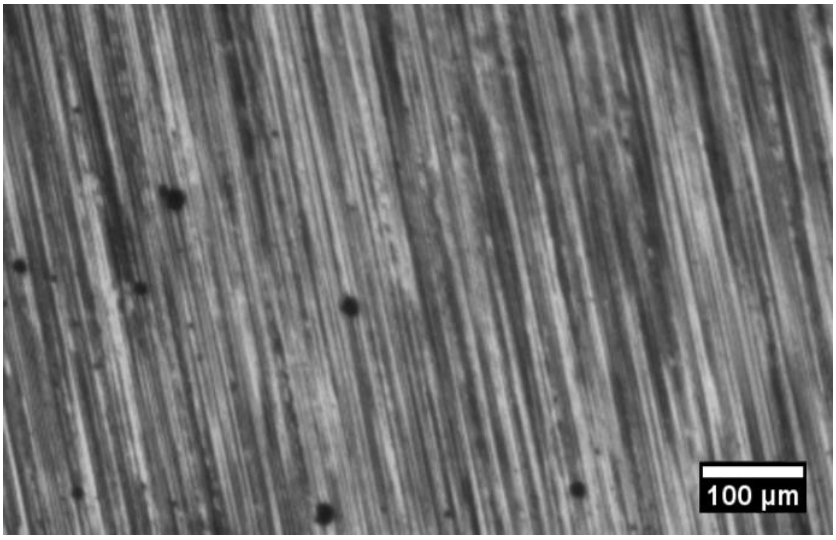

Figure 3.3 An optical micrograph of the as-received surface of Coating Type A

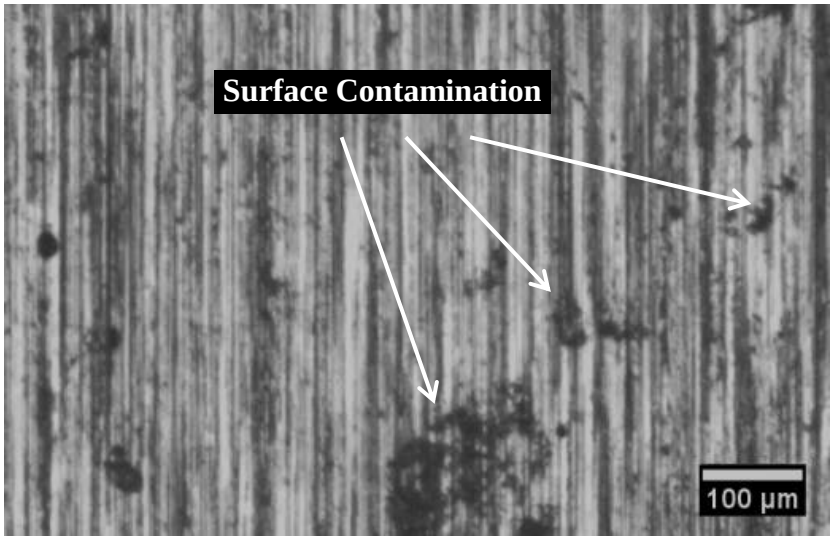

Figure 3.4 An optical micrograph of the surface of Coating Type A after the 24 hour Parr bomb experiment.

Figure 3.3 shows an optical micrograph of the as-received surface of Coating Type A. Following the Parr bomb experiment at 240°C for 24 hours the coating did not suffer any film spallation, as shown in the optical micrograph in Figure 3.4. There was some evidence of contamination on the surface of the sample and in the water during the 24 hour Parr bomb experiment, as shown in Figure 3.4, but the a-C:H coating itself was intact across the sample. The observed contamination is discussed in section 3.2.3

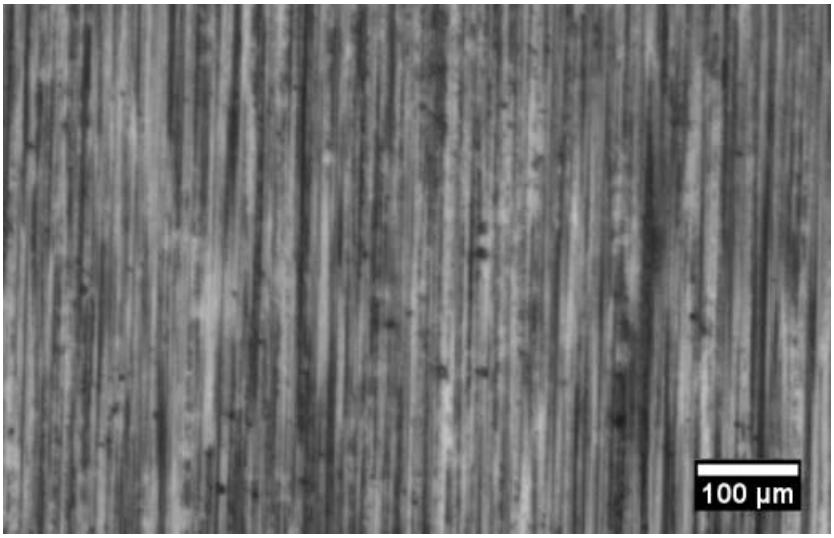

Figure 3.5 An optical micrograph of the surface of Coating Type A after the 7 day hour Parr bomb experiment.

where the water and particulate matter was analysed by inductively coupled plasma mass spectrometry.

When the experiment was repeated for the 7 day Parr bomb exposure there was also no sign of any coating spallation anywhere on the surface of the sample. During the experiments the appearance of the coating in Figure 3.5 remained similar to that of the as-received sample as in Figure 2.1.

Neither of the Parr bomb experiments on Coating Type A caused any film spallation as previously seen in the coating at higher temperatures in the autoclave. In order to study the degradation mechanisms for the coating previously observed by Rolls-Royce it was necessary to perform further experiments in the autoclave to achieve higher water temperatures with a better control of the experimental conditions.

3.2.2 Coating Type B

Figure 3.7 shows a Coating Type B sample after the 24 hour Parr bomb test. Although there were no signs of spallation when compared with the as-received a-C coating shown in Figure 3.6 there appeared to be adherent scales attached to some areas of the coating from the contamination in the vessel which was studied by inductively coupled plasma mass spectrometry in section 3.2.3.

The 7 day Parr bomb experiment also did not cause any obvious degradation or spallation of the coating, as shown in Figure 3.8. These results were as expected as Coating Type B was previously found stable during higher temperature exposure for the two year experiment with the autoclave CAPCIS testing. Unfortunately there was also still some uncertainty associated with the results and subsequent characterisation methods as contamination was found in the vessel after the experiment. The contamination of the vessel was studied using inductively coupled plasma mass spectrometry as recorded in the following section of this thesis. The contamination could have affected the results of the experiment by causing premature material

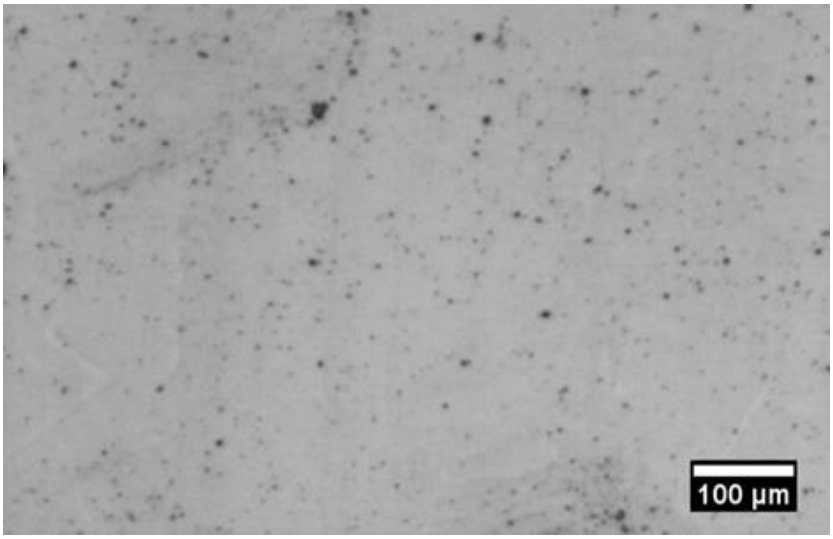

Figure 3.6 An optical micrograph of the as-received surface of Coating Type B

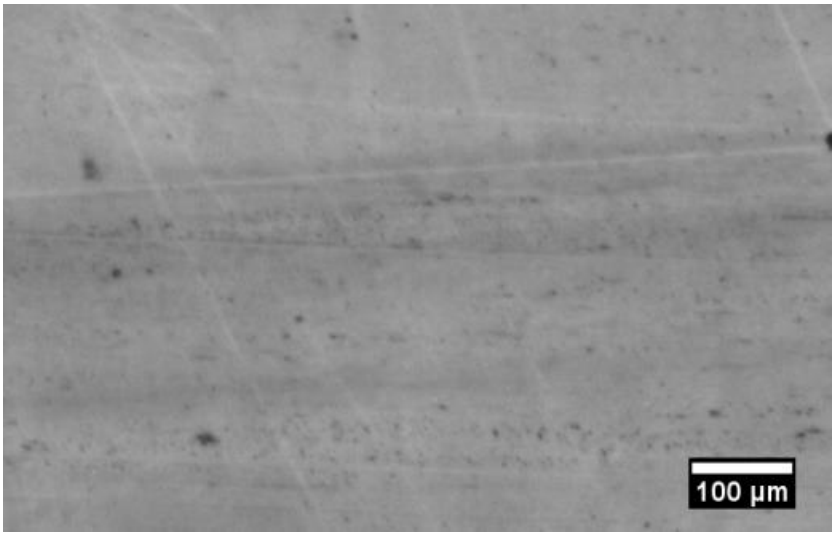

Figure 3.7 An optical micrograph of the surface of Coating Type B after the 24 hour Parr bomb experiment

degradation through corrosion mechanisms not expected to be present in the planned environment of high temperature deionised water.

Due to concerns over the contamination of the shared vessel, water samples were studied by inductively coupled plasma mass spectrometry to determine the source. Even with the added risk of additional corrosion mechanisms due to the contamination shown in Table 4 the Parr bomb tests at 240°C were not enough to cause delamination of the

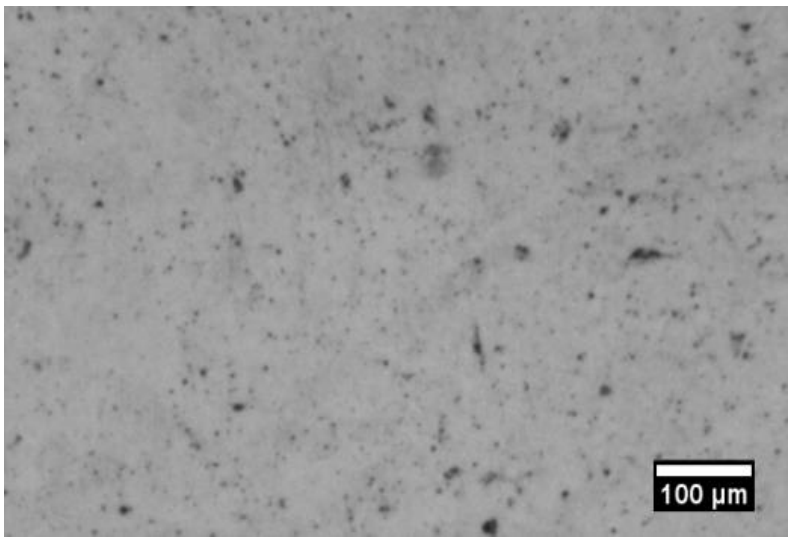

Figure 3.8 An optical micrograph of the surface of Coating Type B after the 7 day Parr bomb experiment.

coatings so further experiments at 280°C in an autoclave were planned to determine their hydrothermal stability limits with additional environmental monitoring and control.

3.2.3 Inductively coupled plasma mass spectrometry results

Inductively coupled plasma mass spectrometry of the water samples taken from after the 7 day Parr bomb experiments revealed that the red particulates observed in the water were predominantly iron based, with several other chemical additions present as recorded in Table 4. Some of the other elements measured like aluminium, copper and zinc are not present in the coatings or substrates as later examined by EDX and EELS which indicates contamination of the vessel from another source.

As the tests in this project were conducted in a shared lab and near the limit of Parr bomb design temperature the contamination could have been due to remaining corrosion material from other experiments leaching into the water from the surface of the PTFE cup material. Some, but not all, of the elements present could have also been from corrosion of the steel substrates. A reduction in concentration of the unexpected elements in parts per billion between the experiment with Coating Type A and subsequent Coating Type B test suggests leaching of material from previous experiments in the PTFE cup at high temperature that were later removed when the vessel was cleaned between tests.

It was possible that the addition of these elements would have resulted in deleterious chemical and mechanical processes occurring in the vessel; however, there was no significant degradation in any of the exposed coating samples. The uncertainties due to the contamination in the Parr bomb experiments were later reduced during the autoclave experiment at the University of Manchester as there was far more control of the environmental conditions. Measuring the conductivity of the deionised water during the experiment could have helped reduce the uncertainty with regards to the unwanted contamination.

Table 4 Inductively coupled plasma mass spectrometry of the liquid and particulates from the 7 day Parr bomb water samples.

Element ppb	Coating Type A (liquid)	Coating Type B (liquid)	Coating Type A (particulates)	Coating Type B (particulates)
Ag	0.0	0.0	0.4	0.3
Al	61.8	44.3	1965.4	186.3
As	1.6	8.7	9.0	0.0
Ba	4.4	16.2	56.4	14.5
Ce	0.0	0.0	10.0	0.5
Co	0.0	0.0	22.2	2.3
Cr	0.7	16.0	480.2	14.5
Cu	13.0	11.7	328.3	411.2
Fe	3.2	5.4	62974.6	2142.2
Ga	0.1	0.5	0.0	0.0
Li	0.2	0.6	0.0	0.5
Mn	4.1	2.6	322.5	17.3
Mo	30.0	10.0	0.0	0.0
Nd	0.0	0.0	0.7	0.0
Ni	19.3	3.6	232.6	411.3
Pb	0.0	0.0	11.9	3.8
Rb	0.9	2.0	0.0	0.0
Se	0.0	0.0	1.1	1.4
Sr	0.9	2.7	0.7	0.0
V	0.3	0.5	2.8	0.0
Zn	11.5	0.9	141.6	53.1

3.3 Autoclave results

The initial impression from the autoclave experiment at the University of Manchester was that Coating Types B, C and D appeared to have survived the experiment intact whereas Coating Type A suffered partial spallation across the coated surface.

3.3.1 Coating Type A

Figure 3.9 shows a photograph of Coating Type A after the 7 day exposure, with patches of the a-C:H coating spalled off across the surface of the sample. Some areas of coating that remained adherent also appeared slightly discoloured.

Previous autoclave testing by Rolls-Royce had shown that amorphous carbon film spallation occurs in Coating Type A at temperatures around 300°C so the autoclave exposure experiments at 280°C at the University of Manchester were expected to result in some degradation of the coating.

Optical microscopy of the sample surface showed that

Figure 3.9 Partially spalled surface of Coating Type A after the 7 day autoclave test.

some areas have a lot of the amorphous carbon coating spalled away to reveal the underlying interlayers, as shown in Figure 3.10, but in some sections the coating has stayed relatively intact, as in Figure 3.11

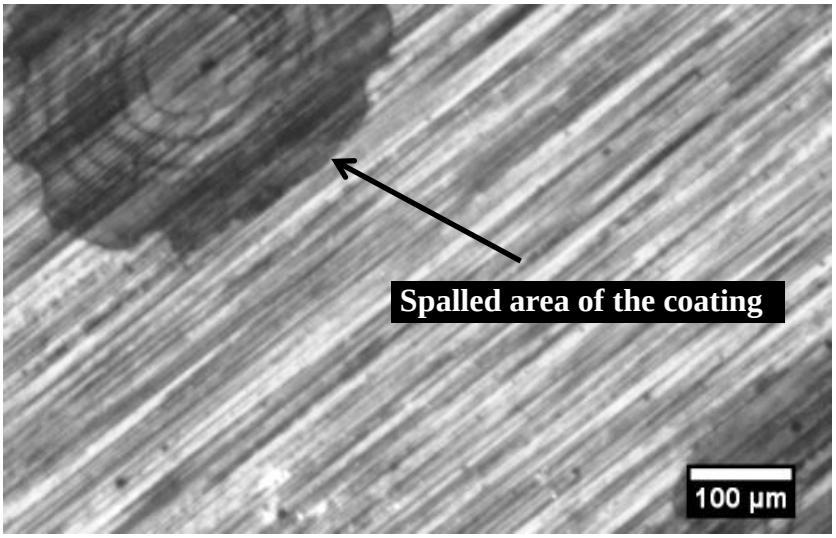

Figure 3.10 An optical micrograph of the spalled surface of Coating Type A after the 7 day autoclave experiment.

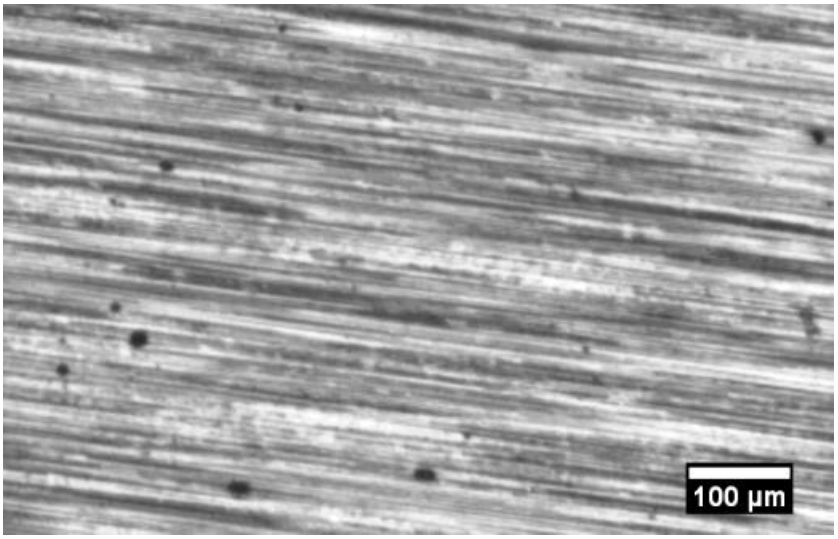

Figure 3.11 An optical micrograph of the intact surface of Coating Type A after the 7 day autoclave experiment.

3.3.2 Coating Type B

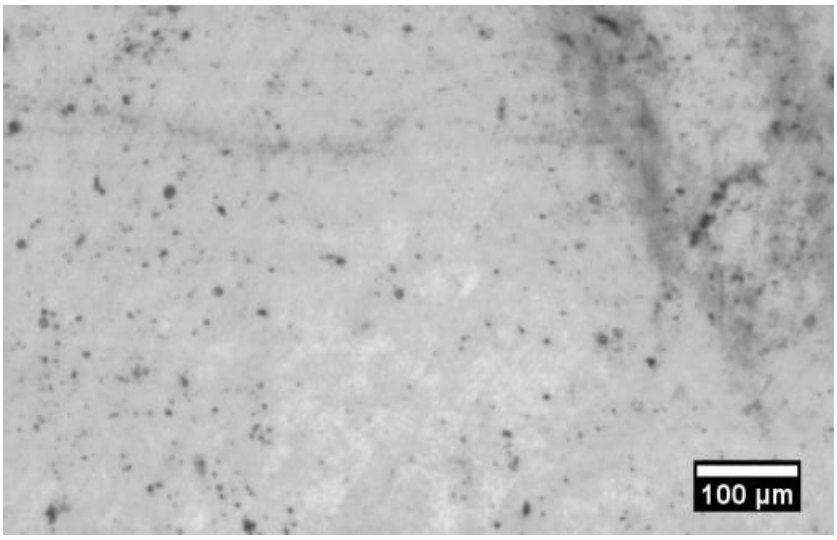

Figure 3.12 An optical micrograph of the surface of Coating Type B after the 7 day autoclave experiment.

As expected based on the results of the previous Rolls-Royce experiments the appearance of Coating Type B did not change over the course of the exposure, as shown in Figure 3.12. The amorphous carbon did not spall away as seen with Coating Type A and remained in a state similar to when it was put into the autoclave at Manchester. For Coating Type B there was previously no indication of significant coating degradation at this temperature so there was no film spallation expected during testing. The result supports the previous Rolls-Royce autoclave studies and shows the hydrothermal stability of the amorphous carbon film and interlayer coating system.

3.3.3 Coating Type C

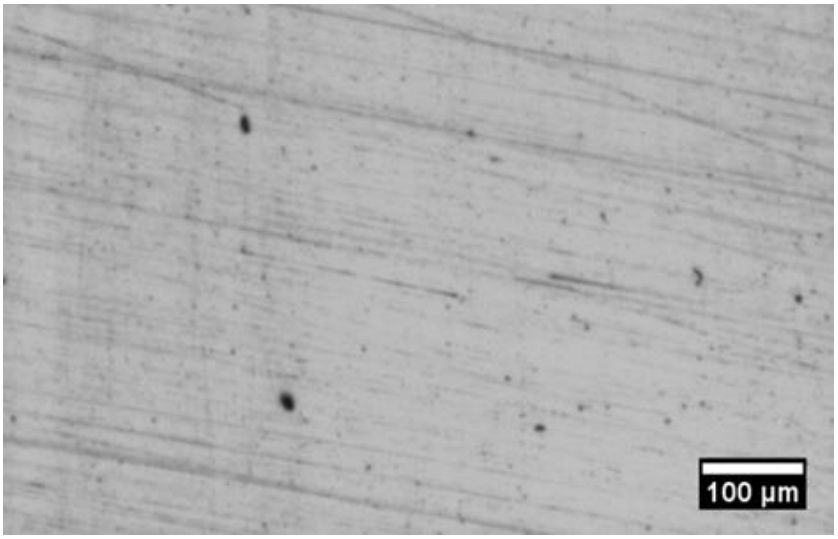

Figure 3.13 An optical micrograph of the as-received surface of Coating Type C.

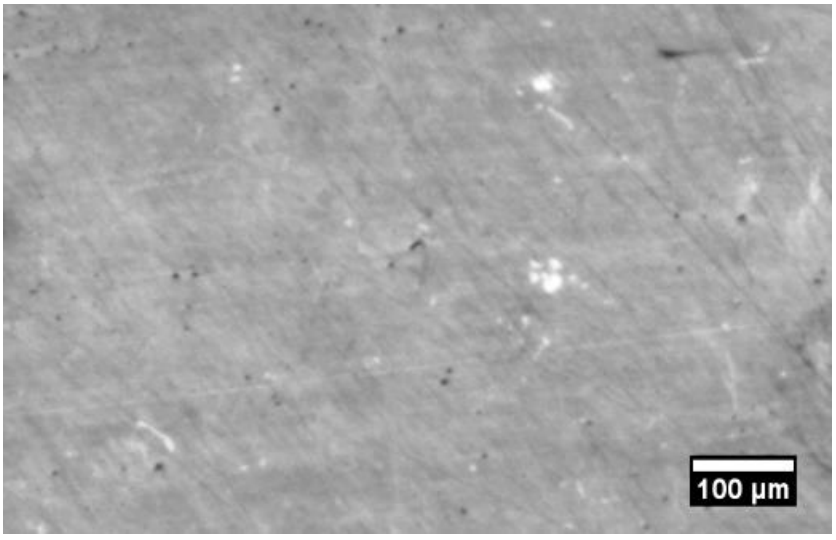

Figure 3.14 An optical micrograph of the surface of Coating Type C after the 7 day autoclave experiment.

The as-received Coating Type C shown in Figure 3.13 did not display any obvious signs of film spallation after the exposure in the autoclave presented in Figure 3.14 There was a slight interference pattern around the edges of the normally uniform dark grey a-C:Cr film following the experiment which could indicate compositional and/ or

structural changes in the carbon film or interlayers causing optical refraction shifts in the observed coating sample [104].

3.3.4 Coating Type D

When compared with the as-received coating surface in Figure 3.15 the amorphous carbon film in Coating Type D also appeared to have remained intact during the 7 day autoclave experiment with no exposes of the interlayer materials across the a-C:Ti coated surface during optical microscopy as shown in Figure 3.16.

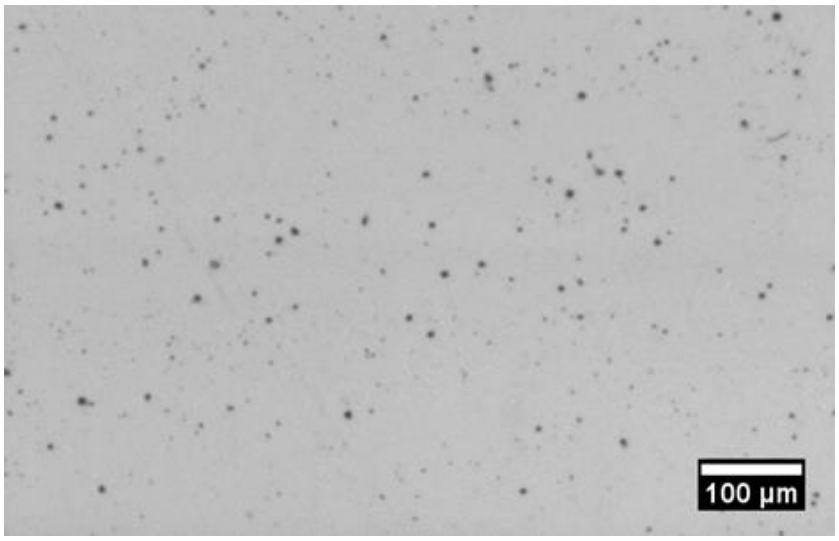

Figure 3.15 An optical micrograph of the as-received surface of Coating Type D.

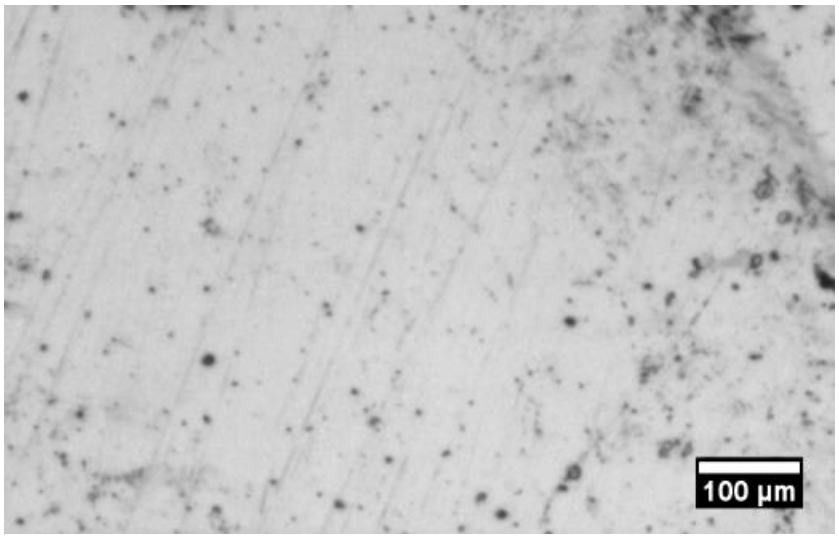

Figure 3.16 An optical micrograph of the surface of Coating Type D after the 7 day autoclave experiment.

3.4 Scratch adhesion testing results

Figure 3.17 shows the results of the scratch adhesion testing on the as-received amorphous carbon Coating Type A. A composite optical micrograph of the entire scratch was aligned above the graph of force against scratch distance to show changes in appearance with the increasing applied load. There are also two additional micrographs

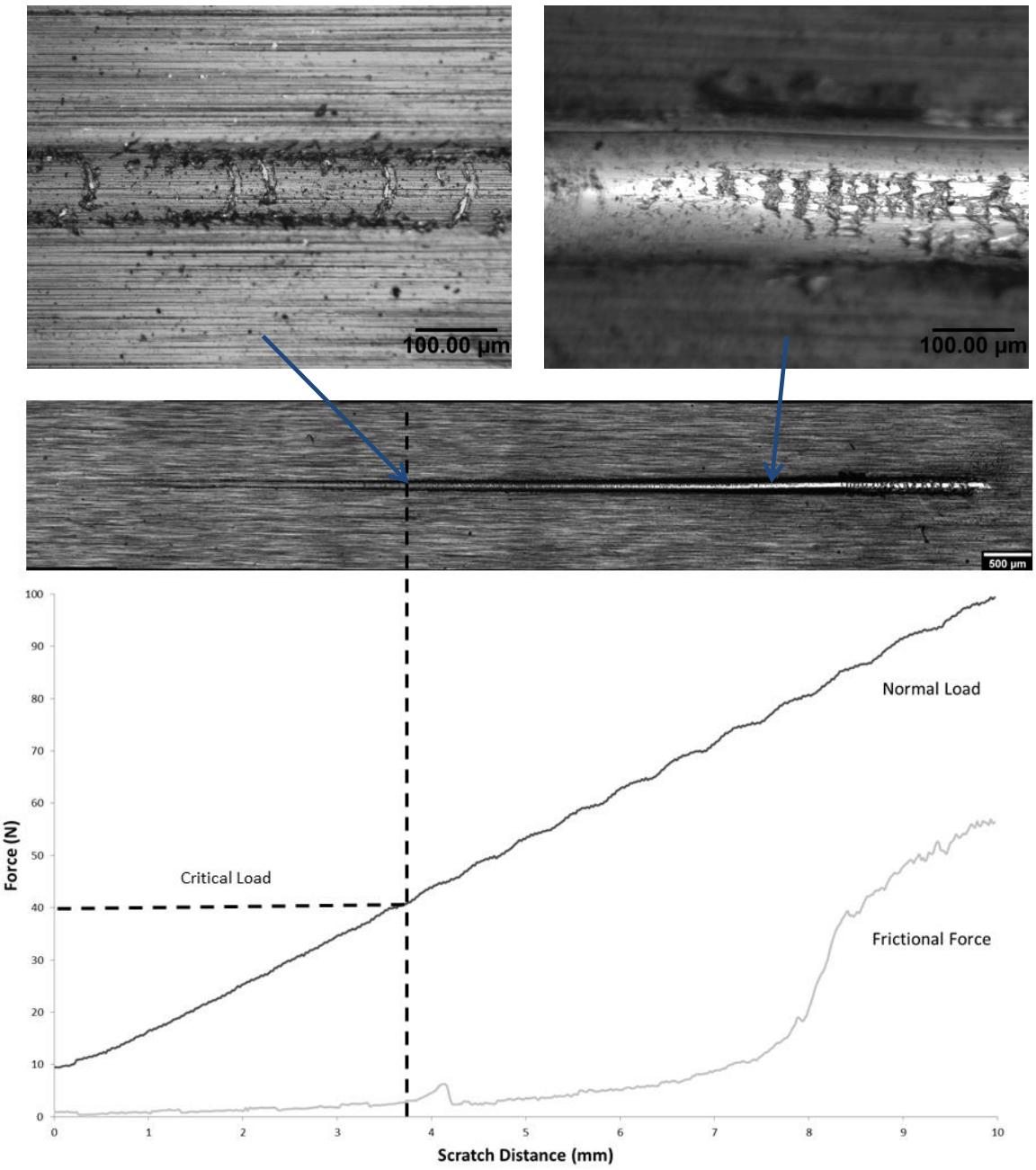

Figure 3.17 Graph of force against scratch distance for Coating Type A with aligned optical micrographs.

for each of the scratches to show points at which significant changes in the appearance of the scratch surface occurred. Due to the depth of the scratches sometimes the upper portions were out of focus when looking at the deeper features within.

The as-received amorphous carbon Coating Type A showed signs of coating adhesion failure in the optical microscope with conformal cracking at an applied scratch load of around 40N [95]. The frictional force remained low until a load of around 70N, where

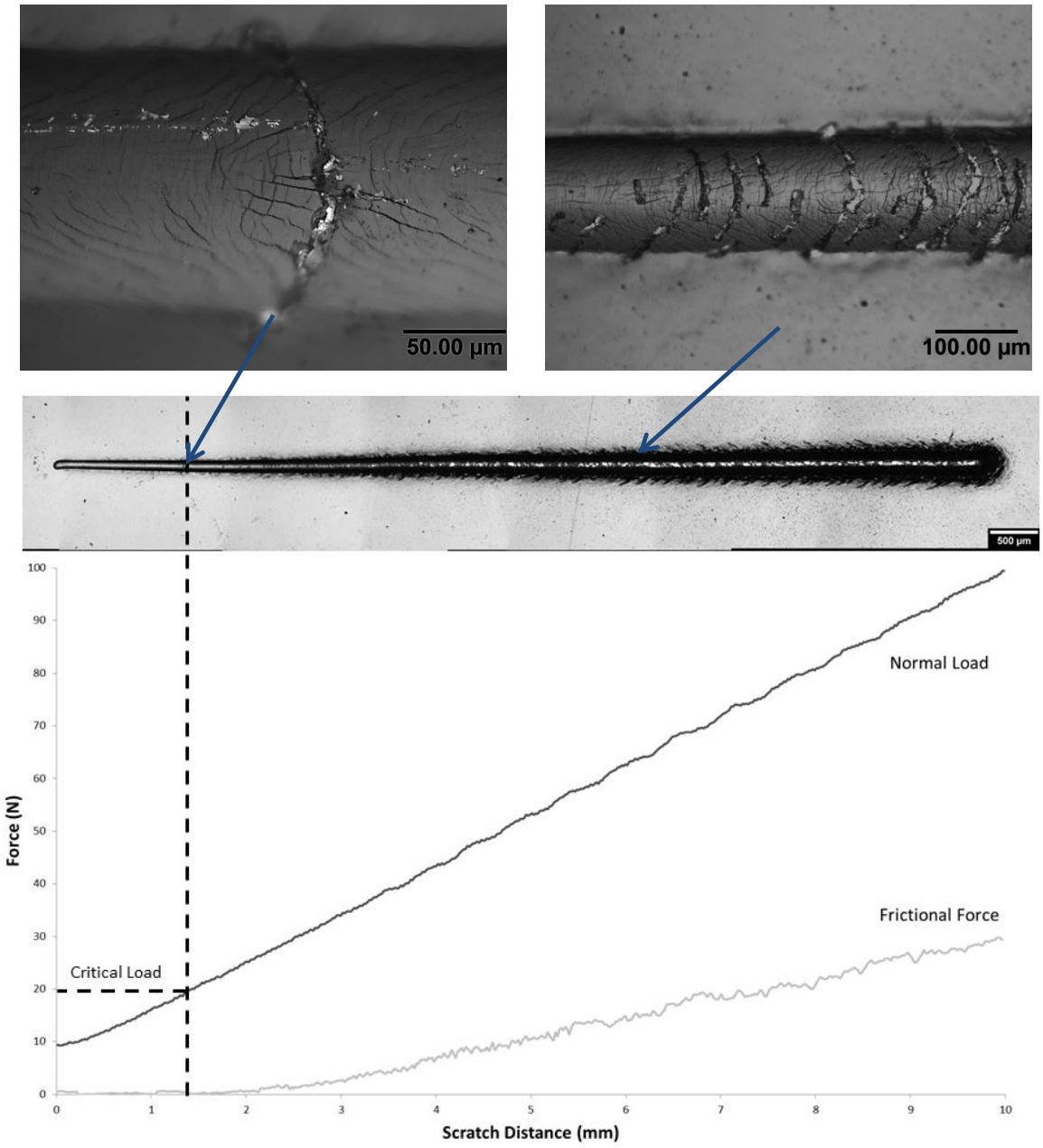

Figure 3.18 Graph of force against scratch distance for Coating Type B with aligned optical micrographs.

the wear increased significantly and gross spallation of the coating occurred.

In Figure 3.18 the results of the scratch adhesion test on Coating Type B are recorded. When compared with Coating Type A the scratch width and depth were larger at the same load and the underlying interlayers were revealed earlier, with conformal cracking at loads of around 20N. At higher applied loads the frictional force increased linearly,

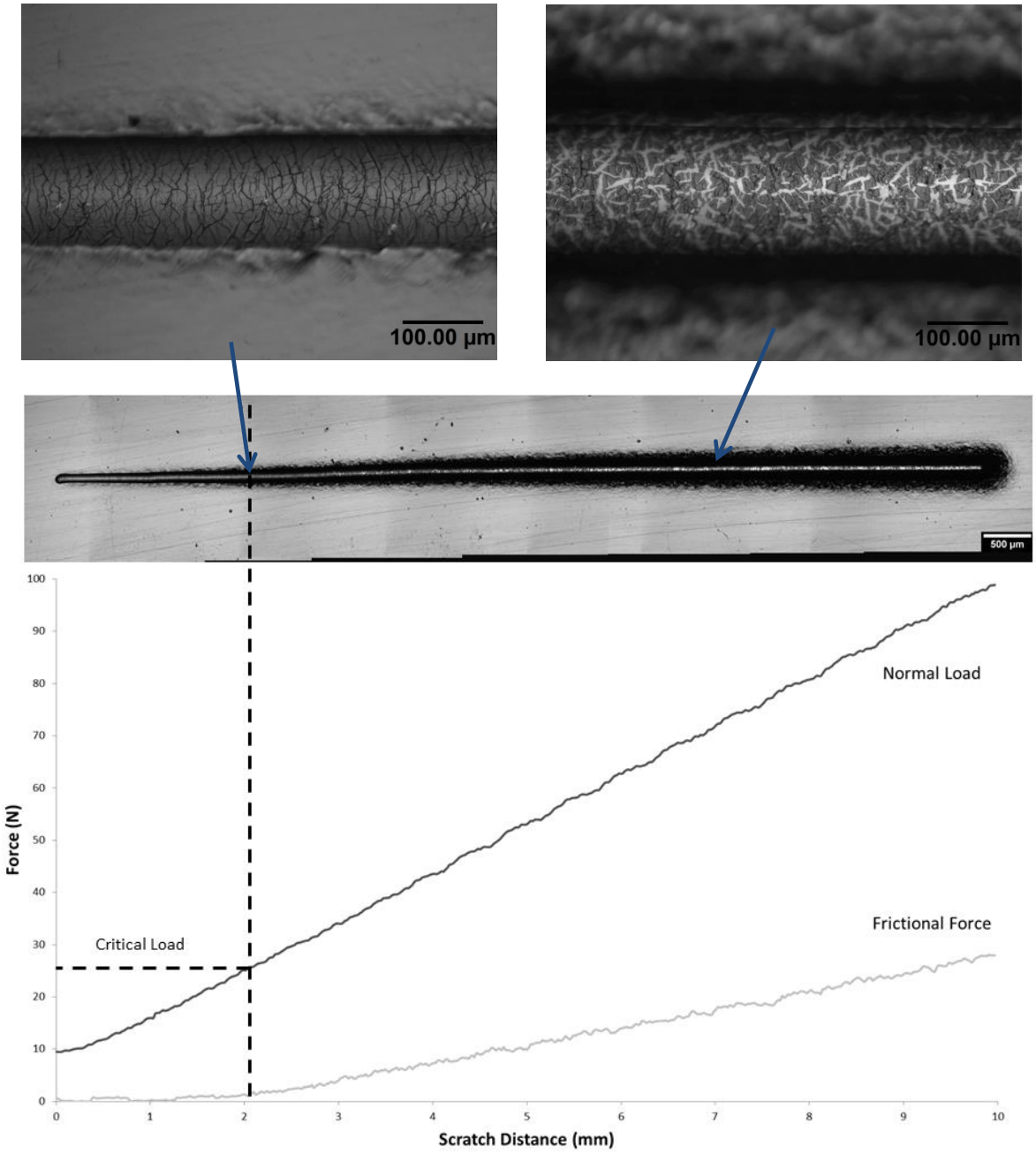

Figure 3.19 Graph of force against scratch distance for Coating Type C with aligned optical micrographs.

but finished lower than that observed in Coating Type A - although gross film spallation was clearly visible.

The results of the scratch adhesion test on Coating Type C are shown in Figure 3.19. At loads of around 25N cohesive cracking of the amorphous carbon was shown to cause delamination of the functional top layer, to reveal the interlayers below. As the load

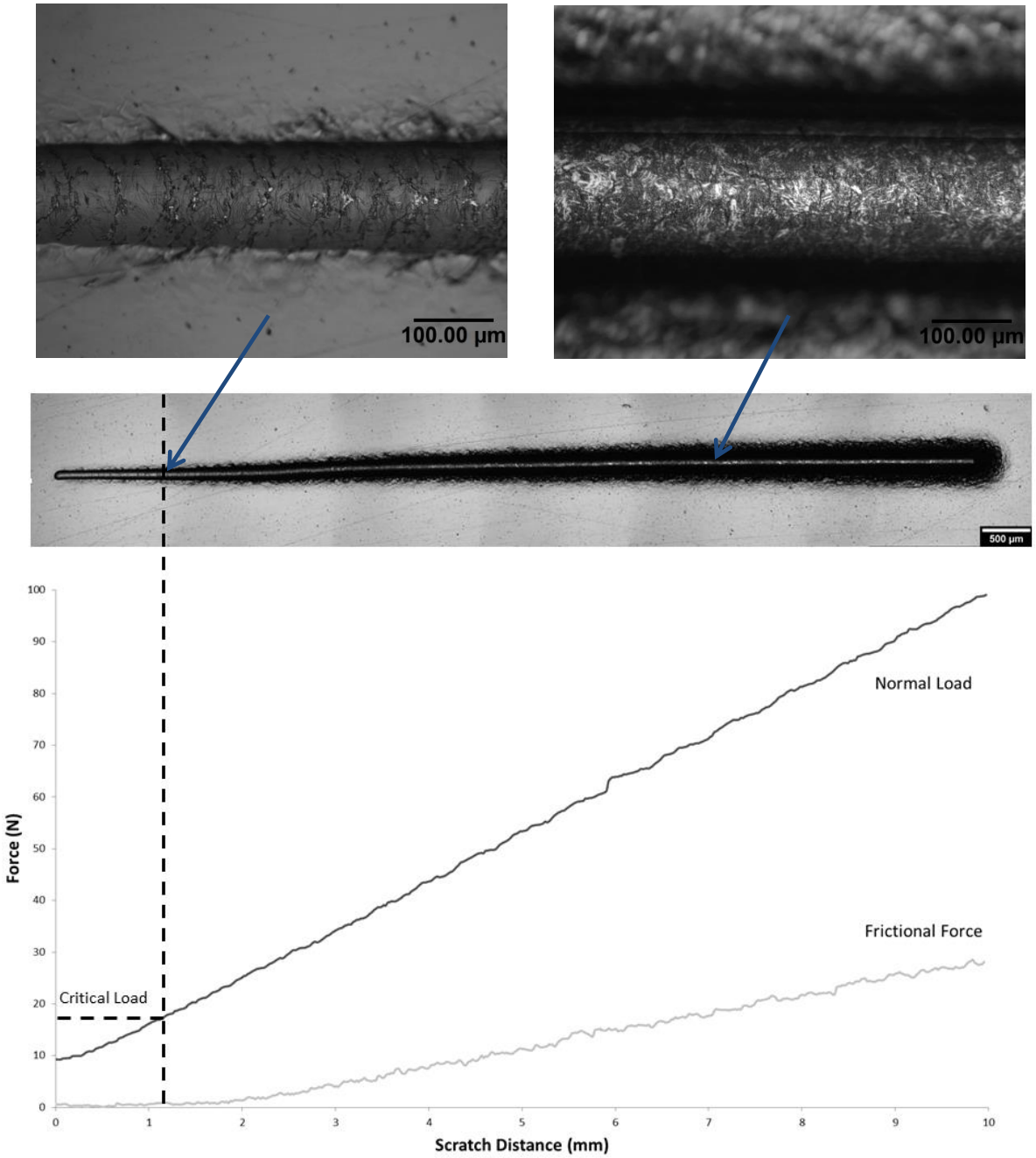

Figure 3.20 Graph of force against scratch distance for Coating Type D with aligned optical micrographs.

increased, the amount of coating delamination grew and the frictional force continued to increase linearly with increasing load, as seen for Coating Type B.

With Coating Type D the film first showed signs of adhesive failure in the sample scratches at loads just below 20N, as illustrated in Figure 3.20. As with Coating Types B and C, the frictional force increased linearly with the increasing applied load and extensive adhesive failure was observed at higher loads.

3.5 Nanoindentation results

Figure 3.21 shows the nanoindentation results in a bar chart of coating hardness against coating type and treatment condition. For Coating Type A the remaining amorphous carbon film was indented to obtain the measurements rather than the exposed interlayer materials.

Coating Type A showed a slight reduction in coating hardness of 2GPa from over 21GPa in the as-received state to around 19.5GPa after the 7 day autoclave and 7 day Parr bomb testing, however the standard deviations were high, limiting the interpretation of the data. Coating hardness after the 24hr Parr bomb test was lower, around 15GPa, which was a reduction of 6GPa. This outcome was unexpected as the

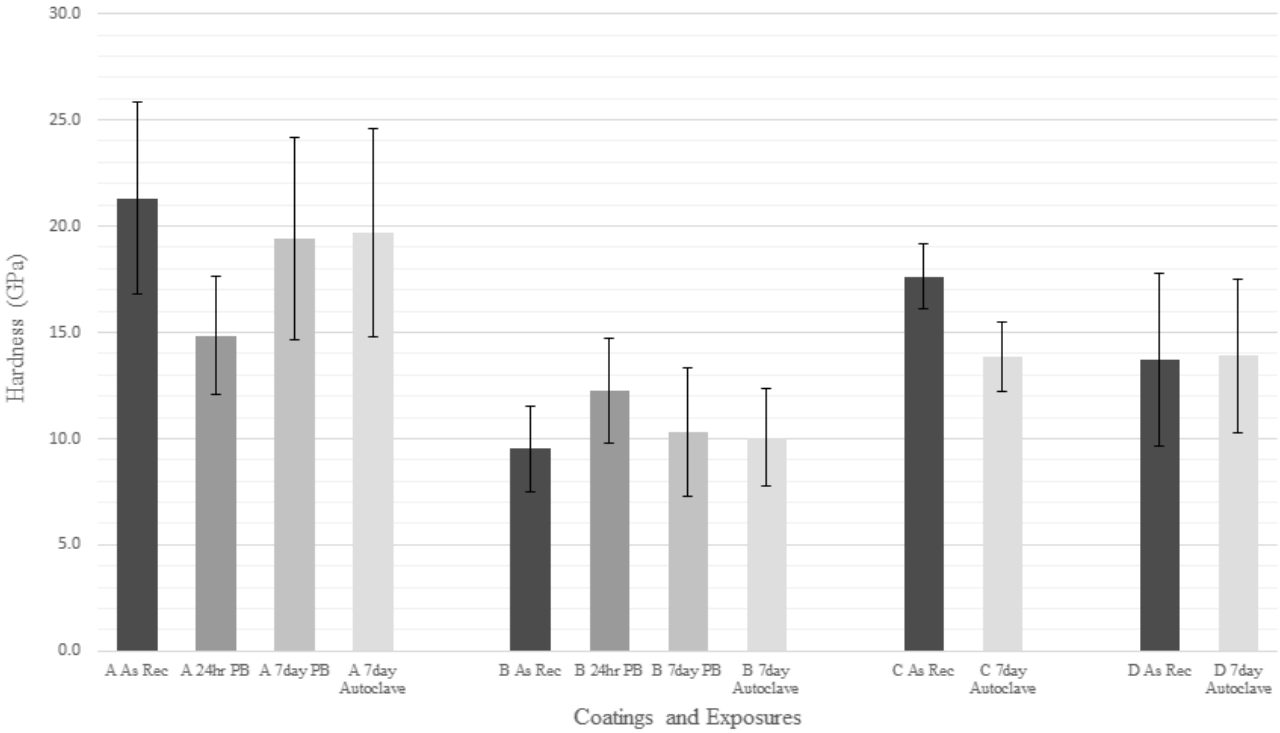

Figure 3.21 Nanoindentation hardness (GPa) results against coating types with different exposures.

reduction in hardness was greater than for the longer 7 day Parr bomb test under the same conditions. This result might have been due to the roughness of the older a-C:H coating samples causing issues with the nanoindentation geometry. Ridges in the surface topography meant that the tip was often measuring in either a peak or trough in the surface as seen the in the optical profilometry image in Figure 2.4. This is reflected in high standard deviations in the hardness data for the samples and the lower result for the 24hour Parr bomb test could be due to a particularly rough portion limiting the collected data to softer areas of the film surface.

The hardness values measured after the 24hr Parr bomb tests might have also been influenced by a layer of vessel contaminants on the sample surface, as seen in the optical microscopy and ICPMS. The measured hardness could have included components from both the coating and contaminants, which might explain why both have shifted towards a common hardness value compared to the other tests.

The hardness of the exposed Coating Type B samples remained very similar to that of the as-deposited sample in both of the autoclave tests, all around 10GPa. However the 24 hour Parr bomb experiment gave a measured hardness higher than the as received coating at just over 12GPa, although again when taking the standard deviations into account the results are similar. The measured nanohardness values for the as-received Coating Types A and B were very similar to the values recorded by Rolls-Royce in previous testing and stated by the manufacturers [1].

Coating Type C showed a reduction in coating hardness of around 4GPa after the 7 day exposure in the autoclave. This drop in a-C:Cr coating hardness could be the result of changes in the amorphous carbon coating properties or bonding, which might also be

related to the film discolouration seen in the optical microscopy as changes in carbon bonding type from sp3 to sp2 can also result in optical changes [104].

After the 7 day autoclave testing of Coating Type D the measured hardness of the sample was very similar to that of the as-deposited coating. When combined with the unchanged appearance of the a-C:Ti coating surface in the optical microscopy the results would suggest that the coating has good hydrothermal stability.

3.6 Raman results

Raman spectroscopy was conducted on the coatings to observe any trends in the material properties after the high temperature water tests. The spectra in this section show plots of the Raman shift against intensity. The intensity plotted on the Y axis was translated into arbitrary units to directly compare the spectra, with each data series offset to avoid overlap.

Figure 3.22 shows the deconvoluted carbon D and G peaks for the Raman spectra of the as-received Coating Type A. The shape of the spectrum is characteristic of an amorphous carbon coating with a significant proportion of sp^3 bonding with the D peak at 1390cm^{-1} and G peak at 1564cm^{-1}, but the presence of the shoulder caused by the D to G peak intensity ratio of 0.9 suggests the film is not a fully tetrahedral amorphous

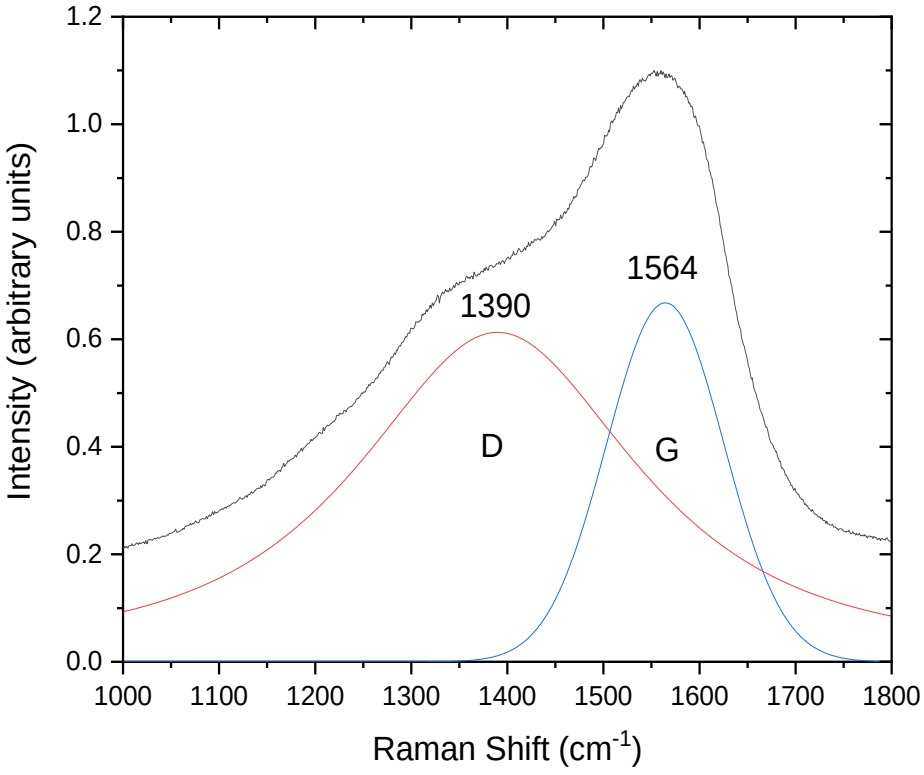

Figure 3.22 Deconvoluted Raman peaks for Coating Type A as-received.

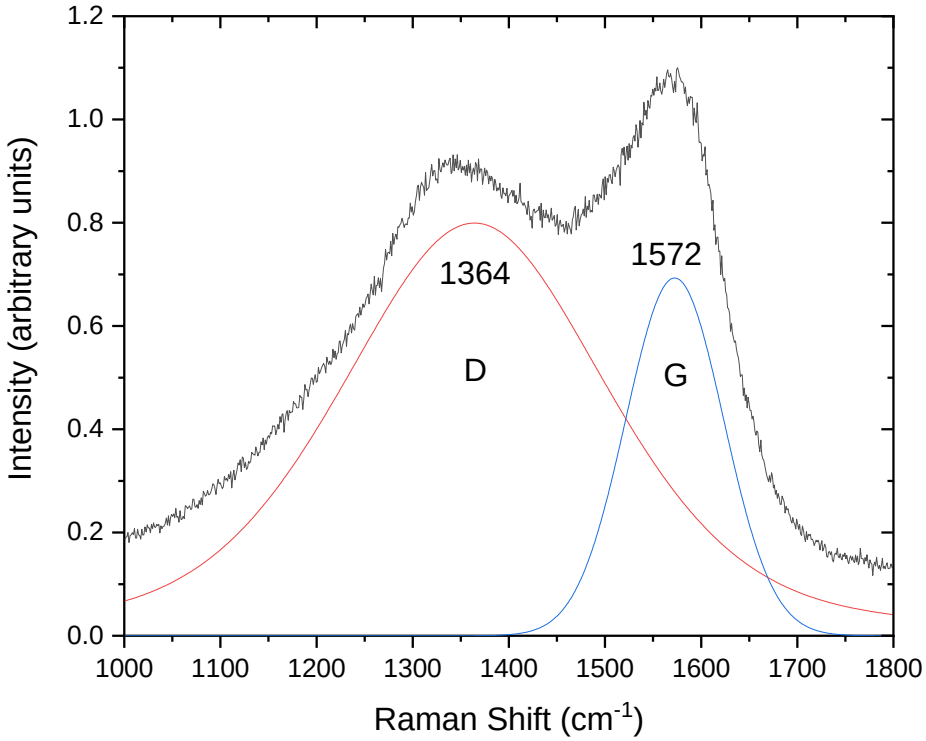

Figure 3.23 Deconvoluted Raman peaks for Coating Type A after the 24 hour 240°C Parr bomb test.

carbon and there is some sp^2 bonding [113].

Table 5 shows the data for the peak positions and intensities for Coating Type A. It also has the intensity I_D/I_G ratio for the peaks to show how they changed with exposure to high-temperature high-pressure water.

The Raman spectrum for the same coating after the 24 hour Parr bomb test is shown in Figure 3.23. The intensity of the D peak relative to the G peak has increased significantly to 1.16, while the G peak has moved to a higher wavenumber at 1572cm^{-1} and become sharper, indicating graphitisation of the coating surface with the exposure to high-temperature water [114].

In Figure 3.24 for the 7 day Parr bomb test the position of the G peak has increased further to 1575 cm^{-1} and the I_D/I_G ratio has also increased to 1.18 indicating additional

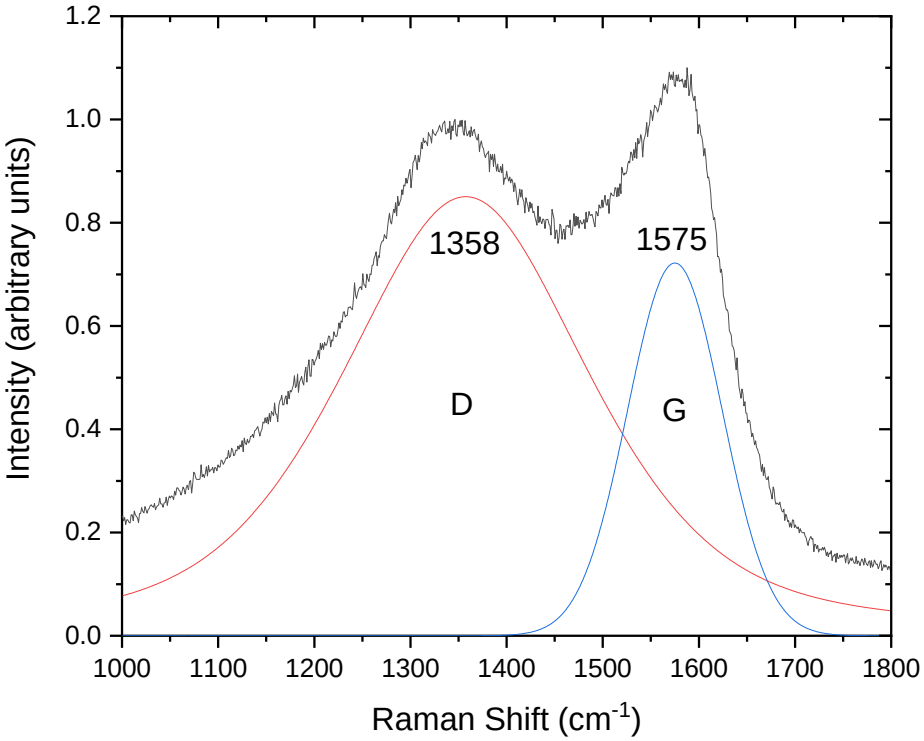

Figure 3.24 Deconvoluted Raman peaks for Coating Type A after the 7 day 240°C Parr bomb test.

graphitisation at the surface as the duration of the experiment was increased whilst the temperature stayed the same.

Figure 3.25 shows the spectrum for Coating Type A after the 7 day autoclave experiment. When compared with the as-received coating there is a definite increase in the G peak position to 1575cm^{-1}, the same as recorded for the 7 day Parr bomb experiment, however the I_D/I_G ratio only increased to 1.04 as the relative intensity increase of the D peak was lower.

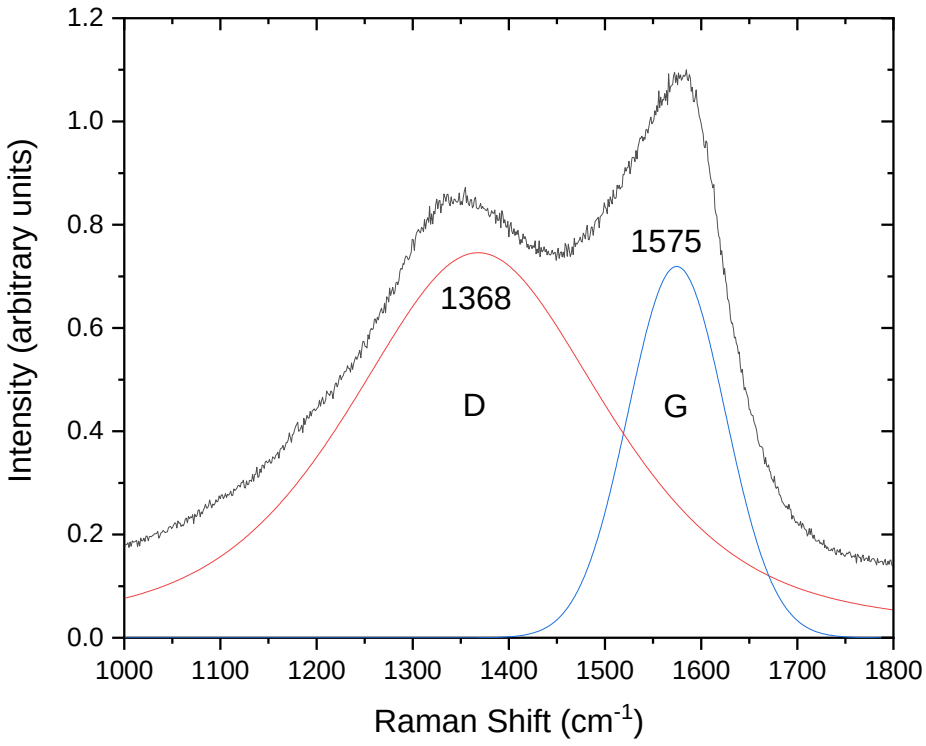

Figure 3.25 Deconvoluted Raman peaks for Coating Type A after the 7 day 280°C autoclave test.

Figure 3.26 shows the evolution of Coating Type A during the Parr bomb experiments. As the exposure duration increased there was a clear increase in the relative intensity of the D peak at around 1350cm^{-1} and a slight shift of the G peak to higher wavenumber from 1564 to 1575cm^{-1} These changes in the spectra indicated the increasing graphitisation of the a-C:H film with increased exposure [103].

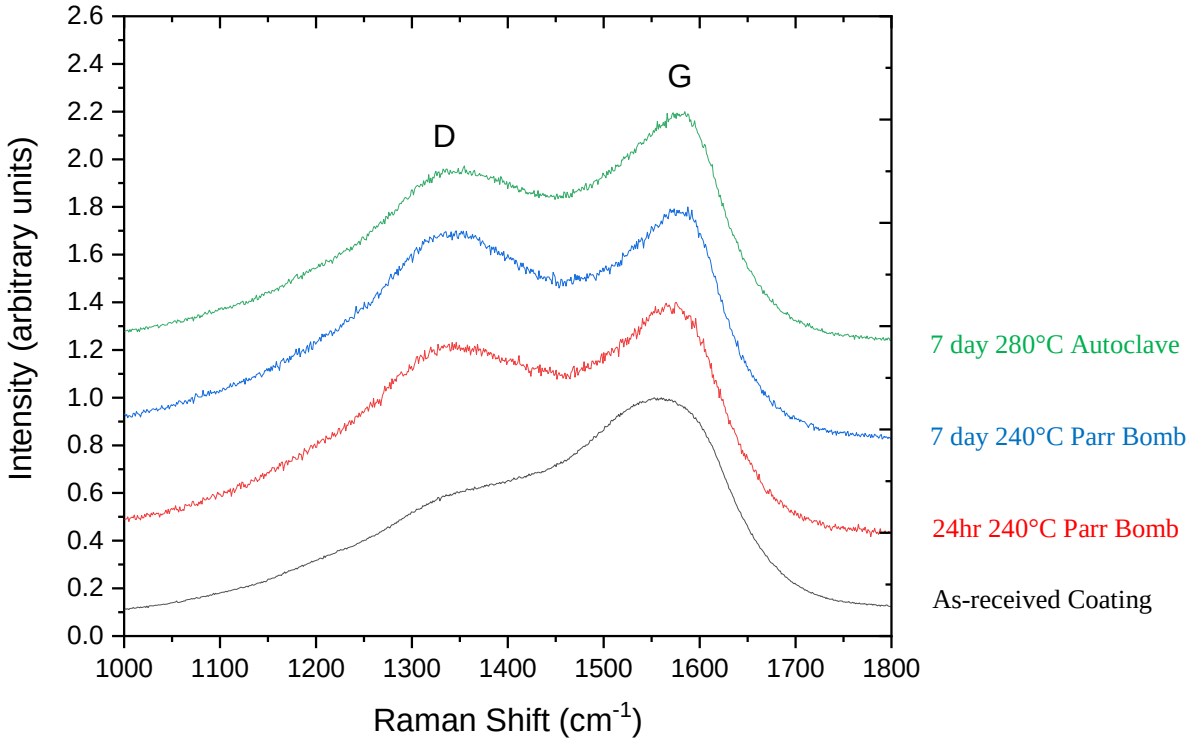

Figure 3.26 Evolution of Coating Type A Raman spectrum with increasing water temperatures and exposure lengths.

Table 5 Deconvoluted Raman peak data for Coating Type A.

Coating Exposure	D Peak Position (cm^{-1})	G Peak Position (cm^{-1})	I_D	I_G	I_D/I_G
As-received	1390	1564	0.61	0.67	0.91
Parr Bomb 24 Hours	1364	1572	0.80	0.69	1.16
Parr Bomb 7 Days	1358	1575	0.85	0.72	1.18
Autoclave 7 Days	1368	1575	0.75	0.72	1.04

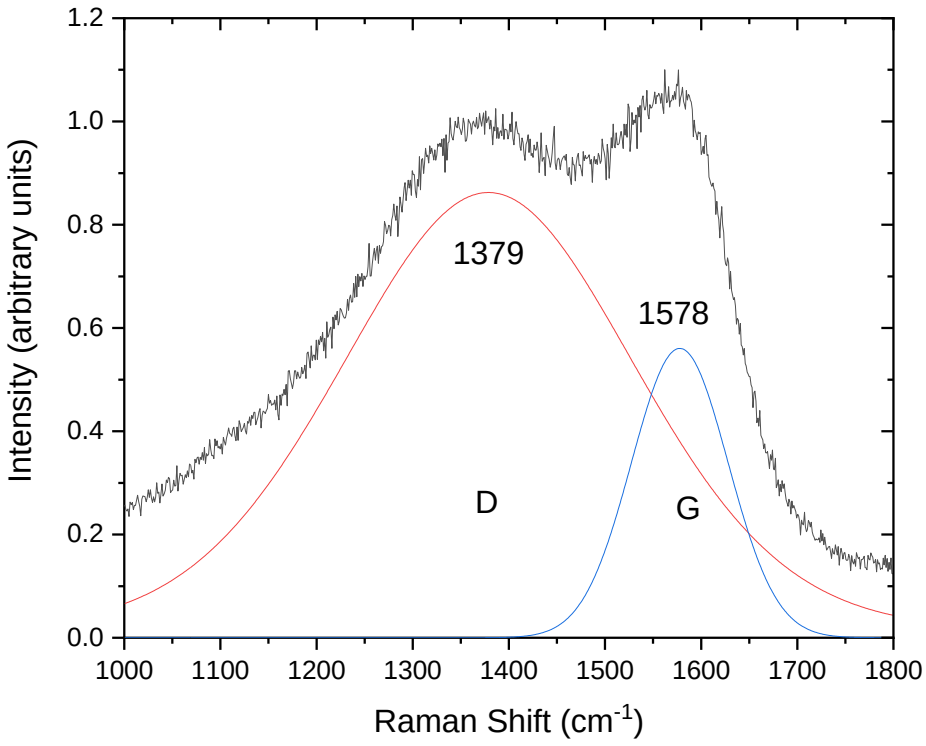

Figure 3.27 Deconvoluted Raman peaks for Coating Type B as-received.

Figure 3.27 shows the Raman spectrum for Coating Type B in the as-received state. When compared to Coating Type A the amorphous carbon films starts out a lot more graphitic in nature, with a G peak at 1578cm^{-1} and an I_D/I_G ratio of 1.54.

The Raman spectrum for the coating after the 24 hour Parr bomb experiment is shown in Figure 3.28. The data shows no large changes from the as-received coating when compared with those seen with Coating Type A, as the G peak has moved to 1582cm^{-1} and the I_D/I_G ratio was slightly lowered to 1.50.

The results of the 7 day Parr bomb experiment were similar to those of the 24 hour test at the same temperature, with the G peak at 1581cm^{-1} and the I_D/I_G ratio the same at 1.50.

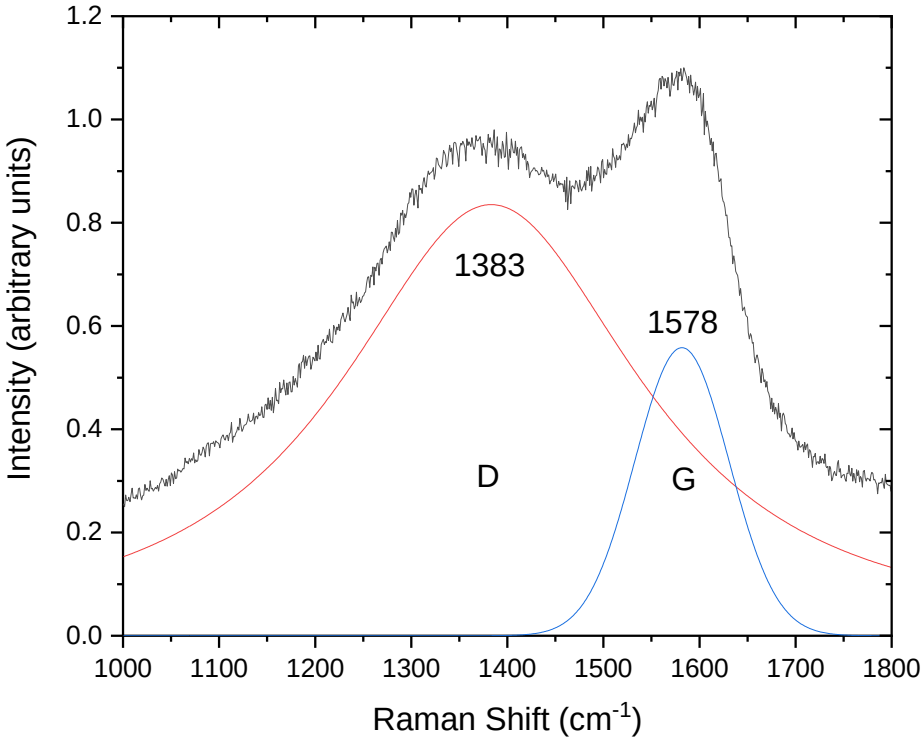

Figure 3.28 Deconvoluted Raman peaks for Coating Type B after the 24 hour 240°C Parr bomb test.

As with Coating Type A the results of the 7 day autoclave test also showed a similar G peak position to the 7 day Parr bomb test, this time at 1574cm^{-1}, however the I_D/I_G ratio was lower than that measured in the as-received coating, down from 1.54 to 1.42.

Table 6 shows the data for the deconvoluted Raman peaks for Coating Type B during the high-temperature water experiments and Figure 3.31shows the evolution of the coating with increasing temperature and duration. Coating Type B showed no large shifts in the Raman spectra after the autoclave tests when compared with the as-received coatings, suggesting the coating had better hydrothermal stability than Coating Type A.

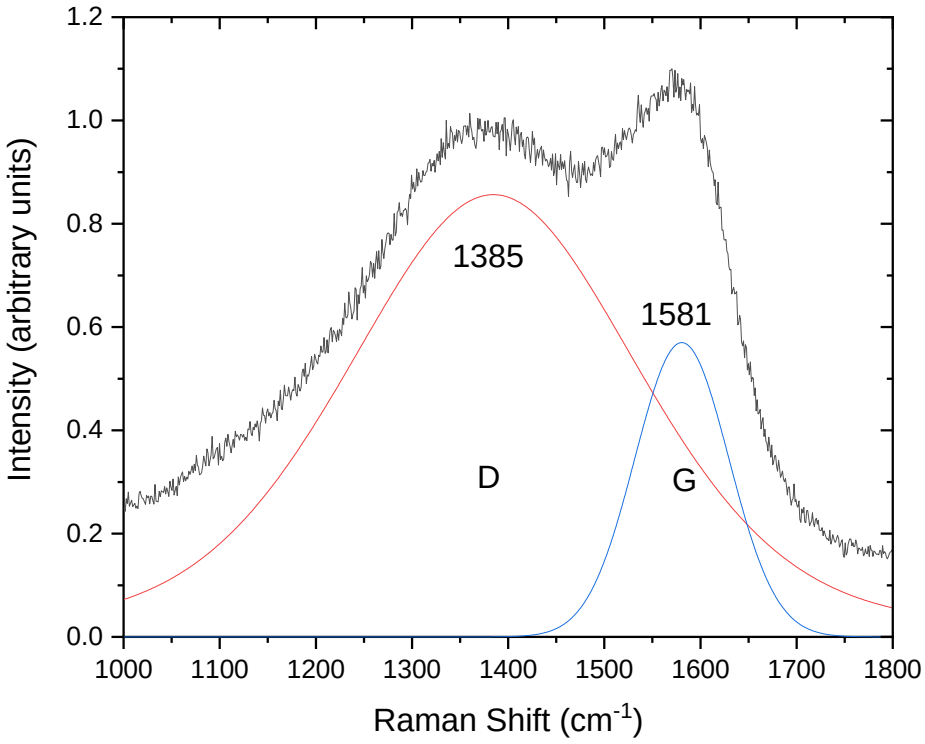

Figure 3.30 Deconvoluted Raman peaks for Coating Type B after the 7 day 240°C Parr bomb test.

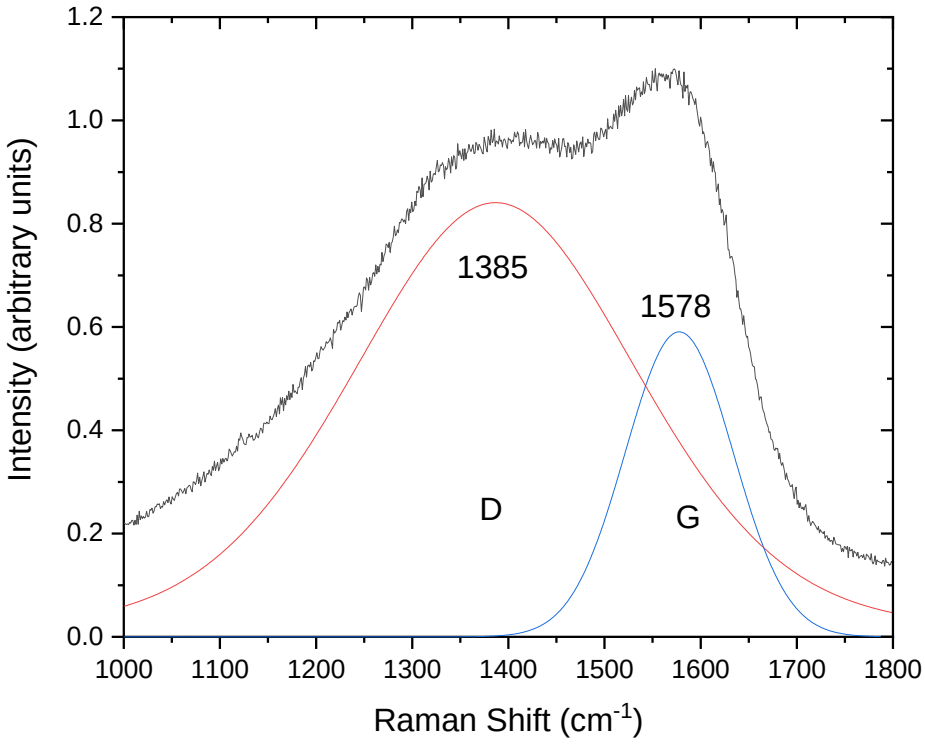

Figure 3.29 Deconvoluted Raman peaks for Coating Type B after the 7 day 280°C autoclave test.

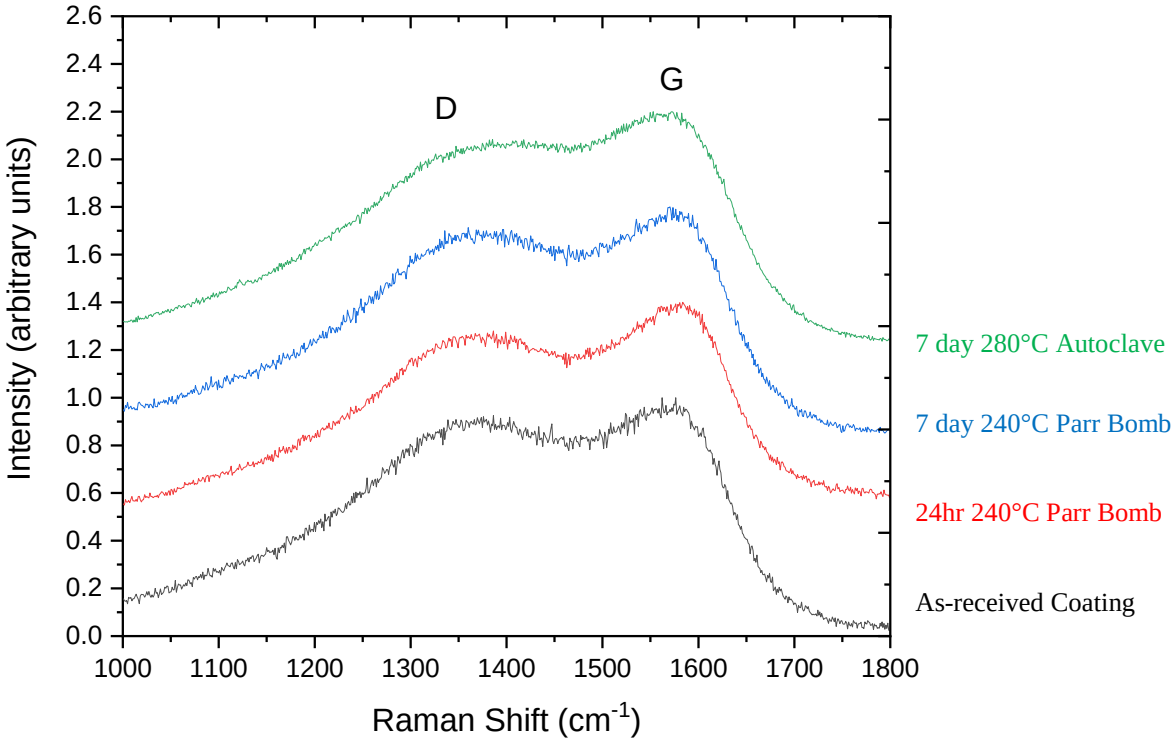

Figure 3.31 Evolution of Coating Type B Raman spectrum with increasing water temperatures and exposure lengths.

Table 6 Deconvoluted Raman peak data for Coating Type B.

Coating Exposure	D Peak Position (cm^{-1})	G Peak Position (cm^{-1})	I_D	I_G	I_D/I_G
As-received	1379	1578	0.86	0.56	1.54
Parr Bomb 24 Hours	1383	1582	0.84	0.56	1.50
Parr Bomb 7 Days	1385	1581	0.86	0.57	1.50
Autoclave 7 Days	1385	1578	0.84	0.59	1.42

Figure 3.32 shows the deconvoluted Raman peaks for the as-received chromium doped amorphous carbon Coating Type C. The G peak at 1565 is similar to that of Coating Type A but the I_D/I_G ratio is higher than Coating type B. The increased I_D/I_G ratio and G peak position can be attributed to the chromium doping causing increased clustering of sp^2 rings in the coating [115]. Table 7 and Figure 3.34 show the evolution of Coating Type C after 7 days in the autoclave at 280°C.

After exposure in the autoclave the G peak position increased significantly to $1580cm^{-1}$ but the I_D/I_G ratio dropped slightly to 1.71, as shown in Figure 3.33. The movement of the G peak to higher wavenumber would suggest graphitisation of the coating, however the chromium doping complicates the analysis of I_D/I_G ratio as the resultant clustering increases the ratio compared with an undoped amorphous carbon coating [116].

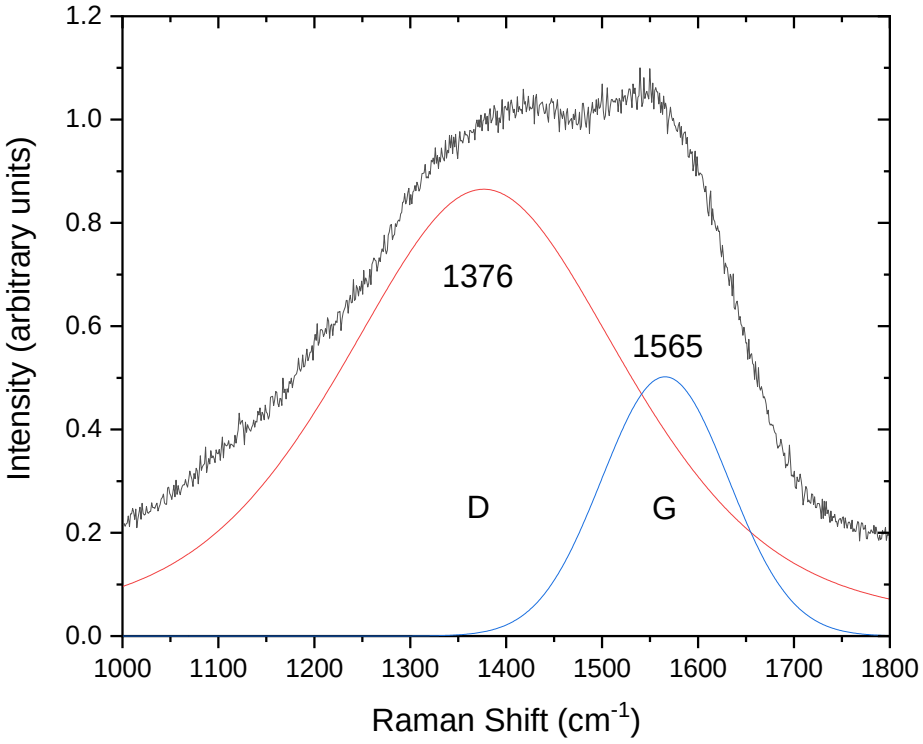

Figure 3.32 Deconvoluted Raman peaks for Coating Type C as-received.

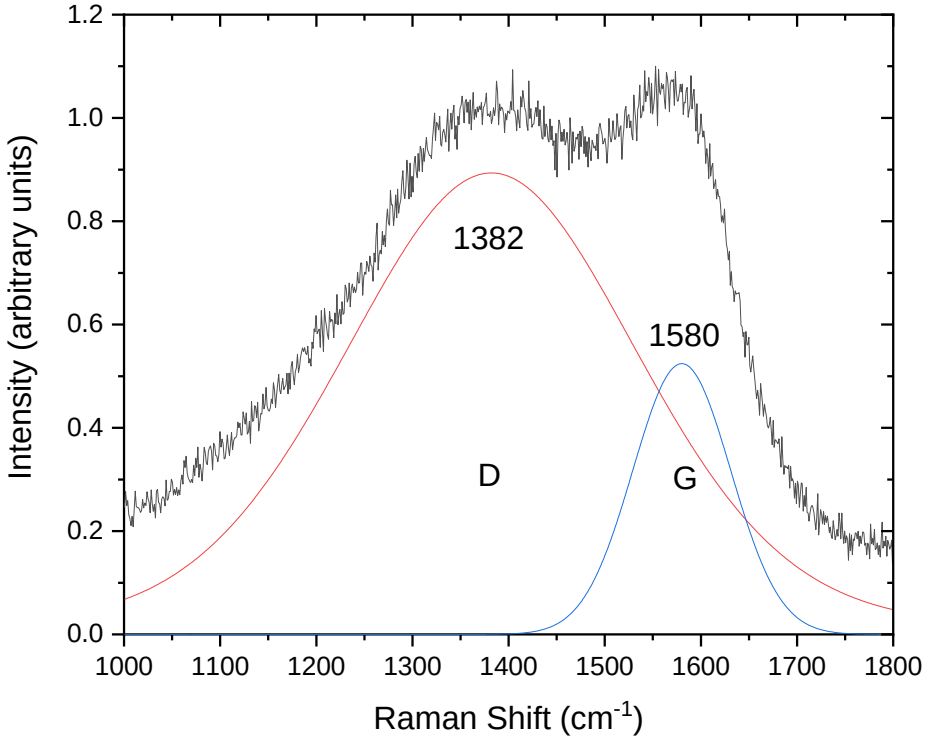

Figure 3.33 Deconvoluted Raman peaks for Coating Type C after the 7 day 280°C autoclave test.

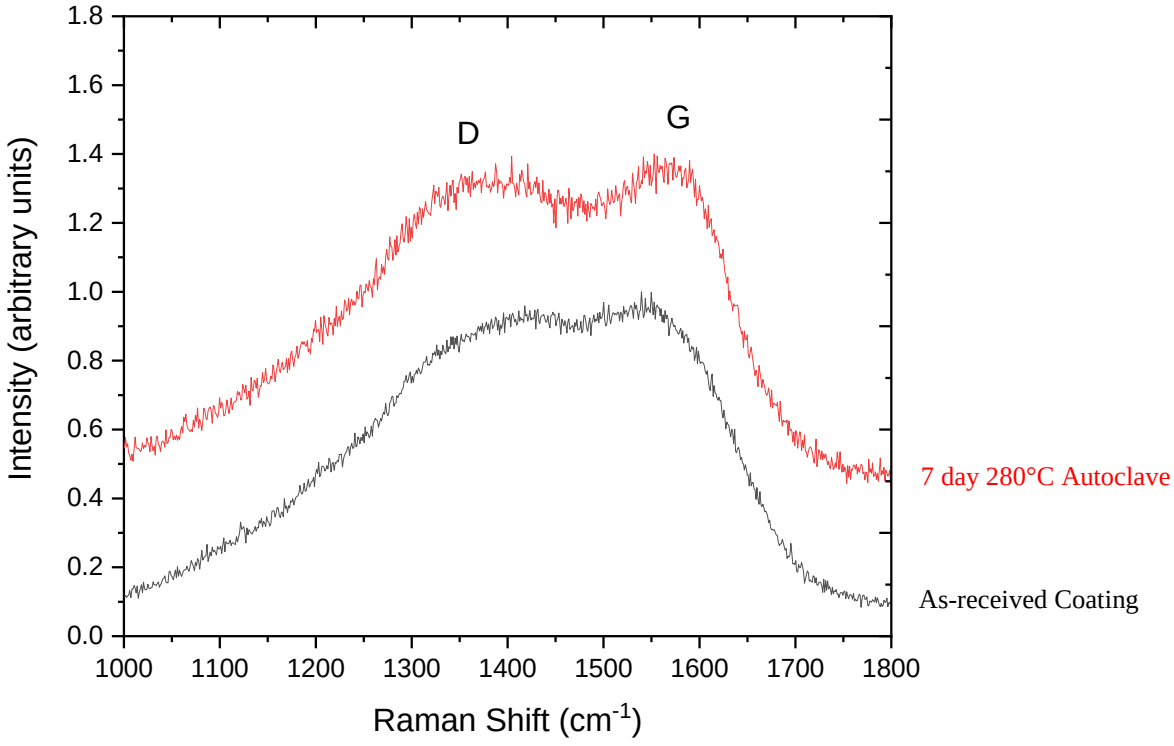

Figure 3.34 Evolution of the as-received Coating Type C Raman spectrum with autoclave exposure at 280°C.

Table 7 Deconvoluted Raman peak data for Coating Type C.

Coating Exposure	D Peak Position (cm^{-1})	G Peak Position (cm^{-1})	I_D	I_G	I_D/I_G
As-received	1376	1565	0.87	0.50	1.74
Autoclave 7 Days	1382	1580	0.89	0.52	1.71

The result of the Raman spectroscopy of the as-received Coating Type D is shown in Figure 3.35. The G peak for the a-C:Ti coating starts similar to Coating Type C at 1566cm^{-1} but the I_D/I_G ratio was the highest measured for any of the coatings at 1.91. As with the chromium doped coating this high I_D/I_G ratio could be due to the effect of metallic doping on the clustering of the carbon in the coating.

After autoclave exposure the wavenumber of the G peak increased from 1566cm^{-1} to 1580cm^{-1}, which was the same wavelength as Coating Type C reached, and the I_D/I_G ratio decreased to 1.77 which was also closer to the results of the autoclave exposure on the other lab-deposited film. Figure 3.37 and Table 8 show how the coating changed before and after the autoclave exposure. .

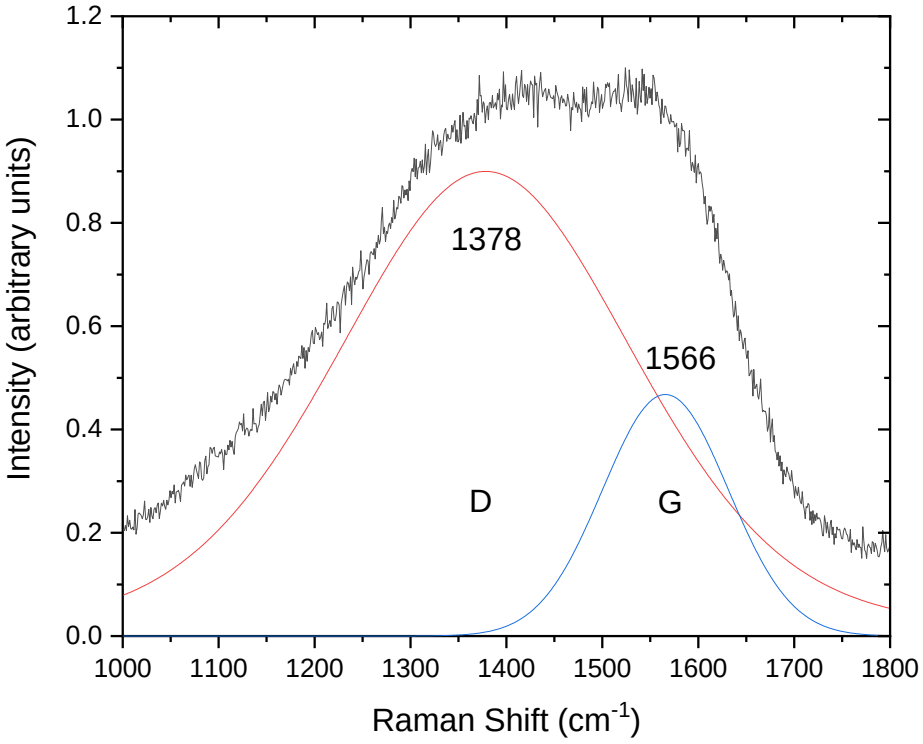

Figure 3.35 Deconvoluted Raman peaks for Coating Type D as-received.

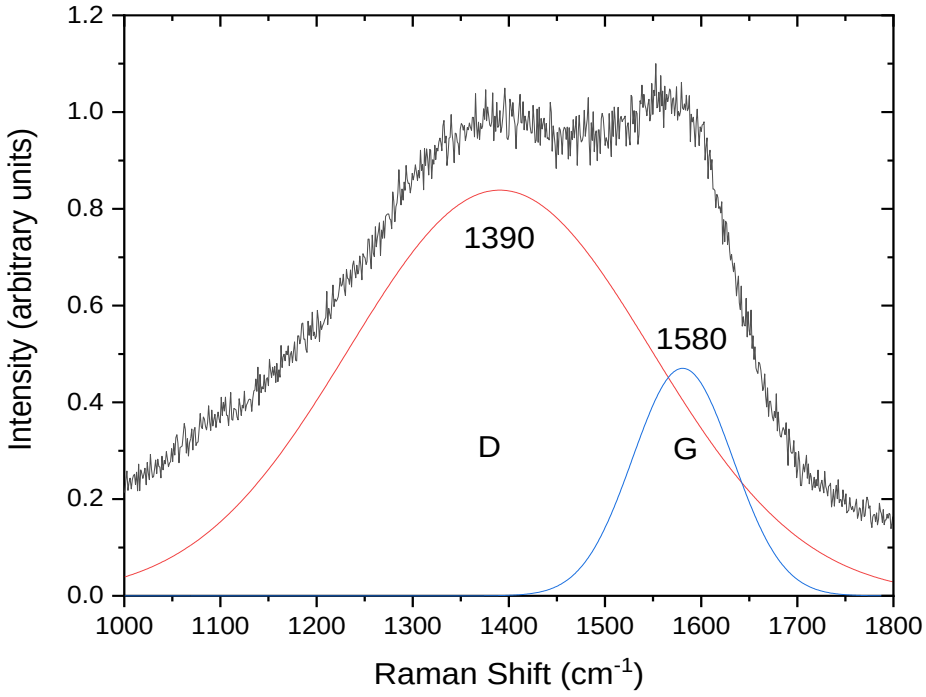

Figure 3.36 Deconvoluted Raman peaks for Coating Type D after the 7 day 280°C autoclave test.

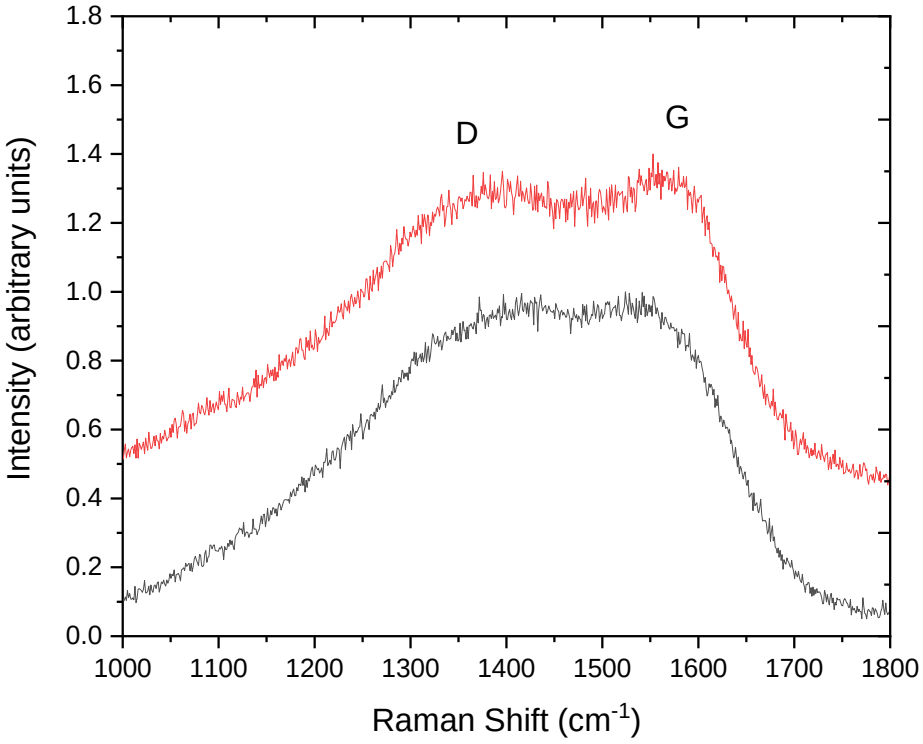

Figure 3.37 Evolution of the as-received Coating Type D Raman spectrum with autoclave exposure at 280°C.

Table 8 Deconvoluted Raman peak data for Coating Type D.

Coating Exposure	D Peak Position (cm^{-1})	G Peak Position (cm^{-1})	I_D	I_G	I_D/I_G
As-received	1378	1566	0.90	0.47	1.91
Autoclave 7 Days	1390	1580	0.83	0.47	1.77

3.7 Summary

The main results from the experimental investigations were that Coating Types A and C had poorer hydrothermal stability based on their changes in hardness and Raman data, with delamination of Coating A at high temperatures in the autoclave.

In comparison Coating Types B and D performed relatively well, maintaining their material properties closer to their as-received values when measured by nanoindentation and Raman spectroscopy after pressure vessel exposure. The influence of the Cr and Ti dopants appeared to give coatings improved thermal stability in the autoclave as the increased sp^2 clustering in the as-received coatings measured by Raman spectroscopy meant that the property changes due to graphitisation were reduced.

The next chapter will explore the second aim of the thesis, understanding the effect different amorphous carbon coating properties have on performance and failure in high-temperature high-pressure water.

Chapter 4: The effect of amorphous carbon coating compositions and structures on performance in high-temperature high-pressure water

4.1 Introduction

One of the aims of this project was to obtain a better understanding of the spallation mechanism exhibited by some of the commercial coatings during the initial autoclave tests.

Coating Type A will be the main focus of this study as Rolls-Royce were interested in attaining an improved understanding of the spallation mechanism encountered in their previous work. The coating could be made to fail consistently in the higher temperature autoclave testing but without total delamination of the film. This meant that it was possible to study the spallation mechanism before the coating was completely detached from the substrate.

4.2 Scanning electron microscopy results

Figure 4.1 shows a top-down view of Coating Type A after the 2 year CAPCIS tests. The dark area in the upper right side of the image was the remaining amorphous carbon film and the lighter area was where the a-C:H coating had spalled away. The edges of the coating spallation were quite sharp and well defined, suggesting the degradation had occurred at the same depth rather than failing in steps. In some areas the spalled edges of the coating had crevices beneath them suggesting they might be in the process of coming away, while other areas of the film maintained adherence up to the edge.

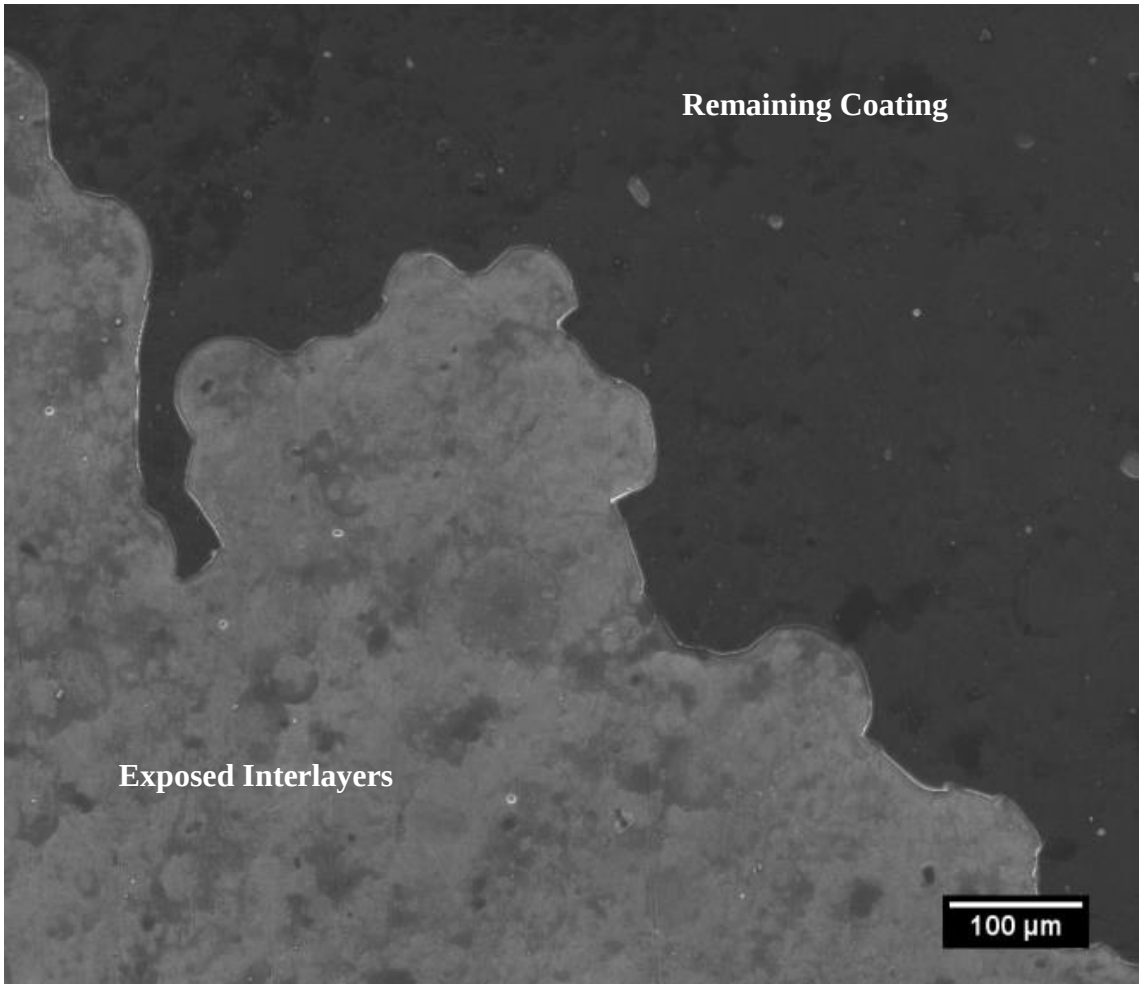

Figure 4.1 A SEM micrograph of the spalled surface of Coating Type A after the 2 year autoclave test.

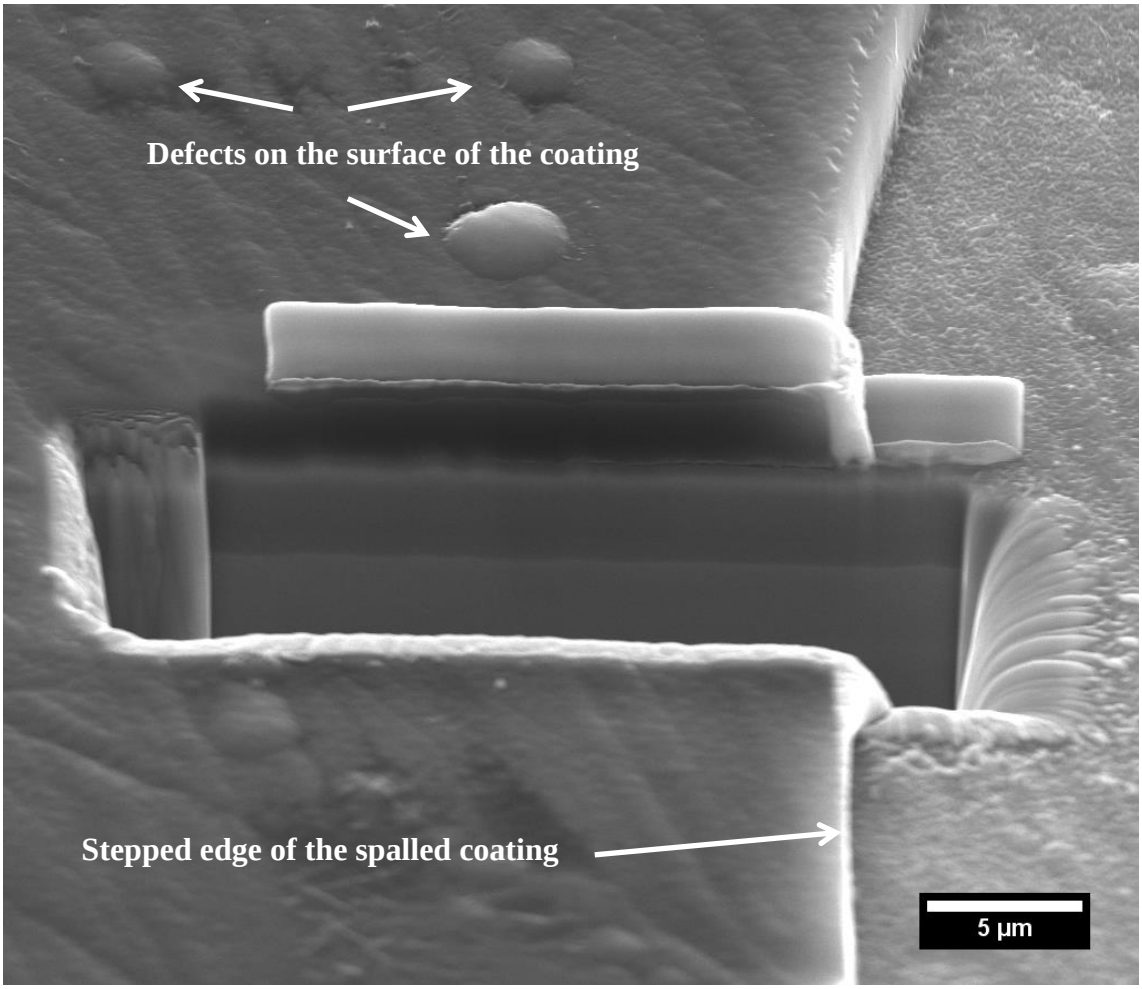

Figure 4.2 A SEM SE micrograph of the FIB cross-section of Coating Type A after the 2 year autoclave test.

Figure 4.2 shows the site of the focused ion beam cross-section at the edge of the spalled coating. There is a layer of protective carbon on top of the film to prevent damage during the milling process. There are also defects present on the surface of the coating as previously seen in the optical micrographs in Figure 2.2.

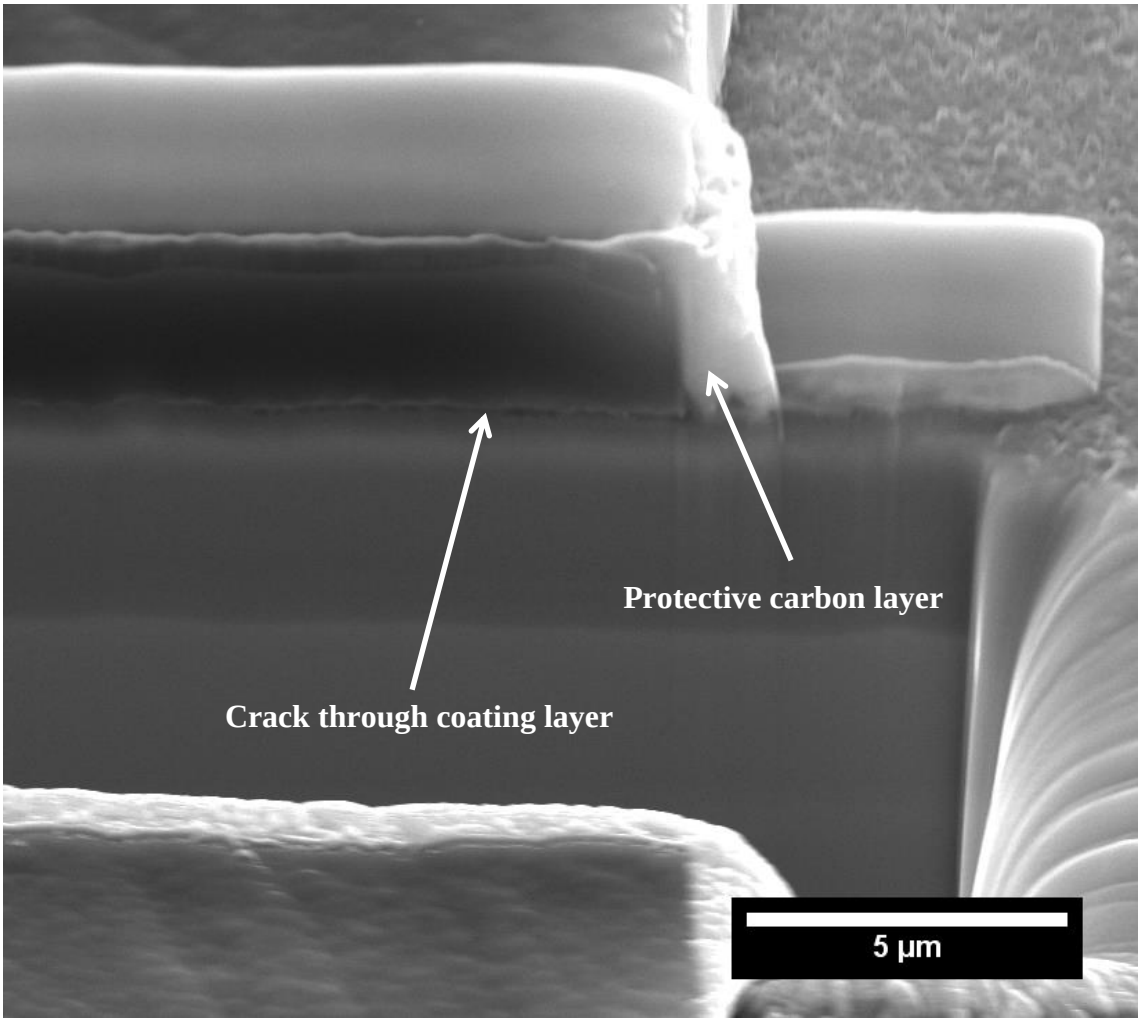

Figure 4.3 A SEM SE micrograph of the FIB cross-section at the edge of Coating Type A after the 2 year autoclave test.

Figure 4.3 is an enlarged micrograph of the focused ion beam cross-section concentrating on the edge of the spalled coating. The crack is visible just below the amorphous carbon film extending from the edge of the spalled step and penetrating to around 7µm in this section of the coating.

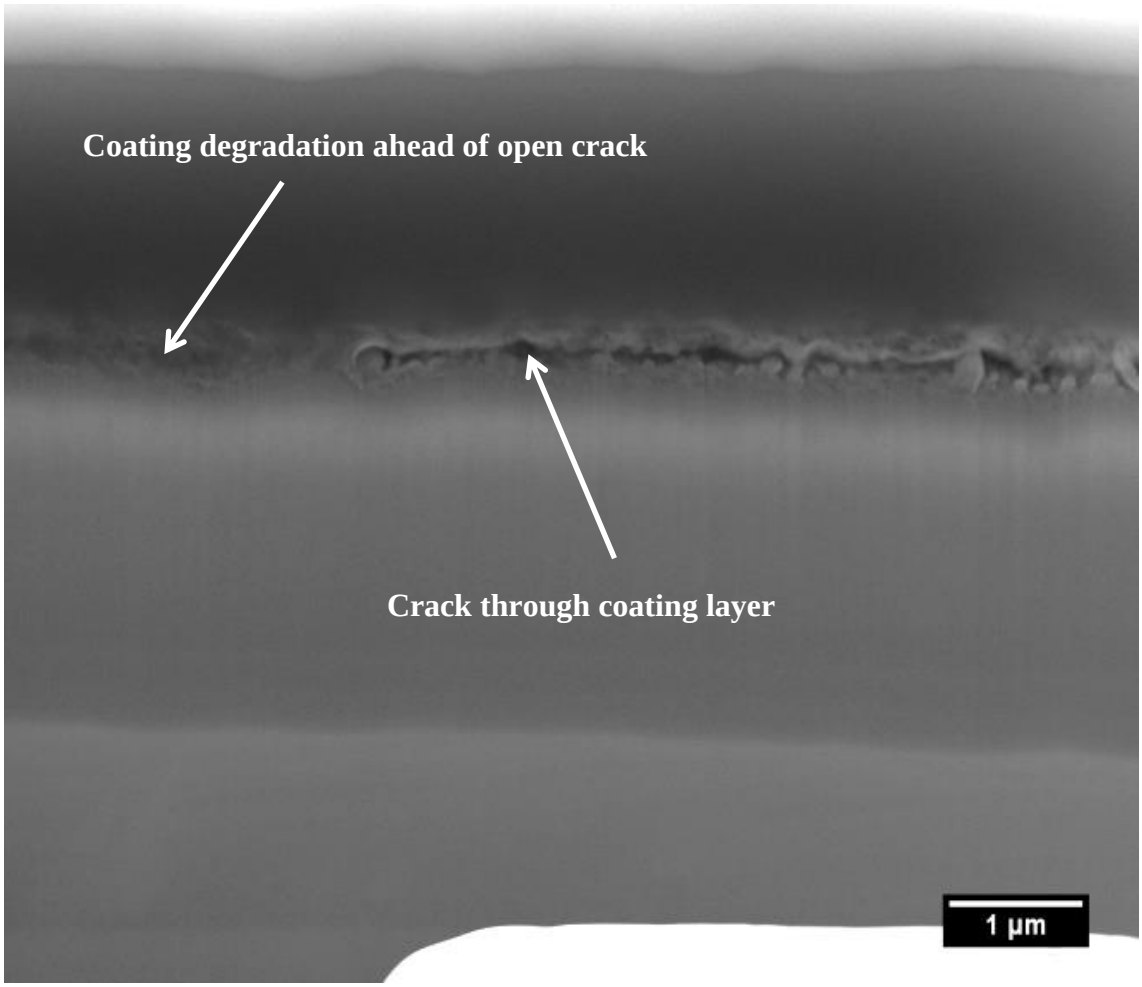

Figure 4.4 A SEM SE micrograph of crack in cross-section of Coating Type A after the 2 year autoclave test.

Figure 4.4 is a secondary electron SEM micrograph from the Inspect F of the coating FIB cross-section showing the cracking occurring in a layer below the dark amorphous carbon film. When compared to the structure of the as-received coating in the TEM sections in Figure 4.10 there also appeared to be some form of coating degradation ahead of the open cracked layer at the same depth.

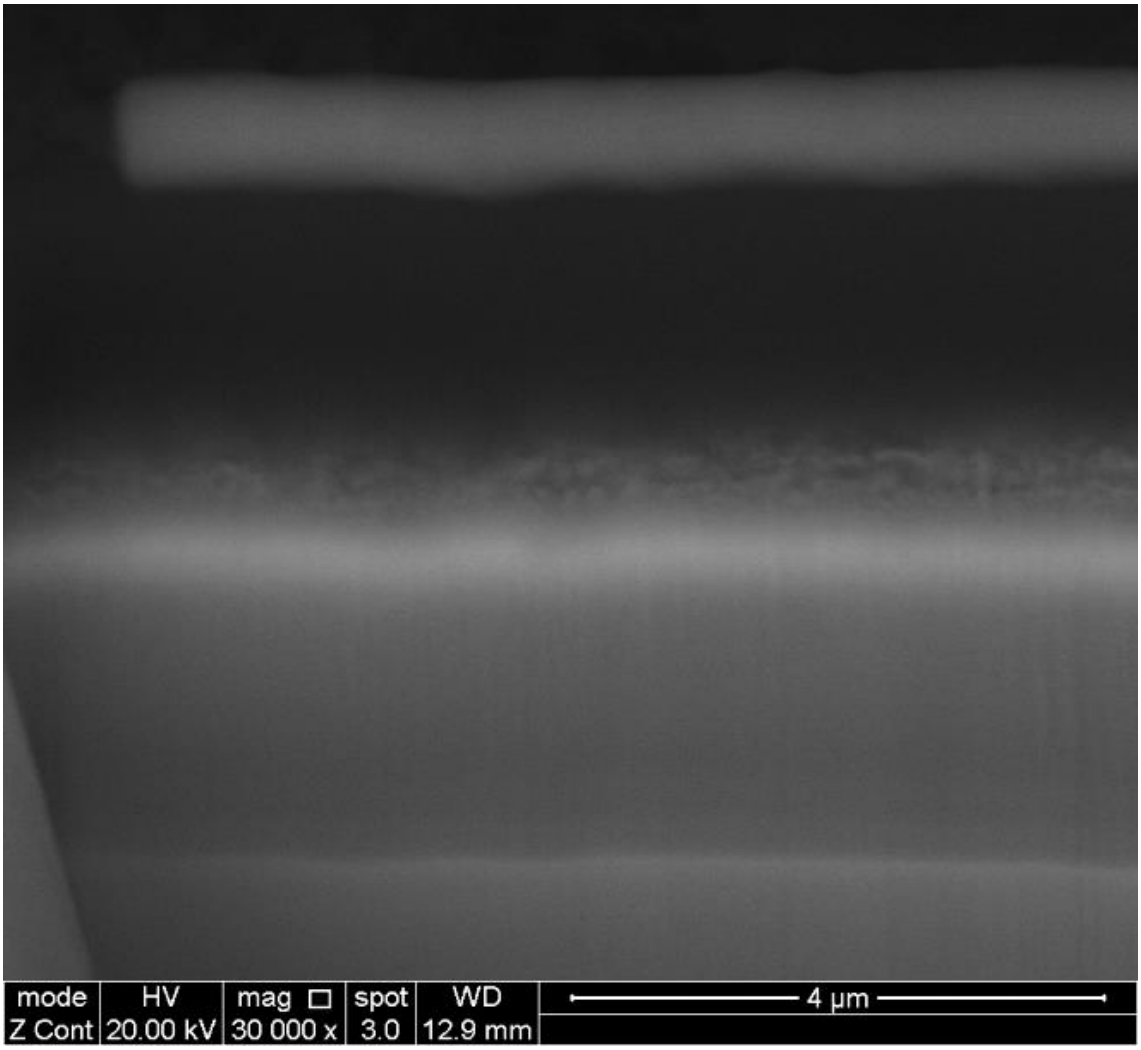

Figure 4.5 A SEM BS micrograph of crack in cross-section of Coating Type A after the 2 year autoclave test.

Figure 4.5 is a backscattered electron micrograph of the same area to show greater contrast between the elements in the different layers. The brighter band below the cracked area correlates with the heavier chromium rich interlayer in the coating.

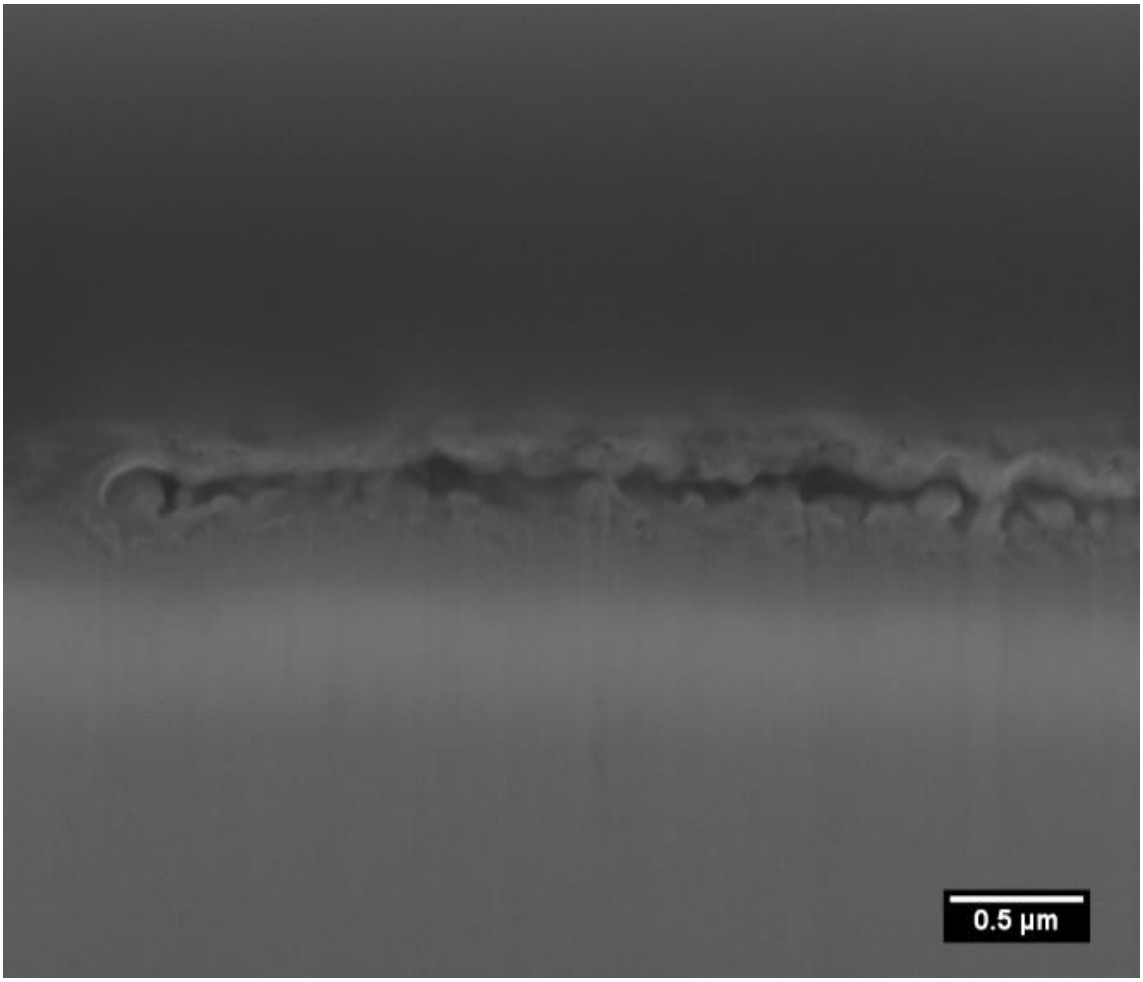

Figure 4.6 A SEM SE micrograph of the cracked area in cross-section of Coating Type A after the 2 year autoclave test.

Figure 4.6 shows a secondary electron micrograph of the area around the crack. The open area had a nodular texture suggesting a possible chemical degradation of the previously intact interlayer below the carbon film, however it was not yet clear whether this was chemical degradation (or another material degradation mechanism), without further investigation .

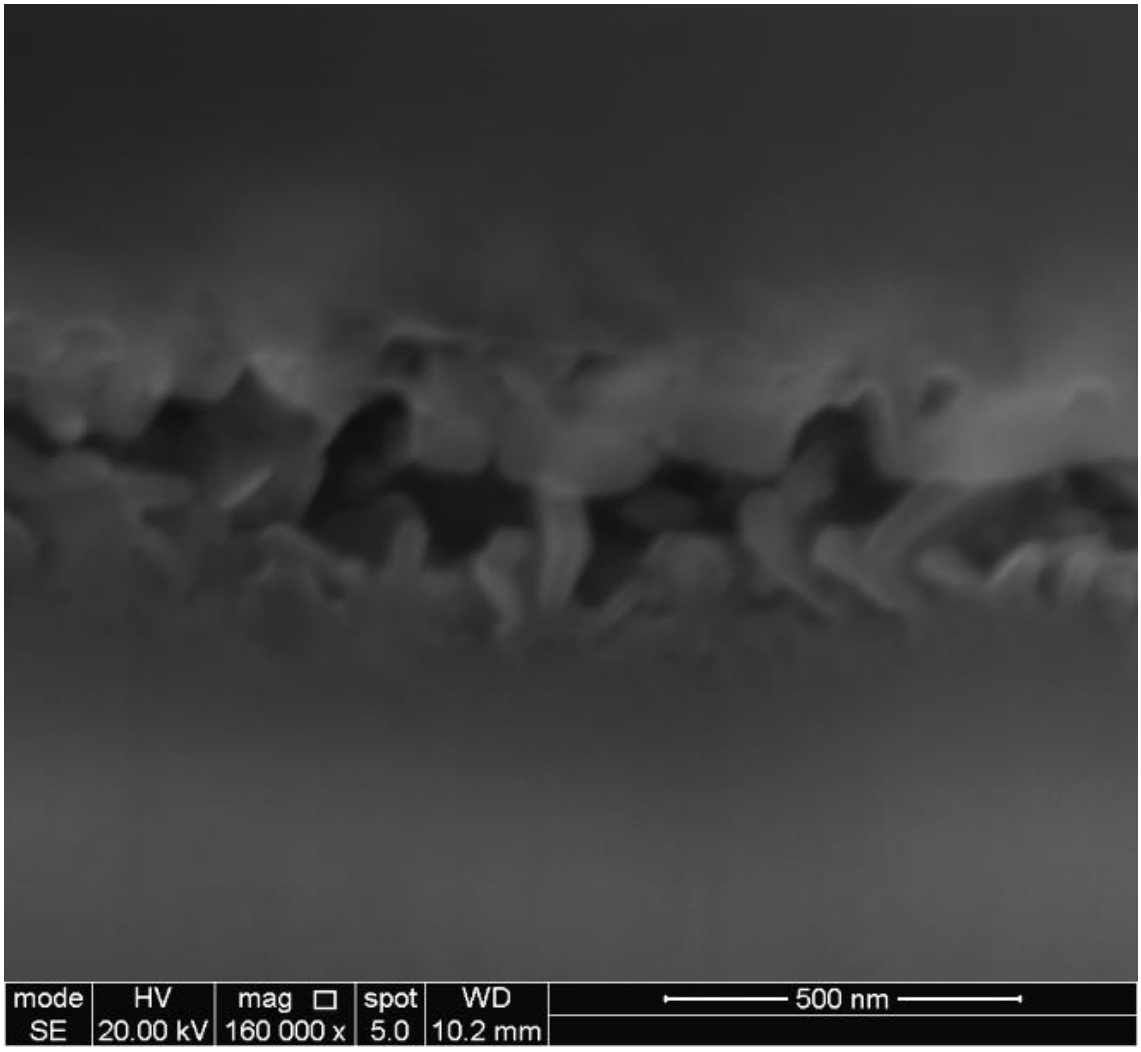

Figure 4.7 A SEM SE micrograph of the cracked area in cross-section of Coating Type A after the 2 year autoclave test.

Figure 4.7 shows the topography inside the crack of Coating Type A where the nodular surface of the cracked area is shown in greater detail. The appearance of this crack would suggest a corrosion mechanism has occurred in the layer at some point during the experimental procedures.

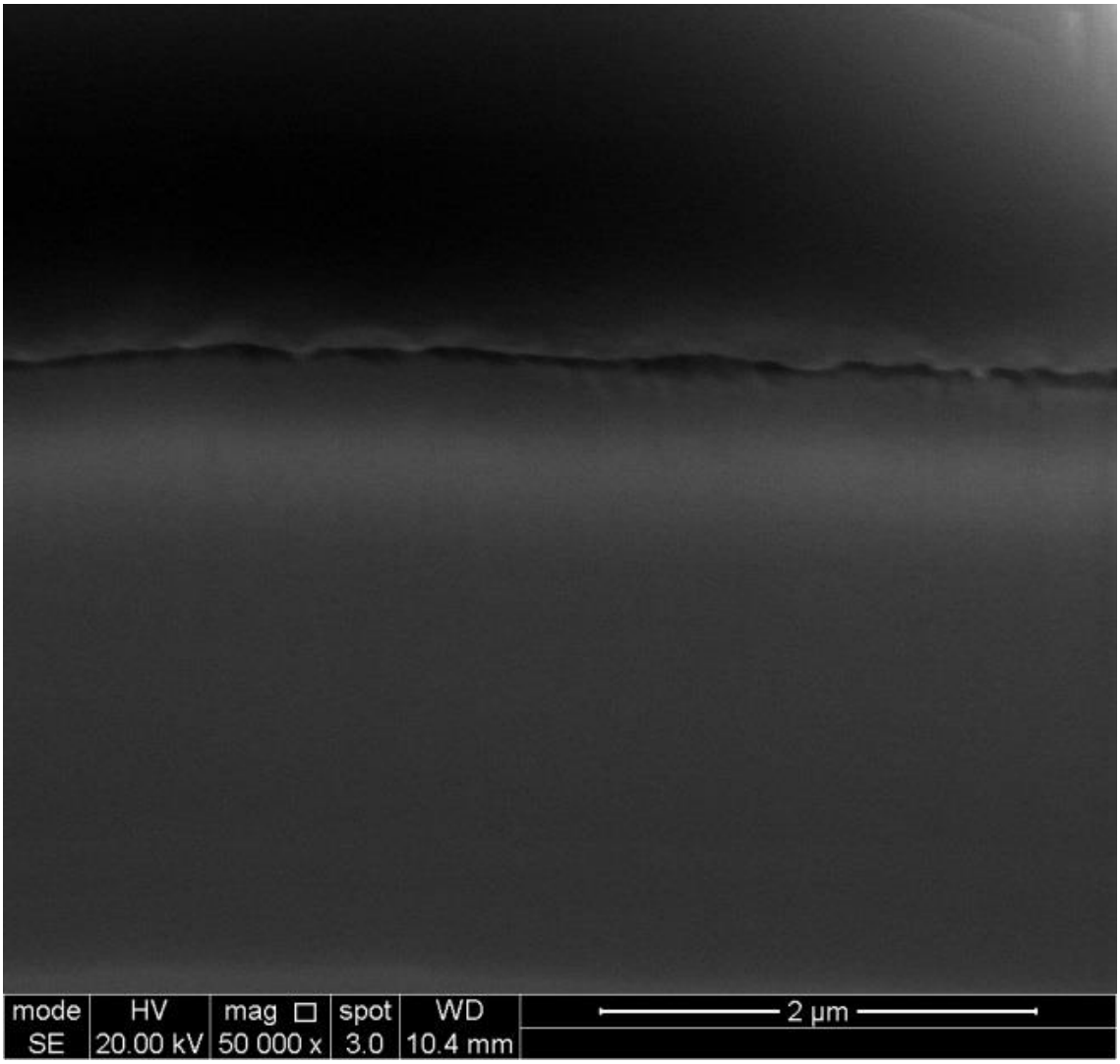

Figure 4.8 A SEM SE micrograph of crack in second cross-section of Coating Type A after the 2 year autoclave test.

Figure 4.8 shows a FIB cross-section of a crack in the coating layers at the edge of another spalled area of the coating. This crack did not display the rough features found in Figure 4.4 but instead had relatively clean pathway through the coating.

Figure 4.9 shows the corresponding backscattered electron image where the change in chemical composition of the cracked area from the surrounding material is shown by differences in image contrast.

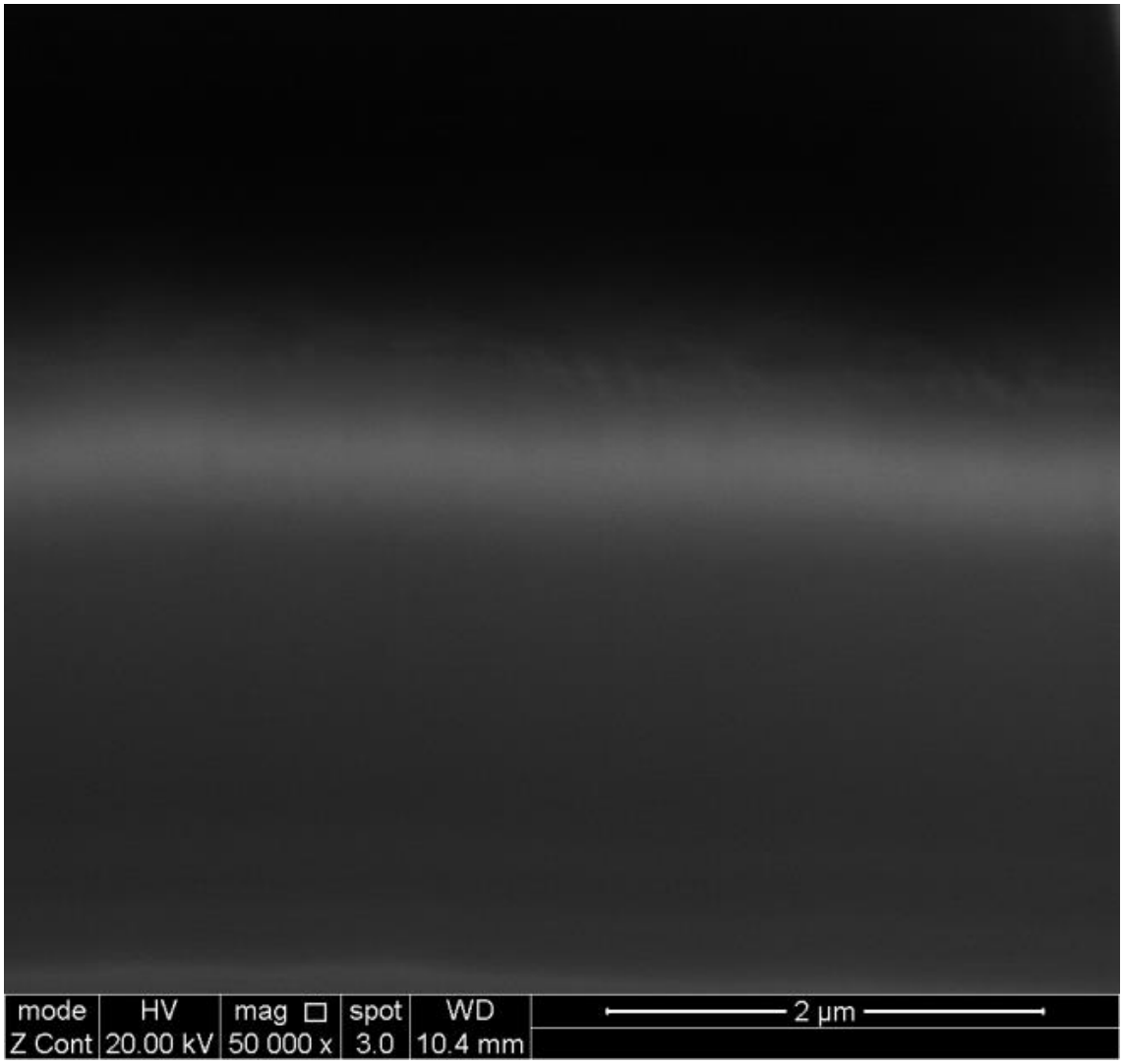

Figure 4.9 A SEM BS micrograph of crack in second cross-section of Coating Type A after the 2 year autoclave test.

The existence of cracked areas with both smooth and rough topologies would suggest that the clean crack occurs first, followed by further chemical degradation of the exposed interlayer materials.

EDX was conducted on the FIB cross-section of Coating Type A alongside the SEM investigation. The EDX elemental mapping was initially focused at the relatively smooth crack tip as shown in Figure 4.10. The presence of carbon, chromium, nitrogen and oxygen was mapped to compare with the secondary electron and backscattered

electron images but the results were unconvincing due to the relative sizes of the interaction volume and features of interest.

Figure 4.11 shows an EDX linescan of Coating Type A with the changes in carbon and chromium shown across a cross-section of the cracked coating.

When it was apparent that the spatial resolution of the EDX in the SEM would not be high enough to determine the exact composition of the thin layers seen in the backscattered electron image it was decided that they instead would be characterised by EDX and EELS in the TEM. The EDX from the TEM samples is recorded in the following section.

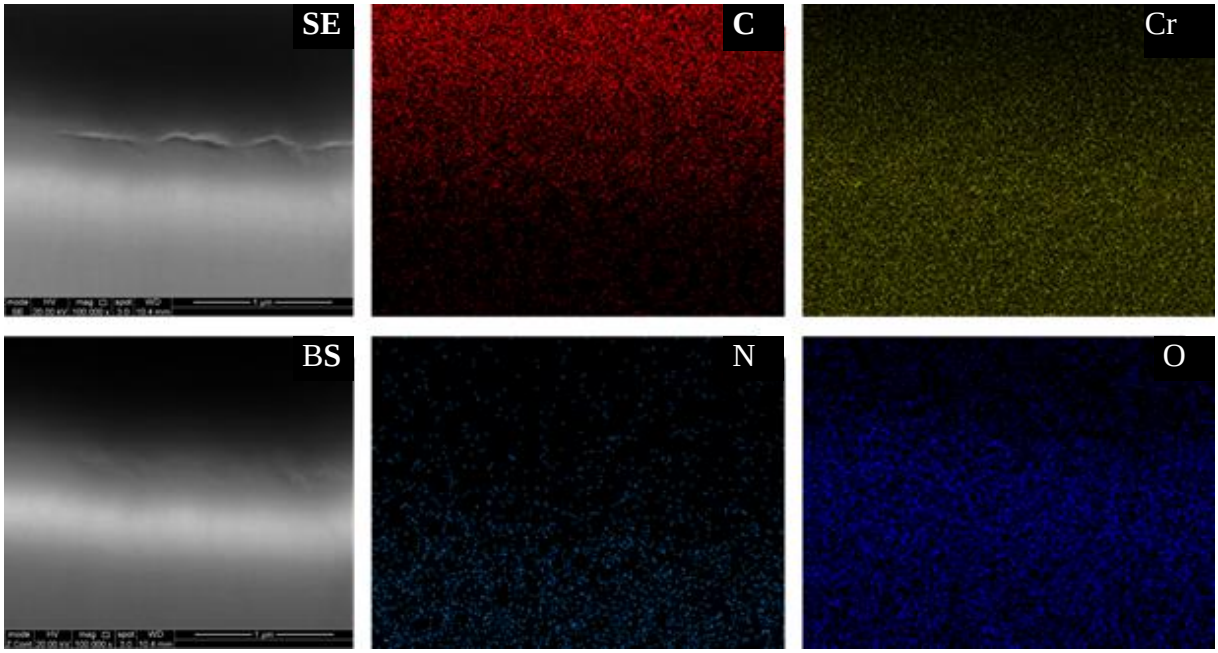

Figure 4.10 SE and BS SEM micrographs with corresponding carbon, chromium, nitrogen and oxygen EDX mapping.

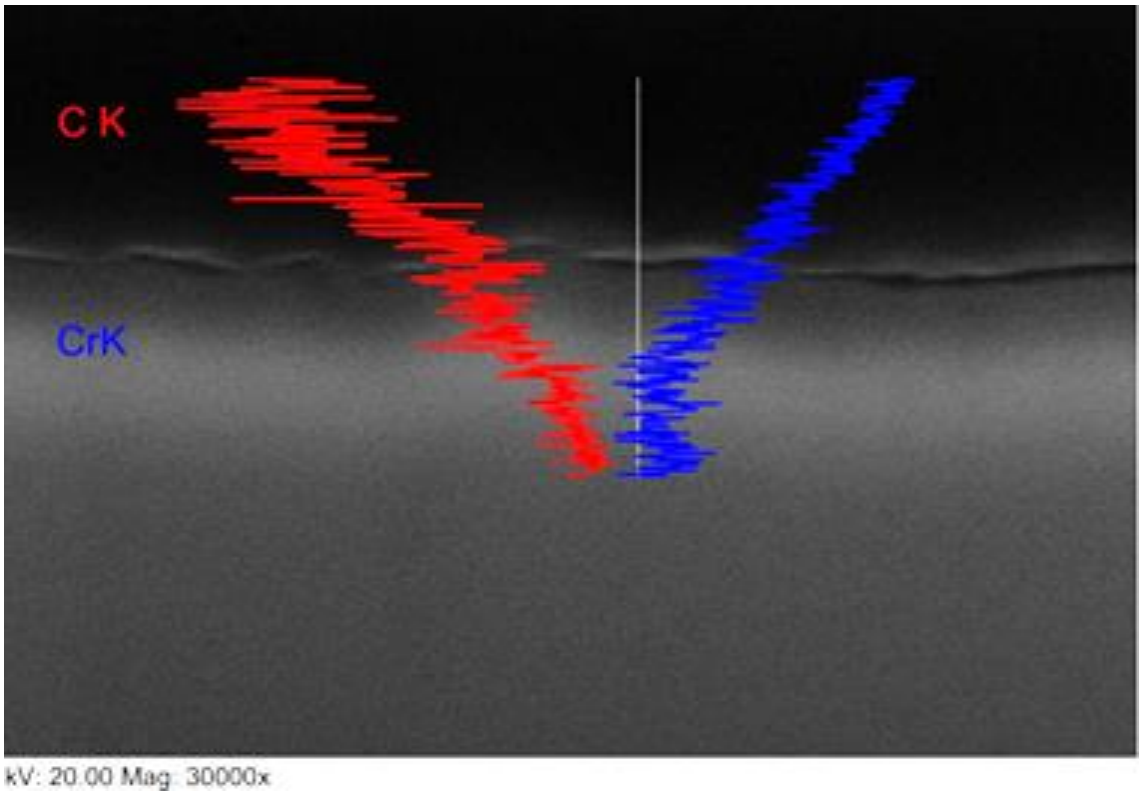

Figure 4.11 EDX linescan across cracked area of Coating Type A with a comparison of the carbon and chromium composition in the coating.

4.3 Transmission electron microscopy results

4.3.1 Coating Type A: As-received

STEM was used in conjunction with EELS and EDX to analyse the amorphous carbon coatings in their as-received state and after exposure to the autoclave testing.

Figure 4.12 and Figure 4.13 show STEM bright field cross-sections of Coating Type A in the as-received condition.

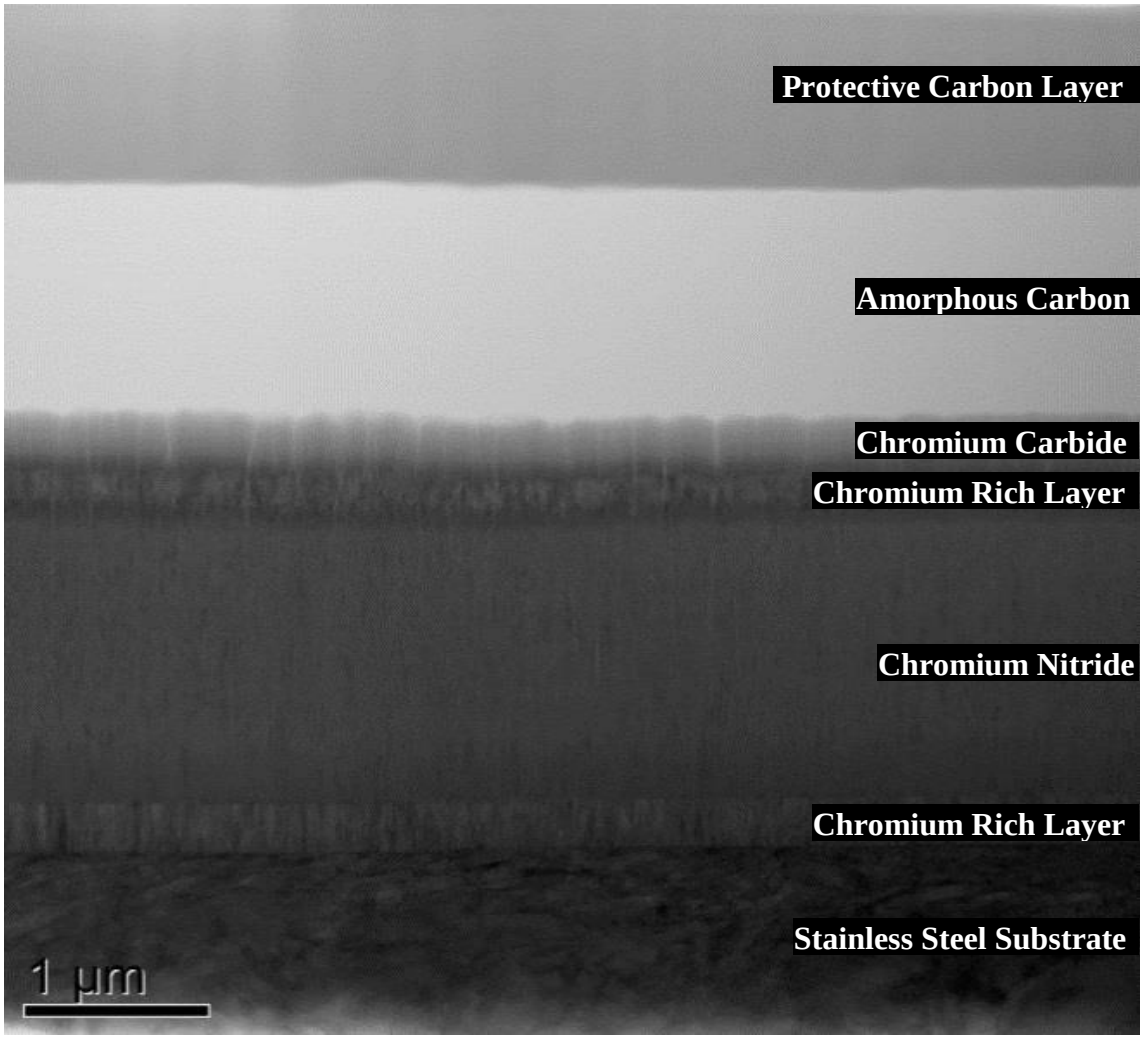

Figure 4.12 STEM BF micrograph of as-received Coating Type A interfacial region.

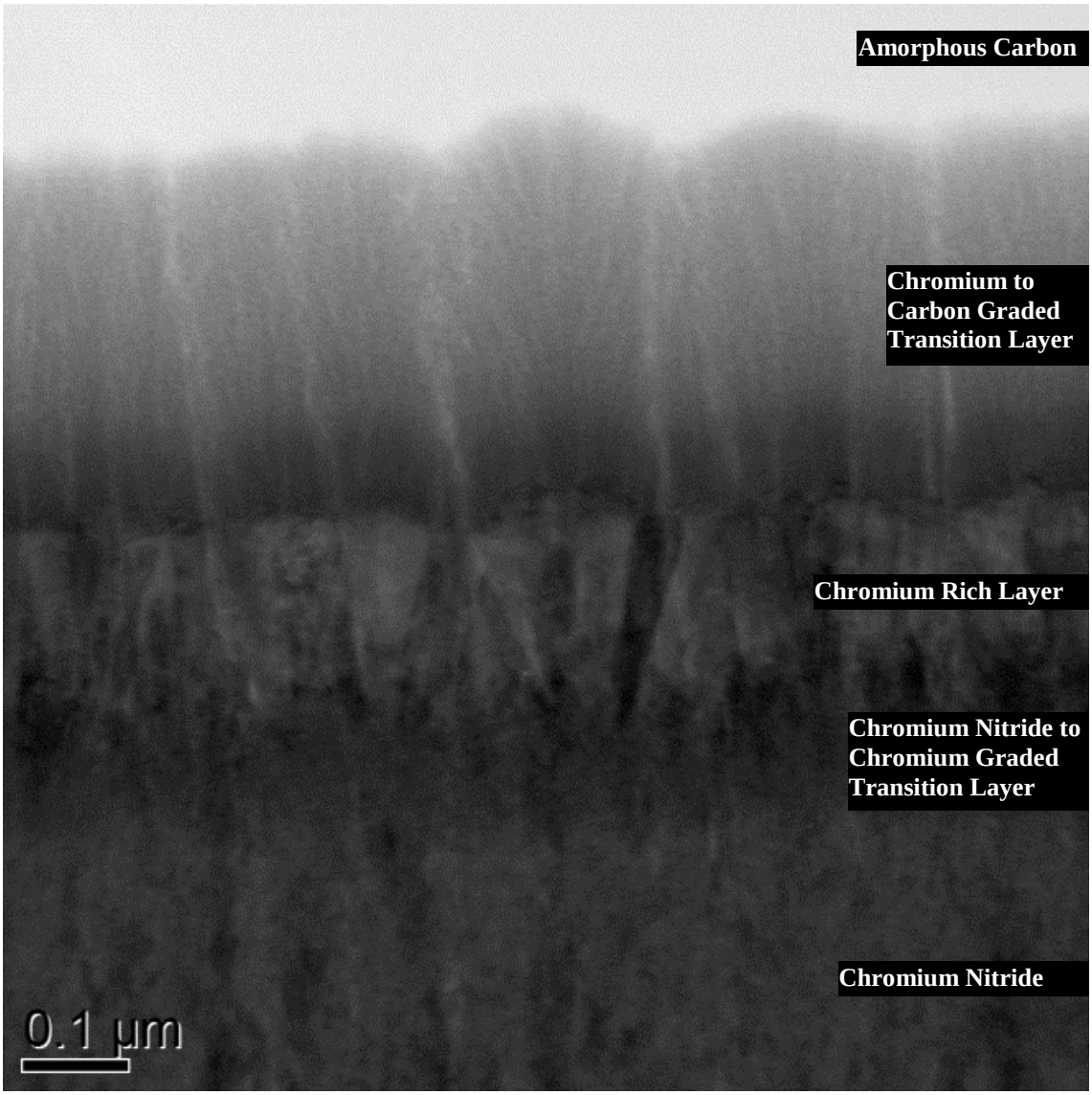

Figure 4.13 STEM BF micrograph of as-received Coating Type A interfacial region.

Figure 4.12 shows the entire coating from the bright amorphous carbon layer, through the interlayer materials, down to the substrate. The darker grey layer at the top of the image is the protective carbon deposited before the focused ion beam milling to protect the coating.

In Figure 4.13 the region just below the amorphous carbon is magnified to reveal several distinct layers as the structure and composition of the coating interlayer

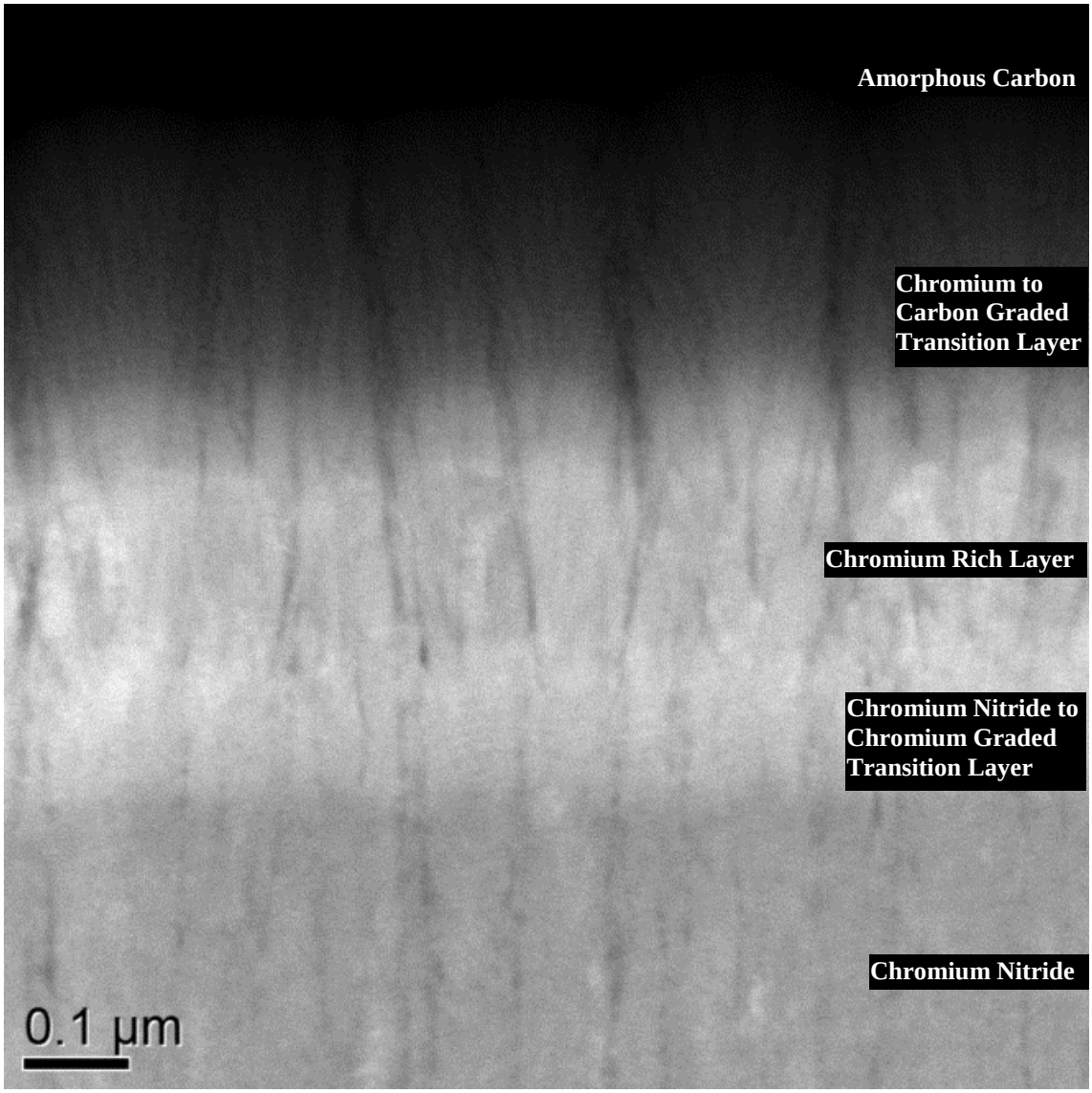

Figure 4.14 STEM ADF micrograph of as-received Coating Type A interfacial region.

materials change. The interlayers of the coating were graded from chromium nitride into a chromium rich layer, then from this chromium rich layer the carbon was gradually increased before deposition of the functional amorphous carbon layer at the surface.

The corresponding annular dark field image is shown in Figure 4.14. The contrast of the image is related to the Z number contrast of the elements present, with heavier elements

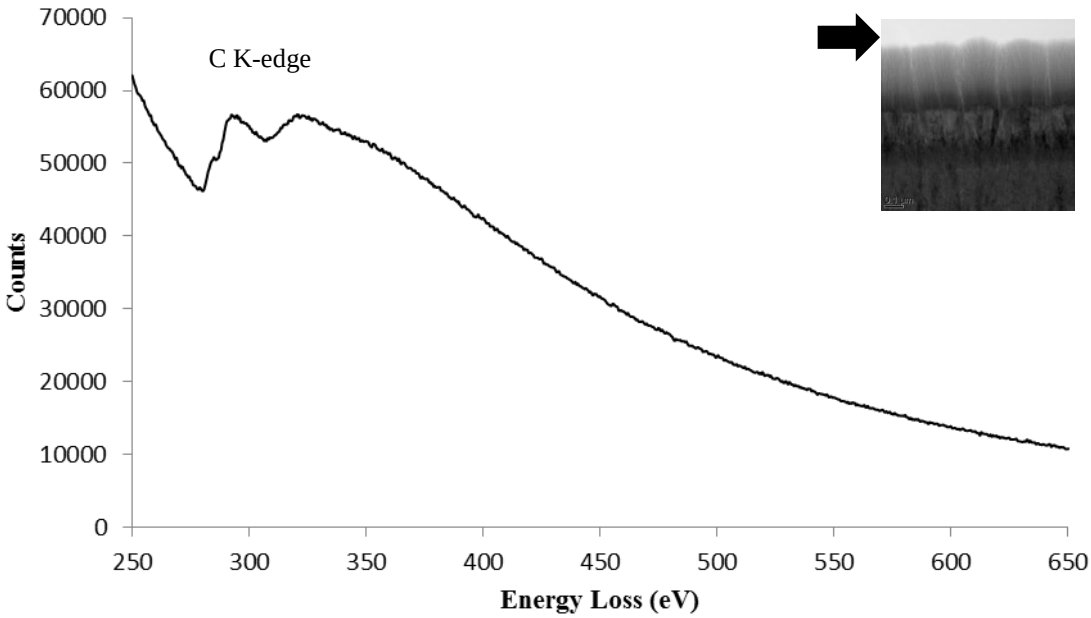

Figure 4.15 An EELS spectrum from the amorphous carbon layer of Coating Type A.

appearing brighter. There are several distinct interlayers in the coating with different compositions, the dark layer on the top of Figure 4.14 is the amorphous carbon and is then followed by a series of brighter strata containing the heavier element chromium. In the as-received sample these different interlayers were studied by EELS and EDX.

Figure 4.15 shows the EELS spectra for the amorphous carbon film in the as-received Coating Type A. The arrows next to the inlaid micrographs indicate the layer in which the spectrum was taken from.

The a-C:H coating contains a strong carbon K-edge peak and no other energy loss peaks, with the peak shape indicating a typical undoped amorphous carbon coating [117].

Figure 4.16 has both chromium L_2 and L_3 energy loss edges in addition to the now weakened carbon K edge indicating a transition from the amorphous carbon into a Cr/C interlayer.

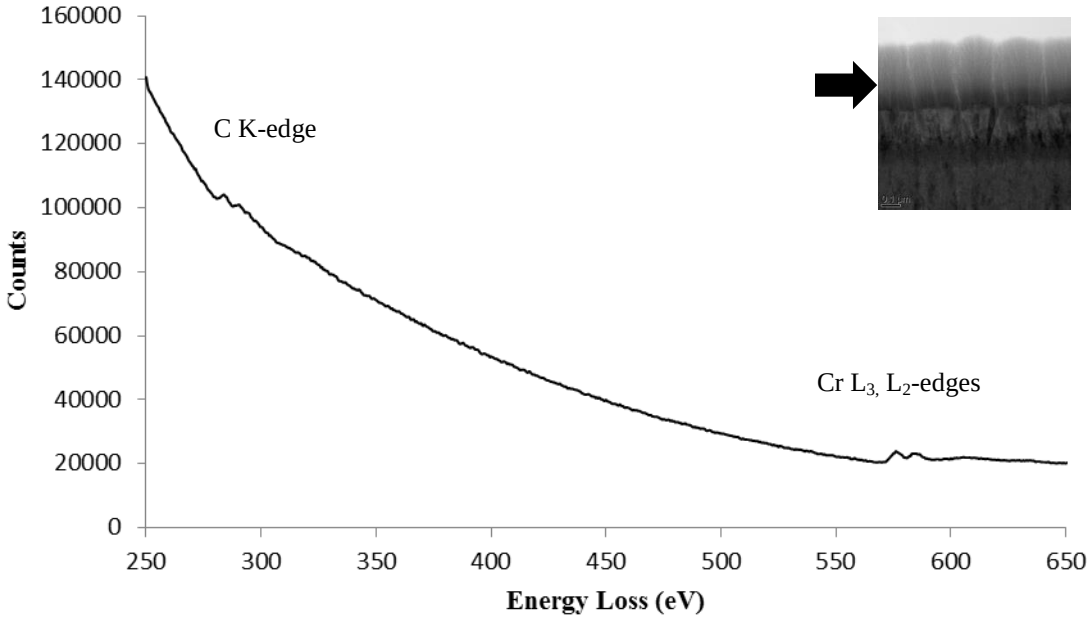

Figure 4.17 An EELS spectrum from the Cr/C transition layer of Coating Type A.

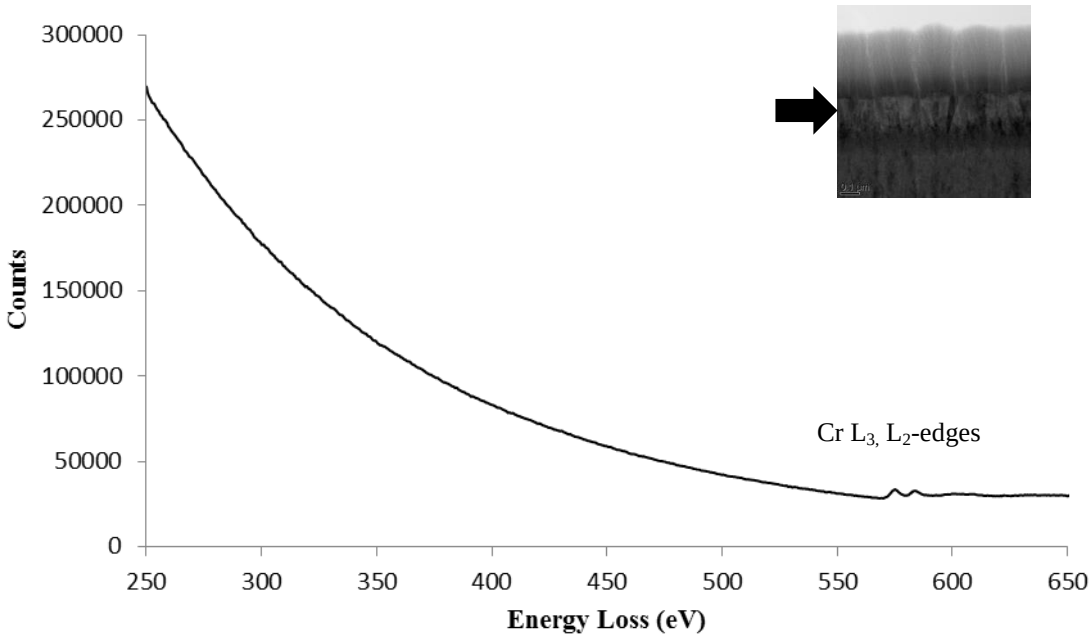

Figure 4.16 An EELS spectrum from the Cr rich layer of Coating Type A.

Figure 4.17 is the EELS spectrum from the brightest layer in the annular dark field micrograph in Figure 4.12. The spectrum from the layer contains just Cr which supports the Z contrast found in the ADF image.

The coating interlayers then transition out of this Cr rich layer as shown in Figure 4.18 with the introduction of the weak nitrogen edge as the coating enters the chromium nitride base layer in Figure 4.19.

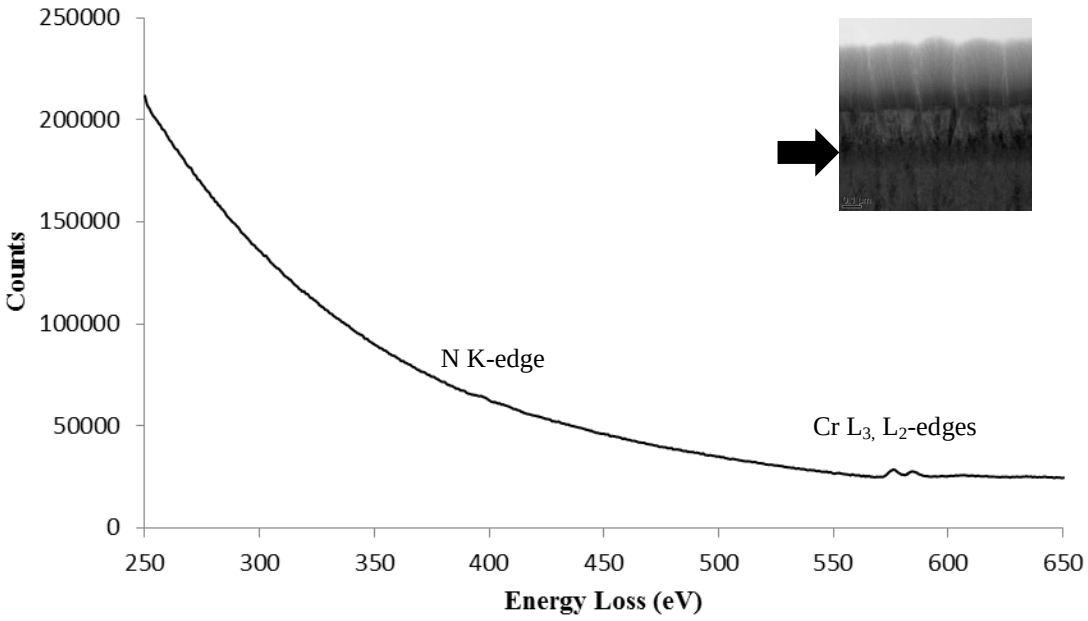

Figure 4.18 An EELS spectrum from the Cr/N transition layer of Coating Type A.

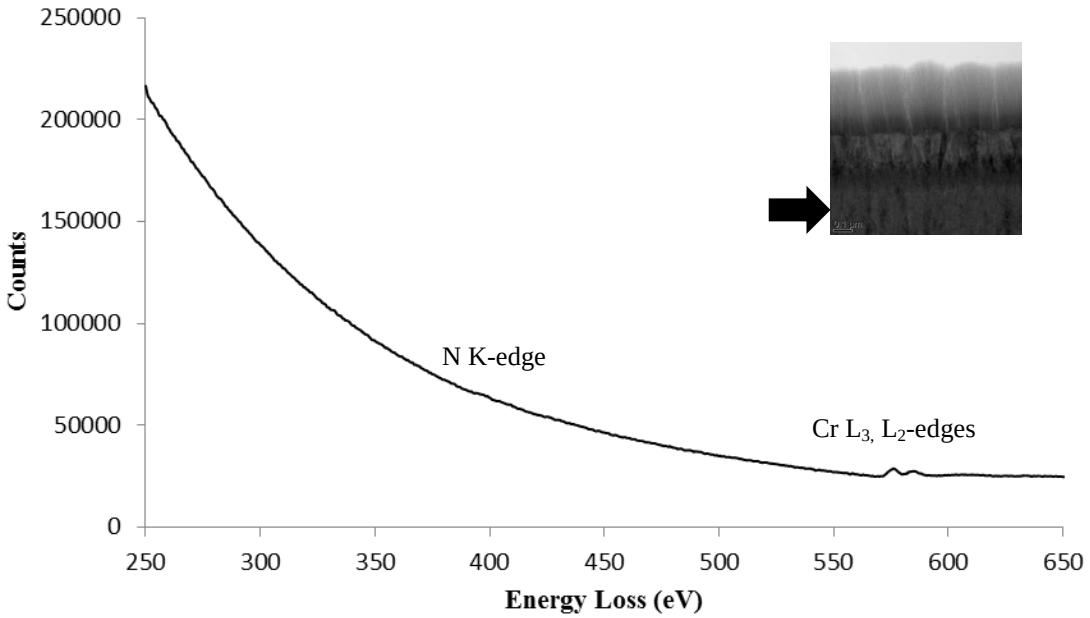

Figure 4.19 An EELS spectrum from the CrN layer of Coating Type A.

From the EELS characterisation of the as-received Coating Type A it was found that the TEM foil prepared by FIB was slightly too thick to give clear energy loss peaks relative to the background signal. It was decided to also conduct some EDX of the sample as the technique gives clearer elemental peaks with the greater interaction volume available.

Figure 4.20 is an EDX spectrum from the amorphous carbon layer. As in Figure 4.15 there was a strong carbon Kα peak from the undoped amorphous carbon film. There were also small traces of copper from the TEM grid, implanted gallium from the focused ion beam, and argon from the plasma deposition process. As EDX is better at detecting elements with higher atomic numbers these trace element peaks were stronger than in the EELS characterisation.

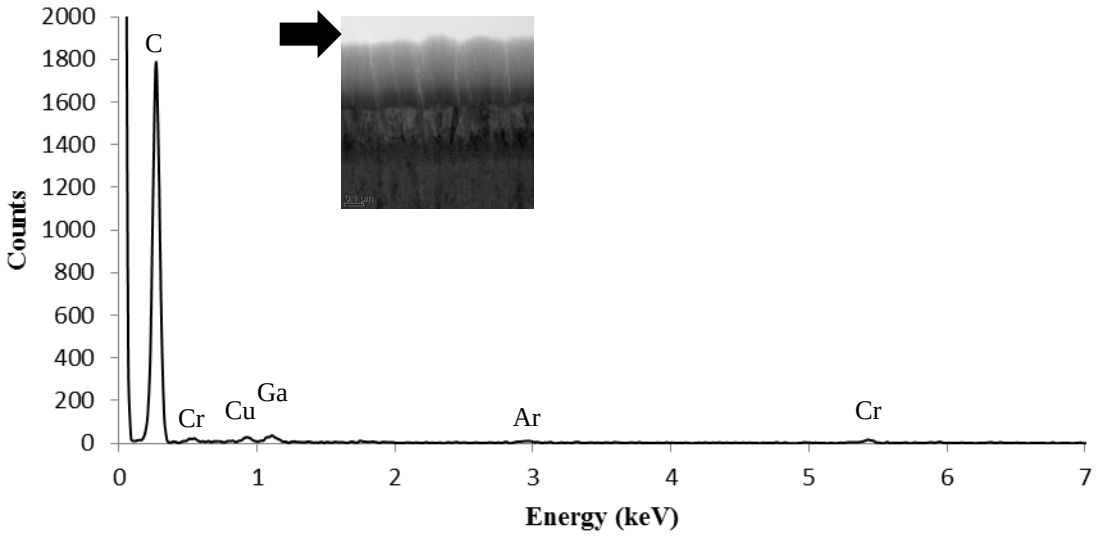

Figure 4.20 An EDX spectrum from the amorphous carbon layer of Coating Type A.

EDX was then used on the Cr/C layer as shown in Figure 4.21. There were strong chromium peaks in addition to the now relatively weaker carbon peak.

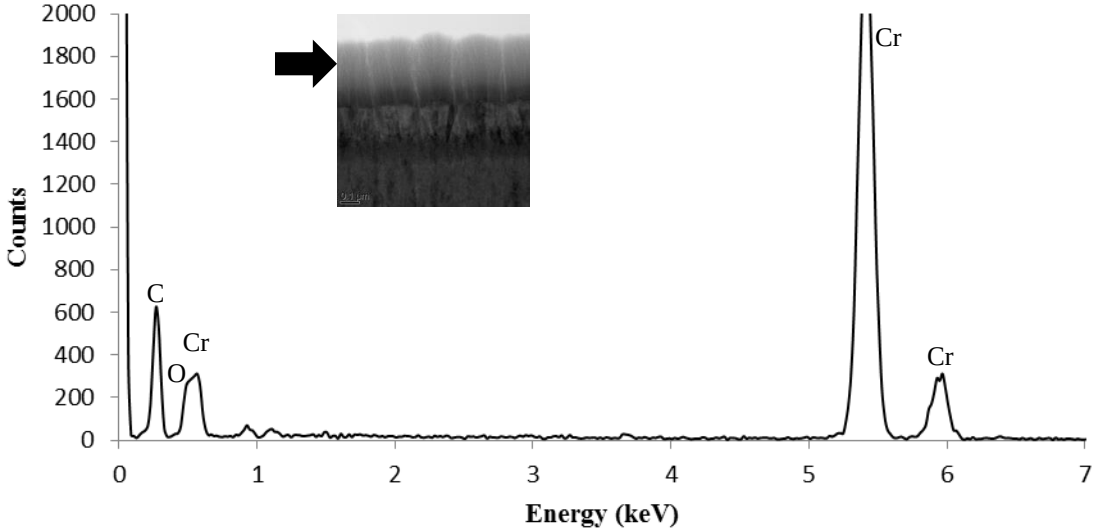

Figure 4.21 An EDX spectrum from the Cr/C layer of Coating Type A.

The shape of the chromium Lα peak at 0.573 indicated the possible presence of an oxygen Kα peak at 0.525 but the overlap created difficulty in separating them. The oxygen signal could have arisen from the oxidation of the chromium exposed by the focused ion beam milling rather than existing in the as-received coating, since pure chromium oxidises very readily when exposed to air. To clarify this it would be necessary to expose the cross-section of the coating and perform spectroscopy while maintaining vacuum to avoid oxidation.

Figure 4.22 is an EDX spectrum from the Cr/C transition layer just above the Cr rich layer from the EELS spectrum in Figure 4.17. There is now a stronger indication of an oxygen Kα peak around 0.525 and the carbon peak has reduced relative to the chromium peaks.

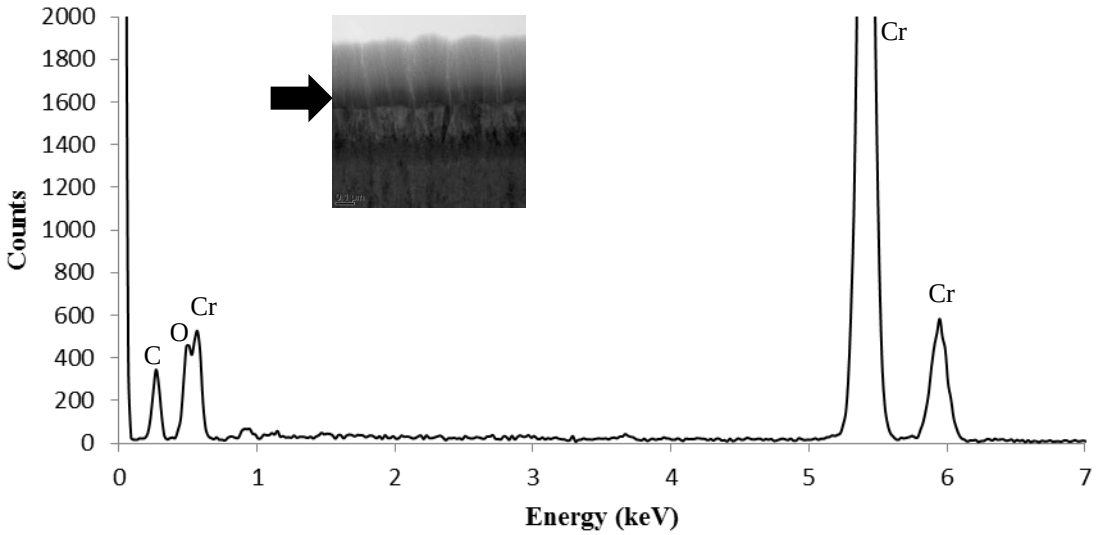

Figure 4.22 An EDX spectrum from the Cr/C transition layer of Coating Type A.

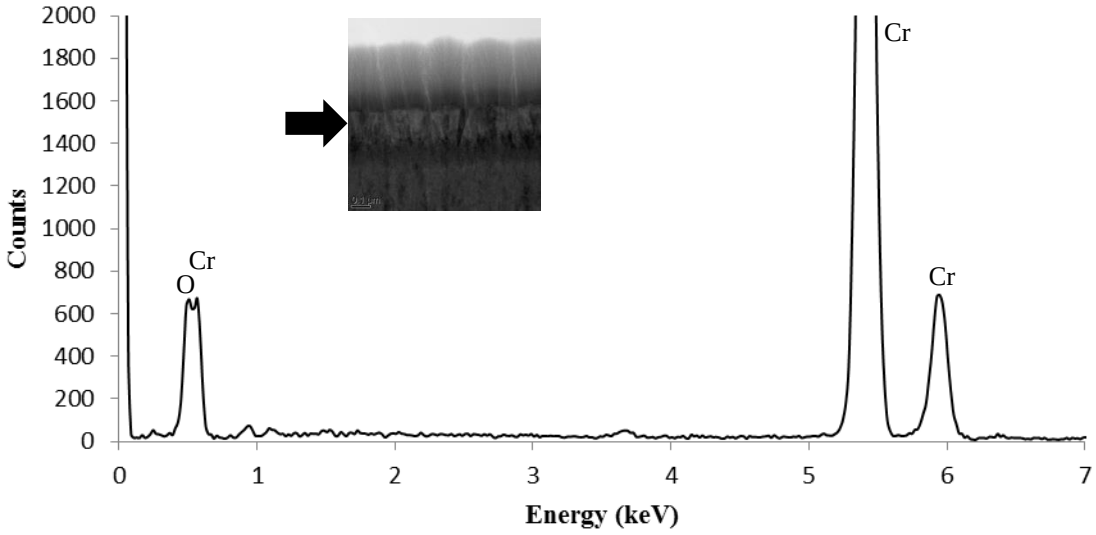

Figure 4.23 An EDX spectrum from the Cr rich layer of Coating Type A.

Figure 4.23 is an EDX spectrum of the Cr rich layer in Coating Type A. The chromium peaks are much higher relative to the other elemental peaks in the upper carbon containing layers.

The EDX spectrum in Figure 4.24 shows the introduction of the nitrogen peak at 0.392 as the coating transitions into the CrN baselayer. This nitrogen EDX peak was slightly unexpected as the EELS characterisation had a very weak N peak compared to the background signal.

EELS should have been better at picking up the lighter elements relative to EDX but the thickness of the sample meant the nitrogen peak was actually clearer with this sample thickness.

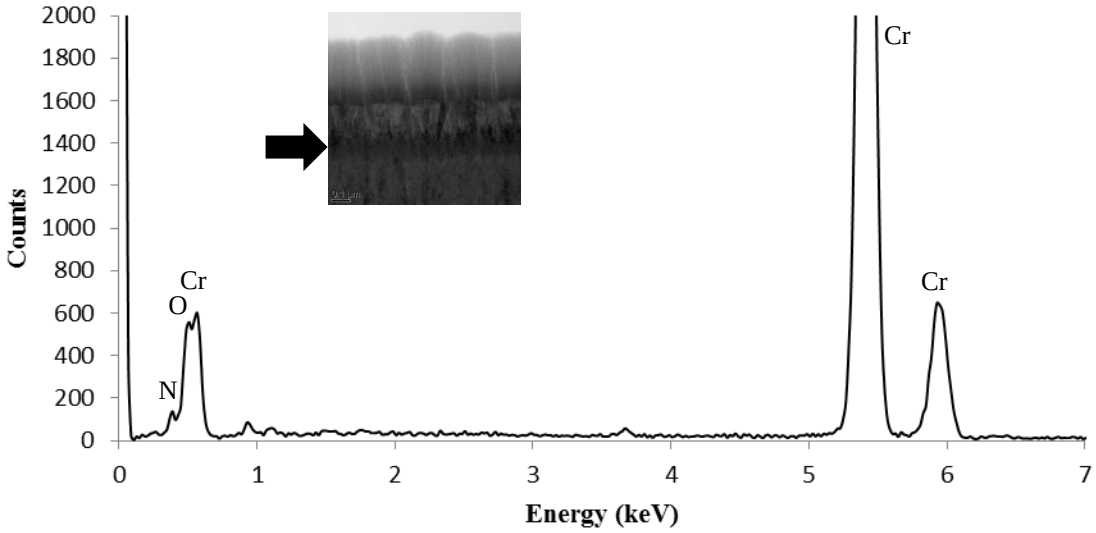

Figure 4.24 An EDX spectrum from the Cr/N transition layer of Coating Type A.

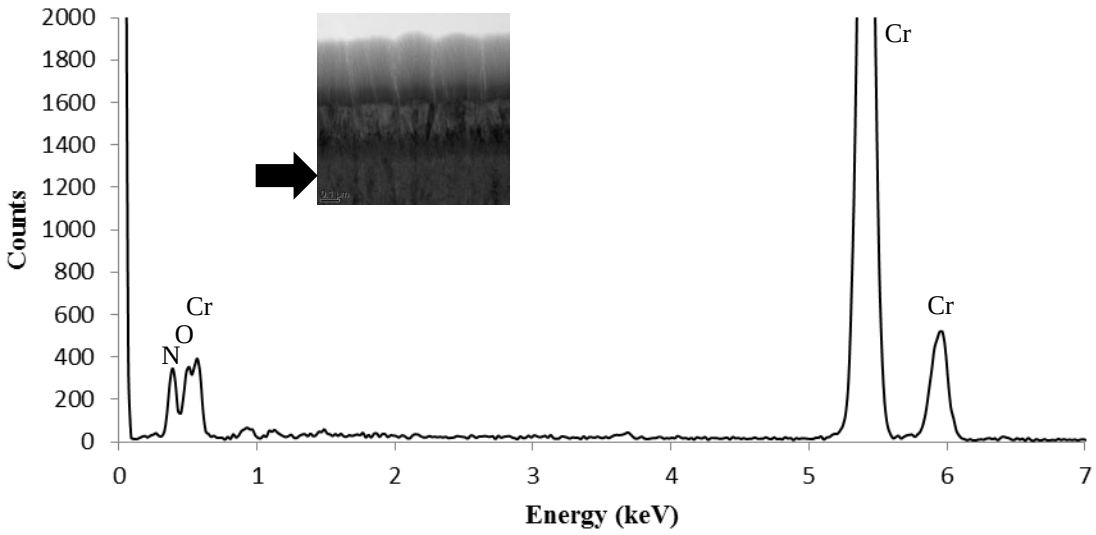

Figure 4.25 An EDX spectrum from the upper CrN layer of Coating Type A.

The EDX spectrum in Figure 4.25 is from the upper CrN layer. There is now no carbon peak and the layer contains a clear nitrogen Kα peak.

Figure 4.26 is a spectrum in the middle of the CrN layer. The chromium peaks increased in intensity with depth in the sample cross-section proportional to the increase in sample

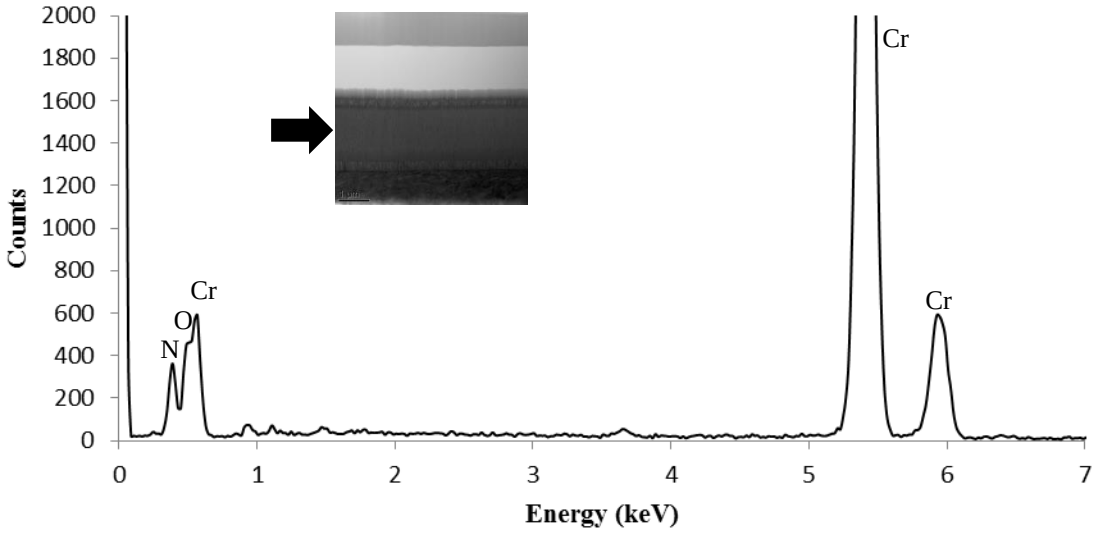

Figure 4.26 An EDX spectrum from the middle of the CrN layer of Coating Type A.

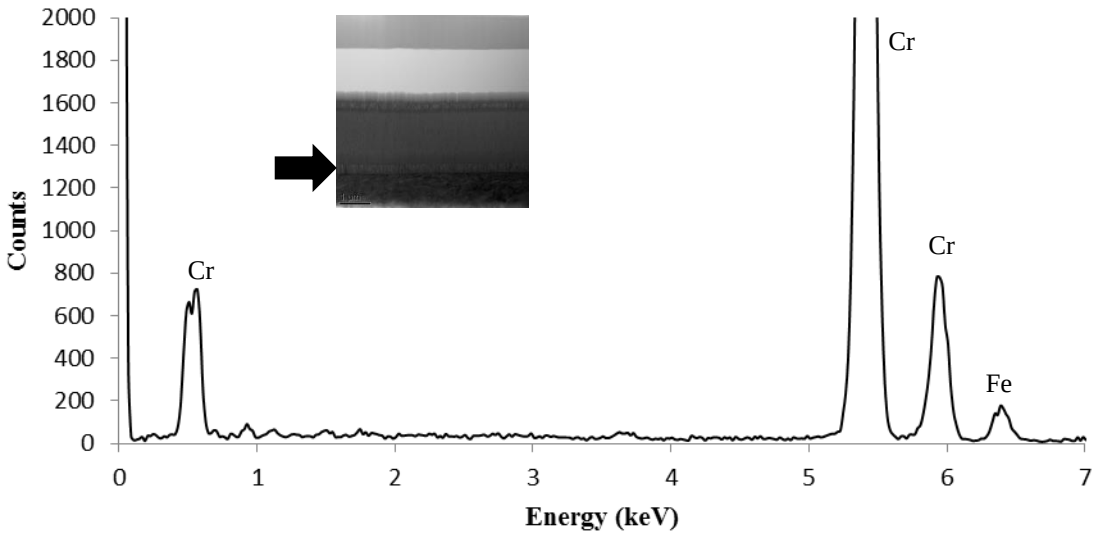

Figure 4.27 An EDX spectrum from the Cr baselayer of Coating Type A.

thickness and therefore EDX interaction volume.

Figure 4.27 is an EDX spectrum from the Cr rich adhesion layer at the bottom of the deposited interlayers just above the substrate in Figure 4.28.

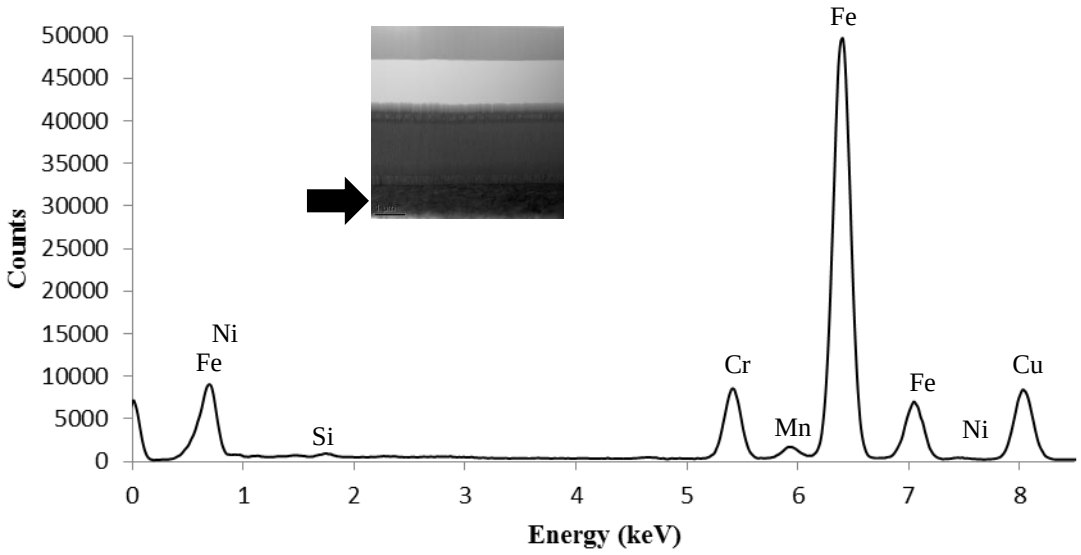

Figure 4.28 An EDX spectrum from the substrate of Coating Type A.

Figure 4.28 shows the EDX spectrum from the HAS40100 substrate. As expected, the alloy peaks present were similar to the composition of the AISI 431 alloy found in Table 2.

4.3.2 Coating Type A: 7 day autoclave exposure

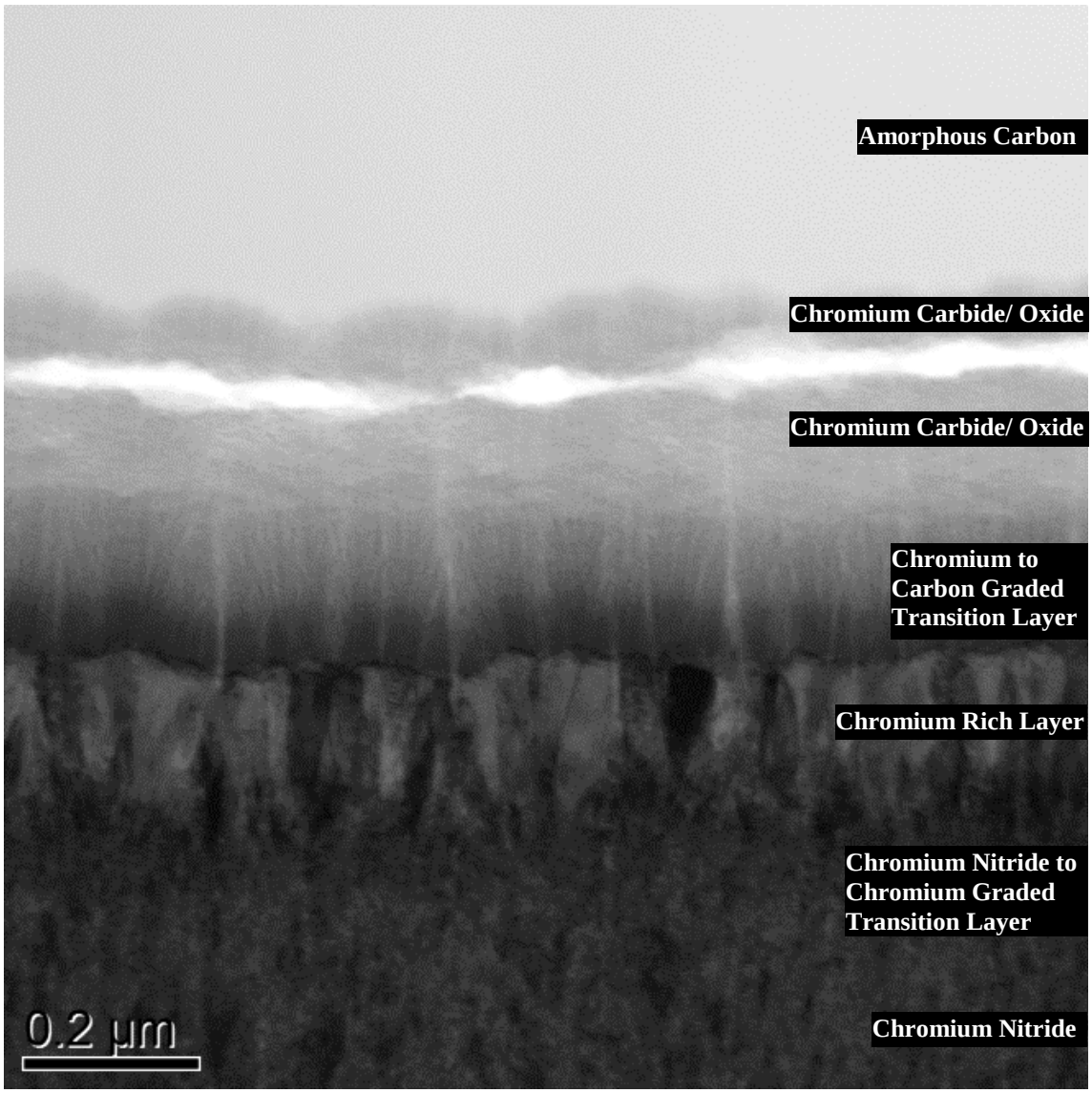

Figure 4.29 A STEM BF micrograph of Coating Type A cross-section after the 7 day autoclave test.

The sample of Coating Type A after exposure in the autoclave for 7 days is shown in the bright field STEM micrograph in Figure 4.29.

The corresponding annular dark field image is shown in Figure 4.30. Failure of the coating was observed within the Cr/C layer just below the amorphous carbon, as previously observed in the SEM imaging. There was also a change in the coating

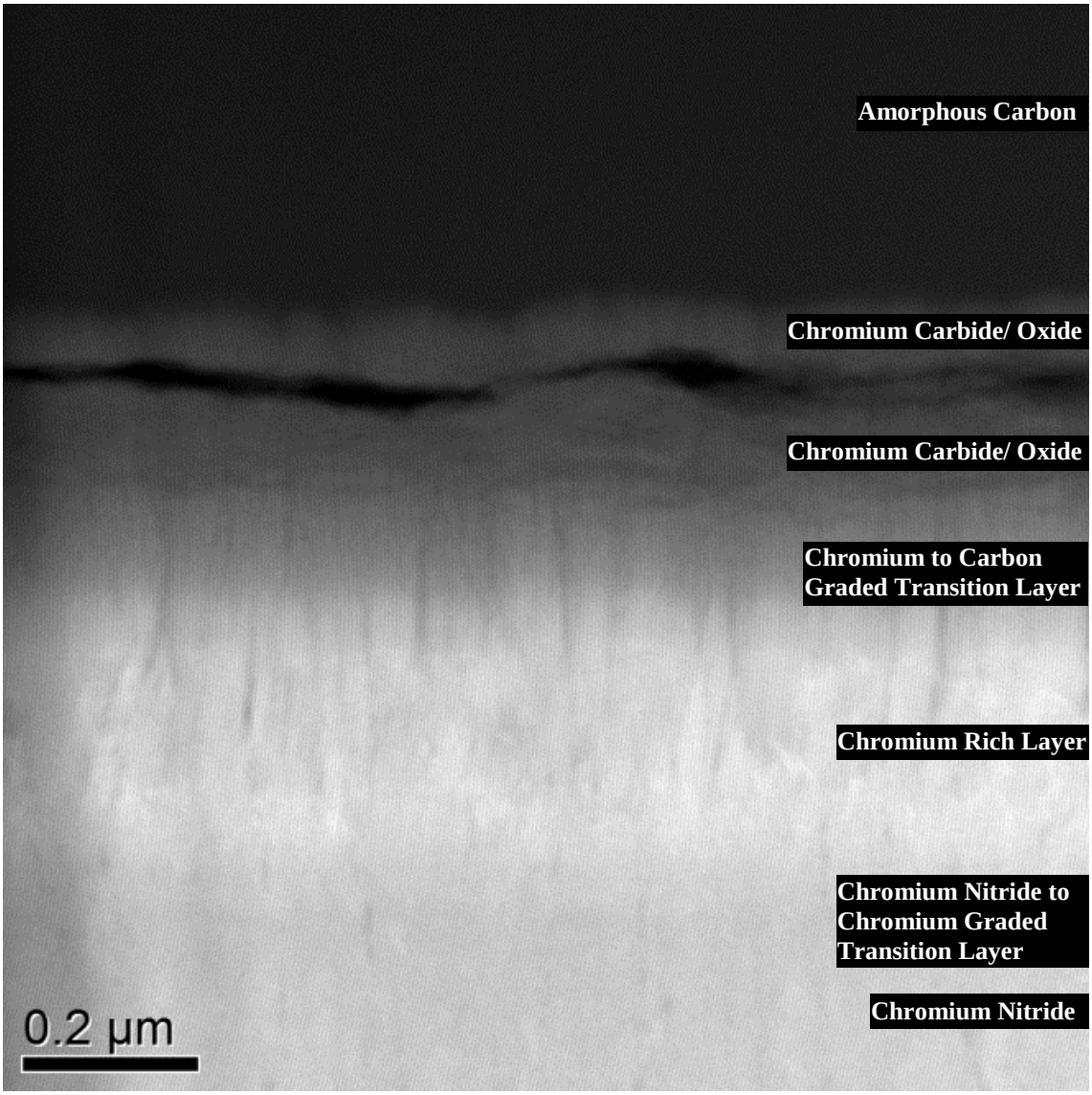

Figure 4.30 A STEM ADF micrograph of Coating Type A cross-section after the 7 day autoclave test.

microstructure surrounding the cracked area when compared with the as-received coating.

Figure 4.31 shows another bright field STEM micrograph of the dendritic structure of the degraded cracked Cr/C layer.

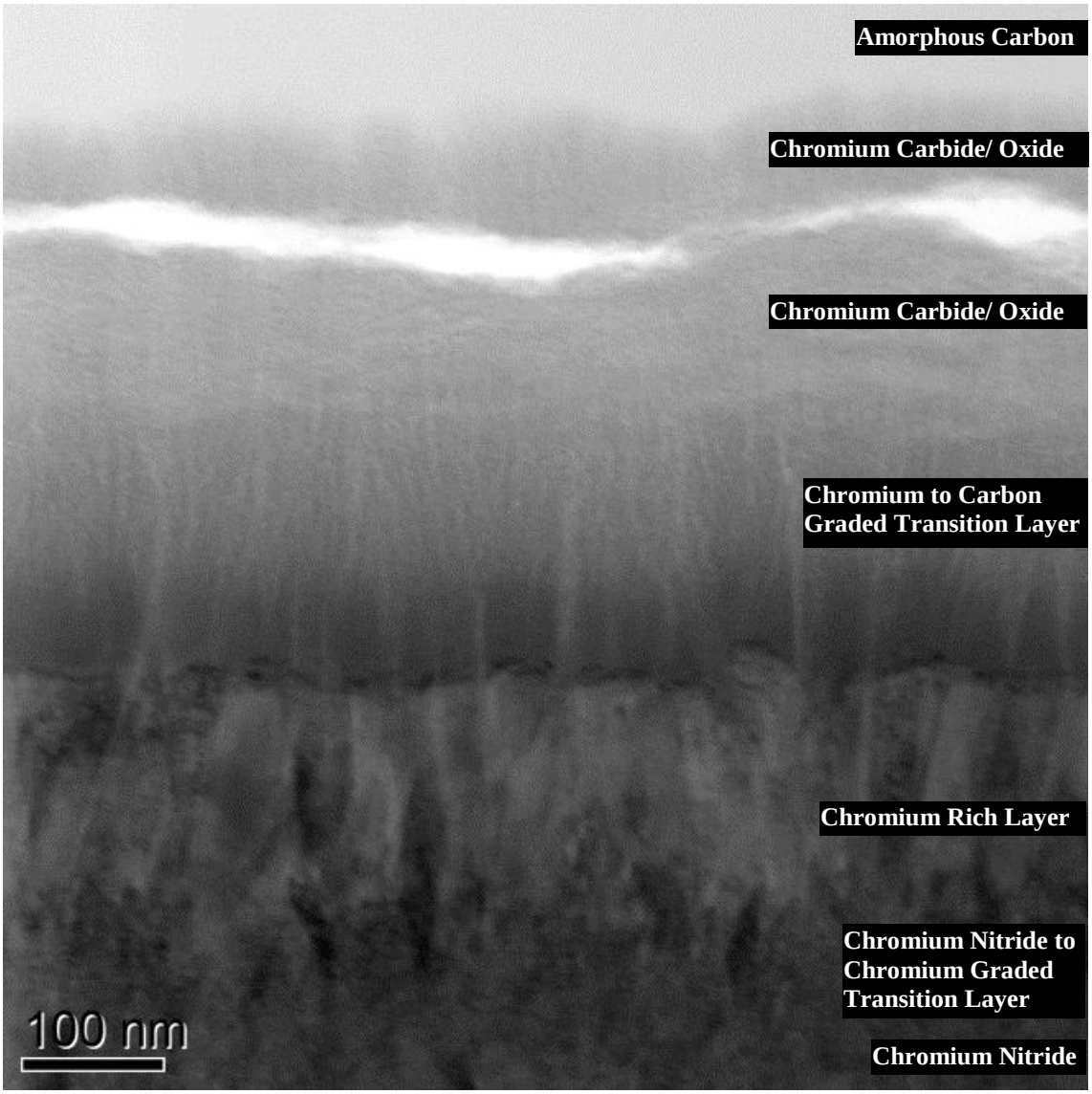

Figure 4.31 A STEM BF micrograph of Coating Type A cross-section after the 7 day autoclave test.

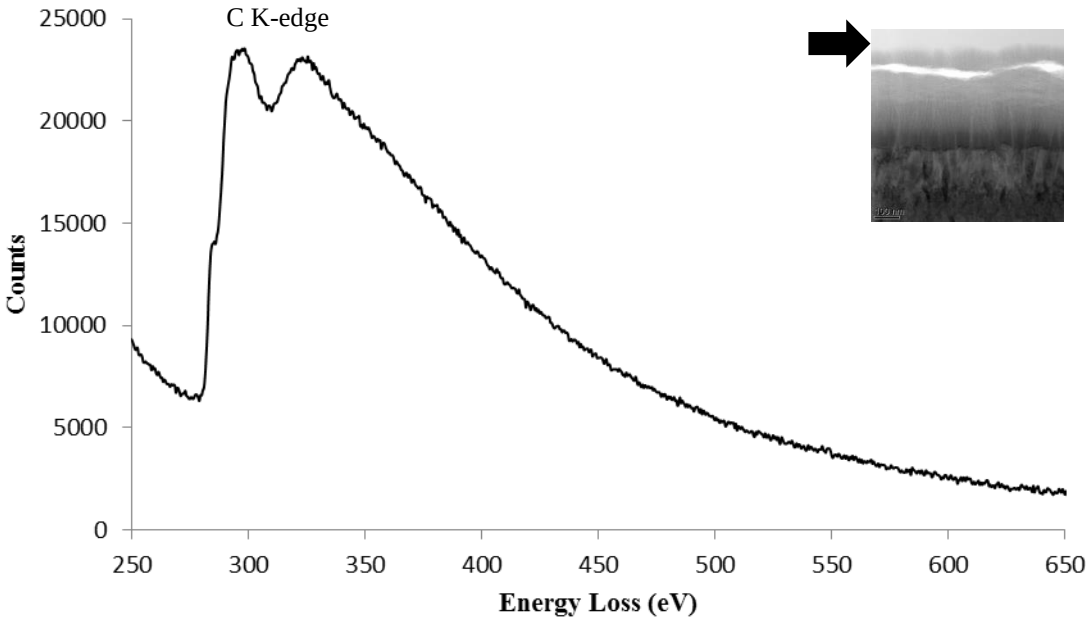

Figure 4.32 An EELS spectrum from the amorphous carbon layer of Coating Type A after the 7 day autoclave experiment.

Figure 4.32 is the EELS spectrum from the amorphous carbon layer in Coating Type A after the 7 day autoclave exposure. The carbon K edge is the only significant peak visible in the energy loss spectrum indicating an undoped amorphous carbon film.

In Figure 4.33 the EELS spectrum from the layer just below the amorphous carbon

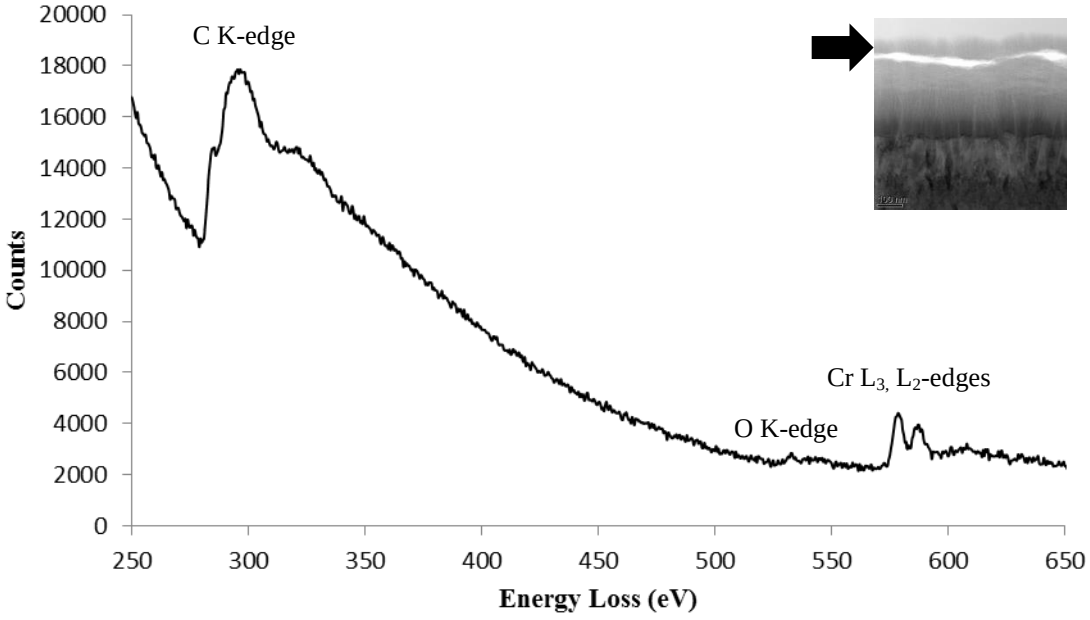

Figure 4.33 An EELS spectrum from just below the amorphous carbon layer of Coating Type A after the 7 day autoclave experiment.

contains carbon, chromium and oxygen energy loss peaks. The top of this layer still adhered to the amorphous carbon but the addition of a stronger oxygen peak suggested some degradation from the as-received state.

Figure 4.34 and Figure 4.35 are EELS spectra from the layers just below the cracked area. Similar to the degradation layer above the crack they contained carbon, chromium and oxygen energy loss peaks.

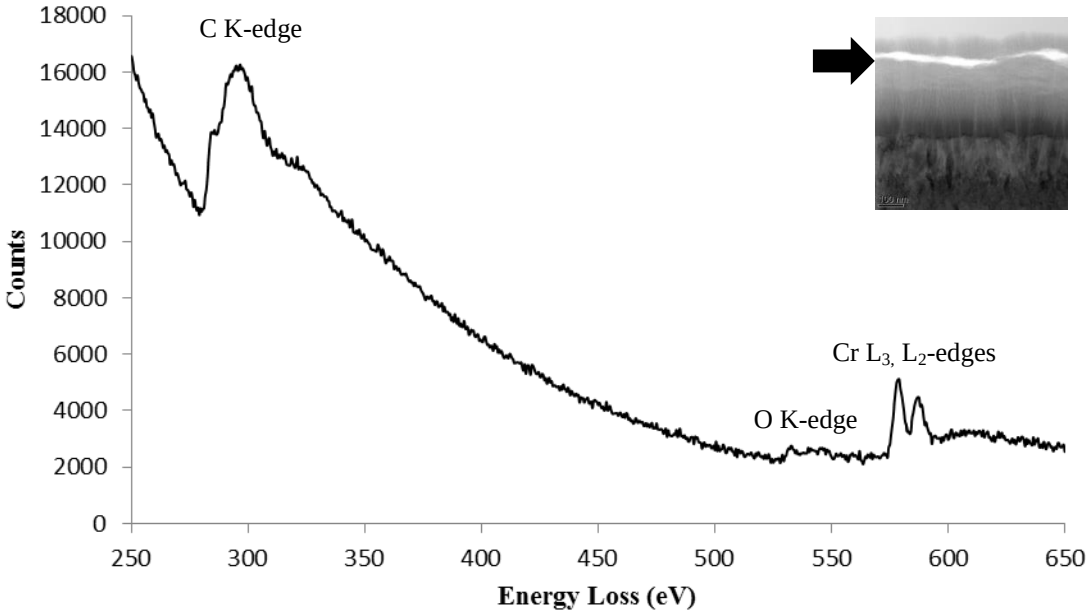

Figure 4.34 An EELS spectrum from the degradation layer near the crack in Coating Type A after the 7 day autoclave experiment.

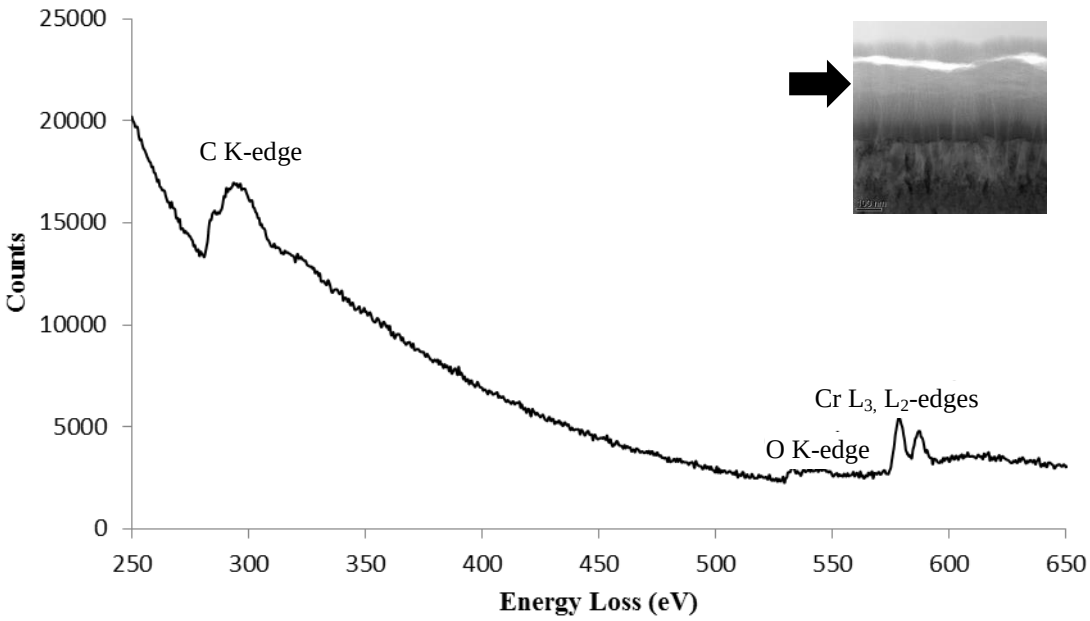

Figure 4.35 An EELS spectrum from the lower degradation layer in Coating Type A after the 7 day autoclave experiment.

Figure 4.36 is an EELS spectrum from lower in the Cr/C layer and has a composition similar to that found in the as-received coating interlayer in Figure 4.14.

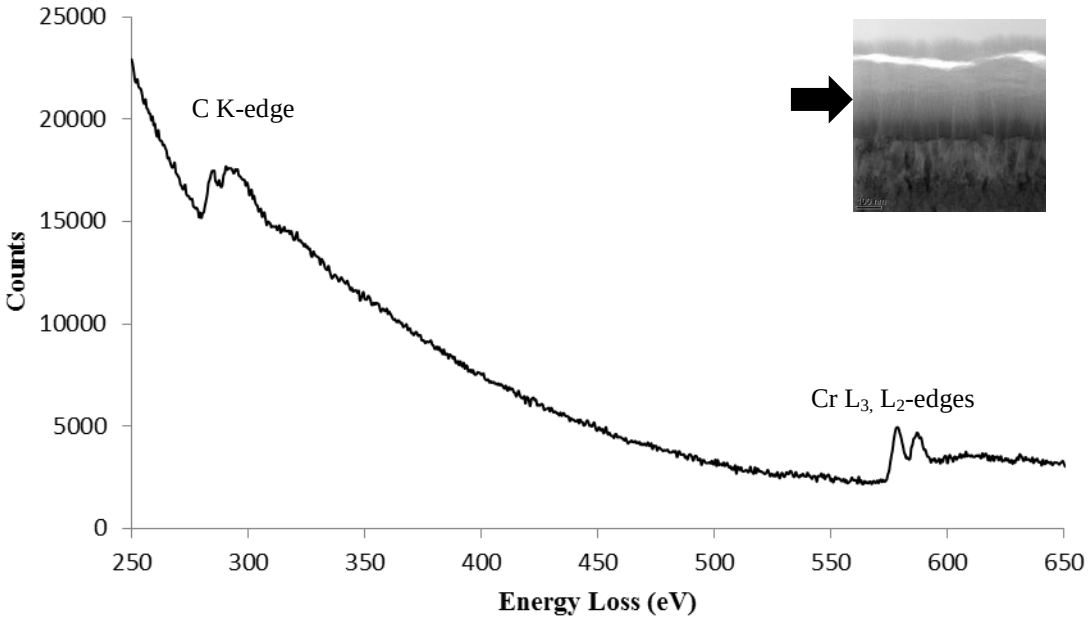

Figure 4.36 An EELS spectrum from the upper Cr/C transition layer of Coating Type A after the 7 day autoclave experiment.

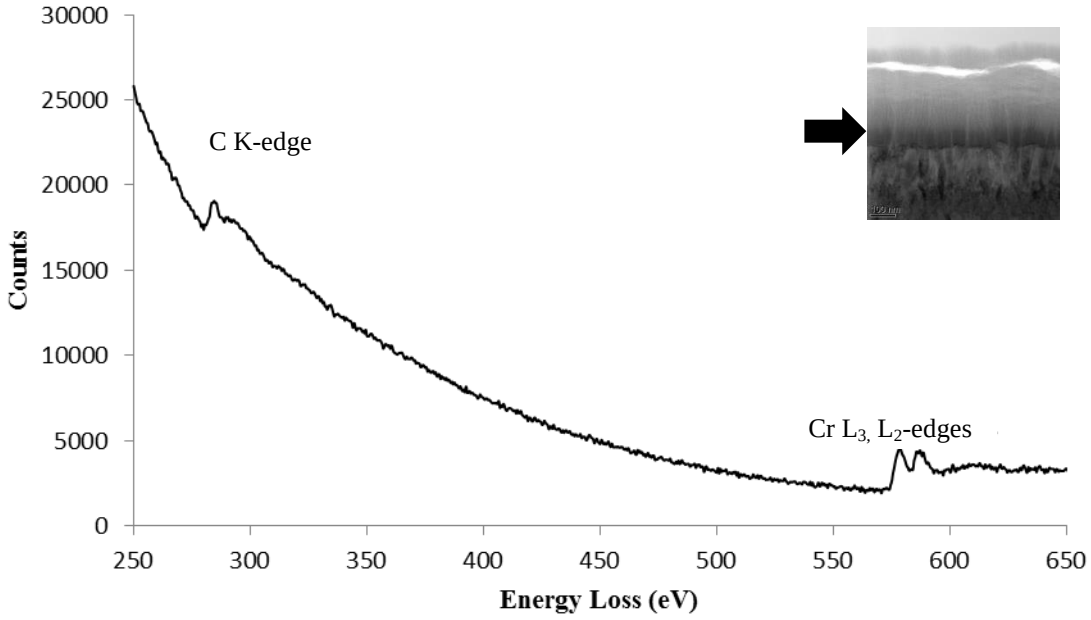

Figure 4.37 An EELS spectrum from the lower Cr/C transition layer of Coating Type A after the 7 day autoclave experiment.

Figure 4.37 shows an EELS spectrum from just above the Cr rich layer, the carbon peak is weaker than the previous spectra as the carbon was graded through the transition layer.

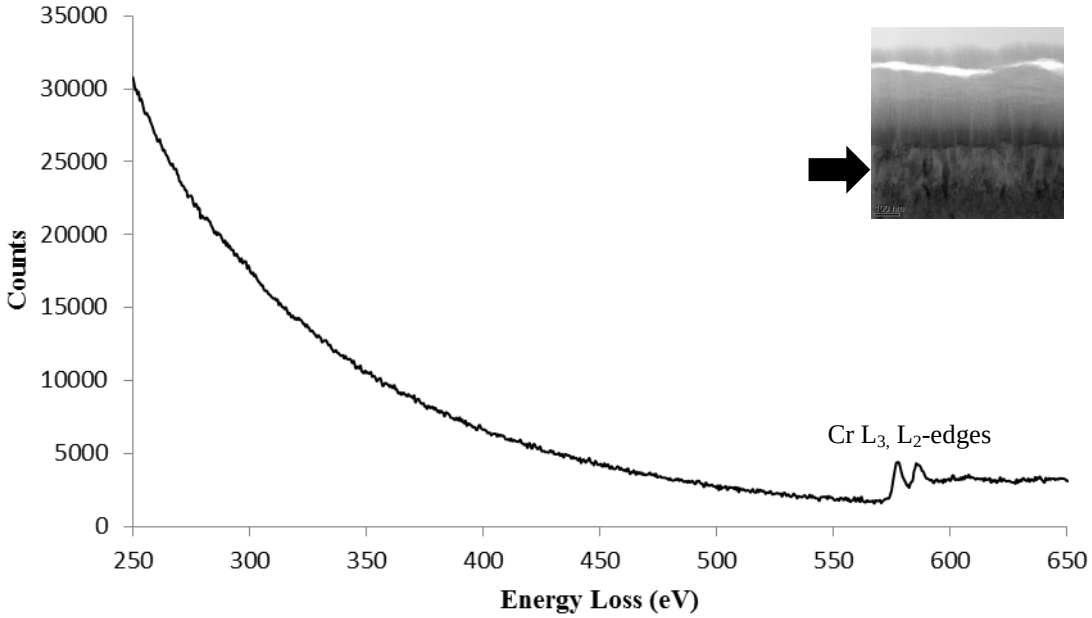

Figure 4.38 An EELS spectrum from the Cr rich layer of Coating Type A after the 7 day autoclave experiment.

The Cr rich layer in Figure 4.38 is a similar spectrum to the corresponding layer in the as-received coating shown in Figure 4.17 which also contained just the chromium peaks.

Figure 4.39 is an EELS spectrum from the CrN layer in Coating Type A after the 7 day autoclave exposure. The nitrogen K edge around 401eV is visible, as well as the chromium L edges.

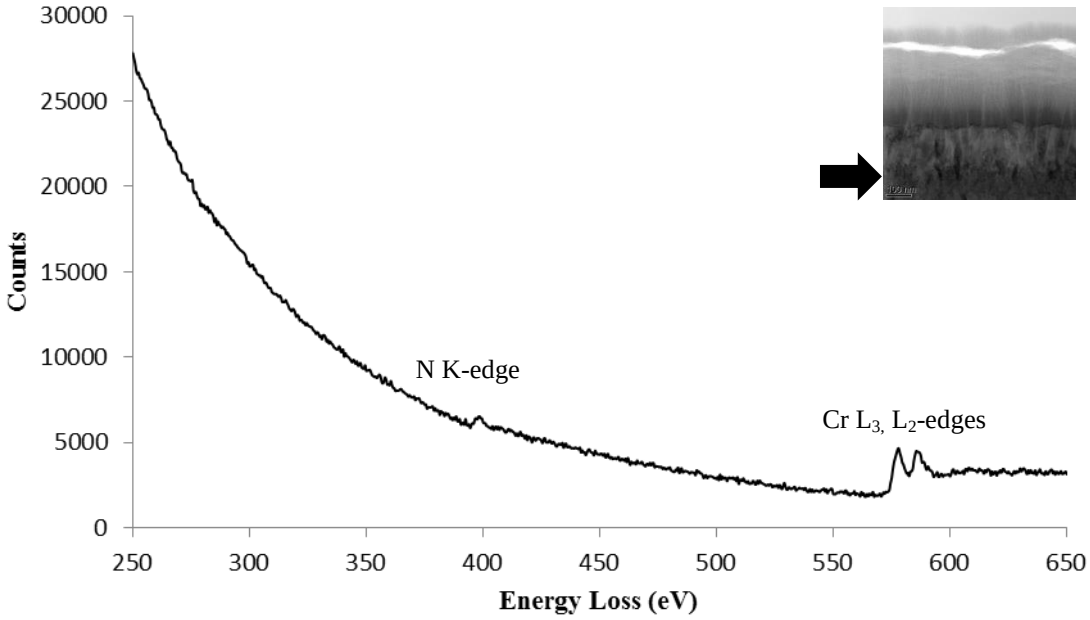

Figure 4.39 An EELS spectrum from the Cr/N transition layer of Coating Type A after the 7 day autoclave experiment.

4.3.3 Coating Type A: 2 year autoclave exposure

Figure 4.40 shows a cross-sectional bright field STEM micrograph of Coating Type A after exposure to high temperature autoclave water for 2 years. As with the 7 day autoclave sample the area above the interlayer region is now a cracked where the amorphous carbon has clearly spalled away from the Cr containing interlayers and the surrounding material has degraded.

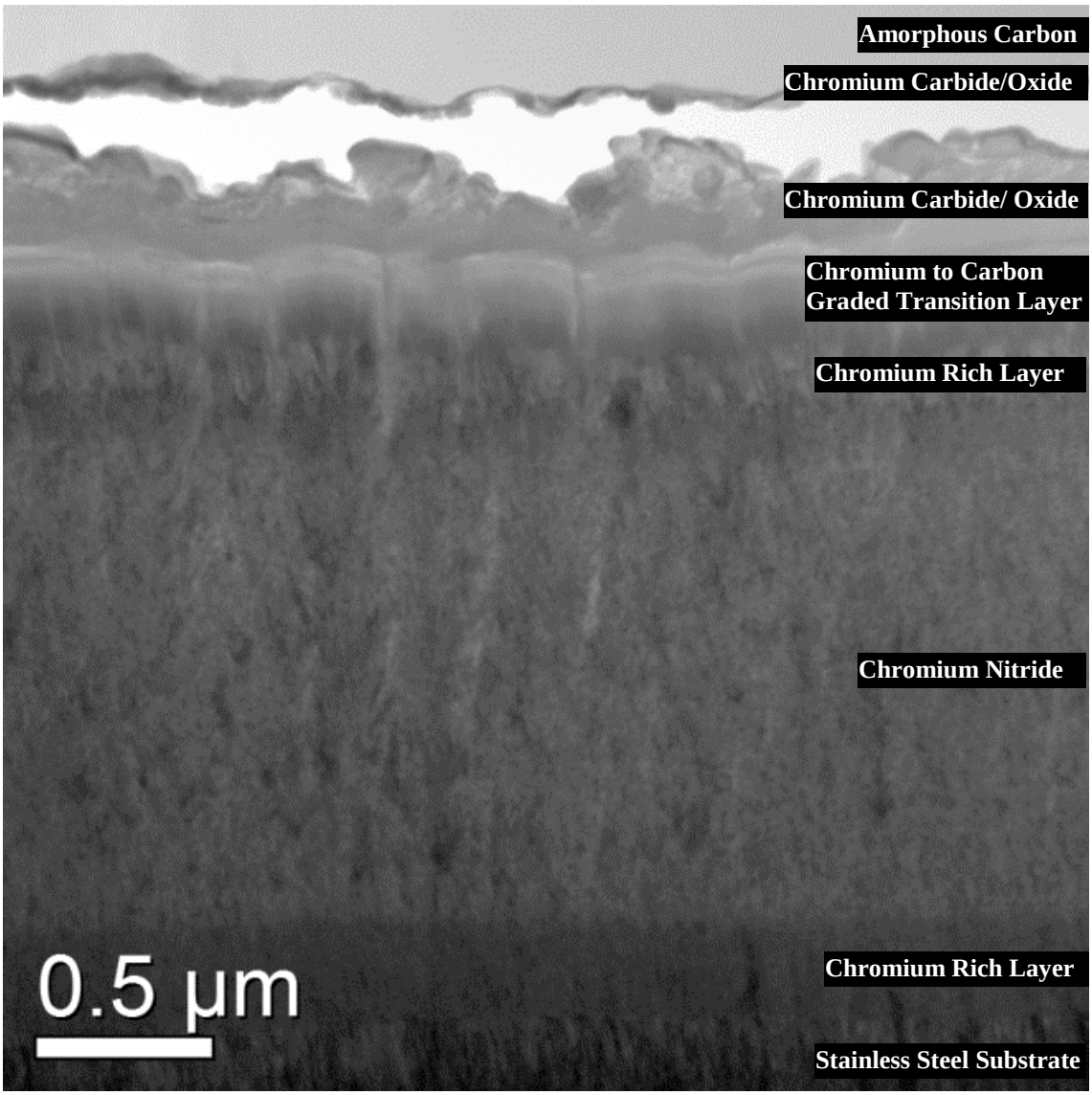

Figure 4.40 A STEM BF micrograph of Coating Type A cross-section after 2 year autoclave test.

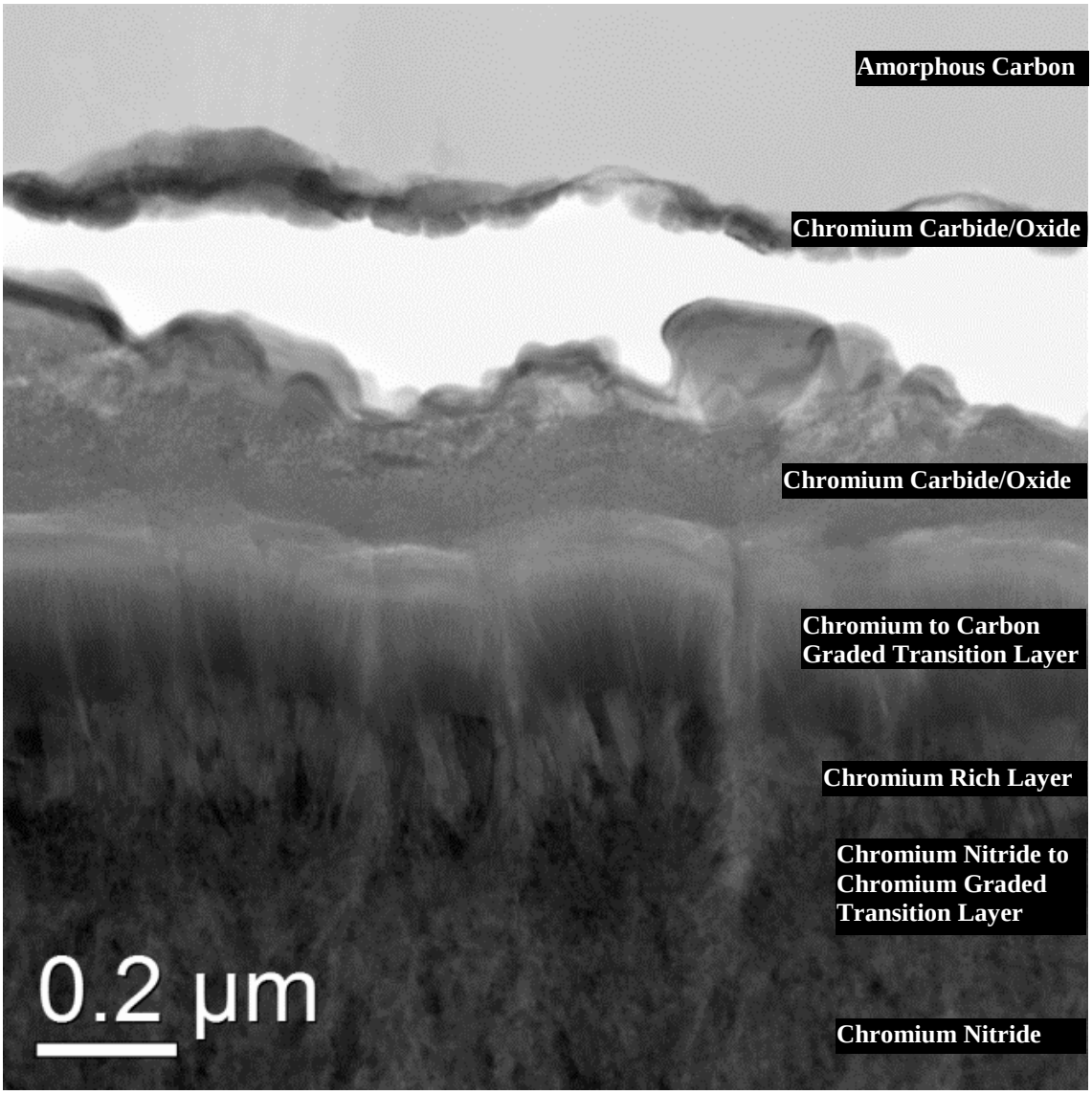

Figure 4.41 A STEM BF micrograph of Coating Type A cross-section after 2 year autoclave test.

Figure 4.41 shows another cross-sectional micrograph of Coating Type A after the 2 year exposure to high temperature water in the autoclave system. The STEM micrographs show the interlayers below the Cr rich layer in the coating are largely unchanged in the as-received and autoclaved samples, while the region just below the amorphous carbon had degraded significantly.

Figure 4.42 shows the EELS spectra for the amorphous carbon in Coating Type A after the 2 year autoclave test. There is only a carbon K edge in the spectrum with no other energy loss peaks.

Figure 4.43 shows an EELS spectrum in the degradation layer similar to that in the 7 day exposure in Figure 4.33. Once again there were carbon, chromium and oxygen energy loss peaks in the spectrum, with the EELS spectrum indicating the presence of chromium oxide [118].

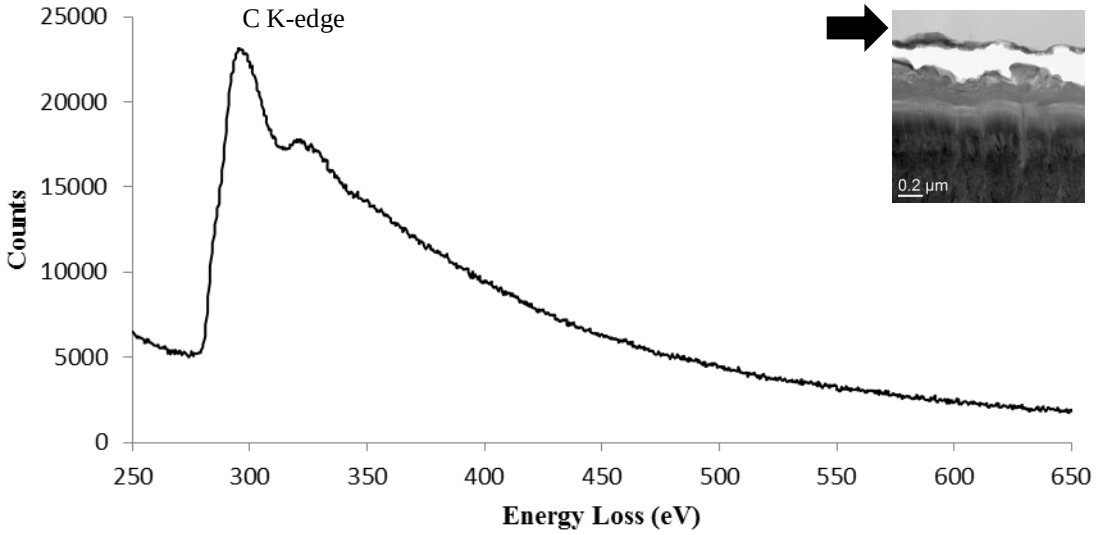

Figure 4.42 An EELS spectrum from the amorphous carbon layer of Coating Type A after the 2 year autoclave experiment.

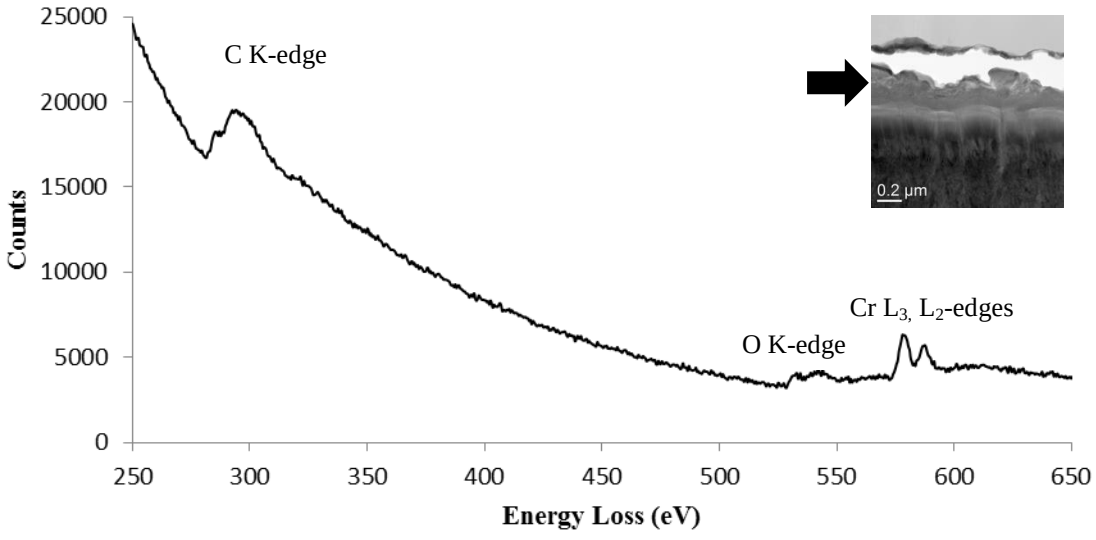

Figure 4.43 An EELS spectrum from the degradation layer of Coating Type A after the 2 year autoclave experiment.

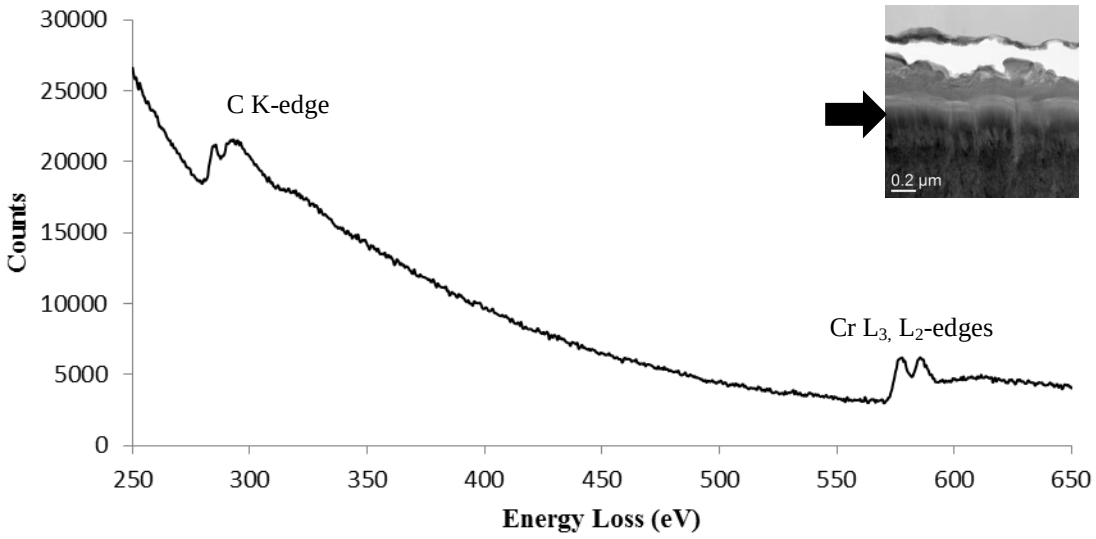

Figure 4.44 An EELS spectrum from the Cr/C transition layer of Coating Type A after the 2 year autoclave experiment.

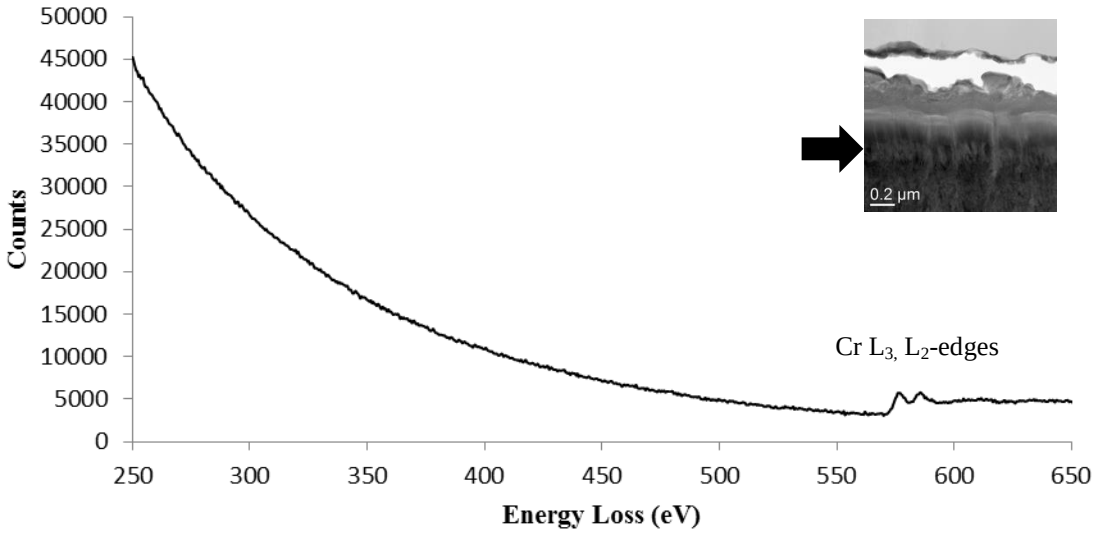

Figure 4.45 An EELS spectrum from the Cr rich layer of Coating Type A after the 2 year autoclave experiment.

Figure 4.44 is an EELS spectrum from the Cr/C transition layer in the coating. There is no significant oxygen peak so the spectrum in this interlayer is similar to that of the spectrum of the as-received Coating Type A shown in Figure 4.16.

Also similar to the as-received coating sample is the EELS spectrum in Figure 4.45 of the chromium rich interlayer, which contains just the chromium L edges.

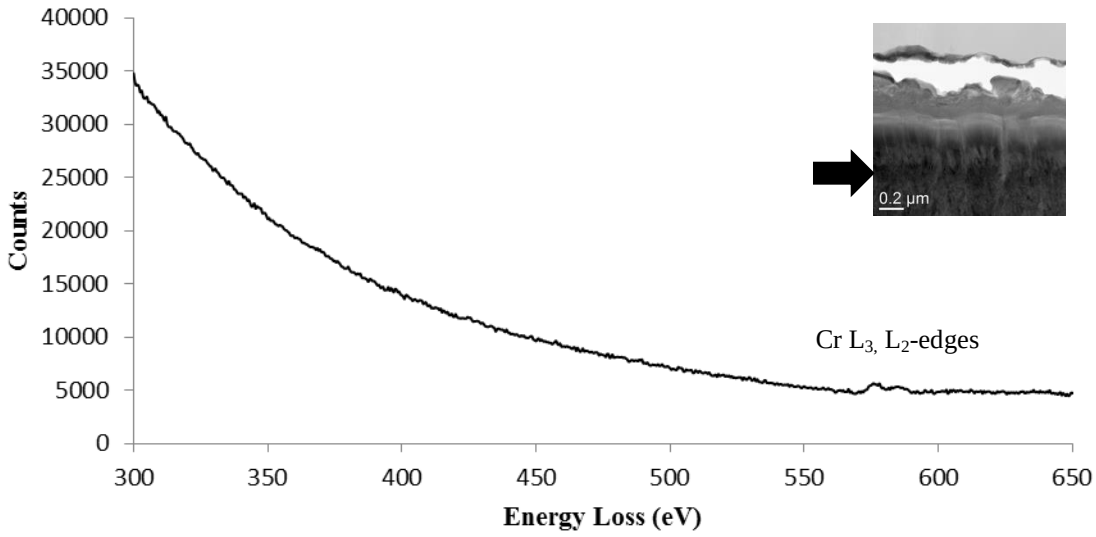

Figure 4.46 An EELS spectrum from the Cr/N transition layer of Coating Type A after the 2 year autoclave experiment.

Figure 4.46 is an EELS spectrum from the transition layer into the CrN interlayer. As the TEM foil was thicker towards the bottom of the sample and therefore lighter elements were harder to detect there was not a clear nitrogen edge visible in the EELS spectrum.

4.3.4 Coating Type B: As received

Figure 4.47 shows the bright field STEM micrograph of the cross-section of as-received Coating Type B. The light layer on top is the amorphous carbon layer, followed by a Cr/C multilayer, on top of a Cr rich layer. These interlayers were deposited on a CrN baselayer on the AISI 304 stainless steel substrate.

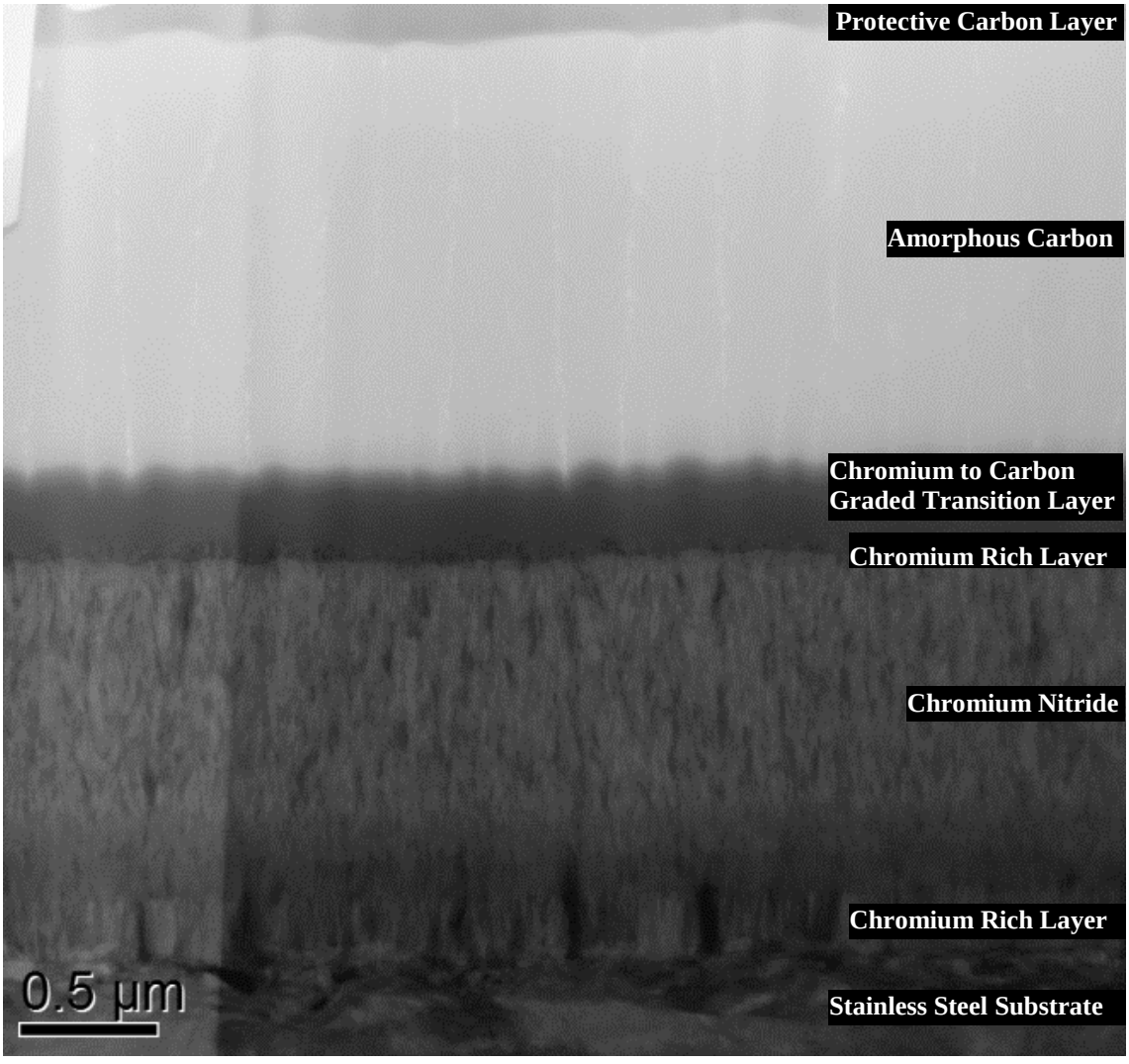

Figure 4.47 A STEM BF micrograph of as-received Coating Type B interfacial region.

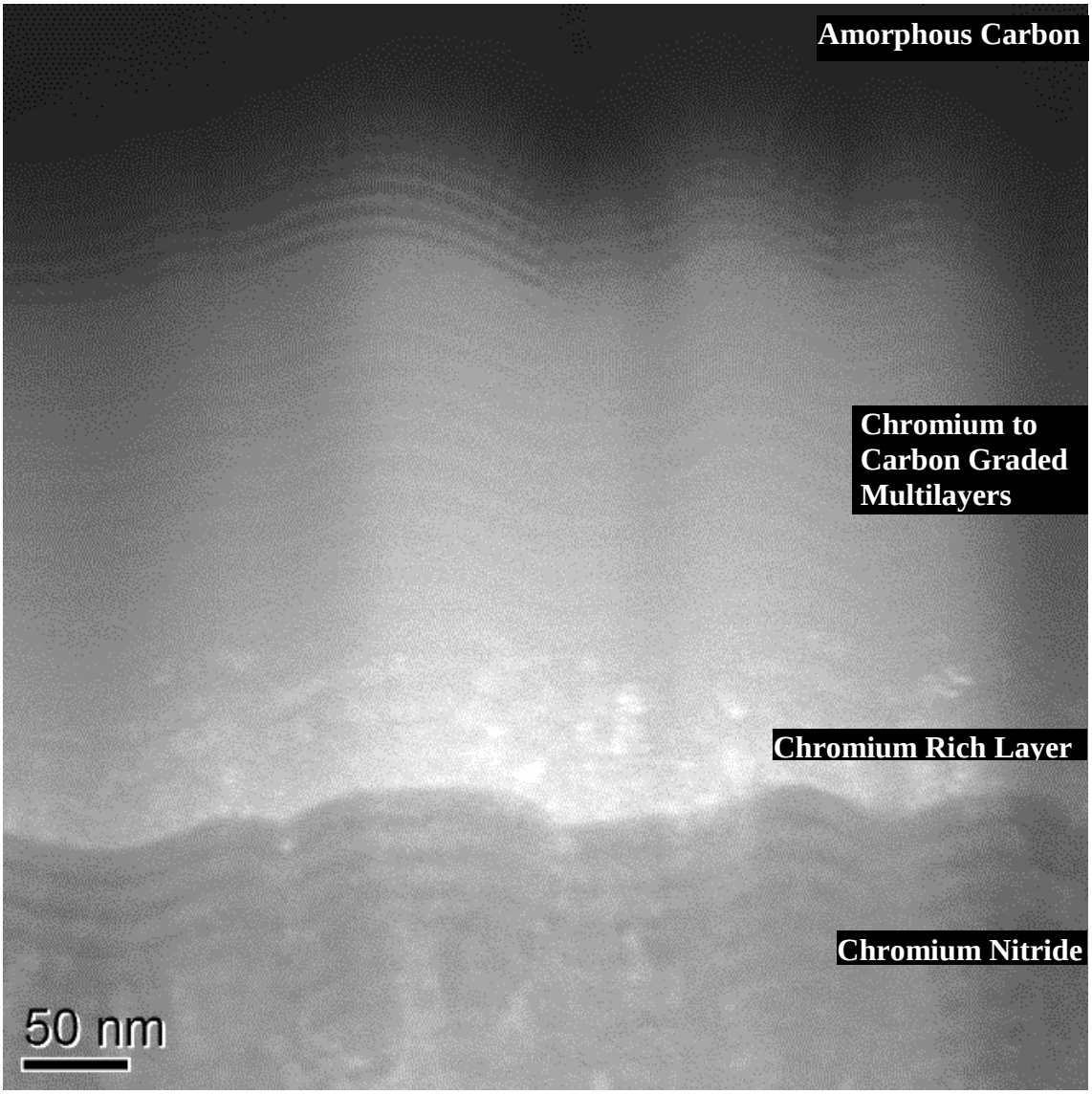

Figure 4.48 A STEM ADF micrograph of as-received Coating Type A interfacial region.

Figure 4.48 shows a STEM Annular Dark Field (ADF) image of the graded multilayer structure at the interface with the amorphous carbon layer. Alternating thin layers of carbon and chromium provides a smoothly graded transition between the carbon film and the chromium rich interlayer below. The darker CrN baselayer at the bottom of the micrograph then provides load support and another corrosion barrier before the substrate.

The EELS spectrum in Figure 4.49 shows the carbon K edge of the amorphous carbon film. There is a very weak Cr edge around 574eV however it is difficult to determine whether the source is from a low percentage Cr doping of the a-C or from material resputtered during FIB milling.

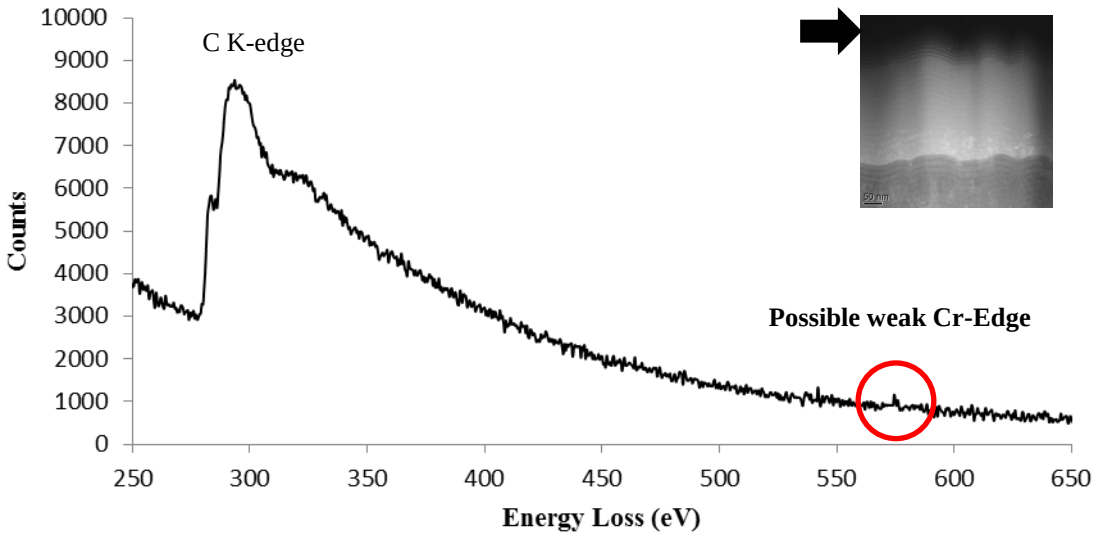

Figure 4.49 An EELS spectrum from the amorphous carbon layer of Coating Type B.

Figure 4.50 is the EELS spectrum from the upper region of the Cr/C multilayer. The composition of these layers was studied in further detail in Figure 4.54.

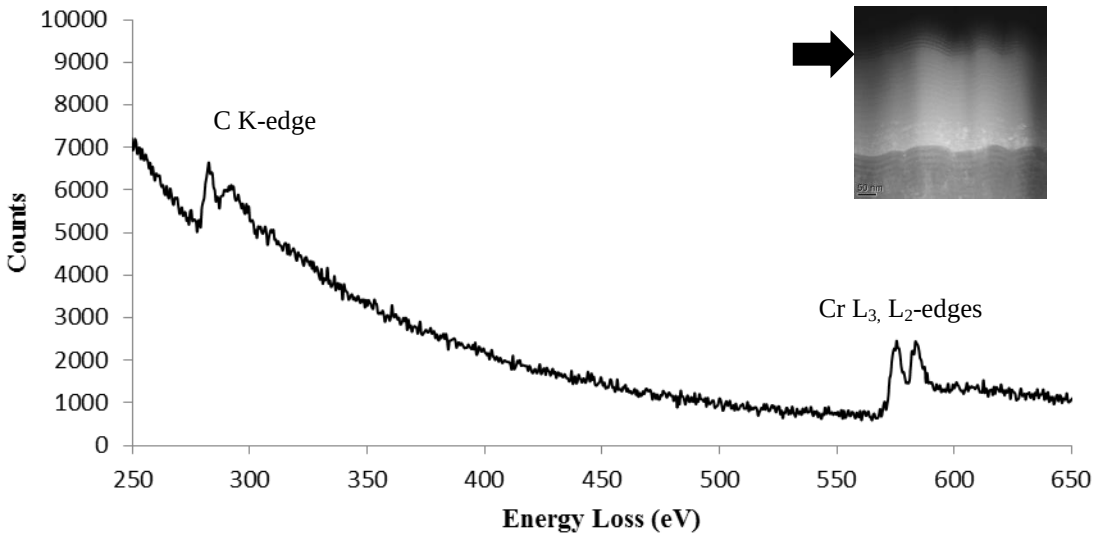

Figure 4.50 An EELS spectrum from the upper Cr/C multilayer layer of Coating Type B.

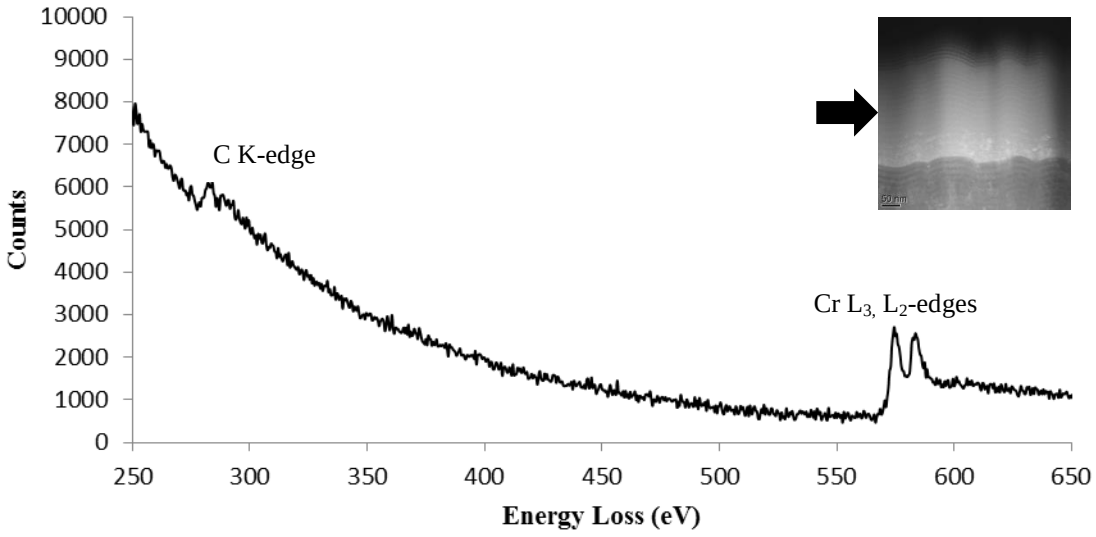

Figure 4.51 An EELS spectrum from the lower Cr/C multilayer layer of Coating Type B.

Figure 4.51 is from the lower Cr/C multilayer and shows the relative changes of the carbon and chromium peaks. The reduction in the carbon peak and increase in the Cr peaks suggested that the two elements were graded during deposition through the transition layers. Figure 4.52 is an EELS spectrum from the Cr rich layer between the Cr/C multilayer and the CrN baselayer. There is a weak carbon edge but it is a lot lower than in Figure 4.49.

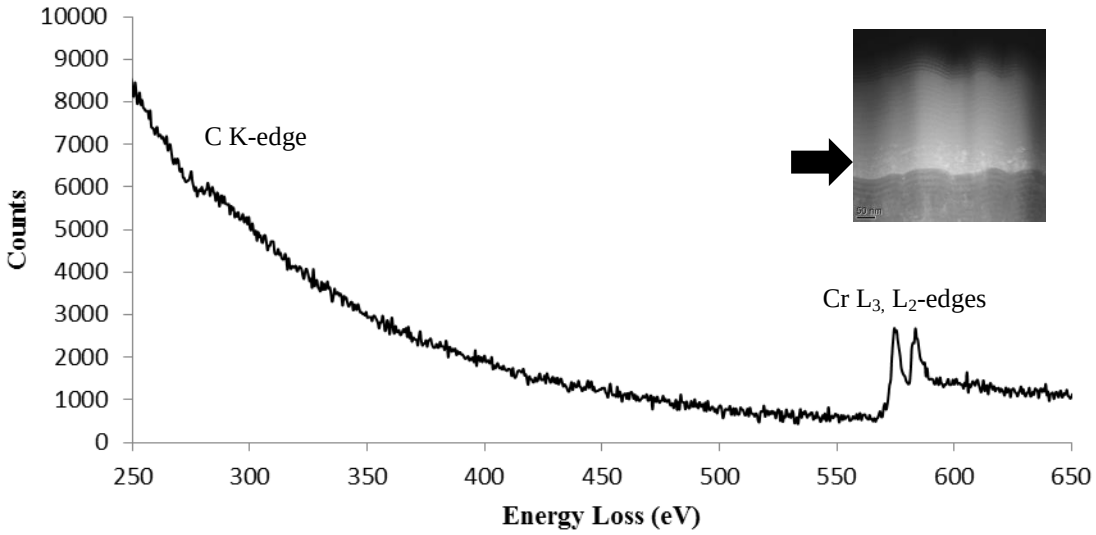

Figure 4.52 An EELS spectrum from the Cr baselayer of Coating Type B.

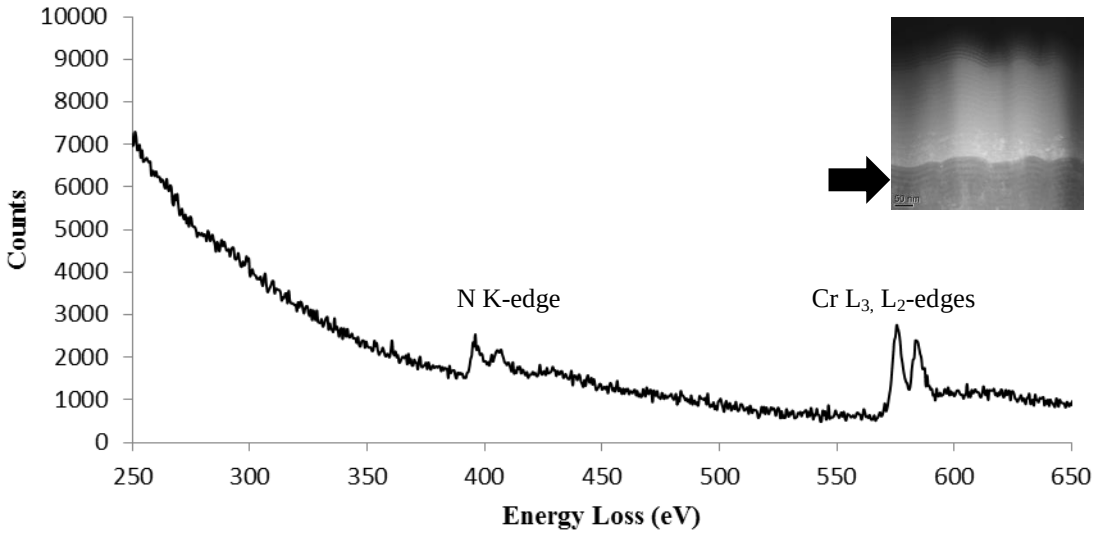

Figure 4.53 An EELS spectrum from the upper CrN layer of Coating Type B.

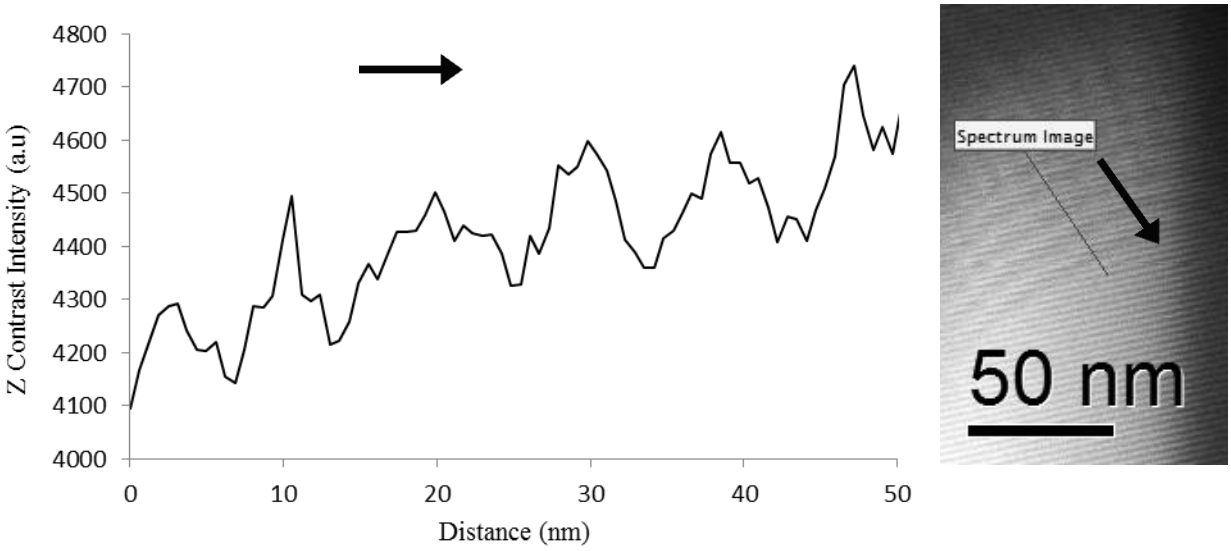

Figure 4.54 A STEM ADF spectrum image of Z contrast intensity in the Cr/C multilayer of Coating Type B.

Figure 4.54 is a graph of the Z contrast intensity against distance along a spectrum image positioned across the Cr/C multilayers. The image contrast of the annular dark field STEM micrograph is proportional to the Z number of the elements present, with lighter elements appearing lighter. As the EELS spectrum in Figure 4.50 showed only the chromium (Z = 24) and carbon (Z = 6) peaks it suggests that the light bands are chromium and the darker bands are carbon. The overall intensity also increased with depth into the sample as the layers are graded from carbon to chromium.

4.3.5 Coating Type C: As received

Figure 4.55 is a bright field STEM micrograph of the cross-section of the as-received Coating Type C. The bottom layer is the stainless steel substrate, on top of which is a Cr adhesion layer, followed by a Cr doped amorphous carbon film.

Figure 4.56 shows a bright field STEM image centred on the chromium adhesion layer. Some of the horizontal lines in Figure 4.56 are a result of image noise experienced during the operation of the JEOL R005 aberration corrected microscope rather than

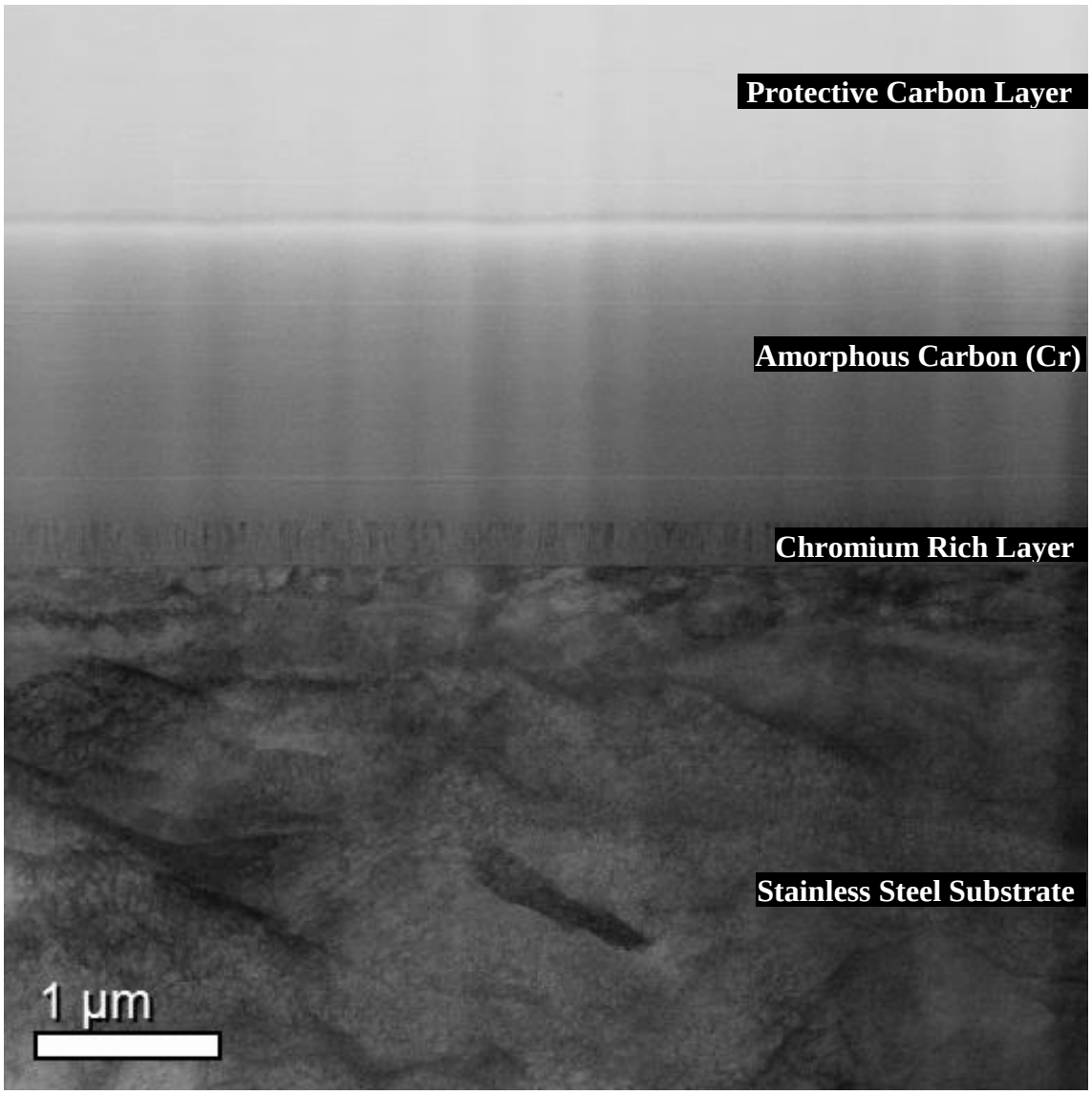

Figure 4.55 A STEM BF micrograph of as-received Coating Type C interfacial region.

actual layers in the coating. This made characterisation of the interlayer microstructure challenging.

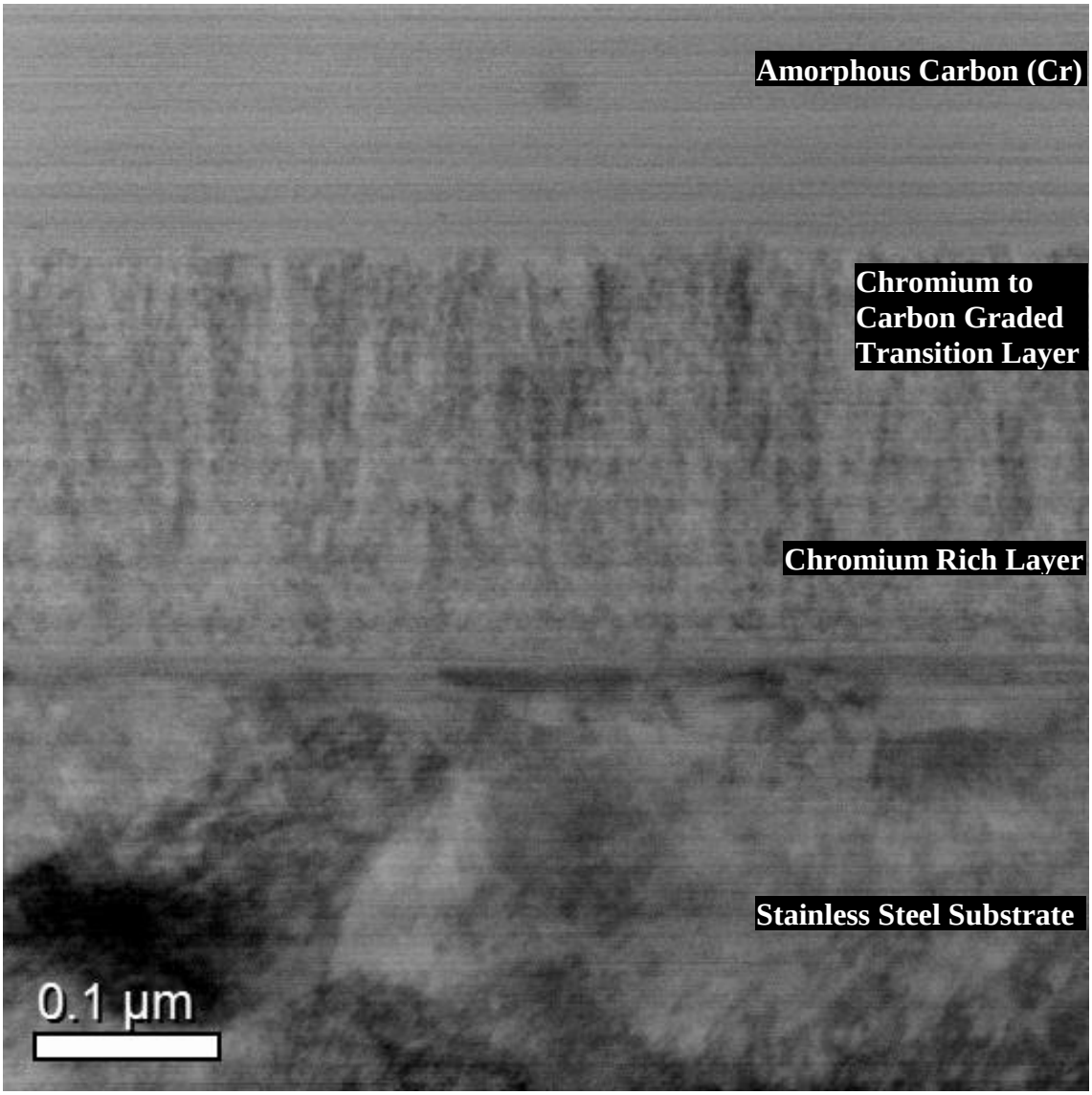

Figure 4.56 A STEM BF micrograph of as-received Coating Type C interfacial region.

Figure 4.57 is an EELS spectrum from the top of the Cr doped amorphous carbon layer with the carbon K edge and the chromium L edges. The EELS spectrum from the middle of the amorphous carbon coating is shown in Figure 4.58 and the lower EELS spectrum from the film is shown in Figure 4.59.

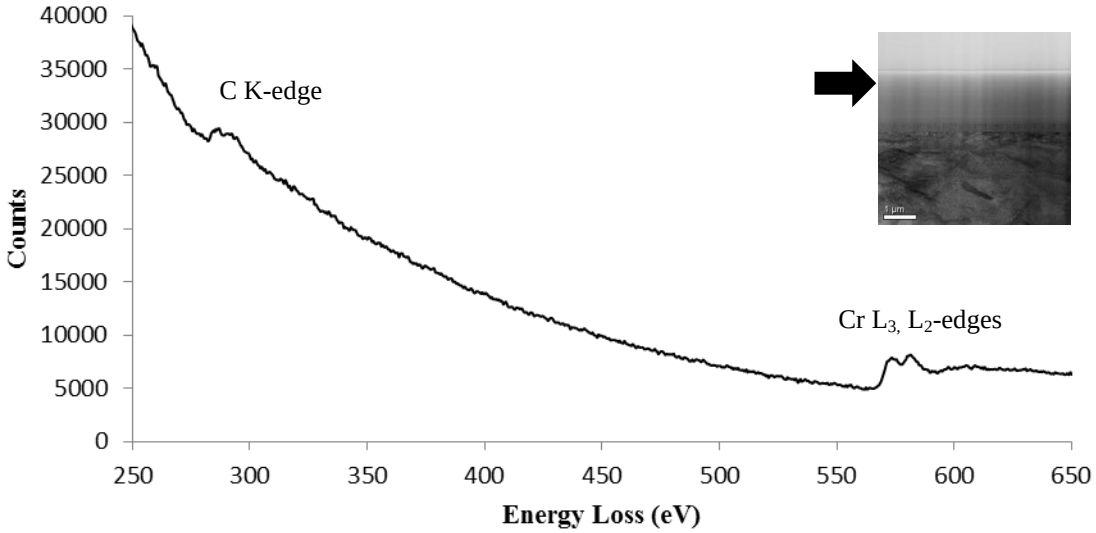

Figure 4.57 An EELS spectrum from the upper Cr doped amorphous carbon layer of Coating Type C.

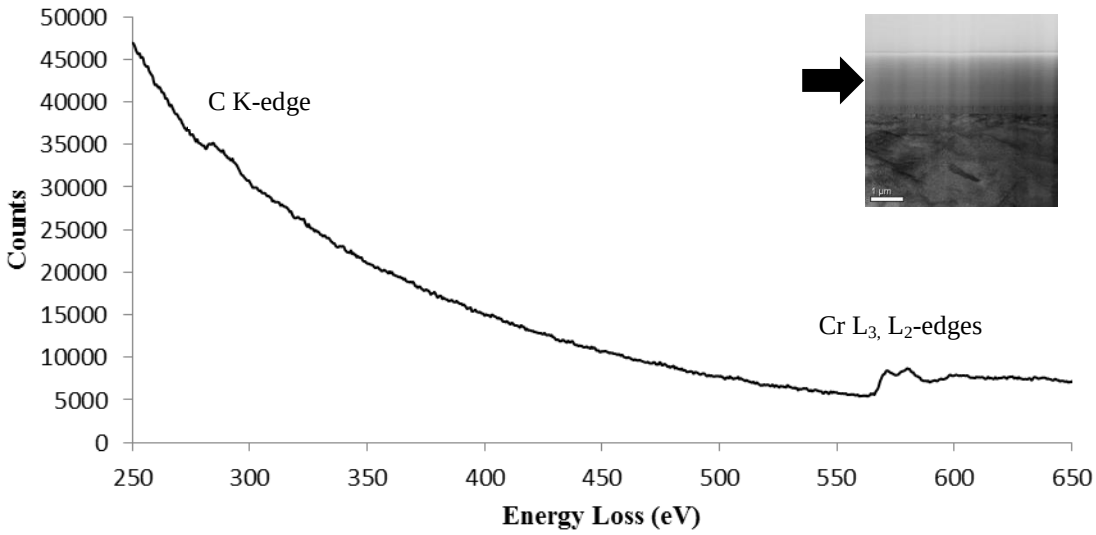

Figure 4.58 An EELS spectrum from the middle of the Cr doped amorphous carbon layer of Coating Type C.

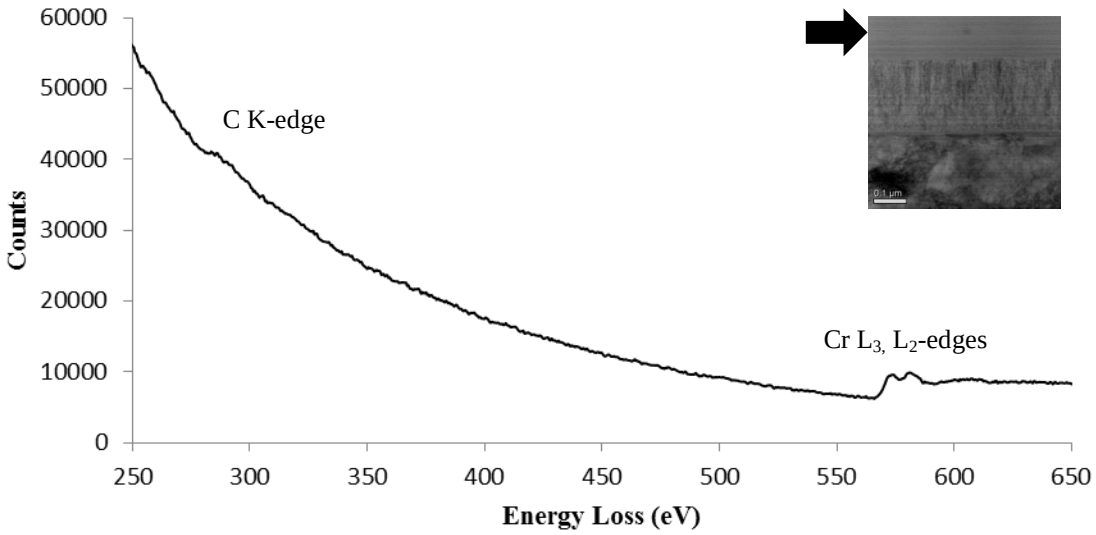

Figure 4.59 An EELS spectrum from the lower Cr doped amorphous carbon layer of Coating Type C.

The EELS spectrum from the upper portion of the Cr/C interlayer is shown in Figure 4. 60. The spectrum showed the chromium L edges and a weak carbon K edge. The EELS spectrum for the lower part of the layer in Figure 4.61 is Cr rich with no carbon edge.

This would suggest that the relative composition is graded through the Cr/C interlayer from carbon to chromium.

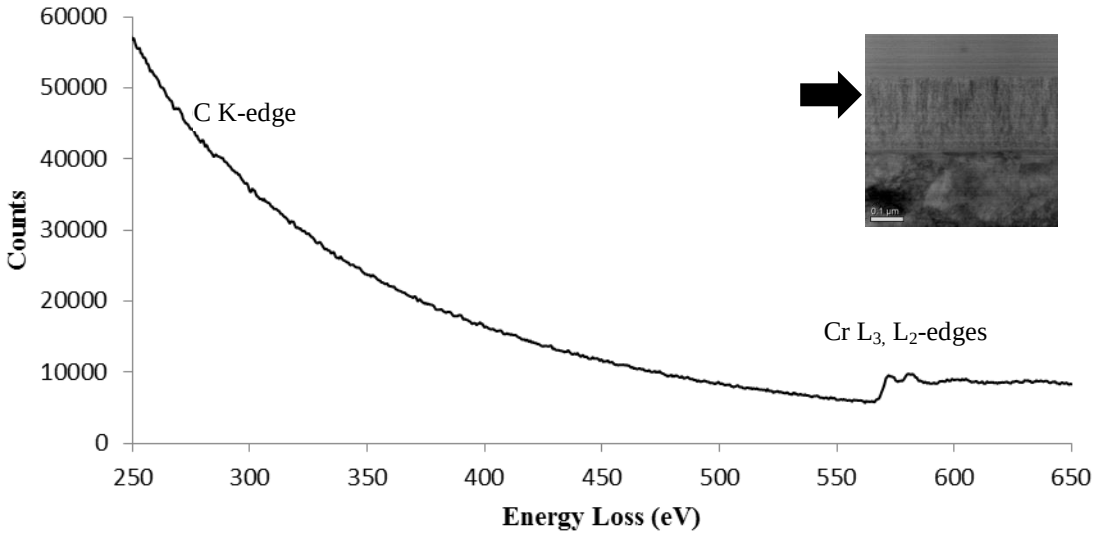

Figure 4.60 An EELS spectrum from the upper Cr/C layer of Coating Type C.

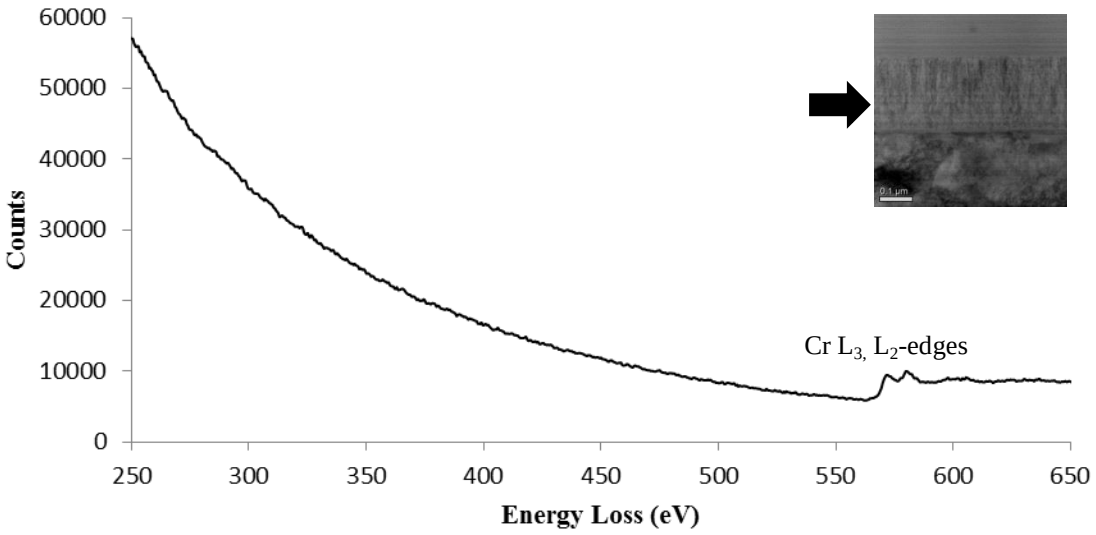

Figure 4.61 An EELS spectrum from the lower Cr/C layer of Coating Type C.

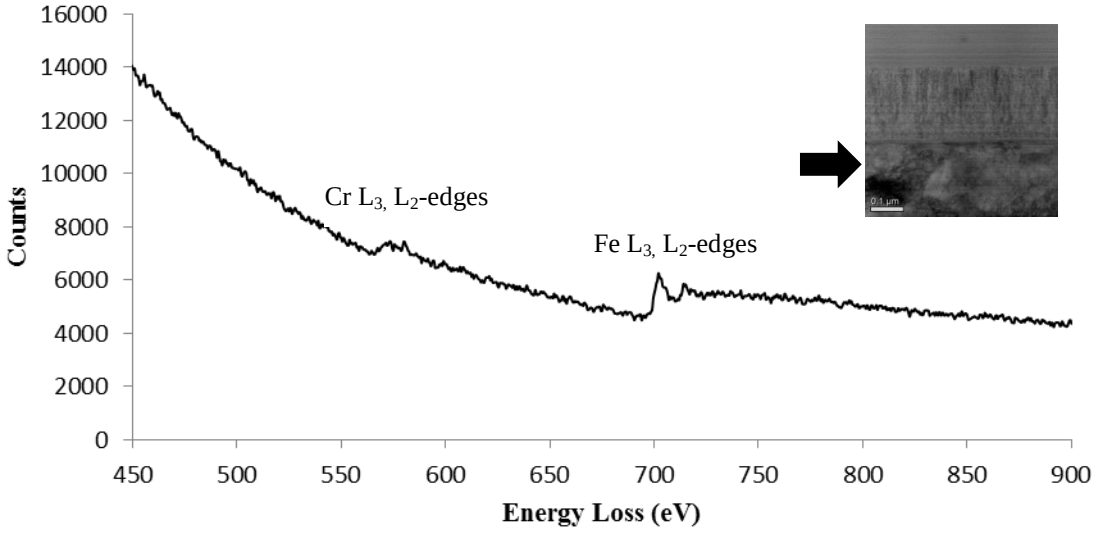

Figure 4.62 An EELS spectrum from the substrate of Coating Type C.

Figure 4.62 shows the EELS spectrum of the substrate of Coating Type C. The elemental composition should be that of AISI 304 as shown in Table 2 but only the chromium and iron edges were visible in the spectrum as the peak to background noise ratio was relatively high.

4.4 Summary

Following the characterisation of the amorphous carbon coating compositions and structures it was found that the commercial diamond-like carbon coating was failing inside the film just below the amorphous carbon layer, resulting in a C/Cr/O layer which increased in thickness with experimental duration. The interlayers below remained the same as in the as-received coating which suggests the cause of failure was related to some degradation mechanism in the area just below the a-C:H and C/Cr interface.

Analysis of the as-received graphite-like carbon non-hydrogenated commercial coating that survived the autoclave tests revealed a graded C/Cr multilayer transitioning into the amorphous carbon with a less sharp interface possibly providing the structure necessary to survive the high temperature water tests. The lab deposited graphite-like carbon Coating Types C and D also had similarly graded C/Cr and C/Ti interfacial layers respectively.

Chapter 5 will discuss the findings of the experimental procedures in relation to the aims and objectives set out at the start of the Engineering Doctorate.

Chapter 5: Discussion

5.1 Introduction

This chapter discusses the experimental results and their significance to their respective project aims and objectives.

It will first discuss the aim of determining the hydrothermal stability of the coatings in high-temperature high pressure water, before discussing the effect of coating composition and structure on performance.

5.2 Hydrothermal stability of amorphous carbon coating properties in high-temperature high-pressure water

The first aim of the project was to assess the hydrothermal stability of selected commercial and lab deposited amorphous carbon coatings in high- temperature high-pressure water conditions to determine how suitable they would be for further development in PWR applications.

The initial objective was to expose the diamond-like and graphite-like amorphous carbon coatings to high temperature water in a Parr bomb pressure vessel to quickly determine whether the coatings were failing at relatively low temperatures of 240°C and exposure periods of 24 hours and 7 days.

Based on previous longer term studies by Rolls-Royce it was expected that the graphite-like coating would survive the experiment with little degradation, however the lower limits of the spalled diamond-like carbon coating were unknown.

The results of the exposure for both 24 hours and 7 days showed that there were no signs of gross spallation of either coating when examined during optical microscopy. This result showed that, at least for temperatures up to 240°C, the diamond-like carbon coating had some potential for future investigation in PWR applications and fulfilled the objective of determining whether the coating was failing straight away in lower temperature water. It also confirmed the previous result of the Rolls-Royce investigations; the graphite-like carbon coating did not spall at these lower water temperatures [1].

The next objective was to expose the commercial and lab deposited coatings to high-temperature high-pressure deionised water at 280°C for 7 days in an autoclave pressure vessel. This experiment was to assess the coating performance in the relatively high water temperatures to compare with the Parr bomb exposure and previous Rolls-Royce autoclave tests.

The results of the experiments fulfil the objective of determining whether the coatings failed at typical pressurised water reactor temperatures. Areas of degradation were also identified with the optical microscope for further assessment. The diamond-like carbon coating spallation supported the coating failures previously observed by Rolls-Royce when exposed in the autoclave but was not quite as extensive as that seen in the 2 year test shown in Figure 2.12 [1]. This suggests that the process of spallation would continue after the 7 day exposure, rather than degrading to the level seen in Figure 2.10 immediately after reaching the experimental temperature. This is supported by the SEM results where some of the spalled areas had relatively smooth crack surfaces, as in Figure 4.6, whereas some cracked areas showed signs of further degradation like the micrograph in Figure 4.2. This result suggested that the coating in its current state would be unsuitable for pressurised water reactor applications above 280°C, but further investigations would be necessary to determine why and how the coating was failing. The optical microscopy also determined that the graphite-like commercial and lab-deposited amorphous carbon coatings survived the exposure without film spallation, indicating that they might be suitable for further development.

Although beyond the scope of this project it is worth mentioning that the water chemistry conditions in both the Parr bomb and autoclave experiments also would not accurately reflect those found in an operational pressurised water reactor as no additives

were used in the deionised water [24]. This might have helped to reduce any corrosion of the sample substrates in the vessel, which could have contributed to the contamination measured. However, it is unlikely that this would have had a negative effect on coating performance as the additives are selected to reduce corrosion therefore further experiments would still have been necessary to study the degradation previously observed with Coating Type A in the autoclave tests as in Figure 2.10.

The next objective in the project was to determine whether the coating delamination seen with Coating Type A was due to fundamentally poor amorphous carbon layer adhesion to the graded interlayer from the deposition process. All of the coating types were examined using scratch adhesion testing to compare their mechanical adhesion with typical coating performance. From the literature for similar coating types it was expected that Coating Type A would show adhesive failure around 15 to 30N [119] [120] and Coating Type B would show loss of adhesion at around 60 N [121].

During the testing Coating Type A first showed signs of coating adhesion failure at around 40N, which was actually higher than expected from the literature data and thus poor mechanical adhesion would likely not be the cause of the film spallation observed in the autoclave. Indeed later on in the project it was found that the interface between the amorphous carbon and the carbon/ chromium layer stayed attached, as seen in Figure 4.27, and the observed degradation happened within the layer itself.

The scratch adhesion tests of the graphite-like carbon commercial coating produced a critical load lower than expected but, as previously discussed, the coating maintained sufficient adherence during the autoclave testing. Both of the lab-deposited coatings also had similar adherence of the carbon top layers to the interlayers and showed that the initial adhesion after deposition for all the films was not the cause of the spallation

in the autoclave testing. In cases where coating failure was observed to have been influenced by corrosion the scratch adhesion tests would not be a useful predictor of coating performance as they only measure the mechanical toughness of the interface [79].

The next step was to use nanoindentation to assess any changes in coating hardness before and after exposure to high-temperature high-pressure water as this has previously been a good indicator for coating graphitisation which could be linked to degradation mechanisms[1]. The results of this objective were a bit mixed due to the large standard deviations seen in some of the samples. Coating Type A in particular was difficult to analyse due to its roughness and any observed drops in hardness would probably need to be further verified using a smoother substrate material [122]. For the partially delaminated sample of Coating Type A it was also necessary to indent in areas with no delamination so that hardness of the remaining coating was measured, rather than that of the exposed substrate or interlayers. This would have perhaps influenced the data to reflect the least degraded areas as they were the only sections remaining to be studied.

The objective of the Raman spectroscopy was to determine the degree of graphitisation in the amorphous carbon films in order to compare their performance during the high temperature water experiments. The spectra were analysed using the carbon ordering trajectory in Figure 2.15 and the schematic diagram of the D and G peaks in Figure 2.16 to determine changes in coating bonding during hydrothermal exposure. The G peak positon was found to be a good indicator of changes in sp^3 content for the films studied, as movement to higher wavenumbers indicated graphitisation of the coatings [104].

As the amorphous carbon Coating Type A started off more ‘diamond-like’, the coating had further to graphitise as the sp^3 bonded carbon ordered to sp^2 bonding when exposed to elevated temperatures; meanwhile, the commercial graphite-like coating tended to remain at similarly low sp^3 content throughout. The doped lab-deposited coatings were a little more complicated to analyse as the metallic dopants increased the clustering of the sp^2 carbon rings in the films [116]. They both saw G peak shifts to higher wavelengths when exposed to high-temperature water, but the nature of the clustering of chromium and carbon in the film would need to be further analysed by TEM and EELS to determine what was happening to the coating nanostructure during the autoclave tests.

The results of the Raman spectroscopy would suggest that coatings with higher sp^2 content have better hydrothermal stability compared with those predominantly sp^3 bonded. Even if the graphitisation was not in itself the cause of the observed spallation this means that smaller changes would be expected in the other coating properties when exposed to high-temperature water. This stability would be useful when trying to predict their behaviour for tribological applications.

5.3 The effect of amorphous carbon coating compositions and structures on performance in high-temperature high-pressure water

The second aim of the EngD was to characterise the composition and structural features of the amorphous carbon coatings to try to understand their varying performance in autoclave conditions. Although the first part of the Engineering Doctorate project dealt with the hydrothermal stability of the coatings it was not yet clear what the degradation mechanism was that was causing the observed spallation of Coating Type A, or where in the coating structure it was occurring. It was also not yet apparent what it was about the structure and composition of the surviving coating types B, C and D that lent themselves to remaining attached while the other coating type delaminated.

The first objective for this experimental investigation involved determining the cause of the spallation seen in Coating Type A during the autoclave testing experiments by analysing the FIB cross-section of the degraded coating by SEM and EDX. This characterisation was necessary as it was not initially clear from the early experiments and investigations in this project whether the delamination was caused by chemical corrosion, a mechanical process, or even some combination of the two mechanisms. If the cause was obvious from these characterisation techniques it would have not been necessary to perform difficult and time-consuming TEM and EELS analysis of the samples.

The coating degradation mechanism in Coating Type A was first observed in the SEM micrographs of the FIB cross-sections, as seen in Figure 4.2. They showed an

underlying crack going through a layer in the coating from the edge of the spalled amorphous carbon film. The specific composition of the coating interlayer this crack was moving through was not immediately clear and it was apparent from the SEM and EDX that there were some very thin layers in the coating around this crack, some a few nanometres thick.

The backscattered SEM micrographs in Figures 4.3 and 4.7 showed the Z contrast of the elements present, the bright layer below the crack was from the chromium seen in the EDX spectroscopy. The EDX of the area around the crack was not sufficient to determine the variation in composition of the thin layers as shown in Figure 4.9 as the interaction volume of the EDX was too large, especially with elements with low atomic numbers [107]. The roughness of the sample would also have affected the EDX results in the SEM as the topology of the crack had many uneven features [108].

The presence of cracks through the coating with both nodular and relatively smooth cracked surfaces would suggest that the formation and degradation of the crack happens progressively during the autoclave exposure. There was also some degradation of the interlayer material ahead of the open cracked area which could possibly support a degradation mechanism where the corrosion was propagating through the material in the layer rather than just growing on the surface of an exposed crack.

Although the scanning electron microscopy provided some very interesting results the knowledge gained was not sufficient to complete the objective of determining the cause of the coating spallation. Further investigations were planned with the transmission electron microscope and electron energy loss spectroscopy to try to progress towards the aim of understanding the observed coating behaviour.

The STEM characterisation was conducted on Coating Types A, B, and C to try to determine the coating compositions and features responsible for each of their respective hydrothermal performances.

The first objective was to use a STEM, EELS and EDX study of Coating Type A to look at the as-received coating, the coating after the 7 day autoclave exposure, and the previous 2 year autoclave experiment to gain evidence to support possible degradation mechanisms.

The TEM, EELS and EDX of the as-received sample of Coating Type A in Figure 4.10 showed that the coating consisted of a Cr rich layer deposited onto the substrate, a CrN baselayer, transition layers into and out of another Cr rich layer, a layer of graded Cr and C, and an undoped amorphous carbon film.

One possibly proposed for the observed degradation was that the differing coefficients of thermal expansion for these coating materials was causing increased stress and subsequent delamination of the film when exposed to high-temperature high-pressure water in the autoclave.

It is possible to calculate the changes in stress arising from mismatch between the thermal expansion coefficients of the amorphous carbon film and the interlayer materials using the equation below [123]:

$$\sigma = \frac{E(\alpha_f - \alpha_s)\Delta T}{(1 - \nu)}$$

Where σ represents the stress, E relates to the elastic modulus of the film; α_f and α_s are the average coefficients of thermal expansion for the film and the substrate, ΔT is the

temperature change between when the coating was deposited and when it was measured, and finally ν which is the Poisson's ratio for the film.

By using typical values from the literature for diamond-like carbon films like Coating Type A the elastic modulus of the coating would be around 87 GPa and with a Poisson's ratio of around 0.22 [124], the coefficient of thermal expansion for the film would be around $2.0x10^{-6}$ K^{-1} [125] and $8.2x10^{-6}$ K^{-1} could be used for the chromium interlayer [126]. Typical deposition temperatures for Coating Type A would be below 250° C, so when the water was raised to 280° C in the autoclave ΔT becomes 30° C [127]. Therefore using these estimated values the stress due to thermal expansion coefficient mismatch between the film and interlayer at 280° C would be around 21 MPa tensile.

For graphite-like carbon films less data on the elastic modulus and Poisson's ratio exist in the literature. Data values for amorphous carbon coatings with higher sp^2 content were used to estimate the typical stress changes relative to the diamond-like carbon coatings. For this calculation the elastic modulus was estimated to be around 40GPa, the Poisson's ratio 0.20 , and the coefficient of thermal expansion $7.0x10^{-6}$ K^{-1} [125]. Typical deposition temperatures for similar coatings would be around 300° C [128]. Using these values the stress due to thermal expansion coefficient mismatch would be around 1.2MPa compressive.

In addition to these stresses due to thermal coefficient of expansion mismatch there would also be residual stresses in the coatings contributing to the total intrinsic stress. The internal stresses of DLC films are most commonly determined by measuring the curvature of a beam after coating deposition and then evaluating the deflection results using the Stoney equation [129]. Differing residual stresses arising from the deposition

techniques for each of the coatings could contribute to the behaviour when exposed to high temperature water. As previously discussed, Coating Type A would typically be deposited at temperatures below 250°C [127], whereas Coating Type B would have a typical deposition temperature of around 300°C [128]. The experiment raised the environmental temperature above the deposition temperature for Coating Type A but was below (or similar to) the temperature at which Coating Type B was deposited. Graphitisation of the coatings might help relieve some of the stresses present, but increased temperatures have also been shown to reduce the adhesion [130].

Evidence in the literature would suggest that these changes in intrinsic film stress with temperature alone would not be enough to cause the delamination seen in the characterisation recorded in this thesis. Amorphous carbon coatings are sometimes annealed post-deposition at temperatures well above the 280°C used in the autoclave to help reduce the stress in the film [131]. During previous Rolls-Royce Raman spectroscopy investigations there was also no recorded delamination of the amorphous carbon coatings when exposed to temperatures up to 600°C by using a heated stage in a nitrogen environment [1].

Due to the smaller differences in temperature between the autoclave and the typical deposition temperature, the calculations for stress arising from thermal expansion coefficient mismatch would suggest the coatings would actually have less additional stress than at room temperature. This would suggest another degradation mechanism associated with the exposure to high-temperature high-pressure water was causing the delamination observed in Coating Type A.

Following the microscopy and spectroscopy studies other possible degradation mechanisms were proposed. Based on the features observed before and after the

autoclave testing, a potential cause of coating failure could have been a stress corrosion cracking process similar to that seen in other pressurised water reactor materials in high-temperature water [132]. As mentioned previously in Sections 1.3.4 and 2.3, although materials used in the pressurised water reactor environment are often selected for their corrosion resistance, the stress corrosion cracking degradation mechanism is still a significant concern to the integrity of plant materials [87].

It was observed that Coating Type A remained largely unchanged below the Cr/C transition layer, although there was significant material degradation and volume change around the cracked area. The alterations in the appearance of the coating and the presence of oxygen in the EELS spectra strongly suggests that corrosion of the interlayer just below the amorphous carbon and carbon/chromium interlayer was involved in the delamination of the coating in the autoclave. In the sample exposed to the autoclave for 7 days failure of the coating was observed occurring just below the interface between the Cr/ C transition layer and the amorphous carbon functional layer above, with the degradation area just around the crack composed of chromium, carbon, and oxygen. The sample of Coating Type A that was exposed for 2 years in the CAPCIS autoclave as described in Section 2.4.2 showed further signs of degradation compared to the 7 day exposure as the volume of the layer containing carbon, chromium, and oxygen had increased below the amorphous carbon film.

A conduit through the amorphous carbon to the underlying chromium containing interlayer would have been necessary in order to initiate the degradation mechanism in these affected regions. Observations that support the possibility of this happening would be the defects or pinholes seen in the optical and scanning electron microscopy in

Sections 2.2 and 4.2. These defects could have acted as pathways through the relatively inert amorphous carbon down to the metal containing interlayers below [133].

Rather than the corrosion occurring between grains in a polycrystalline material, as observed in chromium containing alloys in high- temperature water [134], the degradation process could instead be occurring in the area just below the amorphous carbon, similar to the thin interlayer observed by Hauert *et al.* [79] in their study discussed earlier in the thesis of diamond-like carbon coating adhesion for *in vivo* biomedical applications.

In high-temperature water experiments performed by Moss *et al.* [135] intergranular stress corrosion cracking of chromium containing alloys was observed to occur due to the diffusion of chromium towards the grain boundaries, as shown in Figure 5.1. Grain boundary diffusion of chromium was caused by the ongoing formation of chromium

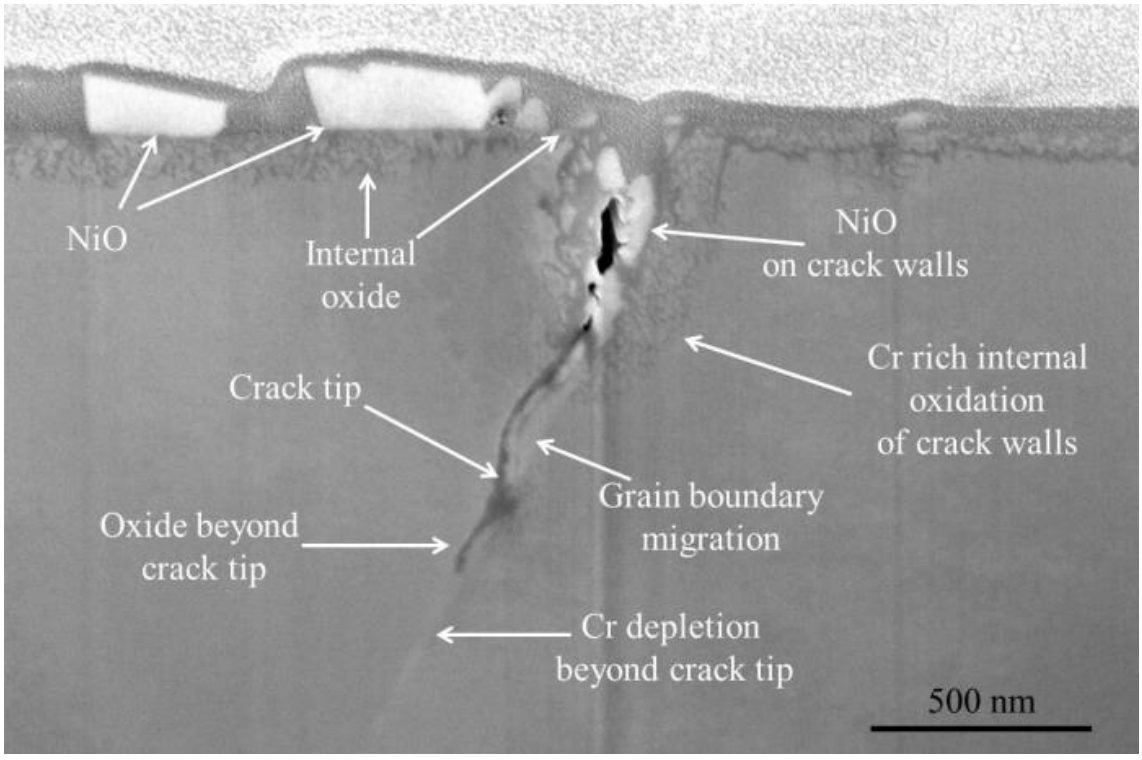

Figure 5.1 SEM of FIB cross-section showing intergranular cracking of Alloy 690 in water at 360°C [135].

oxide spinels in high temperature water, starting at the exposed surface of the material and then progressing preferentially along the grain boundaries [136]. The increased chromium oxide formation at the grain boundary was observed to act as a precursor to intergranular stress corrosion cracking in the material due depletion of ductile chromium being replaced by more brittle chromium oxide [137]. In this particular experiment the stress corrosion cracking was influenced by a strain applied to the specimens and the presence of NiO from the alloying material, however it has also been shown that the stress field induced between the newly formed chromium oxide corrosion product film and chromium depleted area can cause stress corrosion cracking at the grain boundary without this applied load [138].

It is possible that a similar degradation mechanism occurred in Coating Type A during the autoclave exposures. Defect pathways through the amorphous carbon film seen in the SEM could have acted as initiation sites for oxidation on the surface of the exposed chromium containing layer, which then penetrated the interlayer with plentiful chromium just below the amorphous carbon, similar to an intergranular attack [135]. The stress field induced between the corrosion product film and the amorphous carbon film could have then resulted in stress corrosion cracking moving through the observed degradation layer as seen in the micrographs in sections 4.2 and 4.3 of this thesis. As the crack progressed the surface energy of adhesion at this interface could release causing delamination of the stressed amorphous carbon film and further oxidation of the chromium as detected by the oxygen in the interlayer during EELS analysis in Section 4.3. To further support this degradation mechanism the SEM analysis in Figure 4.4 shows an area of the coating ahead of the crack tip that appears to have been degraded compared to the as-received coating, which could indicate oxidation and chromium depletion by diffusion, similar to that observed in Figure 5.1.

Another degradation mechanism that affects PWR materials in high-temperature water is hydrogen embrittlement [139]. It is also possible that the hydrogen in the a-C:H films could have diffused into the interlayer below the amorphous carbon during the autoclave exposure and caused hydrogen embrittlement contributing to the cohesive cracking seen in the layers of the film, which would not have been an issue with the hydrogen free amorphous carbon coatings. Further investigations into the movement of hydrogen in the coating before and after the autoclave experiments would be necessary to confirm whether or not hydrogen embrittlement exacerbated the spallation of the coating.

The other objectives of the STEM characterisation involved examining the as-received samples of Coating Types B and C to determine the coating features that provided the necessary performance to survive the autoclave conditions without film spallation.

The characterisation of Coating Type B showed the coating consisted of a CrN baselayer, on top of which was the typical commercial coating of a chromium adhesion layer, a graded Cr/C multilayer, and an undoped, relatively defect-free, amorphous carbon coating. Analysis of the multilayer structure showed that there were alternating chromium and carbon layers that increased in carbon content towards the amorphous carbon film. This structure would allow a smoother stress gradient across the interlayers to reduce adhesive failure of the coating and also reduce the concentration of chromium near the interface between the functional amorphous carbon and the interlayers for stress corrosion cracking to occur through defects in the film.

STEM and EELS of Coating Type C determined that the coating had a chromium-rich adhesion layer, on top of which was deposited a graded Cr/C layer, followed by a Cr doped amorphous carbon film. These graded interlayers should have allowed the

coating to maintain adherence during the autoclave exposure; however, there was evidence of property changes in the optical microscopy (and of hardness reductions during nanoindentation) that were not yet examined in depth experimentally. In order to fully complete this project objective further investigation into the lab-deposited coatings would be necessary to properly understand the effect of changing doping and interlayer materials.

The commercial coating deposition processes for attaching the amorphous carbon film to the interlayers may have had an effect on performance in autoclave conditions. Thin layers caused by switching between the deposition steps have the potential to cause complete failure of the coating if they are poorly bonded or cause localised structural or electrochemical mismatch between the two surfaces [79].

It is possible that the corrosion occurred in Coating Type A but was not observed in the other coatings, or at lower temperatures, as the stress arising from thermal expansion coefficient mismatch was tensile at 280°C the available pathways to the interlayers was increased, whereas the other coatings would tend to have compressive internal stress, closing possible gaps in the film. This could be explored further by performing corrosion investigations like the salt spray test to determine the porosity and corrosion resistance of the films [140].

5.4 Summary

This chapter discussed the results of the experimental procedures and how well the objectives were met, in order to fulfil the project aims.

The hydrothermal stability of the coatings was examined and the knowledge gained showed that the hydrogen-containing diamond-like hydrogen containing coating properties changed more and suffered partial delamination at higher temperatures whereas the more graphitic, hydrogen-free amorphous carbon coatings tended to stay mostly unchanged. There were some uncertainties with the experimental methods causing difficulty interpreting the data, but as discussed they would probably be resolved with further similar tests to refine and confirm the results obtained.

Significant progress was also made towards understanding how the composition and structure of the coatings affected their performance under hydrothermal degradation conditions. The combination of microscopy and spectroscopy results allowed various degradation mechanisms to be proposed and investigated for Coating Type A and they were backed up by supporting evidence from experiments and the literature. Suggestions were also made relating to the coating features that were responsible for the good performance exhibited by the other amorphous carbon coatings in the autoclave. Further work would be necessary to fully confirm different hypotheses and also to properly explore the effect of changing the metallic doping elements and interlayer structures with the lab-deposited coatings.

The final chapter in this thesis will conclude the investigations covered during the course of this Engineering Doctorate and also suggest avenues for further work to explore and consolidate knowledge and ideas proposed during the discussion chapter.

Chapter 6: Conclusions and further work

6.1 Conclusions

The overall aims of this Engineering Doctorate were to investigate the thermal stability of the amorphous carbon coatings when exposed to high-temperate high-pressure water and then to understand how the composition and features of the coatings affected their performance. It was anticipated that this would help Rolls-Royce to extend their knowledge of the suitability of amorphous carbon coatings in the desired application of pressurised water reactors. The conclusions of the project are listed below:

- Investigations into the hydrothermal stability of the coatings at the relatively low temperature of 240 °C showed that neither of the coating types exhibited any signs of significant degradation, and therefore might be of interest for future development in low temperature PWR systems.

- During the higher temperature autoclave experiments the commercial diamond-like hydrogen containing amorphous carbon Coating Type A had significant amorphous carbon film spallation whereas the commercial graphite-like amorphous carbon Coating Type B showed no delamination. The lab-deposited Cr and Ti doped amorphous carbon Coating Types C and D also showed no sign of film delamination. The results showed that favourable features from Coating Type B could also be used to deposit coatings that remained thermally stable in high-temperature high-pressure water, even when the interlayer material was changed from chromium to titanium.

- Raman spectroscopy and nanoindentation showed that the coatings that started out more diamond-like exhibited greater levels of graphitisation compared with the graphite-like carbon coating which mostly stayed the same. This shows that for tribological applications the graphite-like carbon coatings would probably have more stable material properties when exposed to high-temperature high-pressure water.

- Scratch adhesion testing in conjunction with estimated calculations of the stress arising from thermal coefficient of expansion mismatch were used to confirm the coatings had sufficient mechanical adhesion to the interlayer, which they did; suggesting the cause of the delamination in Coating Type A was at least partially influenced by corrosion instead.

- Investigations into the effect of composition and architecture in the hydrogen-free graphite-like coatings showed that coatings with smoothly graded interfaces between the chromium/ titanium containing multilayers and the defect free graphitic amorphous carbon displayed good hydrothermal stability performance at temperatures around 280°C.

- Degradation methods were proposed based on the observations of cracks propagating through a layer in Coating Type A just below the interface with the carbon. Stress corrosion cracking was discussed as a potential cause based on the results of the microscopy and spectroscopy investigations, however it was suggested that further work would be useful to confirm the influence of other possible processes like hydrogen embrittlement.

In summary, during this project there has been a lot of progress made towards the aims set out by Rolls-Royce at the start of the Engineering Doctorate. The knowledge gained about the stability of the amorphous carbon coatings in high-temperature high-pressure water has shown that all the coatings studied have potential for further development at the relatively low water temperatures, however graphite-like carbon coatings with smoothly graded interfaces tend to retain their properties better at the higher autoclave temperatures without delaminating.

The EngD also provided a greater understanding of why the coatings studied did or did not work well, with discussions of potential degradation mechanisms based on the microscopy and spectroscopy results; as well identifying common features that provide the graphite-like carbon coatings with good adhesion and stability. There few areas in which further work could expand and improve on the knowledge gained towards the project aims as discussed in the next section, however there is now a much better understanding of the degradation mechanism observed in the commercial diamond-like carbon coating and also the promising features and compositions that can used to develop amorphous carbon coatings for PWR applications.

6.2 Further work

Although there was significant knowledge gained during this study, there are a number of unresolved questions that should be explored with further experimentation.

- The project aim to better understand the hydrothermal stability of the coatings could be explored further by determining at which stage in the hydrothermal cycle the a-C:H coating fails; whether it fails straight away when it reaches a certain temperature or whether it fails after a longer exposure at the maximum testing temperature. Use of a windowed autoclave could help to determine the effect of the water heating rate on delamination. From the previous tests the coating starts to delaminate at some point in the 7 day exposure but it could potentially start to fail almost straight away during the process of heating up in the autoclave.

- Improvements on the progress of other objectives could involve the use of autoclave experiments using a high temperature autoclave with a window in combination with Raman spectroscopy to monitor the rate of graphitisation of the coating during the heating process throughout the experiment. An autoclave with a sliding wear tester built into the vessel construction could be also be used to conduct tribological tests to determine wear and friction performance of the coatings in the high-temperature high-pressure water environment, rather than ambient conditions [141].

- It would be useful for the project aim of understanding the effect of composition and coating structure on hydrothermal performance to perform some additional

STEM analysis of Coating Types B, C, and D after the 7 day autoclave tests, which would confirm whether there was any degradation in the interlayers, even though no coating delamination was observed in the optical microscopy.

- An experiment to further investigate the effect of coating composition and structure on hydrothermal performance could involve depositing various amorphous carbon films with different carbide forming interlayer materials like niobium, zirconium, or molybdenum to explore their effect on coating adhesion. These materials are already used in the PWR environment and might better control the thermal stresses related to the specific application compared with the Cr coatings often used commercially in the automotive industry. By keeping the amorphous carbon film the same and systematically changing the interlayer materials, it would be possible to directly compare the effect of the interlayer while keeping the rest of the coating structure the same. This could help Rolls-Royce to develop a bespoke amorphous carbon-based coating system, tailored specifically to the PWR environment, rather than using existing commercial coatings.

- In order to gain a better understanding of the observed degradation mechanism, techniques like electroconductivity analysis of the coatings by impedance spectroscopy or salt spray testing could be used to determine further information about their corrosion behaviour [142]. More STEM studies of samples autoclaved for shorter periods at the higher temperature could also reveal how the cracks are initiated and grow in the layer below the amorphous carbon film before significant spallation occurs.

- Later experiments at higher technology readiness levels could include autoclave tests with the chemical additives used in the PWR environment e.g. lithium hydroxide and boric acid, the effect of water flow on the localised corrosion, or the effect of irradiation on the coating properties, as it would also be interesting to determine what effect the actual reactor conditions have on the coating performance.

References

[1] A. J. Beck, J. Kavanagh, A. Leyland, A. Matthews "Characterisation and Evaluation of DLC Coatings, Rolls-Royce Project Report." 2014.

[2] E. E. Lewis, *Fundamentals of Nuclear Reactor Physics*, Elsevier Science, 2008.

[3] W. F. G. van Rooijen, "Gas-Cooled Fast Reactor: A Historical Overview and Future Outlook," *Science and Technology of Nuclear Installations*, 2009.

[4] *Heat Engines*. Available: http://www.nuclear-power.net/nuclear-engineering/thermodynamics/laws-of-thermodynamics/heat-engines/ (Last Accessed 3 July 2017)

[5] J. H. Rust, *Nuclear Power Safety*, Elsevier Science, 2013.

[6] V. K. M. Cheng and G. P. Hammond, "Life-cycle energy densities and land-take requirements of various power generators: A UK perspective," *Journal of the Energy Institute*, vol. 90, no. 2, pp. 201-213, 2017.

[7] G. L. Pavel, A. R. Budu, and D. E. Moraru, "Optimization of Energy Mix - Nuclear Power and Renewable Energy for Low Emissions Energy Source a Benefit for Generations to Come," *Energy Procedia*, vol. 112, pp. 412-417, 2017.

[8] *The Economics of Nuclear Power*. Available: http://www.world-nuclear.org/information-library/economic-aspects/economics-of-nuclear-power.aspx (Last Accessed 3 July 2017)

[9] *Safeguards to Prevent Nuclear Proliferation.* Available: http://www.world-nuclear.org/information-library/safety-and-security/non-proliferation/safeguards-to-prevent-nuclear-proliferation.aspx (Last Accessed 3 July 2017)

[10] S. Wheatley, B. K. Sovacool, and D. Sornette, "Reassessing the safety of nuclear power," *Energy Research & Social Science,* vol. 15, pp. 96-100, 2016.

[11] *Geological disposal*. Available: http://www.onr.org.uk/geodisposal.htm (Last Accessed 3 July 2017)

[12] *Nuclear Power in Japan*. Available: http://www.world-nuclear.org/information-library/country-profiles/countries-g-n/japan-nuclear-power.aspx (Last Accessed 3 July 2017)

[13] *Nuclear Power in Germany.* Available: http://www.world-nuclear.org/information-library/country-profiles/countries-g-n/germany.aspx (Last Accessed 3 July 2017)

[14] *Toshiba decides on Westinghouse bankruptcy, sees $9 billion in charges: sources.* Available: http://www.reuters.com/article/us-toshiba-accounting-idUSKBN16V04G (Last Accessed 3 July 2017)

[15] *French watchdog deepens probes into Areva nuclear parts.* Available: https://www.ft.com/content/2baf6270-c36a-11e6-81c2-f57d90f6741a?mhq5j=e1 (Last Accessed 3 July 2017)

[16] A. Gilbert, B. K. Sovacool, P. Johnstone, and A. Stirling, "Cost overruns and financial risk in the construction of nuclear power reactors: A critical appraisal," *Energy Policy,* vol. 102, pp. 644-649, 2017.

[17] *Rolls-Royce wins contract to help extend lifetime of Dungeness B nuclear power station.* Available: http://www.rolls-royce.com/media/press-releases/yr-2015/pr-210115-nuclear-power-station.aspx (Last Accessed 3 July 2017)

[18] T. Allen, J. Busby, M. Meyer and D. Petti, "Materials challenges for nuclear systems," *Materials Today 13*, no. 12, pp. 14-23, 2010.

[19] *Nuclear Power Reactors.* Available: http://www.world-nuclear.org/information-library/nuclear-fuel-cycle/nuclear-power-reactors/nuclear-power-reactors.aspx (Last Accessed 3 July 2017)

[20] S. Glasstone and A. Sesonske, *Nuclear Reactor Engineering: Reactor systems engineering*, Chapman & Hall, 1994.

[21] *Pressurized Water Reactor (PWR) Systems.* Available: https://www.nrc.gov/reading-rm/basic-ref/students/for-educators/04.pdf (Last Accessed 3 July 2017)

[22] *Energy density calculations of nuclear fuel.* Available: https://whatisnuclear.com/physics/energy_density_of_nuclear.html (Last Accessed 3 July 2017)

[23] *Nuclear-Powered Ships.* Available: http://www.world-nuclear.org/information-library/non-power-nuclear-applications/transport/nuclear-powered-ships.aspx (Last Accessed 3 July 2017)

[24] D. Kaczorowski, P. Combrade, J. P. Vernot, A. Beaudouin, and C. Crenn, "Water chemistry effect on the wear of stainless steel in nuclear power plant," *Tribology International,* vol. 39, no. 12, pp. 1503-1508, 2006.

[25] *A Short Introduction to Corrosion and its Control.* Available: http://www.npl.co.uk/upload/pdf/basics_of_corrosion_control.pdf (Last Accessed 3 July 2017)

[26] J. Chen, Q. Xiao, Z. Lu, X. Ru, H. Peng, Q. Xiong, and H. Li, "Characterization of interfacial reactions and oxide films on 316L stainless steel in various simulated PWR primary water environments," *Journal of Nuclear Materials,* vol. 489, pp. 137-149, 2017.

[27] P. Kunstadt and W. Gibson, "Transport of cobalt-60 industrial radiation sources," *International Journal of Radiation Applications and Instrumentation. Part C. Radiation Physics and Chemistry,* vol. 35, no. 4–6, pp. 551-559, 1990.

[28] P. M. Scott, "Environment-Sensitive Cracking Problems in Nuclear Installations Containing High Temperature Water A review of environment-sensitive fracture in water reactor materials," *Corrosion Science,* vol. 25, no. 8, pp. 583-606, 1985.

[29] S. De Flora, M. Bagnasco, D. Serra, and P. Zanacchi, "Genotoxicity of chromium compounds. A review," *Mutation Research/Reviews in Genetic Toxicology,* vol. 238, no. 2, pp. 99-172, 1990.

[30] *Zirconium Cladding is the Reactor's Primary Safety Barrier.* Available: http://www.areva.com/EN/operations-2294/zirconium-cladding-is-the-reactors-primary-safety-barrier.html (Last Accessed 3 July 2017)

[31] D. Hertz, "Nuclear fuel assembly with coated sheaths and a method of coating such sheaths," *US4849160A,* 1989.

[32] W. H. Roberts, "Tribology in nuclear power generation," *Tribology International,* vol. 14, no. 1, pp. 17-28, 1981.

[33] F. Cataldo, "A Raman study on radiation-damaged graphite by γ-rays," *Carbon,* vol. 38, no. 4, pp. 634-636, 2000.

[34] *Submarines Capability.* Available: https://www.rolls-royce.com/products-and-services/marine/about-marine/market-sectors/submarines.aspx (Last Accessed 3 July 2017)

[35] *Five reasons why the UK needs Small Modular Reactors*. Available: https://www.rolls-royce.com/products-and-services/nuclear/why-uk-needs-smrs.aspx (Last Accessed 3 July 2017)

[36] *Less Is More for Designers of "Right-Sized" Nuclear Reactors.* Available: https://www.scientificamerican.com/article/small-nuclear-power-plant-station-mini-reactor/ (Last Accessed 3 July 2017)

[37] M. Lehtveer and F. Hedenus, "How much can nuclear power reduce climate mitigation cost? – Critical parameters and sensitivity," *Energy Strategy Reviews,* vol. 6, pp. 12-19, 2015.

[38] J. Robertson, "Diamond-like amorphous carbon," *Materials Science and Engineering: R: Reports,* vol. 37, no. 4-6, pp. 129-281, 2002.

[39] A. K. Geim and A. H. MacDonald, "Graphene: Exploring Carbon Flatland," *Physics Today,* vol. 60, no. 8, pp. 35-41, 2007.

[40] R. Lv and M. Terrones, "Towards new graphene materials: Doped graphene sheets and nanoribbons," *Materials Letters,* vol. 78, pp. 209-218, 2012.

[41] C. Lee, X. Wei, J. W. Kysar, and J. Hone, "Measurement of the Elastic Properties and Intrinsic Strength of Monolayer Graphene," *Science,* vol. 321, no. 5887, pp. 385-388, July 18, 2008.

[42] J. Lee, S. Cho, Y. Hwang, H. Cho, C. Lee, Y. Choi, B. Ku, H. Lee, B. Lee, D. Kim, and S. Kim, "Application of fullerene-added nano-oil for lubrication enhancement in friction surfaces," *Tribology International,* vol. 42, no. 3, pp. 440-447, 2009.

[43] S. V. Hainsworth and N. J. Uhure, "Diamond like carbon coatings for tribology: production techniques, characterisation methods and applications," *International Materials Reviews,* vol. 52, no. 3, pp. 153-174, 2007.

[44] S. K. Field, M. Jarratt, and D. G. Teer, "Tribological properties of graphite-like and diamond-like carbon coatings," *Tribology International,* vol. 37, no. 11–12, pp. 949-956, 2004.

[45] J. Robertson, "Deposition mechanisms for promoting sp3 bonding in diamond-like carbon," *Diamond and Related Materials,* vol. 2, no. 5–7, pp. 984-989, 1993.

[46] M. Zhong, C. Zhang, and J. Luo, "Effect of substrate morphology on the roughness evolution of ultra thin DLC films," *Applied Surface Science,* vol. 254, no. 21, pp. 6742-6748, 2008.

[47] S. Aisenberg and R. Chabot, "Ion-Beam Deposition of Thin Films of Diamond like Carbon," *Journal of Applied Physics,* vol. 42, no. 7, pp. 2953-2958, 1971.

[48] E. G. Spencer, P. H. Schmidt, D. C. Joy, and F. J. Sansalone, "Ion-beam-deposited polycrystalline diamond like films," *Applied Physics Letters,* vol. 29, no. 2, pp. 118-120, 1976.

[49] A. Bubenzer, B. Dischler, G. Brandt, and P. Koidl, "rf-plasma deposited amorphous hydrogenated hard carbon thin films: Preparation, properties, and applications," *Journal of Applied Physics,* vol. 54, no. 8, pp. 4590-4595, 1983.

[50] J. A. Thornton, "The microstructure of sputter-deposited coatings," *Journal of Vacuum Science & Technology A: Vacuum, Surfaces, and Films,* vol. 4, no. 6, pp. 3059-3065, 1986.

[51] D. Depla, S. Mahieu, J. E. Greene, and M. M. Peter, "Chapter 5 - Sputter Deposition Processes," in *Handbook of Deposition Technologies for Films and Coatings (Third Edition)*Boston: William Andrew Publishing, pp. 253-296, 2010.

[52] G. Alfred, "Diamond-like carbon: state of the art," *Diamond and Related Materials,* vol. 8, no. 2-5, pp. 428-434, 1999.

[53] J. Robertson, "Hard amorphous (diamond-like) carbons," *Progress in Solid State Chemistry,* vol. 21, no. 4, pp. 199-333, 1991.

[54] Y. Lifshitz, "Diamond-like carbon - present status," *Diamond and Related Materials,* vol. 8, no. 8-9, pp. 1659-1676, 1999.

[55] L. Martinu, O. Zabeida, J. E. Klemberg-Sapieha, and M. M. Peter, "Chapter 9 - Plasma-Enhanced Chemical Vapor Deposition of Functional Coatings," in *Handbook of Deposition Technologies for Films and Coatings (Third Edition)* Boston: William Andrew Publishing, pp. 392-465, 2010.

[56] A. L. Yerokhin, A. Leyland, C. Tsotsos, A. D. Wilson, X. Nie, and A. Matthews, "Duplex surface treatments combining plasma electrolytic nitrocarburising and plasma-immersion ion-assisted deposition," *Surface and Coatings Technology,* vol. 142–144, pp. 1129-1136, 2001.

[57] X. Zhou, Y. X. Leng, H. Sun, and N. Huang, "The structure and adhesion of hydrogenated amorphous carbon (a-C:H) films synthesized on CoCrMo alloy by plasma immersion ion implantation and deposition at different flow ratios of acetylene to argon," *Surface and Coatings Technology,* vol. 206, no. 5, pp. 994-998, 2011.

[58] A. Mitsuo, S. Uchida, K. Morikawa, M. Kawaguchi, K. Shiotani, and H. Suzuki, "Effect of deposition parameter on hardness of amorphous carbon film prepared by plasma immersion ion implantation using C2H2," *Nuclear Instruments and Methods in Physics Research Section B: Beam Interactions with Materials and Atoms,* vol. 257, no. 1–2, pp. 753-757, 2007.

[59] M. Xu, W. Zhang, Z. Wu, S. Pu, L. Li, and P. K. Chu, "Mechanical properties of tungsten doped amorphous hydrogenated carbon films prepared by tungsten plasma immersion ion implantation," *Surface and Coatings Technology,* vol. 203, no. 17–18, pp. 2612-2616, 2009.

[60] B. P. Wood, I. Henins, W. A. Reass, D. J. Rej, H. A. Davis, W. J. Waganaar, R. E. Muenchausen, G. P. Johnston, and H. K. Schmidt, "Large-scale implantation and deposition research at Los Alamos National Laboratory," *Nuclear Instruments and Methods in Physics Research Section B: Beam Interactions with Materials and Atoms*, vol. 96, no. 1, pp. 429-434, 1995.

[61] S. P. Bugaev, K. V. Oskomov, and N. S. Sochugov, "Deposition of highly adhesive amorphous carbon films with the use of preliminary plasma-immersion ion implantation," *Surface and Coatings Technology*, vol. 156, no. 1–3, pp. 311-316, 2002.

[62] W. Jacob and W. Moller, "On the structure of thin hydrocarbon films," *Applied Physics Letters*, vol. 63, no. 13, pp. 1771-1773, 1993.

[63] K. Bewilogua and D. Hofmann, "History of diamond-like carbon films - from first experiments to worldwide applications," *Surface and Coatings Technology*, vol. 242, pp. 214-225, 2014.

[64] D. R. McKenzie, "Tetrahedral bonding in amorphous carbon," *Reports on Progress in Physics*, vol. 59, no. 12, p. 1611, 1996.

[65] C. Donnet, "Recent progress on the tribology of doped diamond-like and carbon alloy coatings: a review," *Surface and Coatings Technology*, vol. 100-101, pp. 180-186, 1998.

[66] P. Wang, X. Wang, T. Xu, W. Liu, and J. Zhang, "Comparing internal stress in diamond-like carbon films with different structure," *Thin Solid Films*, vol. 515, no. 17, pp. 6899-6903, 2007.

[67] J. Wang Jing and Liu Gui-Chang and Wang Li-Da and Deng Xin-Lü and Xu, "Studies of diamond-like carbon (DLC) films deposited on stainless steel substrate with Si/SiC intermediate layers," *Chinese Physics B,* vol. 17, no. 8, p. 3108, 2008.

[68] S. J. Zinkle and G. S. Was, "Materials challenges in nuclear energy," *Acta Materialia,* vol. 61, no. 3, pp. 735-758, 2013.

[69] K. Holmberg, A. Matthews, and H. Ronkainen, "Coatings tribology—contact mechanisms and surface design," *Tribology International,* vol. 31, no. 1-3, pp. 107-120, 1998.

[70] S. Neuville and A. Matthews, "A perspective on the optimisation of hard carbon and related coatings for engineering applications," *Thin Solid Films,* vol. 515, no. 17, pp. 6619-6653, 2007.

[71] H. Ronkainen, S. Varjus, and K. Holmberg, "Friction and wear properties in dry, water- and oil-lubricated DLC against alumina and DLC against steel contacts," *Wear,* vol. 222, no. 2, pp. 120-128, 1998.

[72] J. M. Calderón-Moreno, "Stability of diamond-like carbon in hydrothermal conditions," *Diamond and Related Materials,* vol. 15, no. 4–8, pp. 958-961, 2006.

[73] D. R. Tallant, J. E. Parmeter, M. P. Siegal, and R. L. Simpson, "The thermal stability of diamond-like carbon," *Diamond and Related Materials,* vol. 4, no. 3, pp. 191-199, 1995.

[74] J. Andersson, R. A. Erck, and A. Erdemir, "Friction of diamond-like carbon films in different atmospheres," *Wear,* vol. 254, no. 11, pp. 1070-1075, 2003.

[75] D. Drees, J. P. Celis, E. Dekempeneer, and J. Meneve, "The electrochemical and wear behaviour of amorphous diamond-like carbon coatings and multilayered coatings in aqueous environments," *Surface and Coatings Technology,* vol. 86–87, Part 2, pp. 575-580, 1996.

[76] L. Chandra, M. Allen, R. Butter, N. Rushton, A. H. Lettington, and T. W. Clyne, "The effect of exposure to biological fluids on the spallation resistance of diamond-like carbon coatings on metallic substrates," *Journal of Materials Science: Materials in Medicine,* vol. 6, no. 10, pp. 581-589, 1995.

[77] M. Masuko, T. Kudo, and A. Suzuki, "Effect of Surface Roughening of Substrate Steel on the Improvement of Delamination Strength and Tribological Behavior of Hydrogenated Amorphous Carbon Coating Under Lubricated Conditions," *Tribology Letters,* vol. 51, no. 2, pp. 181-190, 2013.

[78] J. Stallard, D. Mercs, M. Jarratt, D. G. Teer, and P. H. Shipway, "A study of the tribological behaviour of three carbon-based coatings, tested in air, water and oil environments at high loads," *Surface and Coatings Technology,* vol. 177–178, pp. 545-551, 2004.

[79] R. Hauert, K. Thorwarth, and G. Thorwarth, "An overview on diamond-like carbon coatings in medical applications," *Surface and Coatings Technology,* vol. 233, pp. 119-130, 2013.

[80] D. C. Sutton, G. Limbert, B. Burdett, and R. J. K. Wood, "Interpreting the effects of interfacial chemistry on the tribology of diamond-like carbon coatings against steel in distilled water," *Wear,* vol. 302, no. 1–2, pp. 918-928, 2013.

[81] A. Matthews and S. S. Eskildsen, "Engineering applications for diamond-like carbon," *Diamond and Related Materials,* vol. 3, no. 4–6, pp. 902-911, 1994.

[82] V. Fox, A. Jones, N. M. Renevier, and D. G. Teer, "Hard lubricating coatings for cutting and forming tools and mechanical components," *Surface and Coatings Technology,* vol. 125, no. 1-3, pp. 347-353, 2000.

[83] R. Hauert and U. Müller, "An overview on tailored tribological and biological behavior of diamond-like carbon," *Diamond and Related Materials,* vol. 12, no. 2, pp. 171-177, 2003.

[80] R. K. Roy and K.-R. Lee, "Biomedical applications of diamond-like carbon coatings: A review," *Journal of Biomedical Materials Research Part B: Applied Biomaterials,* vol. 83B, no. 1, pp. 72-84, 2007.

[81] A. Leyland and A. Matthews, "On the significance of the H/E ratio in wear control: a nanocomposite coating approach to optimised tribological behaviour," *Wear,* vol. 246, no. 1-2, pp. 1-11, 2000.

[82] V. Fox, A. Jones, N. M. Renevier and D. G. Teer, “Hard lubricating coatings for cutting and forming tools and mechanical components,” *Surface and Coatings Technology*, vol. 125, no. 1-3, pp. 347-353, 2000.

[83] R. Hauert and U. Müller, “An overview on tailored tribological and biological behavior of diamond-like carbon,” *Diamond and Related Materials,* vol. 12, pp. 171-177, 2003.

[84] R. K. Roy and K.-R. Lee, “Biomedical applications of diamond-like carbon coatings: A review,” *Journal of Biomedical Materials Research Part B: Applied Biomaterials,* pp. 72-84, 2007.

[85] J. C. Sánchez-López and A. Fernández, "Doping and alloying effects on dlc coatings," *Tribology of diamond-like carbon films: Fundamentals and applications,* pp. 311-338, 2008.

[86] A. Leyland and A. Matthews, On the significance of the h/e ratio in wear control: A nanocomposite coating approach to optimised tribological behaviour, *Wear,* vol. 246, no. 1-2, pp. 1-11, 2000.

[87] J. Gupta, J. Hure, B. Tanguy, L. Laffont, M. C. Lafont, and E. Andrieu, "Evaluation of stress corrosion cracking of irradiated 304L stainless steel in PWR environment using heavy ion irradiation," *Journal of Nuclear Materials,* vol. 476, pp. 82-92, 2016.

[88] *Stainless Steel - Grade 304.* Available: https://www.azom.com/article.aspx?articleid=965 (Last Accessed 13 August 2018)

[89] B. Gordon, Corrosion and corrosion control in light water reactors, *JOM*, 2013.

[90] *431 Martensitic Stainless Steel Bar.* Available: http://www.interlloy.com.au/our-products/stainless-steel/431-martensitic-stainless-steel-bar/ (Last Accessed 3 July 2017)

[91] I. Hemmati, V. Ocelík, and J. T. M. De Hosson, "The effect of cladding speed on phase constitution and properties of AISI 431 stainless steel laser deposited coatings," *Surface and Coatings Technology,* vol. 205, no. 21–22, pp. 5235-5239, 2011.

[92] *HAYNES® 25 alloy.* Available: http://haynesintl.com/docs/default-source/pdfs/new-alloy-brochures/high-temperature-alloys/25-brochure.pdf?sfvrsn=6 (Last Accessed 3 July 2017)

[93] *Model 4744 General Purpose Acid Digestion Vessel, 45 mL.* Available: http://www.parrinst.com/products/sample-preparation/acid-digestion/general-purpose-acid-digestion-vessel-model-4744-45-ml/ (Last Accessed 3 July 2017)

[94] *Materials research in the Manufacturing Technology Research Laboratory.* Available: http://www.dalton.manchester.ac.uk/research/manufacturingtechnologyresearchlaboratory/materials/ (Last Accessed 3 July 2017)

[95] S. J. Bull, "Failure modes in scratch adhesion testing," *Surface and Coatings Technology,* vol. 50, no. 1, pp. 25-32, 1991.

[96] S. J. Bull, D. S. Rickerby, A. Matthews, A. Leyland, A. R. Pace and J. Valli, "The use of scratch adhesion testing for the determination of interfacial adhesion: The importance of frictional drag," *Surface and Coatings Technology,* vol. 36, no. 1, pp. 503-517, 1988.

[97] W. C. Oliver and G. M. Pharr, "Measurement of hardness and elastic modulus by instrumented indentation: Advances in understanding and refinements to methodology," *Journal of Materials Research*, vol. 19, no. 1, pp. 3-20, 2011.

[98] W. C. Oliver and G. M. Pharr, "An improved technique for determining hardness and elastic modulus using load and displacement sensing indentation experiments," *Journal of Materials Research*, vol. 7, no. 6, pp. 1564-1583, 1992.

[99] N. A. Sakharova, J. V. Fernandes, J. M. Antunes, and M. C. Oliveira, "Comparison between Berkovich, Vickers and conical indentation tests: A three-dimensional numerical simulation study," *International Journal of Solids and Structures*, vol. 46, no. 5, pp. 1095-1104, 2009.

[100] R. Saha and W. D. Nix, "Effects of the substrate on the determination of thin film mechanical properties by nanoindentation," *Acta Materialia*, vol. 50, no. 1, pp. 23-38, 2002.

[101] A. C. Ferrari and J. Robertson, "Interpretation of raman spectra of disordered and amorphous carbon," *Physical Review B 61*, no. 20, 14095-14107, 2000.

[102] J. R. Ferraro and K. Nakamoto, *Introductory Raman Spectroscopy*. Elsevier Science, 2012.

[103] A. C. Ferrari, "Determination of bonding in diamond-like carbon by Raman spectroscopy," *Diamond and Related Materials*, vol. 11, no. 3–6, pp. 1053-1061, 2002.

[104] J. Robertson, "Electronic structure of diamond-like carbon," *Diamond and Related Materials.* vol. 6, no. 2, pp. 212-218, 1997.

[105] S.-H. Hong and J. Winter, "Micro-Raman spectroscopy on a-C:H nanoparticles," *Journal of Applied Physics,* vol. 98, no. 12, 124304, 2005.

[106] L. A. Giannuzzi and F. A. Stevie, "A review of focused ion beam milling techniques for TEM specimen preparation," *Micron,* vol. 30, no. 3, pp. 197-204, 1999.

[107] *Sample-Electron Interaction.* Available: http://www.nanoscience.com/technology/sem-technology/sample-electron-interaction/ (Last Accessed 3 July 2017)

[108] *Scanning Electron Microscopy Primer.* Available: http://www.charfac.umn.edu/sem_primer.pdf (Last Accessed 3 July 2017)

[109] P. Hawkes and L. Reimer, *Scanning Electron Microscopy: Physics of Image Formation and Microanalysis*, Springer Berlin Heidelberg, 2013.

[110] B. K. E. MacArthur, "The Use of Annular Dark-Field Scanning Transmission Electron Microscopy for Quantitative Characterisation," *Johnson Matthey Technology Review,* vol. 60, no. 2, pp. 117-131, 2016.

[111] T. Walther and I. M. Ross, "Aberration Corrected High-Resolution Transmission and Scanning Transmission Electron Microscopy of Thin Perovskite Layers," *Physics Procedia,* vol. 40, pp. 49-55, 2013.

[112] *EELS Overview.* Available: http://www.gatan.com/techniques/eels (Last Accessed 3 July 2017)

[113] C. Casiraghi, A. C. Ferrari and J. Robertson, "Raman spectroscopy of hydrogenated amorphous carbons," *Physical Review*, no. 8, 085401, 2005.

[114] C. Ziebert, M. Rinke, M. Stüber, S. Ulrich and H. Holleck, “Interfaces and temperature stability of stepwise graded dlc films studied by nanoindentation and raman spectroscopy,” *Surface and Coatings Technology*, vol. 200, no. 1, pp. 1127-1131, 2005.

[115] D. Savchenko, V. Vorlíček, A. Prokhorov, E. Kalabukhova, J. Lančok and M. Jelínek, “Raman and epr spectroscopic studies of chromium-doped diamond-like carbon films,” *Diamond and Related Materials*, vol. 83, pp. 30-37, 2018.

[116] M.-C. Chiu, W.-P. Hsieh, W.-Y. Ho, D.-Y. Wang and F.-S. Shieu, “Thermal stability of cr-doped diamond-like carbon films synthesized by cathodic arc evaporation,” *Thin Solid Films*, vol. 476, no. 2, pp. 258-263, 2005.

[117] L. Lajaunie, C. Pardanaud, C. Martin, P. Puech, C. Hu, M. J. Biggs and R. Arenal, “Advanced spectroscopic analyses on a:C-h materials: Revisiting the eels characterization and its coupling with multi-wavelength raman spectroscopy,” *Carbon*, vol. 112, pp.149-161, 2017.

[118] *Chromium Oxide (Chromia).* Avialable: https://eelsdb.eu/spectra/chromium-oxide-chromia/ (Last Accessed 13 August 2018)

[119] *Tribological testing of DLC coatings for automotive applications.* Available: http://www.diva-portal.org/smash/get/diva2:540693/fulltext01.pdf (Last Accessed 13 August 2018)

[120] C. Heau, L. Bombillon, P. Maurin-Perrier, “Part having a DLC coating and method for applying the DLC coating,” *US9103016*, 2011.

[121] *The Deposition, Tribological Properties, and Applications of Sputtered Carbon Coatings.* Available: http://www.teercoatings.co.uk/files/23_sue1.pdf (Last Accessed 13 August 2018)

[122] W.-G. Jiang, J.-J. Su and X.-Q. Feng, "Effect of surface roughness on nanoindentation test of thin films," *Engineering Fracture Mechanics,* vol. 75, no. 17, 4965-4972, 2008.

[123] *Compilation of diamond-like carbon properties for barriers and hard coatings.* Available: http://www.osti.gov/scitech/servlets/purl/10132872-70Cckc/native/ (Last Accessed 3 July 2017)

[124] S.-J. Cho, K.-R. Lee, Y. Kwang, Eun, J. Hee Hahn and D.-H. Ko, "Determination of elastic modulus and poisson's ratio of diamond-like carbon films", *Thin Solid Films,* vol. 341, pp. 207-210, 1999.

[125] F. C. Marques, R. G. Lacerda, A. Champi, V. Stolojan, D. C. Cox and S. R. P. Silva, "Thermal expansion coefficient of hydrogenated amorphous carbon," *Applied Physics Letters,* vol. 83 no. 15, 3099-3101, 2003.

[126] *Thermal Expansion,* Available: http://www.owlnet.rice.edu/~msci301/ThermalExpansion.pdf (Last Accessed 13 August 2018)

[127] T. Jabs, M. Scharf, M. Grischke, and O. Massler, "DLC (diamond-like carbon) hard coating on copper based material for bearings," *US20050242156A1*, 2004.

[128] *Graphit-iC™ Coatings.* Available: http://www.teercoatings.co.uk/index.php?page=40 (Last Accessed 13 August 2018)

[129] S. Shiri, P. Ashtijoo, A. Odeshi and Q. Yang, "Evaluation of stoney equation for determining the internal stress of dlc thin films using an optical profiler," *Surface and Coatings Technology*, vol. 308, pp. 98-100, 2016.

[130] H. W. Choi, M.-W. Moon, T.-Y. Kim, K.-R. Lee and K. H. C. U. Oh, "The thermal annealing effect on the residual stress and interface adhesion in the compressive stressed dlc film," *MRS Proceedings 795*, U11.42, 2003.

[131] C. Donnet and A. Erdimir, "Tribology of diamond-like carbon films," *Springer US*, 2008.

[132] X. Liu, W. Hwang, J. Park, D. Van, Y. Chang, S. H. Lee, S.-Y. Kim, S. Han and B. Lee, "Toward the multiscale nature of stress corrosion cracking," *Nuclear Engineering and Technology*, vol. 50, no. 1, pp. 1-17, 2018.

[133] J. W. Yi, S. J. Park, M.-W. Moon, K.-R. Lee and S.-S. Kim, "Defect effect on tribological behavior of diamond-like carbon films deposited with hydrogen diluted benzene gas in aqueous environment," *Applied Surface Science*, vol. 255, no. 15, 7005-7011, 2009.

[134] T. Terachi, T. Yamada, T. Miyamoto and K. Arioka, "Scc growth behaviors of austenitic stainless steels in simulated pwr primary water," *Journal of Nuclear Materials*, vol. 426, no. 1, 59-70, 2012.

[135] T. Moss and G. S. Was, "Accelerated stress corrosion crack initiation of alloys 600 and 690 in hydrogenated supercritical water," *Metallurgical and Materials Transactions,* vol. 48, no. 4, 1613-1628, 2017.

[136] K. Kruska, S. Lozano-Perez, D. W. Saxey, T. Terachi, T. Yamada and G. D. W. Smith, "Nanoscale characterisation of grain boundary oxidation in cold-worked stainless steels," *Corrosion Science,* vol. 63, pp. 225-233, 2012.

[137] R. P. Matthews, R. D. Knusten, J. E. Westraadt and T. Couvant, "Intergranular oxidation of 316l stainless steel in the pwr primary water environment," *Corrosion Science,* vol. 125, pp. 175-183, 2017.

[138] W. Wang, Z. Zhang, X. Ren, Y. Guan and Y. Su, "Corrosion product film-induced stress facilitates stress corrosion cracking," *Scientific Reports,* vol. 5 10579, 2015.

[139] *Hydrogen Embrittlement.* Available: https://www.nace.org/corrosion-central/corrosion-101/hydrogen-embrittlement/ (Last Accessed 13 August 2018)

[140] J. L. Daure, K. T. Voisey, P. H. Shipway and D. A. Stewart, "The effect of coating architecture and defects on the corrosion behaviour of a pvd multilayer inconel 625/Cr coating," *Surface and Coatings Technology,* vol. 324, pp. 403-412, 2017.

[141] K.-y. Lee, S.-h. Lee, Y. Kim, H. S. Hong, Y.-m. Oh and S.-j. Kim, "The effects of additive elements on the sliding wear behavior of fe-base hardfacing alloys," *Wear,* vol. 255, no. 1, pp. 481-488, 2003.

[142] F. Indeir, A. Matthews, and A. Leyland, "Development of (AC)DC/AC Cyclic Electrochemical Corrosion Evaluation Protocols for Accelerated Testing of PVD Metallic Coatings," *Society of Vacuum Coaters Annual Technical Conference Proceedings*, 2017.